DISS. ETH NO. 30321

Low-Excitation Shuttling and Separation of Mixed-Species Ion Crystals for Scalable Quantum Information Processing

A thesis submitted to attain the degree of

DOCTOR OF SCIENCES

(Dr. sc. ETH ZÜRICH)

presented by

FRANCESCO LANCELLOTTI

Master of Science in Physics of Complex Systems,
Polytechnic University of Turin

born on 26.01.1993

accepted on the recommendation of

Prof. Dr. J. P. Home
Prof. Dr. F. Schmidt-Kaler

2024

Abstract

Trapped ions are among the leading candidates for universal quantum computing, thanks to their proven high level of control and extended coherence times. However, scalability remains one of the main challenges to overcome. Several proposals have been made, with one of the most promising solutions involving the use of multi-zone traps with mixed-species ion crystals. This approach allows for operations on the individual species with highly suppressed cross-talk, thanks to their spectral isolation. This includes cooling one species while storing quantum information in the other. High-quality shuttling and reconfiguration of the crystals in different zones are crucial in this architecture.

In this thesis, we demonstrate various elements necessary to work with scalable mixed-species ion trap architectures. One of the main achievements is the demonstration of low-excitation transport and separation of single-species ion crystals of up to 7 ions and mixed-species arrays of up to 4 ions, composed of ionic calcium and beryllium. We optimize inter-zone transport of two-ion mixed-species crystals, achieving excitations as low as $\bar{n}_{\mathrm{Z1}} = 0.16(2)$ and $\bar{n}_{\mathrm{Z2}} = 0.14(2)$ quanta for the axial in-phase and out-of-phase modes, respectively. We present the separation of two-ion single-species crystals with excitations of $\bar{n}_{Be} < 0.8$ and $\bar{n}_{Ca} < 2.3$ quanta for beryllium and calcium respectively. In the mixed-species case, additional control challenges arose due to stronger sensitivity to radial electric fields, which induces mass-dependent twists of the ion chains, and to the coupling of normal modes of motion, exacerbated by the high mass ratio of 4.4 for these species. For the two-ion arrays we achieve excitation as low as $\bar{n}_{\mathrm{Be}} = 1.44(9)$ and $\bar{n}_{\mathrm{Ca}} = 1.40(8)$ quanta. These findings are also relevant for architectures for quantum-logic-based spectroscopy of exotic species.

We apply the theory of Landau-Zener-Stückelberg–Majorana transitions to study the coupling of normal modes of motion and develop methods for tuning its strength to enhance or inhibit the transfer of heat. The tunable coupling is employed to demonstrate the manipulation of motional states, where consecutive multiple interactions give rise to interferometric measurements.

We describe a comprehensive framework we developed and expanded in functionalities for controlling the electrode potentials, which manipulate ion positions, and demonstrate its employment. We examine the underlying model of the trap potentials through automated routines, establishing a method for initial verification of experimental deviations from an ideal simulation.

Riassunto

Gli ioni intrappolati sono tra i principali candidati per l' implementazione di computer quantistici, grazie al loro comprovato alto livello di controllo e ai prolungati tempi di coerenza. Tuttavia, la scalabilità rimane una delle principali sfide da superare. Sono state avanzate diverse proposte per fronteggiare questo problema, e una delle soluzioni più promettenti coinvolge l'uso di trappole multi-zona con cristalli di ioni di specie miste. Questo approccio consente operazioni sulle specie individuali con un cross-talk altamente soppresso, grazie al loro isolamento spettrale. Ciò include il raffreddamento di una specie mentre si memorizzano informazioni quantistiche nell'altra. Il trasporto e la riconfigurazione di alta qualità dei cristalli in diverse zone sono cruciali in questa architettura.

In questa tesi, dimostriamo vari elementi necessari per lavorare con architetture scalabili di trappole ioniche di specie miste. Uno dei principali risultati è la dimostrazione del trasporto e della separazione a bassa eccitazione di cristalli di ioni di singola specie fino a 7 ioni e catene di specie miste fino a 4 ioni, composte da calcio e berillio in forma ionizzata. Ottimizziamo il trasporto inter-zona di cristalli di due ioni di specie miste, raggiungendo basse eccitazioni al livello di $\bar{n}_{\mathrm{Z1}} = 0.16(2)$ e $\bar{n}_{\mathrm{Z2}} = 0.14(2)$ fononi per i modi assiali in fase e controfase , rispettivamente. Presentiamo la separazione di cristalli di due ioni di singola specie con eccitazioni di $\bar{n}_{Be} < 0.8$ e $\bar{n}_{Ca} < 2.3$ quanti per berillio e calcio rispettivamente. Nel caso di specie miste, sorgono ulteriori sfide nel controllo a causa di una maggiore sensibilità ai campi elettrici radiali, che inducono torsioni dipendenti dalla massa delle catene di ioni, e all'accoppiamento dei modi normali, esacerbato dall'alto rapporto di massa di 4.4 per queste specie. Per i cristalli di due ioni raggiungiamo una bassa eccitazione di $\bar{n}_{\mathrm{Be}} = 1.44(9)$ and $\bar{n}_{\mathrm{Ca}} = 1.40(8)$ quanti. Queste scoperte possono essere applicate per le architetture basate su spettroscopia logica quantistica di specie esotiche.

Applichiamo la teoria delle transizioni di Landau-Zener-Stückelberg-Majorana per studiare l'accoppiamento dei modi normali e sviluppiamo metodi per regolare la sua intensità per incrementare o inibire il trasferimento di calore. L'accoppiamento regolabile viene impiegato per dimostrare la manipolazione degli stati vibrazionali, dove interazioni multiple consecutive danno luogo a misure interferometriche.

Descriviamo un'architettura che abbiamo sviluppato ed espanso nelle funzionalità per controllare i potenziali degli elettrodi, che manipolano le posizioni degli ioni, e ne dimostriamo l'impiego. Esaminiamo il modello dei potenziali della trappola sottostante attraverso routine automatizzate, stabilendo un metodo per la verifica iniziale delle deviazioni sperimentali da una simulazione perfetta.

Acknowledgements

In the last few years, I have had the immense pleasure of being part of the TIQI group and have met a large number of people who have left me with good memories. I take this opportunity to thank you all!

First of all, I want to thank Prof. Jonathan Home. It has been a great pleasure to work with him, and he has inspired me to do more and think in different ways. His enthusiasm and deep knowledge of a broad range of topics (inside and outside of physics) were fundamental for the work of this thesis and to make the group a welcoming and stimulating environment.

I also thank Matteo Marinelli for all the support he gave me and for teaching me a lot about working with trapped ion experiments. I can't recall the number of hours we spent together collecting yellow and blue 2D plots! Unfortunately, I didn't add them to this thesis as they would have taken all the readers' attention due to their beauty. I hope you will understand! I want to thank also Vlad Negnevitsky for all the help he gave me and for introducing me to the control system. For all the questions I had, he was always very patient to take the time to answer. I also miss the kicker calls at 4 p.m!

I want to thank also Carmelo Mordini for all the support and the intriguing discussions about the experiments of this thesis. I always found his point of view very stimulating. I hope your new laboratory will be running soon, despite Italian bureaucracy, and that you will find people interested in Folk dance! A big thank you also goes to Matteo Simoni, another member of the TIQI Italian community, who joined the experiments at a later stage but made very important contributions with his analytic skills and precious iPad. Unfortunately you went to the dark side of trapped-ions experiments (Penning...) but we all know that Paul traps are cooler! A warm thank you also goes to Stephan Welte. His effort and organizational skills were crucial for obtaining the data we needed. I really hope your experience in your new laboratory will be successful, but don't forget to take a rest sometimes! I thank Karan Mehta, Christa Flühmann, Tanja Behrle and Brennan de Neeve for all the discussions, for collaborating in debugging all the nasty problems in the lab, and for the good times together.

I thank Daniel Kienzler for all the discussions and help in debugging and improving the experimental setup. I thank Florentin Reiter for the discussions related to theoretical aspects and the laughs that made the day go smoother. I thank the control system group and engineers. Martin Stadler, Alexander Ferk, Peter Clements, Bahadir Dönmez, Ilia Sergachev and Cagri Oenal for the constant improvement of the control system and help with electronic systems. I also thank Tenzan Araki, Giorgio Fabris, and Michalis Theodorou for their collaboration on different projects. I hope these projects were useful and interesting for you and your future path. I also thank Mirjam Bruttin for the help in all the boring bureaucratic matters.

I also thank the other members of the TIQI group for all the stimulating discussions and good time together. In random order, these thanks go to Pavel Hrmo, Jeremy Flannery, Diana Prado Lopes Aude Craik, Fabian Schmid, Claudia Politi, Shreyans Jain, Nick Schwegler, Tobias Sägesser, David Holzapfel, Alfredo Ricci Vasquez, Luca Immanuel Huber, Ivan

Rojkov, Gillen Beck, Wojciech Adamczyk, Silvan Koch, Elias Zapusek, Moritz Fontboté Schmidt, Yingying Cui, Robin Oswald, Paolo Colciaghi, Chi Zhang, Maciej Malinowski, Matthew Grau, Oliver Wipfli, Christoph Fischer, Roland Matt, Christopher Axline, Natascha Hedrich, Chiara Decaroli, Mose Müller, Henry Passagem, Simon Ragg and Thomas Lutz.

A special mention goes to Martin Wagener. I remember when he came to visit the group to apply for a PhD position, and in the evening we went to eat sushi. Since then, we have always had very interesting discussions about any topic. Your accident is a big loss for all of us. I dedicate chapter 9 of this thesis to you, as we took the data together. I hope it will be useful for other people, too.

I thank my friends of a lifetime Niccolò, Filippo, Diego, Pes, Francesco, Sara and Claudio. Despite living in different countries, I can always find you for talking and having a good time.

I thank my family and relatives for their love and for believing in me. I thank my mother Martina who taught me perseverance, ambition and passion to reach my interests. I thank my sisters Eliana and Nathalie, and my niece Eva for their support and love. I thank my cousins Kendrick and Francesco as I know I can always count on them. I thank Patty, I will not forget your immense support. I also thank all the other members of my family, the list of whom is quite long. I thank my girlfriend Eszter for her constant love, help and encouragement during these years and for being patient with me (especially when long working hours kept me busy!).

Contents

1 Introduction

In the realm of computer science, Alan Turing proposed a theoretical machine known as the *Turing machine* that could implement any computer algorithm [Tur37]. In later years this concept was further developed by John von Neumann, who presented an architecture for a simpler universal computing device which is still used to describe all contemporary computers, regardless of their specific implementation. These studies sparked the development of new technologies capable of implementing these models, paving the way for modern computers that play a crucial role in our current society.

Computers that are designed based on von Neumann's model inherently process information from the classical realm. The emergence of quantum mechanics in the 19th century unveiled that nature operates under different principles from those of classical mechanics. The transition from quantum to classical mechanics occurs when a system loses its quantum coherence. While classical computers have been employed to simulate quantum systems, they have proven to be inefficient in doing so. Certain problems would demand computational time that increases exponentially with the problem size [Pre18]. In fact, simulating a quantum system with about 50 interacting two-level quantum elements, *quantum bits* or *qubits*, is considered infeasible for a modern classical supercomputer [Aru+19]. To address this issue, Paul Benioff, Yuri Manin and Richard Feynman independently proposed in the early 1980s that quantum systems could be simulated efficiently by devices that harness quantum phenomena, thus introducing the concept of *quantum computers* [Ben82; Fey82]. During this period, the application of quantum principles in quantum cryptography by Charles Bennett and Gilles Brassard [BB84] and in the first quantum algorithm by David Deutsch [Deu85] demonstrated that quantum devices could overcome the limitations of classical ones. This led to the development of several innovative algorithms, including those of Deutsch–Jozsa [DJ92], Bernstein–Vazirani [BV97], Simon [Sim97], Grover [Gro96] and Shor [Sho94], including also for quantum simulation [GAN14]. Since then, extensive efforts have been made to identify new categories of problems that can be solved efficiently on a quantum computer, and the field continues to require collective efforts to push the boundaries.

Quantum computers operate by encoding quantum information, quantified in terms of qubits, into the states of a quantum system. This information is processed by exploiting the principles of superposition, interference and entanglement among different states of the system. For a quantum system to be suitable for Quantum Information Processing (QIP) it must satisfy five necessary conditions, known as the Di Vincenzo criteria [DiV00]. The criteria are: the system must be scalable and have well-defined qubits, it must be capable of implementing a universal set of *quantum gates*, it should have the ability to initialize the state of the qubits to a specific one, it must be able to perform qubit-specific measurements and the qubits should have long coherence times. Several architectures have been developed that meet these requirements, each with its own set of strengths and weaknesses. One of the leading candidates is the architecture based on trapped atomic ions. Originally designed for high-precision spectroscopy and metrology [Deh68; Pau90], trapped ion technology has evolved significantly over the years. The attained level of control of quantum systems has paved the way for its application as an architecture for quantum computing.

The most prevalent ion trap design for QIP is the Radio-Frequency Paul trap. Trapped ion quantum computers store quantum information in the electronic states [Win+98] or in the motional states [GKP01] of ions confined by electric fields. The Coulomb interaction between ions is exploited for implementing quantum gates [CZ95]. Lasers, microwaves and Radio-Frequency (RF) provide a diverse range of high-fidelity tools to manipulate and detect the ions' states [Lei+03]. Ions naturally have a long coherence times [Wan+17] and ions of the same species are identical. One of the significant challenges for quantum computers is scaling up to thousands of qubits. This is necessary to demonstrate an advantage over classical computers for implementing Quantum Error Correction (QEC) schemes [Ste97] and, consequently, useful quantum algorithms [HLH22]. Co-trapping thousands of ions in a single potential well does not offer a scalable solution as the complexity of the system increases. In particular, the number of vibrational modes of an ion string increases linearly with the number of ions, slowing down high-fidelity entangling gates based on collective motional modes, and increasing the likelihood of crosstalk between the modes [MK13]. A promising approach to this challenge is the *Quantum Charge-Coupled Device* (QCCD) architecture [KMW02]. Since its proposal, it has become a standard in many quantum computing devices [Kau+20; Mos+23]. The architecture is based on an extended trap, which is divided into multiple distinct zones. Each zone is dedicated to performing specific tasks such as executing quantum logic operations, storing quantum memories, qubit initialization and detection. The ions are trapped in compact arrays and are transported across these zones by applying time-dependent voltages to the chip electrodes. The design's scalability is derived from the ability to manipulate multiple small arrays in parallel without cross-talk. However, this framework has its drawbacks. There is an increase in the number of required electrodes, electrical connections and laser beams. Despite these challenges, ongoing efforts are being made to address these issues [Meh+20; MAB23]. The design also imposes a demand for high-quality control for the transportation and reconfiguration of the ion arrays. This involves separating longer chains into smaller ones and vice versa, as well as reordering the ions. If done imperfectly, these operations induce significant motional excitation of the ions, thereby degrading the fidelity of subsequent quantum gates [Kau+20]. Furthermore when quantum information is stored in the internal states of the ions, they cannot be directly laser-cooled as the dissipation process destroys the information. To mitigate this issue a second ion species can be co-trapped and used to re-cool the ions by means of sympathetic cooling [Kie+00; HRB08]. The spectral isolation of the two species ensures that the cooling light of one ion species does not affect the information stored in the other [Bar+03]. However, re-cooling is typically slow, making it the primary timescale in quantum operations [Hom+09; Wan+19; Pin+21; Rya+21]. Therefore it is crucial to minimize the excitation induced by the transport, separation, and reconfiguration of ion arrays. Comprehensive studies have been conducted with single species ion chains [Row+02; Lei+07; Bow+12; Wal+12; Rus+14; Kau+14; CE15; Ste+22; Cla+23], achieving low excitation over a wide range of operations. For mixed-species arrays [Bar+04; Hom+09; Pin+21] additional challenges have to be overcome. Generally these studies lack of an in-depth analysis of these sources of heating, relying on intense re-cooling of the ions to compensate [Mos+23].

In this thesis we investigate the transport, separation and reconfiguration of mixed-species ion arrays in a QCCD architecture. We study the manipulation of ion crystals and specify relative constraints to satisfy. We examine the performance of these operations for different ion crystals, identifying and analyzing several factors inhibiting optimality, such as imperfect manipulation, strong electric field noise, presence of stray electric fields and coupling of normal modes of motion. This study was performed with ion strings composed of

beryllium-9 and calcium-40 ions. The advantage of using beryllium ions is that quantum information can be stored in its hyperfine ground state with a long coherence time of up to $\sim$ 4s [Lo15]. The second ion species was selected to have a mass as close as possible to that of the beryllium ion, while still having a hydrogen-like electronic structure that generally presents a simple electronic energy spectrum. A first choice could be the magnesium-25 ion, but the manipulation of the electronic energy states requires UV lasers close to $\sim$ 280 nm, which poses technical challenges. Another choice is the calcium-40 ion, which is widely employed in trapped-ion quantum computing with well-established laser technologies. A drawback is that, together with beryllium, these species present a high mass ratio, which exacerbates the aforementioned effects. Nevertheless, these were counteracted with a tailored combination of measures, that allowed us to operate with single-species chains of up to 7 ions and mixed-species chains of up to 4 ions. This enables the implementation of more complex quantum computing algorithms based on reconfigurable ion strings in future applications.

In the course of this work, we extended the functionalities of a framework used for designing time-varying voltages for the shuttling and reconfiguration of ions called *Pytrans* [Mor+23], which initially developed in [Neg18]. This library was made publicly available to enable its use by other research groups, to accelerate research and unify techniques among different institutes. The design of the voltages is based on a simulation of the trap. Subsequently, we studied the accuracy of this model and explored techniques to quantify and adjust for experimental discrepancies.

Given the high mass ratio of the species involved, the research conducted in this thesis also has implications for architectures used in spectroscopy. In these setups, an ion is co-trapped with charged exotic particles of varying nature, charge and mass, such that the ion can be utilized as a coolant [Sch+05; Kin+22; Sch+23]. For spectroscopy species that are challenging to prepare or maintain, transport and separation may simplify operations. An instance of this is the employment of transport and separation as part of sympathetic cooling protocols for a single antiproton co-trapped with a single beryllium ion, necessary to measure signals that are not degraded by motional excitation [Cor+21].

During the study of transport and separation of ion strings, the coupling of vibrational modes was dynamically tuned to enable or prevent the transfer of energy between the modes. This naturally lead us to study multiple interactions of motional states, which can induce interference between phonon populations. Such phenomenon was not explored in trapped ion architectures before [ISN23] and it can be employed as a resource for quantum computing [LB99].

The thesis is organized as follows:

Chapter 2 introduces the operational principles of Paul traps and presents the experimental setup employed in this thesis. It describes the dynamics of individual ions and mixed-species arrays, with an emphasis on their motional quantum states.

Chapter 3 outlines the process of ion state manipulation through laser interaction, the electronic energy level structure of beryllium and calcium ions and the techniques we employ for cooling the ions close to their motional ground state.

Chapter 4 describes various techniques we employ to manipulate and analyze the electronic and motional states of mixed-species ion crystals. Starting from the typical experimental sequence, we discuss the methods we employ to carefully measure the motional frequencies and phonon populations. Then we discuss in detail the dynamics of the transfer of energy between coupled vibrational modes and the factors that cause this coupling.

Chapter 5 presents the main features of the experimental control system and recent advancements in managing some of the electronic devices used in ion trapping, generation of magnetic fields and laser beams production.

Chapter 6 provides an in-depth analysis of the micromotion affecting the laser-ion interaction in the trap and explains the methods we employ to compensate or account for it. These procedures led us to study the simulation of the trap potentials and to quantify experimental deviations.

Chapter 7 introduces the theoretical framework and practical implementation of the routines for designing the voltages used for transport, separation and reconfiguration of the ion crystals.

Chapter 8 describes the experimental investigations related to static confinement, transport and separation of single- and mixed-species ion chains of different varying lengths and configurations. It provides a quantitative analysis of the heating mechanisms and strategies to minimize excitations and coupling between the modes.

Chapter 9 describes an experiment in which, diversely from the previous chapter, we keep enabled the coupling between the modes and analyze them after multiple interactions, obtaining an interferometric measurement between phonon populations in different vibrational modes of a single calcium ion.

2 Ion dynamics in Paul trap

In this chapter I give the theoretical background describing systems of single and multiple trapped ions and their implementation in the experimental setup of this thesis. The description strongly focuses on the trapping and motional states of mixed-species ion crystals, as this will be relevant in later chapters.

2.1 Paul Trap

Ion traps spatially confine charged particles by means of electromagnetic fields. In order to confine in all three dimensions, it is impossible to employ only *static* electric field due to the *Earnshaw's theorem*. From two of the Maxwell's equations, one retrieves the *Poisson equation*:

$$\nabla^2 V = -\frac{\rho}{\epsilon_0} \tag{2.1}$$

where V is the electric scalar potential, ρ is the electric charge density and ϵ_0 is vacuum permittivity. In a charge-free space, this equation turns into the *Laplace's equation*:

$$\nabla^2 V = \frac{\partial^2 V}{\partial x^2} + \frac{\partial^2 V}{\partial y^2} + \frac{\partial^2 V}{\partial z^2} = 0 \tag{2.2}$$

which means that it is impossible to create positive confining curvature in all three directions at the same time with a static electric field. In order to confine the ions, one needs to use an additional static magnetic field, as in *Penning traps*, or a time-varying inhomogeneous electric field, as in *Paul traps* [Pau90]. In the experiments of this thesis, we employed the latter solution, using a radio-frequency (RF) *linear Paul trap*. A schematic of this configuration is shown in Fig. 2.1. Here the trap is composed of four sets of electrodes, divided into RF and DC electrodes. The RF electrodes are primarily used for confining along the x and y directions, which are referred to as *radial directions*. By applying a time-varying voltage $v(t) = v_{\mathrm{RF}}\cos(\Omega_{\mathrm{RF}}t)$ to these electrodes and considering the DC electrodes as a ground (GND), the potential inside the trap forms a radial saddle point that varies in sign. In order to provide confinement along the z direction, referred to as *axial direction*, the DC electrodes are segmented and a voltage difference between the external electrodes and the central one is applied, v_{D} in the figure. Here we also take into account a possible common voltage offset v_{C} applied to all DC electrodes.

We can then compute the electric potential close to the trap axis for this configuration. Due to the electrode radial symmetries, we expect the linear terms of the potential to vanish. We approximate the potential up to the second order as:

$$V(x,y,z,t) = V_0 + \frac{1}{2}v_{\mathrm{D}}\left(\alpha_z z^2 + \alpha_x x^2 + \alpha_y y^2\right) + \frac{1}{2}v_{\mathrm{RF}}\cos\left(\Omega_{\mathrm{RF}}t\right)\left(\beta_x x^2 + \beta_y y^2\right) \tag{2.3}$$

where V_0 is the potential at the trap center due to the DC and RF voltages, $\alpha_{x,y,z}$ and $\beta_{x,y}$ are geometric factors that depend on the exact trap configuration and are computed through a numerical simulation (see Sec. 7.1).

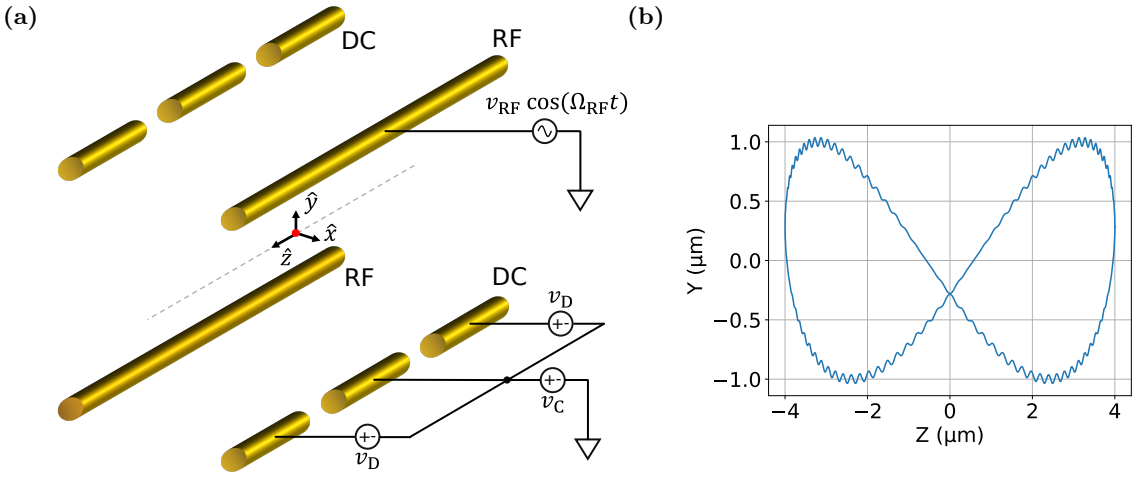

Figure 2.1: (a) Linear Paul trap schematics. Applied voltages for ion trapping are shown. Dashed line indicates the trap axis. (b) Numerical simulation of 2D ion motion in a Paul trap. The time range is over a single period of axial frequency. The frequencies are $[\omega_z, \omega_y] = 2\pi \times [1, 2]$ MHz, $\omega_{RF} = 2\pi \times 100$ MHz. The Mathieu parameters are $a_y = 0$ and $q_y = 0.075$. The micromotion is visible and vanishes close to the trap axis. The secular motion is a closed Lissajous curve.

We are now interested in describing the motion of the ions. For each axis the potentials are independent, consequently we can describe the equations of motion along these directions separately. For a single ion of mass m and charge e, the classical equation of motion for the ion position $\vec{u} = (u_x, u_y, u_z)$ is computed from:

$$\frac{\mathrm{d}^2 u_i}{\mathrm{d}t^2} = -\frac{e}{m}\frac{\partial \Phi}{\partial u} \tag{2.4}$$

with $i = (x, y, z)$. Along the axial direction, it corresponds to:

$$\frac{\mathrm{d}^2 u_z}{\mathrm{d}t^2} = -\frac{e}{m} v_D \alpha_z u_z \tag{2.5}$$

which is the equation of motion of a harmonic oscillator with oscillation frequency:

$$\omega_z = \sqrt{\frac{e\alpha_z v_D}{m}}. \tag{2.6}$$

Radially we have:

$$\frac{\mathrm{d}^2 u_i}{\mathrm{d}t^2} = -\frac{e}{m}\left\{\alpha_i v_D + \beta_i v_{RF}\cos\left(\Omega_{RF}t\right)\right\} u_i \tag{2.7}$$

which can be expressed as the differential equations known as *Mathieu's equations* [Pau90; Win+98]:

$$\frac{\mathrm{d}^2 u_i}{\mathrm{d}\tau^2} + \left(a_i + 2q_i\cos(2\tau)\right) u_i = 0 \tag{2.8}$$

with Mathieu's parameters:

$$a_i = \frac{4e\alpha_i v_D}{m\Omega_{RF}^2}, \quad q_i = \frac{2e\beta_i v_{RF}}{m\Omega_{RF}^2} \quad \text{and} \quad \tau = \frac{\Omega_{RF}t}{2} \tag{2.9}$$

which can be solved by means of an exponential series [Lei+03; McL47]. The solutions of Mathieu's equations and the stability of the trapping depend on a_i and q_i. Generally, linear

Paul traps are operated in a region where $q_i^2 \ll 1$ and $|a| < q_i^2/2$, which is within the first of the stability regions of Mathieu's equations. Here we can approximate at first order the solution of Eq. 2.8 as:

$$u_i(t) \simeq A\cos(\omega_i t)\left[1 - \frac{q_i}{2}\cos(\Omega_{\mathrm{RF}} t)\right] \tag{2.10}$$

where A is given by initial conditions and ω_i is the *secular frequency*:

$$\omega_i = \sqrt{a_i + \frac{q_i^2}{2}}\frac{\Omega_{\mathrm{RF}}}{2}. \tag{2.11}$$

This equation assumes a simple form in the case the contribution from the static potential is negligible ($a_i \to 0$):

$$\omega_i = \frac{e\beta_i v_{\mathrm{RF}}}{\sqrt{2}m\Omega_{\mathrm{RF}}} \tag{2.12}$$

The resulting radial trajectory is composed of the sum of two components. The first is a slow *secular oscillation* of angular frequency ω_i. The second is a faster motion at Ω_{RF}, called *micromotion*, whose amplitude is $q/2$ times smaller than the one of the secular motion and increases with the distance of the ions from the trap center. The resulting trajectory of an ion is shown in Fig. 2.1(b). This shows the existence of two different time scales governing the motion of the ions. If the condition $(|a_i|, q_i^2) \ll 1$ is satisfied, the secular frequency is much smaller than the RF drive frequency. This represents the fact that, while the ion is alternatively attracted and repelled from the trap center by the RF oscillating field, it experiences on average an attractive force, or ponderomotive force. This can be described by an effective static potential called a *pseudopotential*.

2.1.1 Pseudopotential

The pseudopotential is a simple and effective description of RF confinement and in numerical simulations of ion trapping. It is a good approximation when the $q_i \ll 1$. Its derivation is described in [Deh68] and here I summarize the main concept. We can separate the motion of the ion into its fast and slow components, which happen at different timescales. We then time average the force of the RF electric field over the period $1/\Omega_{\mathrm{RF}}$, obtaining at the lowest order a zero net force, meaning that in this timescale the ions move around an average position $\bar{u}_i$. If the RF electric field is inhomogeneous and we Taylor expand it around the average position $\bar{u}_i$ up to the first order, then the time average force affects the slow trajectory:

$$\bar{F}_i(\bar{u}_i) = -e\frac{\partial V_{\mathrm{ps}}(\bar{u}_i)}{\partial \bar{u}_i}, \qquad \text{with } V_{\mathrm{ps}}(\bar{u}_i) \equiv \frac{eE_{\mathrm{RF}}^2(\bar{u}_i)}{4m\Omega_{\mathrm{RF}}^2} \tag{2.13}$$

where $E_{\mathrm{RF}}(u_i)$ is amplitude of the RF electric field along direction i at point u_i and $V_{\mathrm{ps}}(\bar{u}_i)$ is the pseudopotential. The latter is inversely proportional to the mass of the ions, so different ions experience different radial confinements. The ponderomotive force is proportional to the square of the charge e, which means that even negative ions can be confined. By considering only the RF potential in Eq. 2.3, the ponderomotive force becomes:

$$\bar{F}_i(\bar{u}_i) = -\frac{e^2\beta_i^2 v_{\mathrm{RF}}^2}{2m\Omega_{\mathrm{RF}}^2}\bar{u}_i \tag{2.14}$$

which is the equation of a harmonic oscillator of secular frequency:

$$\omega_i = \frac{e\beta_i v_{\mathrm{RF}}}{\sqrt{2}m\Omega_{\mathrm{RF}}} \tag{2.15}$$

which corresponds to Eq. 2.11 in the limit of $a_u \to 0$. The potential energy in the pseudopotential corresponds in fact to the average kinetic energy of the fast motion:

$$\langle W_{\mathrm{mm}}(u_i)\rangle_{\mathrm{av}} = \frac{e^2 E_{\mathrm{RF}}^2(\bar{u}_i)}{4m\Omega_{\mathrm{RF}}^2} = \frac{e^2\beta_i^2\bar{u}_i^2}{4m\Omega_{\mathrm{RF}}^2} = eV_{\mathrm{ps}}(\bar{u}_i) \tag{2.16}$$

The pseudopotential can be used to estimate the trap depth of the radial confinement caused by the RF potential only. The trap depth $E_{\mathrm{trap}}^{\mathrm{RF}}$ is defined as the energy difference computed at the RF potential saddle point and at the nearest local maximum, namely the energy required by an ion to escape the trap. The saddle point is located at the trap center, while the nearest local maximum is close to the electrodes, at a distance R. From Eq. 2.16, we can compute the trap depth similarly to [Mal21]:

$$E_{\mathrm{trap}}^{\mathrm{RF}} = \frac{e^2\beta_i^2 R^2}{4m\Omega_{\mathrm{RF}}^2} \tag{2.17}$$

which is valid for each i. Typical trap depths for 3D linear Paul traps are in the order of a few electron-volts, corresponding to a temperature of thousands of Kelvin, considerably higher than that of the atomic oven and background gas. For the axial direction, the confinement is generated by the DC potential and typical trap depths are in the order of one electron-volt.

We can employ the pseudopotential for a simple simulation of the trapping potentials in the radial plane. An example of this is shown in Fig. 2.2 (a) for the experimental setup of this thesis. We also simulate the contribution of the DC electrodes. The DC potential is responsible for the axial confinement, but due to Laplace's equation, it also induces an anti-confining potential in the radial plane. Along the x and y directions the potential scales differently, breaking the rotational symmetry. Central and external DC electrodes induce quadrupole potentials of different directions and magnitude, such that different combinations of v_{D} and v_{C} induce a rotation and change of intensity in the radial electric fields, as shown in Fig. 2.2 (b) and (c).

2.1.2 Micromotion

Micromotion affects the way the ions interact with the laser beams and, in some specific cases, it can induce motional excitation [Win+98]. Depending on the exact cause, it is referred to as *excess* or *intrinsic* micromotion. The exact definition differs across the literature, but here I use the one according to [Kie15; Ami+11]. The interested reader can compare it with the definition discussed in [Zha21; Ber+98; Kel+15; Ber+17].

Excess micromotion

The excess micromotion happens when uncontrolled stray static electric fields generated by charging up of the trap or imprecisely controlled static potentials cause the minimum of the DC potential to be displaced radially from the RF electric field null. This causes the ion to be trapped around an equilibrium position u_i^{eq} which does not lie on the trap axis. As described in [Kie15; Ber+98], the trajectory of an ion subjected to a radial static stray electric field E_i along direction i can be described as:

$$u_i(t) \simeq A\left[u_i^{\mathrm{eq}} + \cos(\omega_i t)\right]\left[1 - \frac{q_i}{2}\cos(\Omega_{\mathrm{RF}} t)\right], \quad \text{with } u_i^{\mathrm{eq}} = \frac{eE_i}{m\omega_i^2} \simeq \frac{2mE_i\Omega_{\mathrm{RF}}^2}{e\beta_u^2 V_{\mathrm{RF}}^2} \tag{2.18}$$

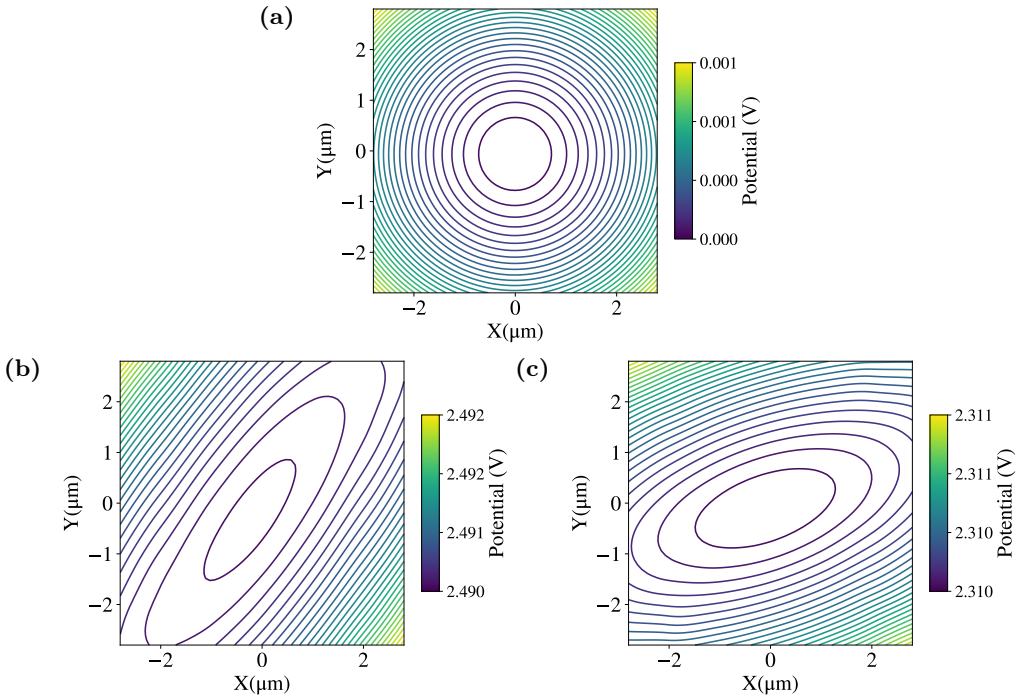

Figure 2.2: Simulation of the radial confinement for a single calcium ion at the trap center of the Paul trap employed in the experimental setup of this thesis, with architecture similar to Fig. 2.1 and parameters described in Sec. 2.2. (a) Pseudopotential in the radial plane in the absence of DC potential. (b) Potential in the radial plane due to the pseudopotential and a DC voltage of 8 V applied to the central electrodes. (c) Potential in the radial plane due to the pseudopotential and a DC voltage of 40 V applied to the external electrodes of only one side. The DC voltages were chosen to generate potentials of similar magnitude and highlight the difference in the directions of the generated quadrupoles.

where the last approximation is valid for the case in which the contribution of the DC potential is negligible with respect to the RF potential, i.e. $a_i \ll q_i^2$. Note that the higher the mass of the ion, the further it gets displaced from the trap center. This might seem counterintuitive, but it is originated from the fact that the ion with higher mass experiences a smaller radial confinement caused by the pseudopotential. This will be particularly important for the experiments involving mixed-species ion chains described in the next chapters. Displaced equilibrium position causes the ion to experience a higher amplitude of micromotion, motivating the name excess micromotion. This has several negative effects on trapped ion systems, as described in [Ber+98; Win+98; Hom13]. Here I only consider the two effects that are most relevant for the experiments described in this thesis. The micromotion induces a phase modulation in the laser light seen by the ion, corresponding to sidebands at the RF frequency in the light spectrum. In the ion rest frame, the laser's electric field is modulated:

$$\vec{E}(t) \simeq \mathrm{Re}\left[\vec{E}_0 e^{\left(i\vec{k}\cdot\vec{u} - i\omega_{\mathrm{laser}}t\right)}\right] \tag{2.19}$$

where ω_{laser} is the frequency of the laser, $\vec{E}_0$ the amplitude of the electric field, $\vec{k}$ the wave vector and $\vec{u}$ the position of the ion, including the shift due to the excess micromotion. The resulting probability of transition between two energy levels of the internal states of the ion

is:

$$P \propto \sum_{n=-\infty}^{\infty} \frac{J_n^2(\beta)}{(\omega_{\text{ion}} - \omega_{\text{laser}} + n\Omega_{\text{RF}})^2 + (\gamma/2)^2)} \tag{2.20}$$

where ω_{ion} is the frequency of the transition, γ is the linewidth, J_n are the Bessel functions of the first kind and β is the amplitude of the phase modulation due to the excess micromotion, computed as:

$$\beta = \left| \frac{1}{2} \sum_{i=x,y} k_i q_i u_i^{\text{eq}} \right|. \tag{2.21}$$

As β increases, the probability of transition at ω_{ion} reduces, decreasing the efficiency of the laser cooling for laser beams with radial wave vectors. For higher β, if $\Omega_{\text{RF}} \ll \gamma$ then the excitation spectrum gets broader, while for $\Omega_{\text{RF}} \gg \gamma$ it forms sidebands at $\pm n\Omega_{\text{RF}}$, with $n \in \mathbb{N}$. In both cases, for some values of $\omega_{\text{ion}} - \omega_{\text{laser}}$ the laser might heat the ion, rather than cooling it. As stated in [Kie15], it is interesting to notice that, for $a_i \ll q_i^2$, β is mass-independent, while it maintains a dependence on the ion species due to the different wavelengths.

The excess micromotion is generally compensated by adding a voltage bias to the electrodes or by means of an additional set of electrodes, aiming to nullify the stray static electric fields. Detailed analysis of this technique can be found in Sec. 6.2.

Intrinsic micromotion

Intrinsic micromotion happens when there is a phase shift between the voltages applied to the RF electrodes, or when the RF electric field has an axial component. The former is minimized by the trap geometry used in the experiments described in this thesis [Kie15], thus I consider it to have negligible effects. The latter instead is caused by manufacturing imperfections of the ion trap, in which the electrodes are not properly aligned. It is also due to the finite length of the electrodes and to the application of the RF potential to only one pair of electrodes radially, inducing intrinsic micromotion along the entire trap axis apart for the center of symmetry. Since this second effect played a more relevant role in the experiments described in this thesis, I give a summary of the underlying mechanism, following [Ami+11; Kie15]. Along the axial direction, we consider the effect of the DC electric field together with the axial component of a homogeneous RF electric field:

$$E_{\text{total}} = -\alpha_z v_{\text{D}} z + E_{\text{RF,z}} \cos(\Omega_{\text{RF}} t). \tag{2.22}$$

The resulting equation of motion is a harmonic oscillator subject to a sinusoidal driving force with solution:

$$z(t) = A\cos(\omega_z t + \varphi) + \frac{eE_{\text{RF,z}}}{m(\omega_z^2 - \Omega_{\text{RF}}^2)} \cos(\Omega_{\text{RF}} t) \tag{2.23}$$

where ω_z is the usual axial secular angular frequency given in Eq. 2.6 and A and φ are given by initial conditions. The first term in $z(t)$ describes the usual axial secular motion, while the second represents the drive of the axial RF field. If we consider $\Omega_{\text{RF}} \gg \omega_z$, the amplitude of this drive does not depend on ω_z, but it is inversely proportional to the mass of the ion. Consequently also $\beta \propto 1/m$ and the probability of transition between the internal levels gets modulated by Bessel functions, causing detrimental effects analogous to the excess micromotion. Intrinsic micromotion, independently from the cause, affects laser beams with non-negligible wave vectors components along the trap axis.

Differently from the excess micromotion, the intrinsic one we consider here cannot be simply compensated by acting on the trap voltages. For this reason, we account for it by phase-modulating the laser beam through some Electro-Optic Modulators (EOMs) to maximize the absorption profile, when necessary. Detailed analysis of this technique can be found in Sec. 6.1.

2.2 Segmented 3D Paul Trap

The experiments performed in this thesis were implemented in a linear Paul trap. It was designed and developed by Daniel Kienzler [Kie15] and a schematic of the trap structure is shown in Fig. 2.3. The trap is made from different layers of aluminium oxide (Al_2O_3), which were laser-machined to create specific slots and subsequently gold plated. The outermost wafers are masks which avoid excessive deposition from the atomic source ovens on the trap electrodes, which would increase heating rates and motional decoherence [Win+98]. The two inner wafers have one RF electrode and 15 DC electrodes each in an anti-symmetric configuration, which are used for generating the trapping potentials. Around them, there are two additional wafers and each has 7 *shim* electrodes for each side of the trap, for a total of 28 shim electrodes, which are used to compensate stray electric fields causing excess micromotion. Each wafer is separated by spacers from the others and all the layers have a thickness of 125 µm.

The DC electrodes in this trap have non-uniform widths depending on the exact location along the trap axis to satisfy different requirements. This allows to have zones or regions for specific operations, fulfilling one of the conditions of the QCCD architecture. At each end of the trap there are two loading zones where neutral atoms, generated in the atomic ovens, get ionized and trapped. Two sets of atomic ovens are directed at each loading region for redundancy, but currently only the left zone is used. Due to the large width of 500 µm of the electrodes in this zone, the achievable maximum axial frequency is lower than in the other regions. There are also three experimental zones composed by electrodes of 300 µm width. The leftmost and rightmost ones are currently used as storage for multi-well operations, while the central one is used for the quantum control of the ion arrays. This is performed not exactly at the center of the DC electrodes 8 and 23 but displaced by 20 µm to the right to minimize the axial pseudopotential gradient [Bla+09] experienced by the ions. In this thesis, all three experimental zones were used, but I generally refer to the central one when not specified. On either side of the central zone, there are two separation zones composed of three narrow electrodes of 150 µm width each, enabling generating stronger higher-order terms in the potential for separation and recombination of ion chains. All the electrodes are separated from their neighbour by 20 µm gaps. The distance from the trap axis to the electrodes is roughly 184 µm, which was chosen due to the trade-off between smaller distances allowing the production of higher electric field gradients in the trap at lower voltages, and larger distances which result in lower heating rates and increased optical access.

The trap stack is mounted on a filterboard and the electrodes are connected through wirebonds. In the filterboard, most of the DC and shim lines are filtered against electrical noise by first-order RC low pass filters, with $R = 240(20)\,\Omega$ and $C = 820(40)\,\text{pF}$ which lead to a cut-off frequency of 809(78) kHz. Four shim lines are only connected to capacitors to generate additional RF electric fields known as *tickle* and for microwave driving of magnetic dipole transitions of the ions. The chip and the filterboard are located inside the vacuum chamber (also shown in Fig. 3.4) and connected to external lines to control the electrode

voltages. The DC electrode 11 shown in Fig. 2.3(e) is not properly connected to the outside line, preventing appropriate voltage control. Generally this does not affect daily operations, apart for experiments involving the transport of ions in front of this electrode, which will be described in Subsec. 8.2.3.

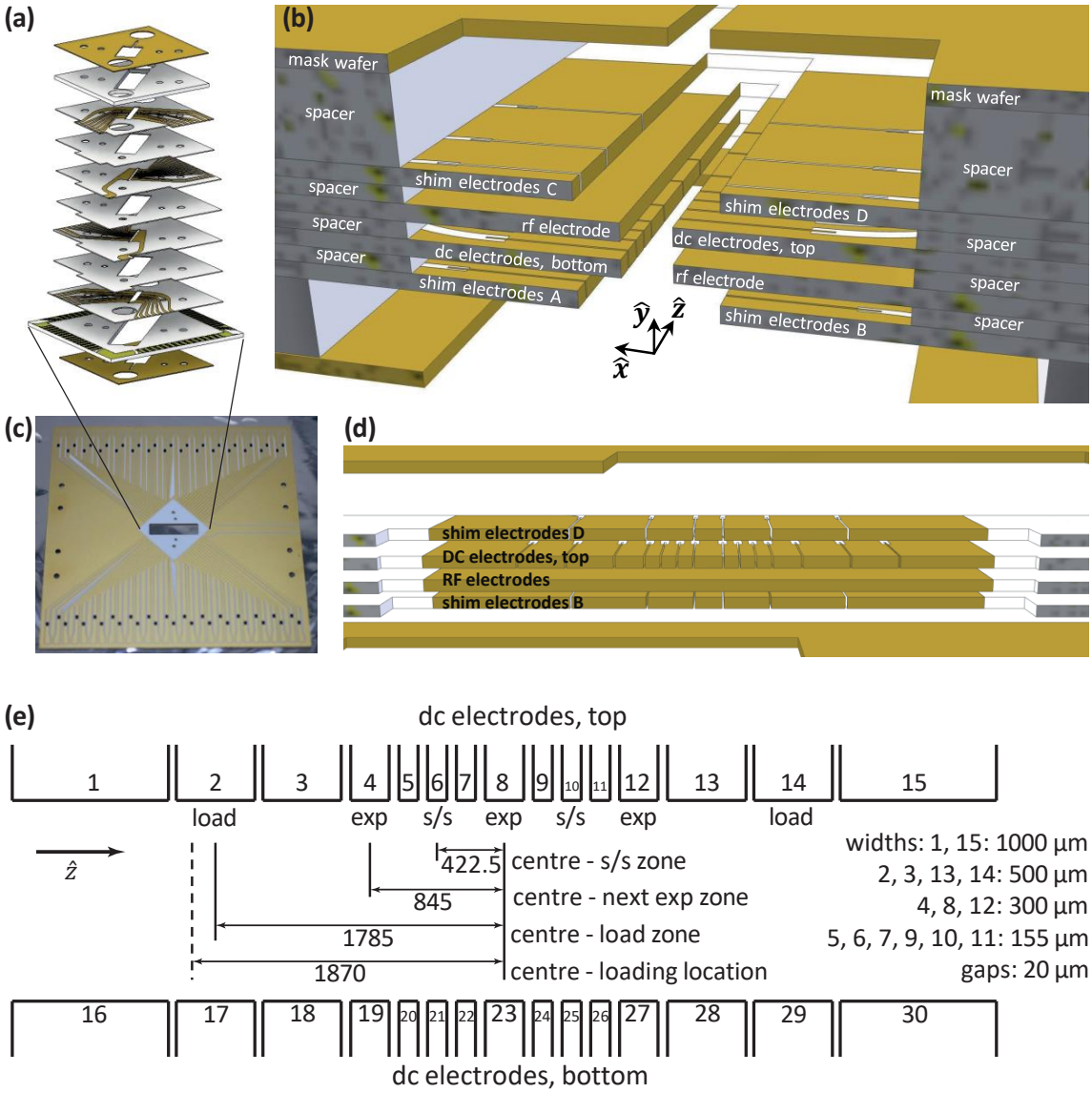

Figure 2.3: Segmented 3D trap structure. (a) Exploded-view diagram of the wafer stack. (b) Closed view of the electrodes of the assembled chip. (c) Empty filterboard. (d) Side view of the DC, RF and shim electrodes. (e) DC electrodes numbering and dimensions, in µm. The image is modified from [Neg18].

The trapping potential inside the chip can be well approximated by the one described in Eq. 2.3, in which we neglect higher order terms due to the small size of the ion wave packets (on the order of 10 nm) or small ion arrays (on the order of 10 µm) compared to the electrodes distance. Here the potential offset V_0, the factors $\alpha_{x,y,z}$ and $\beta_{x,y}$ are modified according to the trap geometry. Their value is non-analytical and requires a numerical simulation, as described in detail in Sec. 7.1. The DC electrodes are driven by custom arbitrary-waveform generators [Cle15] which span a voltage range of [-10, +10] V and are

described more in detail in Sec. 5.2. The RF voltage is generated by a stable RF voltage source, which gets amplified and filtered by a helical resonator, as described more in detail in [Col18]. The RF amplitude is currently around $v_{\mathrm{RF}} = 374\,\mathrm{V}$, meeting the requirements of having higher amplitudes to increase the secular frequencies according to Eq. 2.11, while being lower than the electrical breakdown safe limit which we conservatively estimate to be 400 V. The RF angular frequency is currently around $\Omega_{\mathrm{RF}} = 2\pi \times 113.733\,\mathrm{MHz}$. A lower RF frequency is desirable for increasing the secular frequency, but it cannot be reduced arbitrarily as the Mathieu parameter has to lie in the stability region. Moreover, the trapping has to be stable for both ion species used in this thesis, $^{40}\mathrm{Ca}^{+}$ and $^{9}\mathrm{Be}^{+}$, at the same time. A conservative approach is to have $\omega_i/\Omega_{\mathrm{RF}} < 0.2$ for all modes [Kie15]. Generally the highest radial secular angular frequency for $^{9}\mathrm{Be}^{+}$ ($^{40}\mathrm{Ca}^{+}$) for the experiments of this thesis is around $2\pi \times 14\,\mathrm{MHz}$ ($2\pi \times 4\,\mathrm{MHz}$), resulting in a ratio of $\omega_i/\Omega_{\mathrm{RF}} = 0.12$ (0.04), satisfying the requirement mentioned above.

2.3 Normal modes of motion

For the experiments described in this thesis, trapped mixed-species ion arrays were employed. The goal here is to compute the equilibrium positions and the motional frequency of a chain of N mixed-species ions subjected to harmonic trapping potentials generated in a Paul trap. The approach I describe here follows [Hom13; Mar20].

We first assume that the temperature of the ions is low enough such that their oscillations around their equilibrium positions are small compared to the inter-ion separation. In the chain of N ions, the mass of each of them is m_j, with $j \in [1, N]$ and the charge is e. We have that the ions' position are a set of N vectors $\vec{u}_1, \ldots, \vec{u}_N$, which will be indexed by the subscript j. It is convenient to rewrite the position coordinates as $3N$ scalar parameters $z_1, \ldots, z_{3N}$, indexed by the subscript i. At this point, we consider the ions to be affected by a trapping potential $V(\vec{u}_j, m_j)$ given by the sum of DC potential of Eq. 2.3 and the pseudopotential of Eq. 2.13. The energy of the ions is given by $E = T + U$, where T is the kinetic energy and U is the potential energy computed as:

$$\begin{aligned} T &= \sum_{j=1}^{N} \frac{m_j}{2} \dot{\vec{u}}_j^2, \\ U &= \sum_{j=1}^{N} eV(\vec{u}_j, m_j) + \frac{1}{2} \sum_{j,l=1, j\neq l}^{N} \frac{e^2}{4\pi\varepsilon_0 |\vec{u}_l - \vec{u}_j|}. \end{aligned} \tag{2.24}$$

The equilibrium positions of the ions $\{z_i^0\}$ can be computed by solving $\partial U/\partial z_i = 0$. This can be solved analytically only up to $N = 3$ [Kie+00]. For longer chains, a numerical method based on the minimization of the potential energy U is generally used. Along the trap axis, the potential energy is independent of the mass, so the equilibrium positions are independent of the exact species of the ions in a mixed-species chain.

Once the equilibrium positions are found, we can Taylor expand the potential up to the second order around these points and neglect the constant terms, which do not affect the dynamics, and the first order terms, as they vanish around the equilibrium positions. The second order terms can be employed to retrieve the $3N \times 3N$ symmetric Hessian matrix according to:

$$H'_{ik} = \frac{1}{\sqrt{m_i m_k}} \frac{\partial^2 U}{\partial z_i \partial z_k}\bigg|_{\{z_i^0\}}. \tag{2.25}$$

We can rewrite the coordinates z_i with mass-weighted coordinates $z'_i = \sqrt{m_i} z_i$, which makes the kinetic energy T to be written in a mass-independent form, which is more convenient for mixed-species ion arrays. We also indicate the ions' displacement from their equilibrium position as $\zeta'_i = z'_i - z_i^{0\prime}$. This allows us to rewrite the Lagrangian of the system in terms of the Taylor expanded potential and ζ'_i:

$$L = \frac{1}{2}\left[\sum_{i=1}^{3N} \dot{\zeta}_i'^2 - \sum_{i,j=1}^{3N} H'_{ik}\zeta'_i\zeta'_j\right] \tag{2.26}$$

from which we retrieve the $3N$ equations of motions from the Euler-Lagrange formula:

$$\ddot{\zeta}'_k + \sum_{i=1}^{3N} H'_{ik}\zeta'_i = 0. \tag{2.27}$$

Assuming a fiducial solution $\zeta'_k = \zeta_k^{0\prime} e^{i\omega t}$, we retrieve a linear system of coupled equations. By diagonalizing the Hessian matrix H'_{ik}, we obtain a set of uncoupled equations. This allows us to describe the ion oscillations in terms of the so-called *normal modes*. These form a basis for the collective motion of the ions, in which they vibrate at specific frequencies and with fixed phase relations. The eigenvalues of the Hessian matrix correspond to the angular frequencies ω_α^2 of each normal mode α. The normalized eigenvectors can be rewritten as a matrix $(e'_{i,\alpha})$ and used to obtain the normal-mode coordinates ξ'_α from the individual ion coordinates through the transformation:

$$\xi'_\alpha = \sum_{i=1}^{3N} e'_{i,\alpha}\zeta'_i. \tag{2.28}$$

The momentum of the ions in the normal modes description can also be transformed analogously. Since the Hessian matrix is real and symmetric, the inverse transformation can be obtained:

$$\zeta'_i = \sum_{\alpha=1}^{3N} e'_{i,\alpha}\xi'_\alpha. \tag{2.29}$$

Each normal mode acts as an independent oscillator.

The eigenvector matrix can also be used to study the features of the normal modes, which depend on the relative masses of the ion species, their order in the chain and the relative contributions of the ponderomotive potential and the static potential for the ions' confinement. For a specific normal mode α, the relation between the signs of the eigenvector elements $e'_{i,\alpha}$ indicates if the ions oscillate in-phase or out-of-phase to each other. The amplitudes of the eigenvector elements indicate the relative participation of the ith ion to the mode α. For single-species arrays they often show symmetries. In the mixed-species case the participation can be very different, with increasing deviations for higher ion mass ratios, as shown in Fig. 2.4. This phenomenon, which could lead to some ions having close to zero participation for a specific mode [SCM21], is more pronounced for the radial modes than for axial ones. The radial frequencies have a stronger dependence on the ion mass (compare Eq. 2.11 with Eq. 2.6). The Coulomb interaction, which couples the modes, is far from resonance and has a small influence on the motion [Hom13]. In the axial direction the mode of highest frequency is the out-of-phase mode, while radially this is the lowest one. Radially this is due to the increase in the ion distance that lowers the Coulomb interaction

energy, while in the axial case this is the opposite. For axial and radial lowest frequency modes, the heaviest ion has the highest participation.

The study of normal modes for chains of mixed-species ion arrays is fundamental for the experiments described in this thesis, as discussed in Ch. 7 and 8. The participation of the ions in these modes has important consequences on the laser-ion interaction (described in Sec. 3.1) and coupling to electric field noise sources (described in Subsec. 8.2.3). For these reasons, I give now some examples of normal modes for mixed-species arrays composed of 2, 3 and 4 ions of $^{40}Ca^+$ and $^{9}Be^+$.

From now on, I use the convention to indicate ion chains by the chemical symbols of their constituents, separated by dashes, in which the order reflects the order of the ions in the trap according to Fig. 2.3(e). For example, a two-ion crystal composed of one $^{9}Be^+$ on the left and one $^{40}Ca^+$ on the right will be indicated as Be–Ca. Moreover along the trap axis the in-phase or center-of-mass (COM) vibrational mode will be indicated as $Z1$, while all the others will have increasing numbers according to the increasing frequencies, e.g. $Z2$, $Z3$ and so on. For each of the radial directions, the COM modes have the highest frequencies and will be indicated as $Y1$ and $X1$. The two lowest frequency out-of-phase or stretch (STR) modes will be labeled as $Y2$ and $X2$, while all the other modes will have increasing numbers according to the increasing frequencies, e.g. $Y3$, $X3$ and so on. This convention differs from [Mar20; Neg18].

In the case of a single trapped ion, the vibrational modes ω_z and $\omega_{x,y}$ are given by Eqs. 2.6 and 2.11, respectively. For a two-ion crystal, composed of Be–Ca (as stated above, the order does not matter), the vibrational frequencies can be computed analytically according to [Wüb+12], while an example of numerically simulated normal modes is shown in Fig. 2.4. The axial separation of the ions is given by $s_2 = 2^{1/3}s$, where $s = [e/(4\pi\varepsilon_0\alpha_z v_D)]^{1/3}$, obtained from [Win+98] together with Eq. 2.6. Typical axial distances in our trap are on the order of 5 µm. We can define the mass ratio as $\mu = m_{Be}/m_{Ca} = 0.225$. The axial angular frequencies can be computed as:

$$\begin{aligned}\omega_{Z1} &= \sqrt{\frac{1+\mu-\sqrt{1-\mu+\mu^2}}{\mu}}\omega_z \simeq 1.19\,\omega_z,\\ \omega_{Z2} &= \sqrt{\frac{1+\mu+\sqrt{1-\mu+\mu^2}}{\mu}}\omega_z \simeq 3.08\,\omega_z,\end{aligned} \tag{2.30}$$

while the axial elements of the eigenvector of Z1 can be computed as:

$$\begin{aligned}e'^2_{Ca,Z1} &= \frac{1-\mu+\sqrt{1-\mu+\mu^2}}{2\sqrt{1-\mu+\mu^2}} \simeq 0.93,\\ e'^2_{Be,Z1} &= 1 - e'^2_{Ca,Z1} \simeq 0.07,\end{aligned} \tag{2.31}$$

while for Z2 they are swapped and with discordant signs. The ratio between the axial mode frequencies is:

$$\omega_{Z2}/\omega_{Z1} \simeq 2.6 \tag{2.32}$$

For the radial normal modes the analysis becomes more complicated, but the interested reader can find the analytical expressions in [Wüb+12].

In the three ion case, the axial vibrational frequencies can be computed analytically according to [Kie+00], while two examples of numerically simulated normal modes are

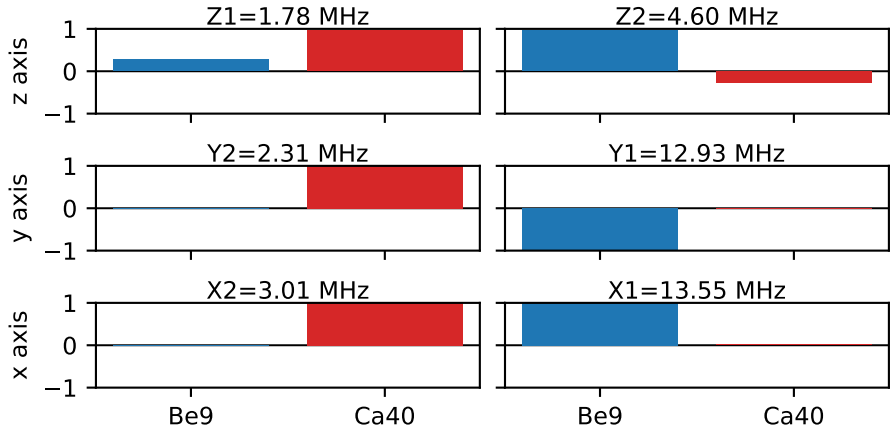

Figure 2.4: Normal mode frequencies and eigenvectors for a Be–Ca crystal. The trapping potentials are such that for a single $^{40}Ca^{+}$ the secular frequencies are $[\omega_z, \omega_y, \omega_x] = 2\pi\times$ [1.5, 2.5, 3.2] MHz. For each direction, the bars indicate the mass-weighted components of the eigenvectors $e'_{i,\alpha}$. On top, the mode frequencies are shown together with the naming convention we adopted. The coordinate system is oriented along the normal modes.

shown in Fig. 2.5. The axial distance of the ions is given by $s_3 = (5/4)^{1/3}s$ [Win+98]. We now focus on the configurations Be–Ca–Be and Ca–Be–Ca, as these were employed in the experiments described in this thesis. For the first case we define the mass ratio as $\mu_1 = m_{\mathrm{Ca}}/m_{\mathrm{Be}} \simeq 4.44$, while for the second we have $\mu_2 = m_{\mathrm{Be}}/m_{\mathrm{Ca}} = 0.225$. The axial angular frequencies can be computed as:

$$\begin{aligned}
\omega_{\mathrm{Z1}} &= \left[\frac{13}{10} + \frac{1}{10\mu_j}(21 - \sqrt{441 - 34\mu_j + 169\mu_j^2})\right]^{1/2}\omega_z, \\
\omega_{\mathrm{Z2}} &= \sqrt{3}\omega_z, \\
\omega_{\mathrm{Z3}} &= \left[\frac{13}{10} + \frac{1}{10\mu_j}(21 + \sqrt{441 - 34\mu_j + 169\mu_j^2})\right]^{1/2}\omega_z,
\end{aligned} \tag{2.33}$$

where ω_z is computed in the usual way with the mass of the ions located externally and μ_j corresponds to μ_1 or μ_2 depending on the exact ion configuration. The axial elements of the eigenvector of Z1 can be computed as:

$$\begin{aligned}
\vec{e}'_{*,\mathrm{Z1}} &= N_1\left(1, \frac{\sqrt{\mu_j}}{8}(13 - 5\omega_{\mathrm{Z1}}^2), 1\right), \\
\vec{e}'_{*,\mathrm{Z2}} &= N_2(1, 0, -1), \\
\vec{e}'_{*,\mathrm{Z3}} &= N_3\left(1, \frac{\sqrt{\mu_j}}{8}(13 - 5\omega_{\mathrm{Z3}}^2), 1\right),
\end{aligned} \tag{2.34}$$

where N_1, N_2 and N_3 are normalization factors. It is interesting to notice that $\vec{e}'_{*,\mathrm{Z2}}$ is null for the central ion, which is typical for an odd number of ions in a symmetric ion chain. Regarding the ratio between the modes, for the Be–Ca–Be case they are $\omega_{\mathrm{Z2}}/\omega_{\mathrm{Z1}} \simeq 2.68$, $\omega_{\mathrm{Z3}}/\omega_{\mathrm{Z1}} \simeq 2.74$ and $\omega_{\mathrm{Z3}}/\omega_{\mathrm{Z2}} \simeq 1.02$. For the Ca–Be–Ca case they are $\omega_{\mathrm{Z2}}/\omega_{\mathrm{Z1}} \simeq 1.52$, $\omega_{\mathrm{Z3}}/\omega_{\mathrm{Z1}} \simeq 3.93$ and $\omega_{\mathrm{Z3}}/\omega_{\mathrm{Z2}} \simeq 2.58$. For the radial normal modes the analysis becomes more complicated, but the interested reader can find more information in [Kie+00].

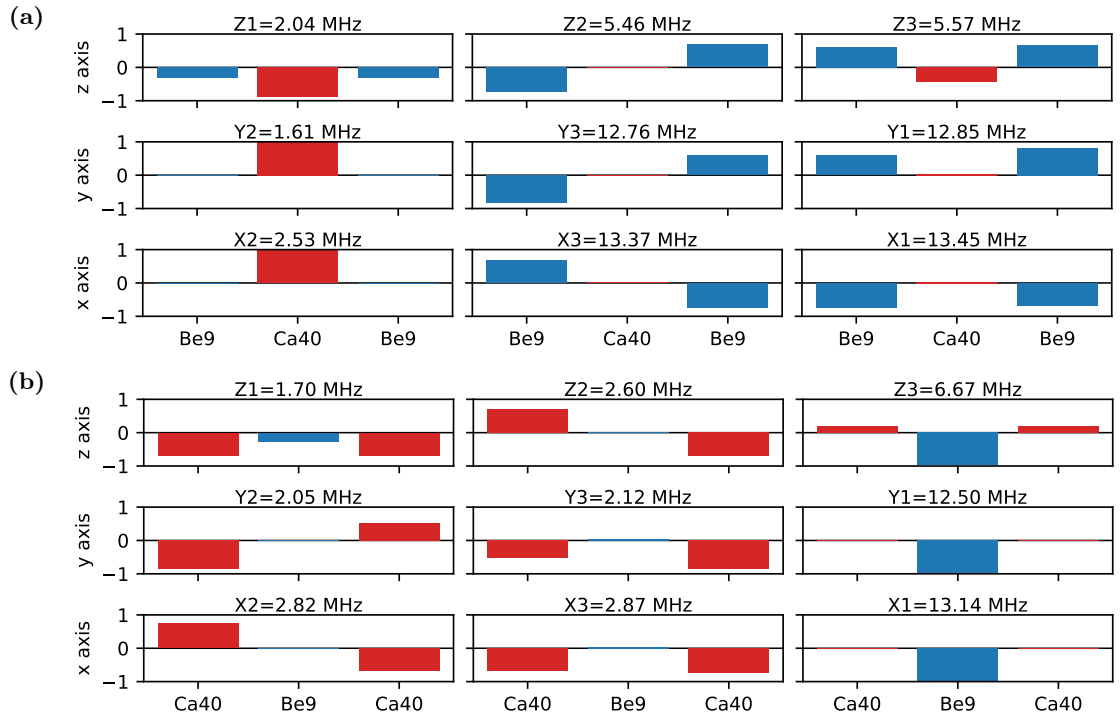

Figure 2.5: Normal mode frequencies and eigenvectors for a (a) Be–Ca–Be and (b) Ca–Be–Ca crystals. The trapping potentials are such that for a single $^{40}Ca^{+}$ the secular frequencies are $[\omega_z, \omega_y, \omega_x] = 2\pi\times$ [1.5, 2.5, 3.2] MHz. For each direction, the bars indicate the mass-weighted components of the eigenvectors $e'_{i,\alpha}$. On top, the mode frequencies are shown together with the naming convention we adopted. The coordinate system is oriented along the normal modes.

In the four ion case, the axial vibrational frequencies cannot be computed analytically, but an example of numerically simulated normal modes is shown in Fig. 2.6. The axial minimum distance of the ions also needs to be computed numerically, with a value that is around $s_4 = 2sN^{-0.56}$, where N is again the number of ions [Win+98]. For longer ion chains, the inter-ion distances increase with the distance from the center, and anharmonic potential terms need to be employed to compensate [Lin+09].

There is an additional factor to take into account. The radial in-phase mode frequency should be set sufficiently higher than the axial in-phase one to have the ions aligned along the trap axis. To avoid the formation of 2D or 3D structures (e.g. zig-zag configuration), for single-species arrays it is required to have $\omega_{Y1}/\omega_{Z1} > 1$ for two ions and $\omega_{Y1}/\omega_{Z1} > 1.55$ for three ions and $\omega_{Y1}/\omega_{Z1} \gtrapprox 0.73N^{0.83}$ [Win+98]. In the mixed-species case the ions participate unevenly in the different modes, then the exact conditions are not trivial to describe due to the complexity of analyzing the radial frequencies mentioned above. Having non-zero Y2 and X2 modes is important, as described in [Wüb+12]. A numerical simulation for $N \leq 9$ is performed in [Kie+00].

2.4 Quantum motional states

Although it is possible to describe the motion of ions in RF traps with a full quantum mechanical treatment that includes micromotion [Lei+03], treating the RF field in the pseudopotential approximation already captures the quantum dynamics of the motional

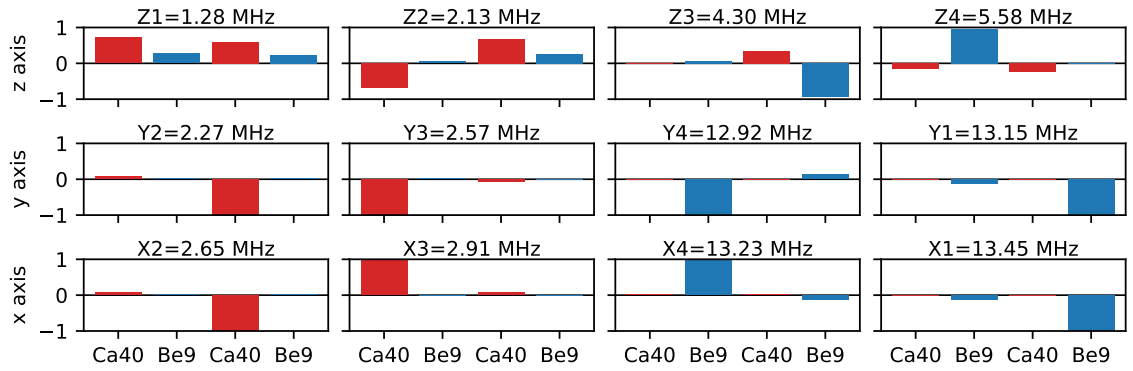

Figure 2.6: Normal mode frequencies and eigenvectors for a Ca–Be–Ca–Be crystal. The trapping potentials are such that for a single $^{40}Ca^{+}$ the secular frequencies are $[\omega_z, \omega_y, \omega_x] = 2\pi\times$ [1.0, 2.8, 3.1] MHz. For each direction, the bars indicate the mass-weighted components of the eigenvectors $e'_{i,\alpha}$. On top, the mode frequencies are shown together with the naming convention we adopted. The coordinate system is oriented along the normal modes.

modes. In this approximation, the motion of the ion along each direction as an independent quantum harmonic oscillator with Hamiltonian:

$$\hat{H} = \frac{\hat{p}^2}{2m} + \frac{1}{2}m\omega^2\hat{x}^2 \tag{2.35}$$

where $\hat{x}$ and $\hat{p}$ are the position and momentum operators, respectively. The quantum harmonic oscillator can be described in terms of its energy eigenstates called *Fock basis* $|n\rangle$, with the *ladders operators* defined as:

$$\begin{aligned} \hat{a} &= \sqrt{\frac{m\omega}{2\hbar}}\left(\hat{x} + \frac{i}{m\omega}\hat{p}\right), \\ \hat{a}^\dagger &= \sqrt{\frac{m\omega}{2\hbar}}\left(\hat{x} - \frac{i}{m\omega}\hat{p}\right), \end{aligned} \tag{2.36}$$

which act on the Fock states according to:

$$\begin{aligned} \hat{a}|n\rangle &= \sqrt{n}|n-1\rangle \\ \hat{a}^\dagger|n\rangle &= \sqrt{n+1}|n+1\rangle, \\ \hat{N}|n\rangle &= \hat{a}^\dagger\hat{a}|n\rangle = n|n\rangle. \end{aligned} \tag{2.37}$$

where $\hat{N} = \hat{a}^\dagger\hat{a}$ is the number operator. The position and momentum operators can be expressed as:

$$\begin{aligned} \hat{x} &= \sqrt{\frac{\hbar}{2m\omega}}(\hat{a}^\dagger + \hat{a}) \\ \hat{p} &= i\sqrt{\frac{\hbar m\omega}{2}}(\hat{a}^\dagger - \hat{a}). \end{aligned} \tag{2.38}$$

The Hamiltonian is then quantized as:

$$\hat{H} = \left(\hat{a}^\dagger\hat{a} + \frac{1}{2}\right)\hbar\omega \tag{2.39}$$

with energy eigenvalue of the state $|n\rangle$:

$$E_n \equiv \left(n + \frac{1}{2}\right)\hbar\omega. \tag{2.40}$$

In this way any motional state can be expressed as a superposition of the Fock states:

$$\Psi = \sum_{n=0}^{\infty} c_n |n\rangle \tag{2.41}$$

where c_n is the probability amplitude of the state $|n\rangle$.

In the presence of an array of ions, the dynamics of each normal mode α can be described as a set of independent oscillators, with its own raising (lowering) ladder operator $\hat{a}_\alpha^\dagger$ ($\hat{a}_\alpha$) [Hom13]. The normal modes are then described as (using the notation of Sec. 2.3):

$$\begin{aligned} \hat{\xi}'_\alpha &= \frac{\sigma'_\alpha}{\sqrt{2}}\left(\hat{a}_\alpha + \hat{a}_\alpha^\dagger\right), \\ \hat{p}'_\alpha &= i\frac{\hbar}{\sqrt{2}\sigma'_\alpha}\left(\hat{a}_\alpha - \hat{a}_\alpha^\dagger\right), \end{aligned} \tag{2.42}$$

where $\sigma'_\alpha = \sqrt{\hbar/\omega_\alpha}$. The displacement of the ith ion is then:

$$\hat{\zeta}_i = \frac{1}{\sqrt{m_i}} \sum_{\alpha=1}^{3N} e'_{i,\alpha}\sigma'_\alpha \left(\hat{a}_\alpha + \hat{a}_\alpha^\dagger\right) \tag{2.43}$$

with a wave packet size of $\sqrt{\hbar/(2m\omega_\alpha)}e'_{i,\alpha}$ in the ground state.

I now focus on a set of different motional states of a single harmonic oscillator as described by Eq. 2.41. Each state is characterized by different c_n and they are relevant for the experiments described in this thesis.

Thermal state

The oscillator is subjected to coupling with the environment at a temperature T. At the thermal equilibrium, the oscillator is in a fully mixed state with no phase coherence between the Fock states. The population of each Fock state is weighted by the Boltzmann factor $\exp\{-n\hbar\omega/(k_B T)\}$, where k_B is the Boltzmann constant. The thermal state can be represented by the density matrix:

$$\rho_{\text{th}} = \frac{1}{1+\bar{n}} \sum_{n=0}^{\infty} \left(\frac{\bar{n}}{1+\bar{n}}\right)^n |n\rangle\langle n| \tag{2.44}$$

with the average occupation following the *Bose-Einstein distribution*:

$$\bar{n} = \frac{1}{(\mathrm{e}^{\hbar\omega/k_B T} - 1)}. \tag{2.45}$$

The occupation probability is then:

$$P_{\text{th}} = \frac{1}{1+\bar{n}} \left(\frac{\bar{n}}{1+\bar{n}}\right)^n, \tag{2.46}$$

Coherent state

Another important class of motional states is the *coherent state* $|\alpha\rangle$ [Lei+03]. The coherent state can be represented in the Fock basis as:

$$|\alpha\rangle = \mathrm{e}^{-|\alpha|^2} \sum_n \frac{\alpha^n}{\sqrt{n!}} |n\rangle \tag{2.47}$$

where α is a complex number and the probability distribution of the states is Poissonian:

$$P_n = |c_n|^2 = |\langle n|\alpha\rangle|^2 = \frac{\overline{n}^n e^{-\overline{n}}}{n!} \tag{2.48}$$

where $\overline{n} = |\alpha|^2$ is the average number of the distribution.

3 Trapped ion quantum information processing

In this chapter I describe the theory of the interaction between ions and light fields, including their manipulation and cooling. I then explain the structure of the laser related elements of the experimental setup, which is based on the use of beryllium and calcium ions.

3.1 Coherent laser-ion interaction

In this section I describe the interaction of a trapped ion with a laser field and briefly summarize the main concepts, derived from [Lei+03; Mar20].

We consider a trapped ion whose motional state is described by a quantum harmonic oscillator of angular frequency ω_α. The internal structure of the ion is such that we can approximate it to a two-level system whose transition frequency is close to the laser driving field frequency. This is a valid approximation as long as the coupling strengths of the laser field to the off-resonant transitions are much smaller than the detuning to them. The two internal states of the ion are indicated as $|\downarrow\rangle$ and $|\uparrow\rangle$ for the lowest and highest energy states, respectively. The energy difference between the states is $\hbar\omega_0$, with ω_0 being the frequency of the transition. The two states will be used later as a qubit to store quantum information. For the experiments of this thesis, the states that are used as qubits have typical transition frequencies of $\omega_0 \sim 2\pi \times 1\,\mathrm{GHz}$ for beryllium and $\omega_0 \sim 2\pi \times 400\,\mathrm{THz}$ for calcium. The Hamiltonian for the internal states of the ion and motional state of the quantum harmonic oscillator is then:

$$\hat{H}_0 = \hat{H}_{\text{qubit}} + \hat{H}_{\text{motion}} = \frac{\hbar\omega_0}{2}\hat{\sigma}_z + \sum_{\alpha=1}^{3} \hbar\omega_\alpha(\hat{a}_\alpha^\dagger \hat{a}_\alpha + 1/2) \tag{3.1}$$

where $\hat{\sigma}_z = |\uparrow\rangle\langle\uparrow| - |\downarrow\rangle\langle\downarrow|$ is one of the Pauli operators. For the laser field, we consider its wavelength to be much larger than the size of the interacting electron wave function. This allows us to consider only the lowest orders in the multipole expansion of the driving field [Lei+03]. The resulting Hamiltonian describing the interaction of the ion with the field becomes:

$$H_I = \frac{\hbar\Omega_0}{2} e^{i\vec{k}\cdot\hat{\vec{R}}} e^{i(\phi-\omega_l t)}\hat{\sigma}_+ + \text{h.c.} \tag{3.2}$$

where h.c. is the Hermitian conjugate of the first term. $\vec{k}$, ω_l and ϕ are the wave vector, frequency and phase of the driving field, respectively. $\hat{\vec{R}}$ is the position operator of the center of mass of the ion in a coordinate system aligned along the normal mode directions. $\hat{\sigma}_+ = |\uparrow\rangle\langle\downarrow|$ is the spin-flip operator. Ω_0 is the *resonant Rabi frequency* which defines the coupling strength between the laser field and the transition. It depends on the underlying transition and the amplitude of the field. In the work of this thesis, we consider only dipole allowed, quadrupole allowed or Raman transitions (see Sec. 3.2), which are all treated in the same way through the use of the Rabi frequency parameter. The term $\vec{k}\cdot\hat{\vec{R}}$ can be

described in terms of the *Lamb-Dicke parameter* η_α as:

$$\vec{k}\cdot\hat{\vec{R}} = \sum_{\alpha=1}^{3}\eta_\alpha\left(\hat{a}_\alpha^\dagger + \hat{a}_\alpha\right), \quad \eta_\alpha = k_\alpha\sqrt{\frac{\hbar}{2m\omega_\alpha}}, \tag{3.3}$$

where k_α is the projection of the laser wave vector along the direction of the normal mode α and $\sqrt{\hbar/(2m\omega_\alpha)}$ is the wave packet size in the ground state. In the experiments of this thesis, for an axial motional frequency of 2 MHz, the calcium ion qubit transitions are driven by a laser with wavelength of 729.35 nm at 45°with respect to the trap axis has a typical value of $\eta_\alpha \simeq 0.05$, while for a single beryllium ion trapped with the same axial curvature (frequency of $\simeq 4.2$ MHz) manipulated by Raman beams with resulting wave vector along the trap axis it has $\eta_\alpha \simeq 0.4$. The wave function of a single calcium ion in the ground state has an axial extension of ~ 8 nm, while for beryllium it is ~ 12 nm due to the lower mass. For the radial modes the secular frequency scales as $\omega \propto 1/m$ according to Eq. 2.12, resulting in the same wave packet size for both ion species of ~ 7 nm for a voltage configuration that gives a radial motional frequency of 2.5 MHz for calcium. The Lamb-Dicke parameter is different for both species due to the different wave vectors involved. In the case of an array of N ions, the term $\vec{k}\cdot\hat{\vec{R}}_j$ for the oscillation of ion j due to the normal mode α can be computed as [Hom13]:

$$\vec{k}\cdot\hat{\vec{R}}_j = \sum_{\alpha=1}^{3N}\eta_{j,\alpha}\left(\hat{a}_\alpha^\dagger + \hat{a}_\alpha\right), \tag{3.4}$$

where the Lamb-Dicke parameter is given by:

$$\eta_{j,\alpha} = \sqrt{\frac{\hbar}{2m_j\omega_\alpha}}\vec{k}\cdot\vec{e}'_{j,\alpha}. \tag{3.5}$$

We can represent Eq. 3.2 in the interaction picture with respect to $\hat{H}_0$. We use the *rotating-wave approximation* (RWA) in which fast rotating terms are neglected and only slowly rotating terms near resonance are kept. Moreover we consider only one motional mode to be near resonance with the laser field at a time (avoiding using the index α for now), while the others can be neglected, resulting in:

$$H'_I = \frac{\hbar}{2}\Omega_0 e^{i\eta\left(\hat{a}^\dagger e^{i\omega t} + \hat{a}e^{-i\omega t}\right)}\hat{\sigma}_+ e^{i(\phi-\delta t)} + \text{h.c} \tag{3.6}$$

where $\delta = \omega_l - \omega_0$ is the detuning of the laser frequency from the transition. This Hamiltonian has resonances at $\delta = s\omega$, where s is an integer number. These resonances perform the transitions $|\downarrow, n\rangle \leftrightarrow |\uparrow, n+s\rangle$ and the main ones considered here are:

- *carrier transition* (CAR): where $s = 0 \rightarrow \delta = 0$ and the interaction induces Rabi oscillations that just flip the spin $|\downarrow, n\rangle \leftrightarrow |\uparrow, n\rangle$;
- *blue sideband transition* (BSB): where $s = +1 \rightarrow \delta = +\omega$ and the interaction induces Rabi oscillations that flip the spin and change the energy of the Fock state by a single quantum according to $|\downarrow, n\rangle \leftrightarrow |\uparrow, n+1\rangle$;
- *red sideband transition* (RSB): where $s = -1 \rightarrow \delta = -\omega$ and the interaction induces Rabi oscillations that flip the spin and change the energy of the Fock state by a single quantum according to $|\downarrow, n\rangle \leftrightarrow |\uparrow, n-1\rangle$.

A simple explanation for the formation of the sidebands can be seen in the reference frame of the ion, in which it experiences a light field that is phase-modulated at the secular and micromotion frequencies due to its motional state. The Rabi frequency is given by:

$$\begin{aligned}\Omega_{n+s,n} &= \Omega_0 \left| \left\langle n+s \left| e^{i\eta\left(\hat{a}+\hat{a}^\dagger\right)} \right| n \right\rangle \right| \\ &= \Omega_0 e^{-\eta^2/2} \eta^{|s|} \sqrt{\frac{n_{\min}!}{n_{\max}!}} L_{n_{\min}}^{(|s|)}\left(\eta^2\right)\end{aligned} \tag{3.7}$$

where $n_{\min} = \min(n, n+s)$, $n_{\max} = \max(n, n+s)$ and $L_{n_{\min}}^{(|s|)}\left(\eta^2\right)$ are the generalized Laguerre polynomials defined as:

$$L_{n_{\min}}^{(|s|)}\left(\eta^2\right) = \sum_{k=0}^{n_{\min}} (-1)^k \begin{pmatrix} n_{\min}+|s| \\ n_{\min}-k \end{pmatrix} \frac{\eta^{2k}}{k!}. \tag{3.8}$$

Eq. 3.6 can be simplified by working in the *Lamb-Dicke regime* where $\eta\sqrt{\langle(\hat{a}^\dagger+\hat{a})^2\rangle} = \eta\sqrt{2n+1} \ll 1$, which means that the ion's wave function is much smaller than $1/k$. We can then expand Eq. 3.6 at the first order:

$$\hat{H}_{\mathrm{I}}'^{\mathrm{LD}}(t) = \frac{\hbar}{2}\Omega_0\hat{\sigma}_+ \left[1 + i\eta\left(\hat{a}e^{-i\omega t} + \hat{a}^\dagger e^{i\omega t}\right)\right] e^{i(\phi-\delta t)} + \text{h.c.} \tag{3.9}$$

and the Rabi frequency is approximated to:

$$\Omega_{n+s,n} \simeq \Omega_0 \eta^{|s|} \sqrt{\frac{n_{\min}!}{n_{\max}!}} \frac{1}{|s|!}. \tag{3.10}$$

By using the RWA, the CAR, BSB and RSB transition Hamiltonians can be expressed as:

$$\begin{aligned}\hat{H}'_{\mathrm{CAR}} &= \frac{\hbar}{2}\Omega_0\left(\hat{\sigma}_+ e^{i\phi} + \hat{\sigma}_- e^{-i\phi}\right), \\ \hat{H}'_{\mathrm{BSB}} &= \frac{\hbar}{2}\Omega_0\eta\left(i\hat{a}^\dagger\hat{\sigma}_+ e^{i\phi} - i\hat{a}\hat{\sigma}_- e^{-i\phi}\right), \\ \hat{H}'_{\mathrm{RSB}} &= \frac{\hbar}{2}\Omega_0\eta\left(i\hat{a}\hat{\sigma}_+ e^{i\phi} - i\hat{a}^\dagger\hat{\sigma}_- e^{-i\phi}\right).\end{aligned} \tag{3.11}$$

with Rabi frequencies:

$$\begin{aligned}\Omega_{n,n}^{\mathrm{CAR}} &= \Omega + O(\eta^2), \\ \Omega_{n+1,n}^{\mathrm{BSB}} &= \Omega\eta\sqrt{n+1} + O(\eta^2), \\ \Omega_{n-1,n}^{\mathrm{RSB}} &= \Omega\eta\sqrt{n} + O(\eta^2).\end{aligned} \tag{3.12}$$

For a sideband of higher order j the Rabi frequency scales as η^j. For each transition a full Rabi oscillation requires a time $t = 2\pi/\Omega_{n+s,n}$ to make the spin to return to the original state (apart for a global phase). This is commonly referred to as a "2π pulse". If the transition is driven for half this time we have a "π pulse", which flips the spin state. For a fourth of the time we have a "$\pi/2$ pulse" which creates an equal superposition of $|\downarrow\rangle$ and $|\uparrow\rangle$.

Fig. 3.1 (a) shows a pictorial representation of the coupled system of spin and motional state, which is also referred to as *state ladder*. This is useful to understand the energy of the states and the most important transitions we consider here. The Rabi frequencies for the carrier, first and second blue sideband transitions for different number states are shown in Fig. 3.1 (b).

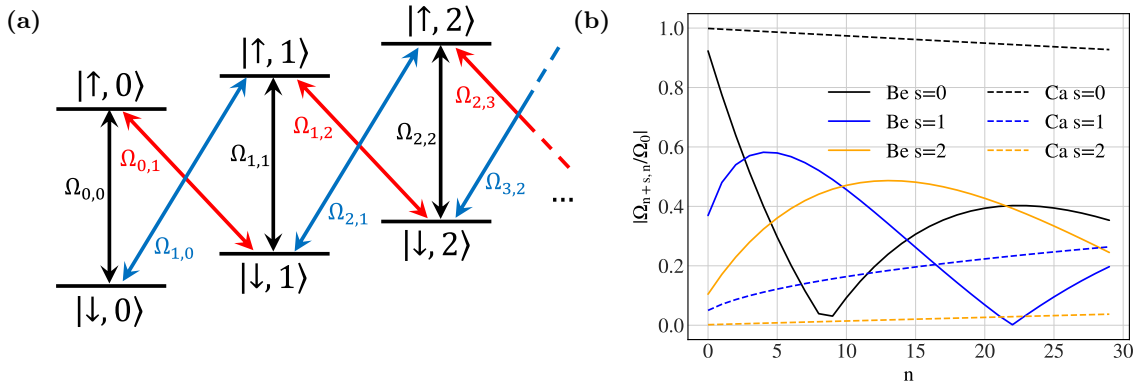

Figure 3.1: (a) State ladder of the coupled spin-motion system. Carrier (black), red sideband (red) and blue sideband (blue) transitions for each state are indicated by the arrows, with relative Rabi frequency. (b) Rabi frequency amplitudes as a function of the Fock state number from Eq. 3.7 for |s|=0,1 and 2. Beryllium frequencies are computed for $\eta = 0.4$, while for calcium $\eta = 0.05$, typical for single ion experiments.

3.1.1 Rabi oscillations

In the state ladder, a general superposition of states is given by:

$$|\Psi(t)\rangle = \sum_{n=0}^{\infty} c_{\downarrow,n}(t)|\downarrow, n\rangle + c_{\uparrow,n}(t)|\uparrow, n\rangle \tag{3.13}$$

This state evolves under the influence of the Hamiltonian of Eq. 3.6. We can compute the evolution of the probability amplitudes through the Schrödinger equation, which result in:

$$\begin{pmatrix} c_{\uparrow,n+s}(t) \\ c_{\downarrow,n}(t) \end{pmatrix} = \hat{R}_n^s(t,\delta,\phi) \begin{pmatrix} c_{\uparrow,n+s}(0) \\ c_{\downarrow,n}(0) \end{pmatrix} \tag{3.14}$$

where $\hat{R}_n^s$ is the rotation operator:

$$\hat{R}_n^s(t,\delta,\phi) = \begin{bmatrix} e^{-i\delta' t/2}\left(\cos\frac{\tilde{\Omega}_n^s t}{2} + i\frac{\delta'}{\tilde{\Omega}_n^s}\sin\frac{\tilde{\Omega}_n^s t}{2}\right) & e^{-i\delta' t/2}\left(-i\frac{\Omega_{n+s,n}}{\tilde{\Omega}_n^s}e^{i\left(\phi+|s|\frac{\pi}{2}\right)}\right)\sin\frac{\tilde{\Omega}_n^s t}{2} \\ e^{i\delta' t/2}\left(-i\frac{\Omega_{n+s,n}}{\tilde{\Omega}_n^s}e^{-i\left(\phi+|s|\frac{\pi}{2}\right)}\right)\sin\frac{\tilde{\Omega}_n^s t}{2} & e^{i\delta' t/2}\left(\cos\frac{\tilde{\Omega}_n^s t}{2} - i\frac{\delta'}{\tilde{\Omega}_n^s}\sin\frac{\tilde{\Omega}_n^s t}{2}\right) \end{bmatrix} \tag{3.15}$$

where $\delta' = \delta - s\omega_m$ is the detuning of driving field from the s sideband frequency and $\tilde{\Omega}_n^s = \sqrt{\Omega_{n+s,n}^2 + \delta'^2}$ is the "effective" Rabi frequency, which differs from the common one due to the detuning of the laser frequency.

As an example let's assume that initially the state of the system is in the lower spin state ($c_{\uparrow,n+s}(0) = 0$), and we are interested in studying the probability that the system, interacting with a laser field, undergoes a spin-flip at time t. The probability is then given by:

$$\begin{aligned} P_{|\uparrow,n+s\rangle}(t) = |c_{\uparrow,n+s}(t)|^2 &= \left| e^{-i\delta' t/2}\left(-i\frac{\Omega_{n+s,n}}{\tilde{\Omega}_n^s}e^{i\left(\phi+|s|\frac{\pi}{2}\right)}\right)\sin\frac{\tilde{\Omega}_n^s t}{2}\right|^2 = \\ &= \frac{\Omega_{n+s,n}^2}{\Omega_{n+s,n}^2 + \delta'^2}\sin^2\left(\frac{\sqrt{\Omega_{n+s,n}^2 + \delta'^2}}{2}t\right) \end{aligned} \tag{3.16}$$

which shows periodic oscillations. If the driving field is on resonance the oscillations have higher contrast, while if it is off-resonance the oscillations are faster.

If the laser is on resonance with a specific transition $\delta' = 0$, the resonant rotation operator describing a generalized Rabi oscillation is:

$$\hat{R}^s_{n,\,\mathrm{res}}\left(\theta_{n+s,n},\phi\right) = \begin{bmatrix} \cos\frac{\theta_{n+s,n}}{2} & -ie^{i\left(\phi+|s|\frac{\pi}{2}\right)}\sin\frac{\theta_{n+s,n}}{2} \\ -ie^{-i\left(\phi+|s|\frac{\pi}{2}\right)}\sin\frac{\theta_{n+s,n}}{2} & \cos\frac{\theta_{n+s,n}}{2} \end{bmatrix} \tag{3.17}$$

where $\theta_{n+s,n} = \Omega_{n+s,n}t$ and ϕ are the rotation angles. This means that we can drive a laser pulse with area $\theta_{n+s,n}$ and ϕ which coherently control the internal (spin) and external (motion) states of the ion.

3.2 Ions

3.2.1 Beryllium ion

Beryllium is the lightest species which has been employed for trapped ion QIP. It is generally chosen due to the low mass that induces tight confinement, strong light-motion coupling and long coherence time qubit. On the other side, many of the internal transitions are in the UV region, which causes technological challenges and might induce charging of the trap. The isotope ^{9}Be is the only stable one. In the experiments of this thesis, we work with singly ionized beryllium ions $^9\mathrm{Be}^+$. Now I give a summary of the internal structure and how we manipulate the state of this ion. More details can be found in [Lo15; Mar20].

The generation of beryllium atoms is performed in an atomic oven [Kie15]. The atomic beam reaches the loading zone of the trap, where it gets singly ionized through a two-photon ionization (PI) process by a laser beam at 235 nm [Lo+14]. The electrical structure of beryllium ion is similar to alkali neutral atoms, with just one valence electron. The relevant electronic energy levels for our experiments are $2^2S_{1/2}$, $2^2P_{1/2}$ and $2^2P_{3/2}$, which I indicate from now as $S_{1/2}$, $P_{1/2}$ and $P_{3/2}$ respectively for simplicity. The energy levels of the valence electron at the magnetic field of 119.45 G are shown in Fig. 3.2, while the beam configuration is shown in Fig. 3.4. Beryllium ion has a hyperfine structure due to the coupling of the total angular momentum J with the nuclear spin $I = 3/2$, creating two manifolds of $F = 1$ and $F = 2$ for the levels mentioned above. The degeneracy of the sublevels is lifted by the magnetic field due to the Zeeman effect. Transitions between the sublevels of the ground state can be driven with microwave fields or two-photon stimulated Raman process [Win+98]. In our setup, the latter approach is exploited. The transitions $S_{1/2} \leftrightarrow P_{1/2}$ and $S_{1/2} \leftrightarrow P_{3/2}$ are dipole allowed. The manipulation of the electron state is performed by means of lasers at 313 nm.

In our experiments state of the ion is always initialized in $\left|S_{1/2}, F = 2, m_F = 2\right\rangle$ by optical pumping. To perform state detection, the ion in the initialized state is almost resonantly excited to $\left|P_{3/2}, F = 3, m_F = 3\right\rangle$ with a σ^+ polarized light. This is a cycling transition with a linewidth of $2\pi \times 19.4$ MHz (lifetime of 8.2 ns), which makes the ion quickly decay to the original level while emitting a photon at 313 nm, which is detected with a photomultiplier tube (PMT) or a camera. Ideally, no other states are detected with this method, but polarization impurity and off-resonant pumping slightly reduce the fidelity of this process. Doppler cooling, described in Subsec. 3.3.1, is also performed on this transition.

The initialization and repumping of the ion from any state of the $S_{1/2}$ manifold is performed by means of two repump lines F1 and F2 which drive the transitions $|S_{1/2}, F = 1, m_F = 1\rangle \leftrightarrow |P_{1/2}, F = 2, m_F = 2\rangle$ and $\left|S_{1/2}, F = 2, m_F = 1\right\rangle \leftrightarrow \left|P_{1/2}, F = 2, m_F = 2\right\rangle$, respectively. F1 and F2 are σ^+ polarized. They also off-resonantly drive the other states of the $S_{1/2}$ manifold.

To manipulate the state of the ion in the $S_{1/2}$ manifold, we employ a Raman transition. This is performed by means of two lasers that couple the $S_{1/2}$ to the $P_{1/2}$ states. A specific transition in the $S_{1/2}$ manifold can be driven by choosing the frequency difference of the two lasers equal to the frequency of the transition. To minimize the population of the $P_{1/2}$ manifold, which would increase the scattering rate, the frequencies are detuned by $\sim 230\,\mathrm{GHz}$. This cannot be increased arbitrarily, as it would reduce the Rabi frequency of the Raman transition. Multiple configurations are used for the beam directions of the Raman lasers. Two of them are used in a co-propagating configuration, while two have an angle of 90°between each other. The polarization of the common laser is π along the magnetic field, while the other two are linearly polarized perpendicular to the magnetic field, such that the ions experience a mixture of σ^+ and σ^-. For the Raman transition the effective wave vector is given by the difference of the wave vectors of the beams $\vec{k} = \vec{k_1} - \vec{k_2}$. In the co-propagating configuration the effective wave vector has a magnitude of $k_{\mathrm{co}} \simeq 30\,\mathrm{m}^{-1}$, while in the 90°setting it is $k_{90} \simeq 2.8 \times 10^7 \mathrm{m}^{-1}$. In the co-propagating configuration the Lamb-Dicke parameter of Eq. 3.3 is $\eta \simeq 0$, which makes it suitable to drive motion-insensitive transitions, decoupling from the ion's motion induced by heating, micromotion or other sources. In the 90°configuration the Lamb-Dicke parameter is higher, making it convenient for driving motion-sensitive transitions, such as secular and micromotion sidebands. This feature is used to detect and compensate the presence of axial micromotion, as explained in detail in Sec. 6.1.

For the implementation of the qubit we use the state $\left|S_{1/2}, F = 2, m_F = 0\right\rangle$ as $|\downarrow\rangle$ and $\left|S_{1/2}, F = 1, m_F = 1\right\rangle$ as $|\uparrow\rangle$ because this transition is first-order insensitive to magnetic field fluctuations at 119.45 G magnetic field. This transition is referred to as *field-independent qubit* (FIQ) and has a coherence time of $\sim$ 4s [Lo15]. Another interesting transitions is $\left|S_{1/2}, F = 2, m_F = 2\right\rangle \leftrightarrow \left|S_{1/2}, F = 1, m_F = 1\right\rangle$ which is used for initializing the qubit or as a *field-dependent qubit* (FDQ). The transition $\left|S_{1/2}, F = 2, m_F = 0\right\rangle \leftrightarrow \left|S_{1/2}, F = 1, m_F = -1\right\rangle$ is referred to as *field-independent shelving* (FIS) which is used for shelving during state readout.

It is interesting to notice that beryllium ions in an excited state, e.g. in P states, might induce the endothermic chemical reaction $\mathrm{Be}^+ + \mathrm{H}_2 \rightarrow \mathrm{BeH}^+ + \mathrm{H}$ [Saw+15]. This forms a hydride that cannot be controlled by our laser setup, for this reason we generally empty the trap once we think such a hydride has formed. This reduces the lifetime of the trapped ion down to a few hours. This phenomenon can be mitigated by photodissociation with a laser beam at 157 nm or by reducing the saturation parameter of the detection/cooling laser [Saw+15]. In our setup, we noticed an increase in ion lifetime up to several hours by reducing the duty cycle of the detection/cooling laser. Although the lower duty cycle cannot be exploited while running an experiment, it is used while performing other operations to reduce the necessity of loading new ions, which we find can charge the trap and increase background vacuum levels.

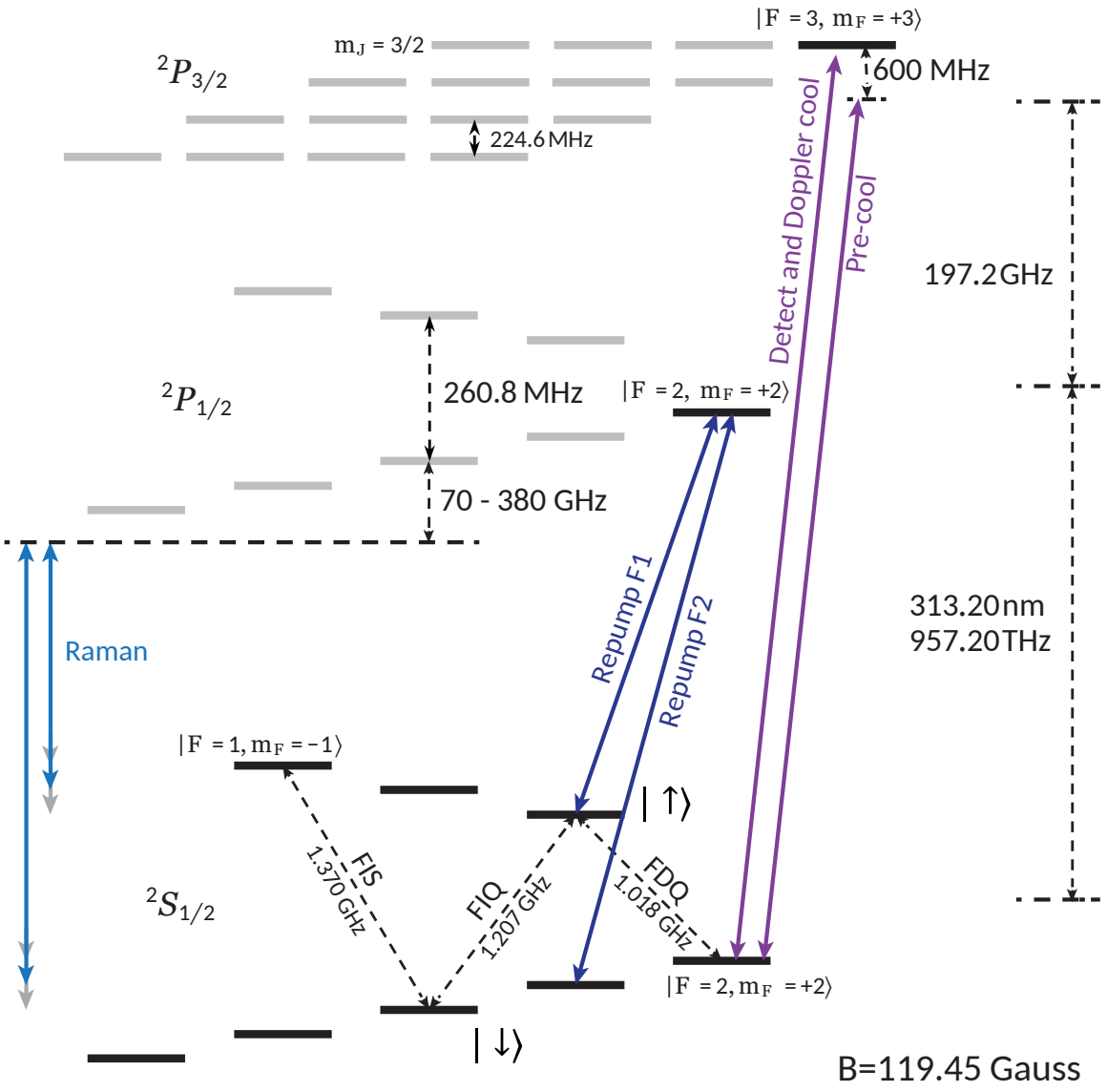

Figure 3.2: $^9Be^+$ energy level structure at 119.45 G. The solid lines are the transitions excited by laser beams. The highlighted energy levels are typically manipulated in experiments.

3.2.2 Calcium ion

The second species used in our experiments is calcium. The advantage of this species is that the wavelengths of the lasers used to drive the internal transitions are in the optical region. The mass of this atom is ≈ 4.4 times the mass of beryllium. The ^{40}Ca is one of the stable isotopes and the most abundant. In the experiments of this thesis, we work with singly ionized calcium ions. Now I give a summary of the internal structure and how we manipulate the state of this ion. More details can be found in [Lo15; Mar20].

The generation of calcium atoms is performed in an atomic oven [Kie15]. The atomic beam reaches the loading zone of the trap, where it gets singly ionized through a two-photon ionization (PI) process by laser beams at 423 nm and 375 nm. The electrical structure of calcium ion is similar to alkali neutral atoms, with just one valence electron. The relevant electronic energy levels for our experiments are $4^2S_{1/2}$, $4^2P_{1/2}$, $4^2P_{3/2}$, $3^2D_{3/2}$ and $3^2D_{5/2}$,

Transition	λ (nm)	$\Gamma/2\pi$ (MHz)	τ (ns)
$S_{1/2} \leftrightarrow P_{1/2}$	397	22.7	7.7 ns
$S_{1/2} \leftrightarrow D_{5/2}$	729	1.5×10^{-7}	1.045×10^{9}
$D_{3/2} \leftrightarrow P_{1/2}$	866	1.7	94.3
$D_{5/2} \leftrightarrow P_{3/2}$	854	1.57	101

Table 3.1: Transition wavelength (λ), linewidth (Γ) and lifetime (τ) of the $^{40}Ca^{+}$ transitions.

which I indicate from now as $S_{1/2}$, $P_{1/2}$, $P_{3/2}$, $D_{3/2}$ and $D_{5/2}$ respectively for simplicity. The energy levels of the valence electron at the magnetic field of 119.45 G are shown in Fig. 3.3, while the beam configuration is shown in Fig. 3.4. Calcium ion has no hyperfine structure and the degeneracy of the sublevels is lifted by the magnetic field due to the Zeeman effect. The transitions $S_{1/2} \leftrightarrow P_{1/2}$, $S_{1/2} \leftrightarrow P_{3/2}$, $D_{3/2} \leftrightarrow P_{1/2}$ and $D_{5/2} \leftrightarrow P_{3/2}$ are dipole allowed. The transition $S_{1/2} \leftrightarrow D_{3/2}$ and $S_{1/2} \leftrightarrow D_{5/2}$ are quadrupole allowed. The transition $P_{1/2} \leftrightarrow D_{5/2}$ is not allowed.

A summary of the properties of the transitions is shown in Tab. 3.1. The state of the ion is always initialized in $|S_{1/2}, m_J = 1/2\rangle$. To perform state detection, the ion in the initialized state is almost resonantly excited to $|P_{1/2}, m_J = 1/2\rangle$ with a π polarized light at 396.96 nm. This transition is not closed, then an ion in $P_{1/2}$ state can decay emitting a photon either to the $S_{1/2}$ or to the meta-stable $D_{3/2}$ manifold, with a branching ratios of 95% and 5%. To remove population from $D_{3/2}$ and repump into the $P_{1/2}$ manifold we use a 866.45 nm laser. This light is modulated to have two frequency components such that any sublevel can be repumped [Kie15], thus it has a polarization of σ^+ and σ^-. Doppler cooling is also performed on the transition $|S_{1/2}, m_J = 1/2\rangle \leftrightarrow |P_{1/2}, m_J = 1/2\rangle$.

The initialization and repumping of the ion $|S_{1/2}, m_J = -1/2\rangle \leftrightarrow |S_{1/2}, m_J = 1/2\rangle$ is performed by having a second beam at 396.96 nm linearly polarized orthogonal to the magnetic field, such that the ion experience a mixture of σ^+ and σ^- polarized light. The σ^- is far-off resonant, then it does not drive any transition. The repumping from the meta-stable $D_{5/2}$ manifold (for which I explain the use below) is performed by coupling it to the $P_{3/2}$ manifold with a 854 nm laser with two frequencies and polarization of σ^+ and σ^-. The $P_{3/2}$ state quickly decays either to the $S_{1/2}$ (emitting a photon at 393 nm), to the $D_{3/2}$ manifold or back to $D_{5/2}$, with probabilities of around 94%, 6% and <1% respectively.

For the implementation of the qubit there are typically two choices. The first one, not used in our experiment, is between the two levels of the $S_{1/2}$ manifold and is referred to as *Zeeman qubit*. This qubit can be manipulated with a radio-frequency magnetic field or a stimulated Raman process [Hom+06; Pos+09] and has a long coherence time but suffers from strong dephasing due to high sensitivity to magnetic field noise, requiring specific measures [Rus+16]. The second choice is on the quadrupole transition $\left|S_{1/2}, m_J = 1/2\right\rangle \leftrightarrow \left|D_{5/2}, m_J = +3/2\right\rangle$ which is referred to as *optical qubit*. The qubit is manipulated by means of a 729 nm beam at 45°to the trap axis which gives a Lamb-Dicke parameter of $\eta \simeq 0.05$, which fulfills the Lamb-Dicke approximation for all the applications of this thesis. The optical qubit has a coherence time of ~ 1.7 ms in our setup, mostly limited by magnetic field noise. This makes this qubit a worse choice than the one implemented by the beryllium ion. For this reason, the calcium ion is better used as a coolant ion for the QCCD architecture.

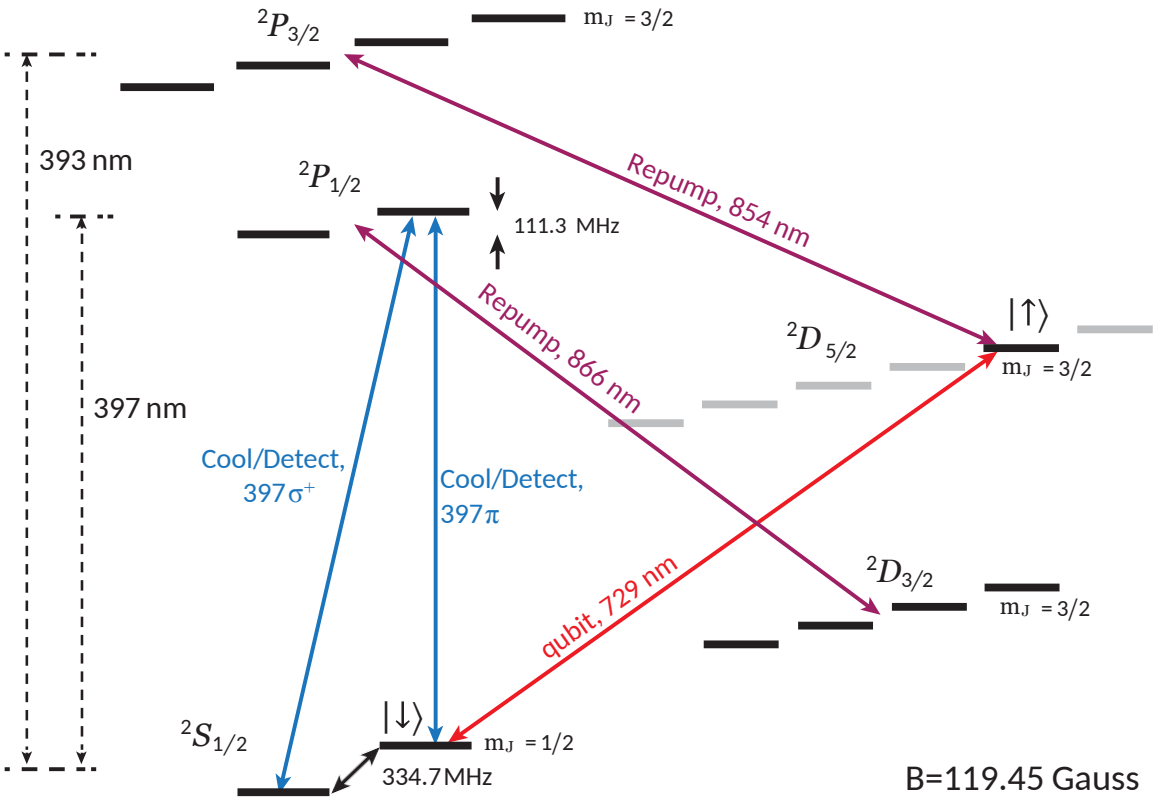

Figure 3.3: $^{40}Ca^+$ energy level structure at 119.45 G. The solid lines are the transitions excited by laser beams. The highlighted energy levels are typically manipulated in experiments.

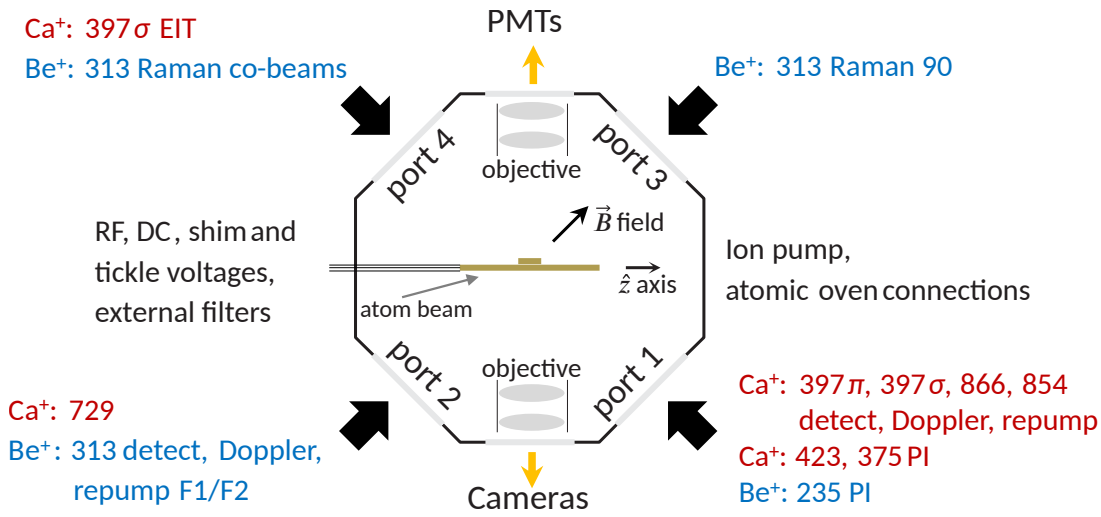

Figure 3.4: Top-down view of the vacuum chamber. At the center the trap chip is shown, highlighting the orientation of the trap axis, magnetic field and neutral atom beam currently used. The laser beam directions and entry viewports are indicated. Laser wavelengths are in nm. PI beams are directed toward the left loading zone. Raman, 729 nm and 397 nm EIT beams are aligned along the central experimental zone. The remaining beams are split between the two zones.

3.3 Cooling of vibrational modes

High-fidelity quantum operations on trapped ions require their motional states to be as close as possible to the ground state. Motional energy can be caused by collisions with background gases, electric field noise, imperfect shuttling operations and state detection. To remove it, we employ different cooling techniques. The general sequence is composed by far-detuned Doppler cooling (pre-cool), standard Doppler cooling, Electromagnetically-induced transparency (EIT) cooling on calcium only and resolved-sideband cooling (SBC). This allows us to prepare ions close to the vibrational ground state. The use of mixed-species arrays also allows for cooling normal modes for which one species has low participation by applying dissipation on the other species, performing sympathetic cooling.

Here I summarize the theory behind these methods, more details can be found in [Hom13; Lei+03; Mar20]. I then describe the performances when they are applied to the mixed-species setup.

3.3.1 Doppler cooling

Doppler cooling is performed by means of a laser beam red detuned from a dipole-allowed transition. An ion moving toward the laser beam will experience a blue-shifted frequency, which makes it closer to resonance and increases the probability of photon absorption. The photon momentum is then transferred to the ion, which gets slowed down. The decay from the excited state makes the ion emit a photon, which happens probabilistically in the whole solid angle, resulting in a net reduction in the initial velocity and kinetic energy. This also imposes limits on the final achievable temperature, which is limited by the random walk in momentum space. If the laser wave vector has a projection on all the normal modes, they can all be cooled at the same time. It is important to not have degenerate modes as their directions are not well-defined and only the motion along the laser wave vector is cooled down, while the orthogonal ones are heated by photon recoil [Ami+11].

More in detail, we consider the motional frequency ω_m smaller than the dipole transition linewidth Γ. The probability of exciting the ions by the laser beam is given by:

$$p_{\mathrm{ee}} = \frac{s/2}{1 + s + (2\Delta/\Gamma)^2}, \tag{3.18}$$

where $s = 2|\Omega_0|^2/\Gamma^2$ is the saturation parameter, Ω_0 is the resonant Rabi frequency and Δ the detuning from the resonance. The rate of reduction in kinetic energy is then:

$$\frac{dE_K}{dt} = \frac{2\hbar\Gamma}{m}\left(\frac{dp_{ee}}{d\Delta}\right)\frac{(\vec{k}\cdot\vec{p})^2}{2m}, \tag{3.19}$$

where m is the ion mass, $\vec{k}$ is the laser wave vector and $\vec{p}$ the ion momentum. In terms of the normal modes we have:

$$\vec{k}\cdot\vec{p} = \sum_{\alpha=1}^{3}\sqrt{m}\vec{k}\cdot\vec{e}'_\alpha p'_\alpha \tag{3.20}$$

with $\vec{e}'_\alpha$ the eigenvector of the normal mode. The resulting cooling rate is:

$$\frac{dn_\alpha}{dt} = 2\omega_\alpha\eta_\alpha^2(n_\alpha + 1/2)\Gamma\left(\frac{dp_{ee}}{d\Delta}\right). \tag{3.21}$$

where η_α is the Lamb-Dicke parameter for the mode α.

As mentioned before, the cooling process is limited by the random emission of photons. Assuming $\Omega \ll \Delta, \Gamma$, the absorption and emission of photons can be considered independent and the heating rate is:

$$\frac{dn_\alpha}{dt} = \Gamma p_{ee} \left(\eta_\alpha^2 + \frac{2/5\hbar^2 |\vec{k}|^2 |\vec{e}_\alpha|^2}{2m} \right) \tag{3.22}$$

and the equilibrium temperature is for $\Delta = \Gamma\sqrt{1+s}/2$:

$$T_{\mathrm{D}} = \frac{\hbar\Gamma\sqrt{1+s}}{4k_{\mathrm{B}}}(1+2/5). \tag{3.23}$$

Calcium ions are Doppler cooled through the transitions $\left|S_{1/2}, m_J = 1/2\right\rangle \leftrightarrow \left|P_{1/2}, m_J = 1/2\right\rangle$ and $\left|S_{1/2}, m_J = -1/2\right\rangle \leftrightarrow \left|P_{1/2}, m_J = 1/2\right\rangle$. the pre-cool stage is red detuned by roughly 40 MHz from the first transition and 200 MHz from the second, and it lasts for several milliseconds. Standard Doppler cooling is performed with the lasers red detuned by 5-10 MHz and it lasts for about 600 µs. The resulting mean thermal occupation for the axial and radial modes are $\bar{n}_{ax} \simeq 5$ and $\bar{n}_{rad} \simeq 3-4$ quanta.

Beryllium ions are Doppler cooled through the transition $\left|S_{1/2}, F = 2, m_F = 2\right\rangle \leftrightarrow \left|P_{3/2}, F = 3, m_F = 3\right\rangle$. Pre-cool is red detuned by roughly 600 MHz and it lasts for 2-3 ms. Standard Doppler cooling is red detuned by about 10 MHz and it lasts for about 600 µs. The resulting mean thermal occupation for the axial and radial modes are $\bar{n}_{ax} \simeq 4$ and $\bar{n}_{rad} \simeq 1$ quanta.

3.3.2 Electromagnetically-induced transparency cooling

The final temperature reached after Doppler cooling is limited by the natural linewidth of the transition, as shown in Eq. 3.23. To further reduce the final temperature, the electromagnetically-induced transparency (EIT) cooling creates a narrower spectral feature.

EIT cooling requires a three-level lambda system in which there are two ground states $|g\rangle$ and $|f\rangle$ and a short-lived excited state $|e\rangle$. A strong laser beam is blue detuned by Δ_σ from the transition $|f\rangle \leftrightarrow |e\rangle$, with a Rabi frequency of Ω_σ. Due to the *AC Stark effect*, the light shifts the energy levels of the states by:

$$\delta = \frac{1}{2}\left(\sqrt{\Omega_\sigma^2 + \Delta_\sigma^2} - |\Delta_\sigma|\right) \tag{3.24}$$

creating shifted states called *dressed states* $|\tilde{f}\rangle$ and $|\tilde{e}\rangle$, and pumps the ion to state $|g\rangle$. A second weaker probe beam drives the transition $|g\rangle \leftrightarrow |\tilde{e}\rangle$ with detuning Δ_π and Rabi frequency $\Omega_\pi \ll \Omega_\sigma$. This creates a sharp Fano-like absorption profile, with an excited state $|\tilde{e}\rangle$ probability:

$$\rho_{ee}(\Delta) = \frac{4\Delta^2\Omega_\pi^2\Omega_\sigma^2\Gamma}{D} \tag{3.25}$$

where $\Gamma = \Gamma_\pi + \Gamma_\sigma$ is the total decays rate of the two transitions, ρ_{ee} is the population in the excited state as function of the detuning $\Delta = \Delta_\pi - \Delta_\sigma$ and the denominator is:

$$\begin{aligned} D =& 8\Delta^2\Omega_\sigma^2\Omega_\pi^2\Gamma + 4\Delta^2\Gamma^2\left(\Omega_\sigma^2\Gamma_\pi + \Omega_\pi^2\Gamma_\sigma\right) \\ &+ 16\Delta^2\left[\Delta_\sigma^2\Omega_\pi^2\Gamma_\sigma + \Delta_\pi^2\Omega_\sigma^2\Gamma_\pi\right] + 8\Delta_\sigma\Delta\Omega_\pi^4\Gamma_\sigma \\ &- 8\Delta_\pi\Delta\Omega_\sigma^4\Gamma_\pi + \left(\Omega_\sigma^2 + \Omega_\pi^2\right)^2\left(\Omega_\sigma^2\Gamma_\pi + \Omega_\pi^2\Gamma_\sigma\right). \end{aligned} \tag{3.26}$$

The absorption profile is shown in Fig. 3.5. The population in the excited state features a zero for $\Delta_\pi = \Delta_\sigma$ and a sharp resonance at $\Delta_\pi = \Delta_\sigma + \delta$. To cool the vibrational mode m with frequency ω_m, it is possible to set $\Delta_\pi = \Delta_\sigma$ and $\delta = \omega_m$. In this way the transition $|g, n\rangle \leftrightarrow |\tilde{e}, n\rangle$ is suppressed, where n is the n-th Fock state, but maximizes the red-sideband transition $|g, n\rangle \leftrightarrow |\tilde{e}, n-1\rangle$, removing a quantum of motion $\hbar\omega_m$ and cooling the mode. Cooling is limited by the probability of exciting the blue-sideband transition $|g, n\rangle \leftrightarrow |\tilde{e}, n-1\rangle$, which is smaller than for the red-sideband. The resulting final temperature is then [MEK00; Lei+03]:

$$\bar{n} \simeq \left(\frac{\Gamma}{4\Delta_\sigma}\right)^2 \tag{3.27}$$

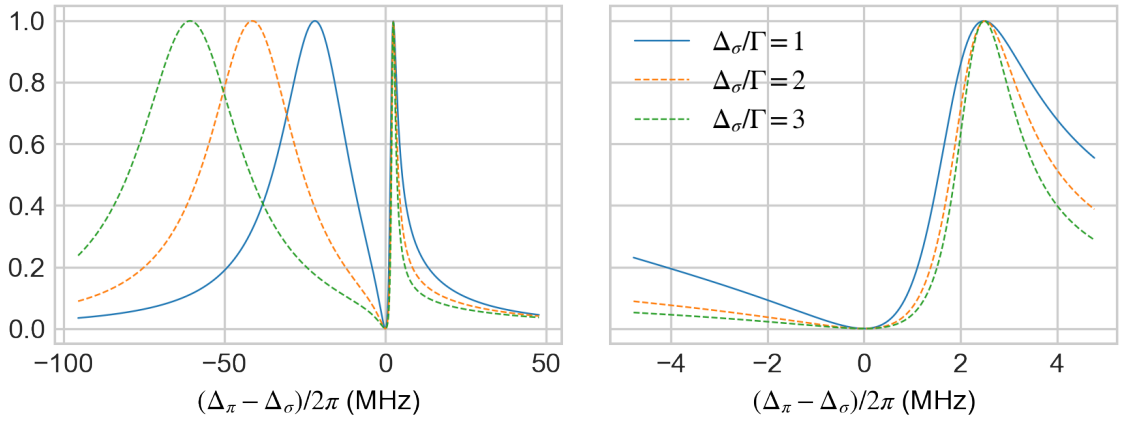

Figure 3.5: EIT absorption profile as a function of the probe laser detuning Δ_π, for three different pump detunings Δ_σ. The value of Ω_σ is adjusted such that the EIT resonance is at $\Delta = 2\pi \times 2.5$ MHz, with $\Omega_\pi = \Omega_\sigma/100$ and $\Gamma = 2\pi \times 22.7$ MHz. The image is taken from [Mar20].

In our experimental setup EIT cooling is performed on calcium. There are two counter-propagating 397 nm beams at 45°to the trap axis such that the wave vector difference has a projection on all the vibrational modes. The employed states are $|g\rangle = |S_{1/2}, m_J = 1/2\rangle$, $|f\rangle = |S_{1/2}, m_J = -1/2\rangle$ and $|e\rangle = |P_{1/2}, m_J = 1/2\rangle$. We generally set $\Delta_\sigma \simeq \Gamma$, reducing the calcium motional energy $\bar{n} < 1$ in $\sim 300\,\mu$s. For mixed-species ion arrays we generally set δ to the frequency of the lowest radial mode Y2, due to the highest participation of the calcium ion in this mode. This mode is therefore cooled to the lowest occupancy, while the cooling also shows a significant effect for the X2 mode. For the Be–Ca crystal, mean occupancies of $\bar{n}_{Y2}$=0.14(6) and $\bar{n}_{X2}$=0.36(7) quanta were measured after EIT cooling.

3.3.3 Resolved-sideband cooling

Resolved-sideband cooling, referred also as sideband cooling (SBC), is used as the last cooling step to reach the motional ground state for specific vibrational modes, most often the axial modes in our setup.

If the motional mode frequency ω_m is big compared to the linewidth of the transition Γ used for cooling, then the motional energy can be reduced by driving several cycles of red-sideband transitions $|\downarrow, n\rangle \leftrightarrow |\uparrow, n-1\rangle$ followed by optical pumping into the internal ground state $|\downarrow, n-1\rangle$. The latter is performed by excitation to a short-lived additional state ($P_{1/2}$) in the ion from which it subsequently rapidly decays. The initial phonon population generally follows a thermal distribution, where each Fock state has a different red-sideband

Rabi frequency. To ensure that the population is cooled over the whole distribution, the duration of the sideband pulse is linearly increased during the process. The cooling process is primarily limited by the off-resonant carrier and blue-sideband excitation, which increase the temperature and limit the ground-state occupation probability to $p_0 \approx 1-(\Gamma/2\omega_m)^2$, which can be made close to 1. These limitations are mitigated by shaping the pulse amplitude, which reduces the bandwidth.

We apply sideband cooling on both calcium and beryllium ions. For beryllium, the red-sideband Rabi frequency is zero for some Fock states in the relevant region. For this reason in single-species crystals we implement second-order sideband cooling. Moreover we can only sideband cool the axial modes due to the direction of the wave vector of the 90°Raman configuration. In the case of mixed-species crystals, these problems are solved by sympathetically cooling the modes through the calcium ion. Generally, we employ calcium sideband cooling on the axial in-phase mode (Z1) and beryllium one on the out-of-phase mode (Z2), resulting in thermal mean phonon occupations of $\bar{n}_{Z1}$=0.03(2), $\bar{n}_{Z2}$=0.01(2) quanta.

4 Mixed-species experimental operations

4.1 Typical experimental sequence

The mixed-species experiments performed on this experimental setup follow a standard basic sequence. Each experimental shot starts with cooling of the vibrational modes and internal state preparation. These steps are then followed by a set of operations on the ions and/or the qubits, with intermediate detections when needed. Afterward both ions' internal states are detected. Lastly the far-detuned Doppler "pre-cooling" is left active until the next shot. The involved laser pulses are shown in Fig. 4.1. This sequence is typically repeated hundreads of times to obtain significant statistics, retrieving a data point. Tens of data points with different experimental parameters are generally collected to form a scan.

The duration of the pre-cool part of the sequence is relatively long (5-8 ms) for the experiments related to the transport and separation of ions, as they might induce intense heating when not correctly calibrated. Additional cooling might be required in between the separation sequence when unoptimized. The other cooling methods (EIT and sideband cooling) require specific parameters depending on the exact ion crystal configuration, as described in Sec. 3.3.

I describe now a set of experimental techniques we employ to diagnose and manipulate the states of the ions.

4.2 Tickle

Applying an oscillating electric field in the ion trap can be used to probe the trap potentials, diagnose the normal modes and manipulate motional states. This oscillating field is generally referred to as *tickle* (or more informally *DC tickle*). It creates a force on the ion given by:

$$F_0 \cos(\omega_\mathrm{d} t + \phi_\mathrm{d}) \tag{4.1}$$

where F_0 is the amplitude of the force, ω_d the angular frequency and ϕ_d the phase. In the interaction picture with respect to the simple harmonic oscillator with angular frequency ω_α describing the mode α of the ion, applying the RWA, we obtain the interaction Hamiltonian [Lee+05; Zha21]:

$$\hat{H}_\mathrm{I} = \frac{F u_0}{2} \hat{a}^\dagger \mathrm{e}^{\mathrm{i}\delta t} + \frac{F^* u_0}{2} \hat{a} \mathrm{e}^{-\mathrm{i}\delta t} \tag{4.2}$$

where $F \equiv F_0 \mathrm{e}^{-\mathrm{i}\phi_\mathrm{d}}$, $\delta \equiv \omega_\alpha - \omega_\mathrm{d}$ is the detuning of the drive from the frequency of the mode and $u_0 = \sqrt{\hbar/(2m\omega_\alpha)}$ is the wave packet size in the ground state. We can compute the unitary propagation of the driven harmonic oscillator and approximate it at the first order, obtaining the displacement operator with complex displacement amplitude [Lee+05]:

$$\alpha(t) = -\frac{\mathrm{i}}{\hbar} \int_0^t \frac{F u_0}{2} \mathrm{e}^{\mathrm{i}\delta t'} \mathrm{d}t'. \tag{4.3}$$

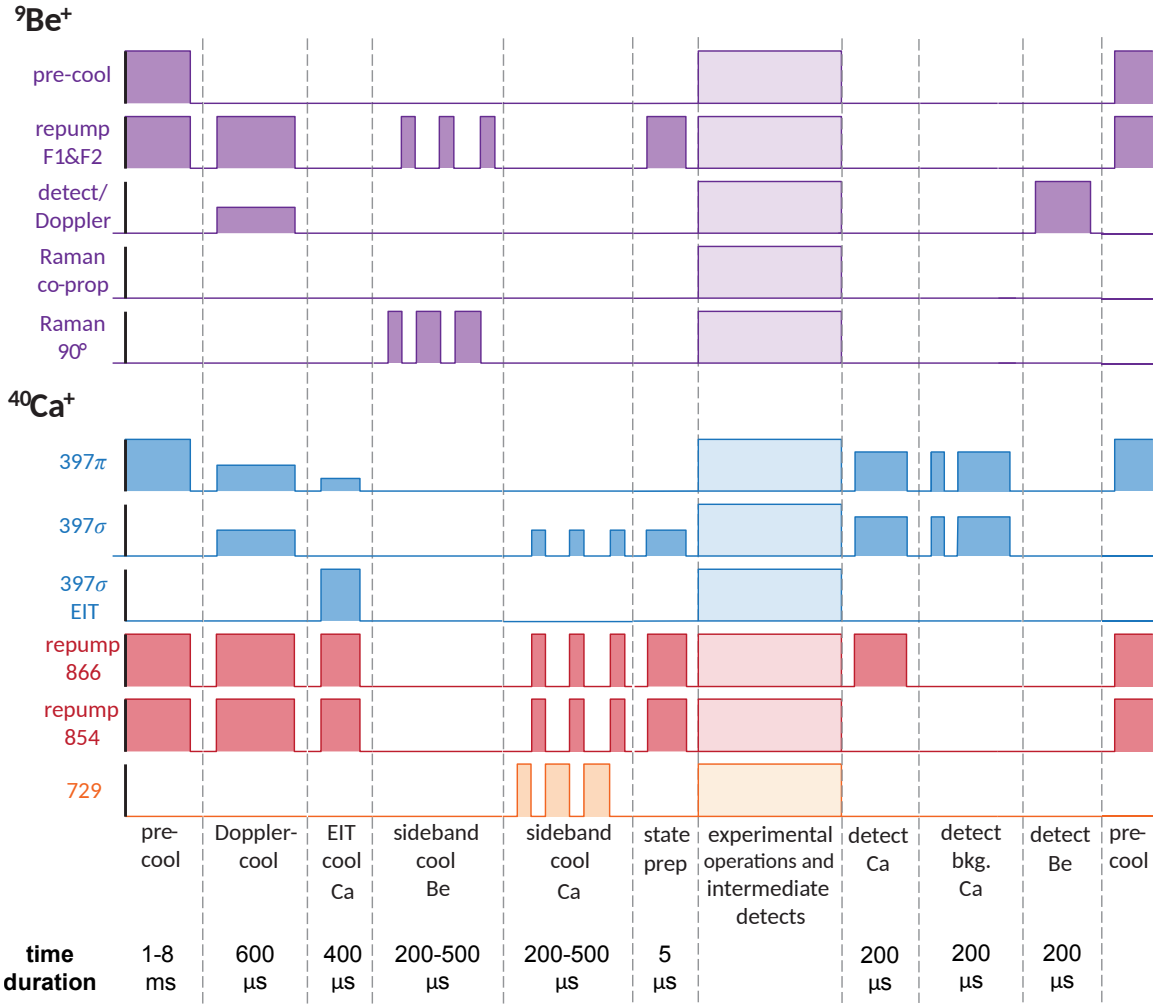

Figure 4.1: Pulse sequence diagram for a single experimental shot of mixed-species ion crystals. For each pulse the typical time duration is shown on the bottom. The pulse shapes are just indicative and not on scale. For single-species experiments, only the relevant pulses for that species are used.

For a constant detuning δ the trajectory of the oscillator in phase space is circular with period $2\pi/\delta$:

$$\alpha(t) = \frac{Fu_0}{2\hbar\delta}(1 - \mathrm{e}^{\mathrm{i}\delta t}). \tag{4.4}$$

On resonance $\delta = 0$ the period tends to infinity and the oscillator is displaced on a straight line without returning to the origin, and its amplitude increases linearly in time:

$$\alpha(t) = -\frac{iFu_0}{2\hbar}t. \tag{4.5}$$

In the case of a single trapped ion $F_0 = eE_0$, where E_0 is the amplitude of the electric field along the oscillation direction. For mixed-species ion chains, the force due to the electric field interacting with the normal mode α has amplitude $F_{0,\alpha} = eE_0 \left(\sum_{j=1}^{N} e'_{j,\alpha}/\sqrt{m_j}\right)$ [Hom13].

In the 3D segmented Paul trap the tickle is generated by modulating the voltage applied to one of the DC electrodes, through a capacitive coupling that bypasses the out-of-vacuum low pass filters with a cut-off frequency of 100 kHz. Different electrodes can be bypassed, but

currently we apply the drive such that the resulting oscillating electric field has components in both radial and axial directions near the central experimental zone. There are also some additional shim lines whose filters can be bypassed, but these are currently not exploited.

4.3 Motional frequency measurement

There are several methods to measure the motional frequency of the vibrational modes. Here I just described the methods employed in this thesis, but the interested reader can find a detailed discussion in [Win+98].

The first method involves using a resonant drive of a motional sideband transition as described in Sec. 3.1. The driving field can be detuned to $\delta = +\omega_m$ such that the ion undergoes a blue sideband transition $|\downarrow, n\rangle \leftrightarrow |\uparrow, n+1\rangle$, or to $\delta = -\omega_m$ for a red sideband transition $|\downarrow, n\rangle \leftrightarrow |\uparrow, n-1\rangle$. In both cases the internal state of the ion can be detected and the motional frequency retrieved when the transition probability is maximized. This method relies on working in a resolved sideband regime, by means of a narrow-linewidth internal transition and at low power of the driving field, to minimize the AC Stark shift. For an ion cooled to the ground state the red sideband transition cannot be driven, thus we use a blue sideband or a carrier followed by a red sideband transition. In the current setup, this method is restricted to usage only in the central experimental region due to the configuration of the laser beams. At low laser beam power, this method can reach a precision below 100 Hz [Flü19].

Another method we use is based on using the resonant DC tickle to induce a strong excitation in the motional state. When this is high enough, the resulting modulation produces high enough Doppler shifts of the ion's internal transitions. When the shift approaches the linewidth of the dipole transition used for state detection, the observed ion fluorescence reduces. For a single ion, this happens when the vibrational mode gains around 1000 phonons [Hom13]. This method is unsuitable for longer chains as the ion displacements induce vibrational mode frequency shifts due to the anharmonicity of the Coulomb interaction. The advantage of this method is that it is free of AC Stark shift. In the work of this thesis this method was used to measure the vibrational frequencies with an uncertainty of a few hundred of hertz. It can be used near the central experimental zone and in the left separation zone, while for other regions the oscillating voltage source is currently not connected. An alternative to this method is modulating the RF amplitude to induce excitation in the motional state. It can can be used for ions confined along the entire trap axis and for both radial and axial modes, due to the axial RF fields, but it is generally less precise. More details are given in Subsec. 6.2.1.

A more sensitive method is based on cooling the vibrational mode close to the ground state, applying a DC tickle pulse with a given driving frequency, and then diagnosing the subsequent excitation by performing a red sideband transition and detecting the internal state. Only if the DC tickle is resonant with the vibrational mode its motional state gets excited and undergoes the red sideband transition. Otherwise, no transition occurs. The final detection determines if the transitions occurred depending on the DC tickle frequency. This method can be used at the central experimental zone, reaching uncertainties below 20 Hz depending on the probing time [Flü19].

4.4 Motional state analysis

An arbitrary motional state can be represented as a superposition of Fock states as shown in Eq. 2.41. To characterize the distribution of occupied energy eigenstates we can drive the transition $|\downarrow, n\rangle \leftrightarrow |\uparrow, n+s\rangle$, where s is an integer number, which couples to the motional state through the Lamb-Dicke parameter η. Here I focus on using the first blue sideband transition as this is used for the work of this thesis. Considering initially the ion in the state $|\downarrow, n\rangle$, if we drive the blue sideband transition on resonance and detect the internal state, the probability to find the ion in the initial bright state is:

$$\begin{aligned} P_{|\downarrow,n\rangle}(t) = 1 - P_{|\uparrow,n+1\rangle}(t) &= 1 - \sin^2\left(\frac{\Omega_{n+1,n}}{2}t\right) \\ &= \frac{1}{2} + \frac{1}{2}\cos\left(\Omega_{n+1,n}t\right) \end{aligned} \tag{4.6}$$

where we used Eq. 3.16. If the initial state is in a distribution of Fock states $P_n(0)$, then each of them will evolve according to Eq. 4.6 with a different Rabi frequency $\Omega_{n+1,n}$. To retrieve the Fock state distribution, we can measure the internal state of the ion for different pulse durations and fit it to the function:

$$\begin{aligned} P_{|\downarrow\rangle}(t) &= \sum_{n=0}^{\infty} P_n(0) P_{|\downarrow,n\rangle}(t) \\ &= \frac{1}{2} + \frac{1}{2}\sum_{n=0}^{\infty} P_n(0) e^{-\gamma\sqrt{n+1}t}\cos\left(\Omega_{n+1,n}t\right) \end{aligned} \tag{4.7}$$

where we included an exponential decay $\exp\left(-\gamma\sqrt{n+1}t\right)$ to account for the spin decoherence caused by fluctuations in the magnetic field or laser intensity during the probing time [Win+98; Lei+03], with a phenomenological decay constant γ and the term $\sqrt{n+1}$ which accounts for an observed increase of decoherence for higher n (in [Lei+03] the data is consistent with an exponent of $\gamma(n+1)^{0.7}$). To perform the fit, in the work of this thesis we assume $P_n(0)$ to follow the thermal distribution of Eq. 2.46 or the Poisson distribution for the coherent states of Eq. 2.48. In some situations we account for a displaced thermal state by using the distribution function [Rus+14]:

$$\begin{aligned} P_n(0) = \sum_{n=0}^{\infty} &\frac{\bar{n}_{\mathrm{th}}^n}{(\bar{n}_{\mathrm{th}}+1)^{n+1}} e^{-|\alpha|^2} |\alpha|^{2(k+n)} n!k! \\ &\times \left| \sum_{l=0}^{n} (-1)^l \frac{|\alpha|^{-2l}}{l!(n-l)!(k-l)!} \right|^2 \end{aligned} \tag{4.8}$$

where $\bar{n}_{\mathrm{th}}$ is the mean phonon number for the thermal contribution and α is the amplitude of the displaced distribution. This Fock state distribution emerges when a mix of heating and coherent excitation occur. For instance, coherent excitation can be induced by imperfect but repeatable control of transport sequences or by non-adiabatic transport and separation sequences. While performing the fit the summations are truncated at a given $n_{\max}$, above which the terms are negligible. For mean phonon numbers close to the ground state, $n_{\max} \simeq 20$ is generally used. In Fig. 4.2 different simulated resonant blue sideband oscillations are shown for thermal, coherent and displaced thermal states with different mean phonon numbers.

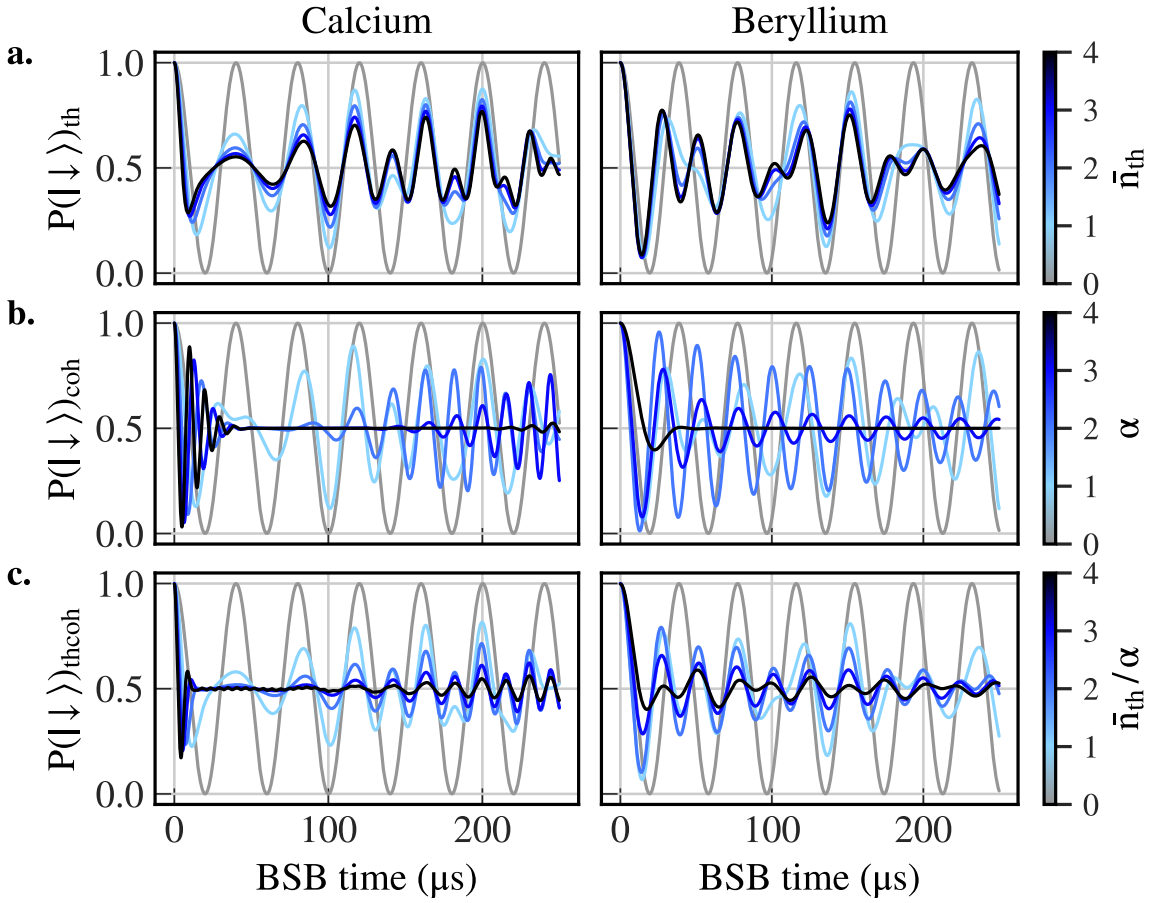

Figure 4.2: Blue sideband Rabi oscillations for different phonon distributions. On the left the populations are computed for calcium, with resonant carrier Rabi frequency $\Omega_0 = 2\pi \times 0.5$ MHz and Lamb-Dicke parameter $\eta = 0.05$. On the right the populations are computed for beryllium, with $\Omega_0 = 2\pi \times 0.07$ MHz and $\eta = 0.4$. These are typical experimental values. The states are: **a.** thermal, **b.** coherent and **c.** thermal coherent. Each distribution is computed for a $\bar{n}_{\mathrm{th}}$ and α in the range [0,4], while for the last both parameters assume identical values.

The use of the first blue sideband transition is suitable for low mean phonon numbers. In the Lamb-Dicke regime, for higher numbers the $\Omega_{n+1,n}$ show smaller variations, while out of this regime it becomes null or degenerate for different n, as shown in Fig. 3.1 (b). Moreover the contrast of the flops reduces, requiring longer probing time to increase the signal-to-noise ratio. We generally employ this method for up to 10 quanta. For higher phonon numbers different methods have to be employed, e.g. driving a carrier transition due to the low dependence on the motional state [Hom+11] or using a combination of carrier and sideband transitions of different orders [Rus+14]. For arrays containing multiple ions of the same species, one has to take into account that more ions participate to the same vibrational mode, thus the probability of having all of them in the $|\downarrow\rangle$ state can be measured through blue sideband oscillations, which have lower contrast and increased Rabi frequency with respect to the single ion case [Hom06].

For thermal distributions with mean phonon number lower than 1, a faster method involves the use of the first blue sideband and the first red sideband for a fixed time t_p and then measuring the spin populations $P^{\mathrm{BSB}}_{|\downarrow\rangle}(t_p)$ and $P^{\mathrm{RSB}}_{|\downarrow\rangle}(t_p)$ respectively. Computing the

ratio of these probabilities $R = P^{\mathrm{RSB}}_{|\downarrow\rangle}(t_p)/P^{\mathrm{BSB}}_{|\downarrow\rangle}(t_p)$, the mean phonon number is given by $\bar{n}_{\mathrm{th}} = R/(1-R)$ [Lei+03].

4.5 Normal mode coupling

Manipulation of motional states can be performed through a controlled coupling of different normal modes. Several methods can be employed. For a single ion it can be mediated by the internal state [Kin+21; SS21], for more ions it can be induced by the anharmonicity of the Coulomb interaction in some resonant conditions [Win+98; MSJ03; NRJ09; Din+17]. For an arbitrary number of ions, it can also be caused by the anharmonicity in the trapping potential in resonant conditions [Win+98; Hom+11] or modulation of the harmonic well curvature at the difference of the vibrational mode frequencies [Gor+14]. Here we focus on the use of a rotation of the harmonic potentials and ion crystals to control the coupling strength of normal modes close to frequency crossing. This occurred naturally in our transport experiments, but could also be used in state engineering tasks, as discussed in Ch. 9.

In this section I first describe the Landau-Zener-Stückelberg-Majorana transitions, in which two coupled vibrational modes are treated as a two-level quantum system. An explanation of the underlying coupling mechanism then follows.

4.5.1 Landau-Zener-Stückelberg-Majorana transitions

In this subsection I consider a coupled two-level quantum system that is subjected to a transfer of population for a linearly varying drive. This was first described by Landau [Lan32], Zener [Zen32], Stückelberg [Stu32] and Majorana [Maj32] independently in 1931-1932. Interestingly, the theory can be derived also classically [Nov10; ISN18]. Here I follow the approach discussed in [ISN23], which reviews the results related to the Landau-Zener-Stückelberg-Majorana (LZSM) theory.

Let's consider an external drive making up the energy difference $\varepsilon(t)$ of two levels going through a crossing. The presence of a constant coupling Δ lifts the degeneracy and creates an *avoided-level crossing* (or *anticrossing*), as shown in Fig. 4.3(a). The system is described by the Hamiltonian:

$$\hat{H}(t) = -\frac{\varepsilon(t)}{2}\hat{\sigma}_z - \frac{\Delta}{2}\hat{\sigma}_x = -\frac{1}{2}\begin{pmatrix} \varepsilon(t) & \Delta \\ \Delta & -\varepsilon(t) \end{pmatrix}. \tag{4.9}$$

For $\Delta = 0$ (uncoupled regime) the Hamiltonian eigenfunctions are:

$$|0\rangle = \begin{pmatrix} 1 \\ 0 \end{pmatrix} \text{ and } |1\rangle = \begin{pmatrix} 0 \\ 1 \end{pmatrix} \tag{4.10}$$

they are defined as *diabatic* states and their energy eigenvalues are:

$$E_{0,1} = \mp\varepsilon(t)/2 \tag{4.11}$$

For $\Delta > 0$ the instantaneous energy eigenstates are obtained by solving the Schrödinger equation $\hat{H}(t)\,|E_\pm(t)\rangle = E_\pm(t)\,|E_\pm(t)\rangle$, which gives:

$$\begin{aligned} |E_\pm(t)\rangle &= \gamma_\mp|0\rangle \mp \gamma_\pm|1\rangle \\ \gamma_\pm &= \frac{1}{\sqrt{2}}\sqrt{1 \pm \frac{\varepsilon(t)}{\Delta E(t)}} \end{aligned} \tag{4.12}$$

which are defined as *adiabatic* states with energy eigenvalues:

$$E_{\pm}(t) = \pm\frac{1}{2}\sqrt{\Delta^2 + \varepsilon(t)^2} = \pm\frac{1}{2}\Delta E(t). \tag{4.13}$$

For $\varepsilon = 0$ the eigenstates becomes $|E_{\pm}(0)\rangle = \frac{1}{\sqrt{2}}(|0\rangle \mp |1\rangle)$ and Δ is the minimum energy spacing.

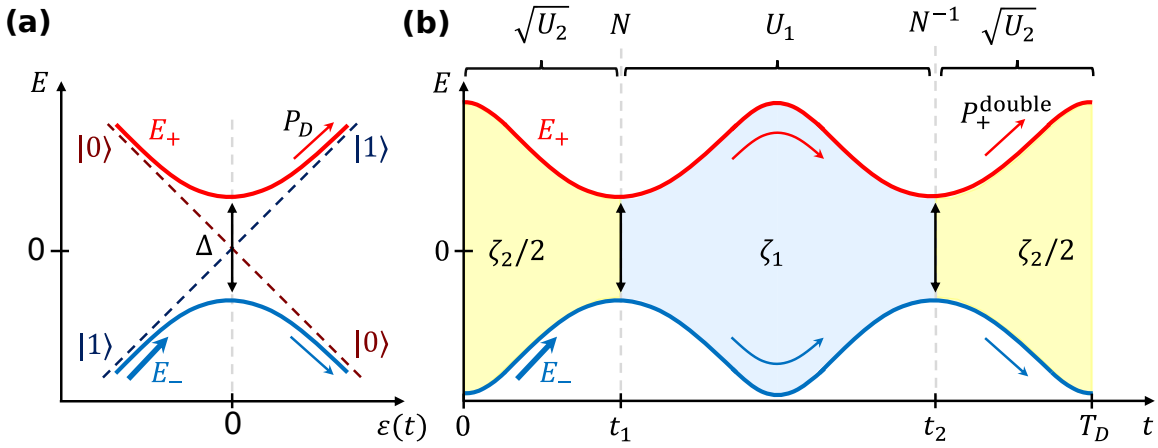

Figure 4.3: LZSM transitions in a two-level system. (a) Energy levels of the adiabatic and diabatic states. The energy difference is driven by $\varepsilon(t)$, while the degeneracy is lifted by Δ. The population transfer in a single passage of the avoided crossing is indicated by the arrows. (b) Energy levels and population transfer in a double passage of the avoided crossing. The system behaves as an interferometer. On top the relevant transition matrices are shown, while the shaded areas indicate the accumulated phases ζ_1 and ζ_2 between the states. Images are modified from [ISN23].

We now study the dynamic evolution of the system as the drive strength changes over time. We consider the system to be initially in the lower energy state $|E_-\rangle$ for an initial $\varepsilon(t) \ll 0$ at $t \to -\infty$. Subsequently, $\varepsilon(t)$ is increased and the diabatic transition probability P_{D} of finding the system in the upper energy state $|E_+\rangle$ for $t \to +\infty$ is studied. The external drive ε is considered to change linearly in time (or approximately linear around the crossing point) as $\varepsilon(t) = vt$, where v is a constant. For slow variations, i.e. $v \ll \Delta^2/\hbar$, the probability of transition $P_{\mathrm{D}} \approx 0$ and the system approximately follows the adiabatic states, according to the adiabatic theorem [BF28]. For fast dynamics, i.e. $v \gg \Delta^2/\hbar$, the probability $P_{\mathrm{D}} \approx 1$ and the system hops from $|E_-\rangle$ to $|E_+\rangle$ during the transition, following the diabatic states far from the avoided crossing. The probability P_{D} for other rates can be calculated in several ways, but here we describe a simple derivation taken from [GS23] and here we describe it. The system evolves according to the Schrödinger equation:

$$i\hbar\frac{d}{dt}\begin{pmatrix}\tilde{a}(t)\\ \tilde{b}(t)\end{pmatrix} = \hat{H}\begin{pmatrix}\tilde{a}(t)\\ \tilde{b}(t)\end{pmatrix} \tag{4.14}$$

with transformed probability amplitudes $\tilde{a}(t) \equiv \exp\left(\mathrm{i}vt^2/4\hbar\right) a(t)$ and $\tilde{b}(t) \equiv \exp\left(-\mathrm{i}vt^2/4\hbar\right) b(t)$ for the states $|0\rangle$ and $|1\rangle$ respectively, such that $|\tilde{a}|^2 = |a|^2$ and $|\tilde{b}|^2 = |b|^2$. This gives two coupled differential equations of first order:

$$\begin{aligned}\frac{da(t)}{dt} &= i\frac{\Delta}{2\hbar}e^{-ivt^2/4\hbar}b(t)\\ \frac{db(t)}{dt} &= i\frac{\Delta}{2\hbar}e^{ivt^2/4\hbar}a(t).\end{aligned} \tag{4.15}$$

We integrate the second equation, with initial condition $b(t \to -\infty) = 0$, and insert into the first equation to obtain:

$$\frac{da(t)}{dt} = -\left(\frac{\Delta}{2\hbar}\right)^2 e^{-ivt^2/4\hbar} \int_{-\infty}^{t} e^{ivt'^2/4\hbar} a(t')dt'. \tag{4.16}$$

We can use the Markov approximation [SZ97] such that $a(t') \approx a(t)$ to solve the integro-differential equation. Having initially the system in the lower energy state sets the initial condition $a(t \to -\infty) = 1$. This gives us the asymptotic transition probability:

$$P_{\mathrm{D}} = a(t \to \infty) \simeq e^{-I(\Delta/2\hbar)^2} \tag{4.17}$$

where:

$$I \equiv \int_{-\infty}^{\infty} e^{-ivt^2/4\hbar} \int_{-\infty}^{t} e^{ivt'^2/4\hbar} dt'dt. \tag{4.18}$$

To compute this integral we rewrite it in the form:

$$\begin{aligned} I = &\int_{-\infty}^{\infty} e^{-ivt^2/4\hbar} dt \int_{-\infty}^{0} e^{ivt'^2/4\hbar} dt' \\ &+ \int_{-\infty}^{\infty} e^{-ivt^2/4\hbar} \int_{0}^{t} e^{ivt'^2/4\hbar} dt'dt. \end{aligned} \tag{4.19}$$

The second term vanishes as it is an integral of an anti-symmetric function, while the first is a product of two Fresnel integrals:

$$\int_0^{\infty} \mathrm{e}^{\pm i\beta\theta^2} d\theta = \frac{1}{2}\sqrt{\frac{\pm i\pi}{\beta}} \tag{4.20}$$

leading to:

$$I = \frac{2\pi\hbar}{v}. \tag{4.21}$$

The resulting diabatic transition probability is:

$$P_D = e^{-2\pi\delta}, \quad \text{where } \delta = \frac{\Delta^2}{4\hbar v}. \tag{4.22}$$

During the transition, the wave function acquires a phase known as the *Stokes* phase [ISN23]:

$$\phi_{\mathrm{S}}(\delta) = \frac{\pi}{4} + \delta(\ln\delta - 1) + \mathrm{Arg}[\Gamma(1 - i\delta)] \tag{4.23}$$

where Γ is the Gamma function. Note that for the adiabatic limit ($\delta \gg 1$) $\phi_S \to 0$, while for the diabatic limit ($\delta \ll 1$) $\phi_S \to \pi/4$.

To study multiple passages through the avoided crossing and systems in a superposition of states, it is convenient to describe their dynamics in the transition matrix formalism [ISN23]. Far from the avoided crossing, the adiabatic states are not subjected to transitions and only acquire a relative phase. The resulting time-evolution operator is:

$$U\left(\zeta\left(t, t_{\mathrm{i}}\right)\right) = \begin{pmatrix} e^{-i\zeta(t,t_{\mathrm{i}})} & 0 \\ 0 & e^{i\zeta(t,t_{\mathrm{i}})} \end{pmatrix} = e^{-i\zeta(t,t_{\mathrm{i}})\hat{\sigma}_z} \tag{4.24}$$

where $\zeta(t, t_\mathrm{i})$ is the phase accumulated during the adiabatic evolution from time t_i to time t:

$$\zeta(t, t_\mathrm{i}) = \frac{1}{2\hbar}\int_{t_i}^{t} \Delta E(t)dt. \tag{4.25}$$

The passage through the avoided crossing is described by the transition matrix:

$$N = \begin{pmatrix} Re^{-i\phi_S} & -T \\ T & Re^{i\phi_S} \end{pmatrix} \tag{4.26}$$

where $T = \sqrt{P_\mathrm{D}}$ is the transmission coefficient and $R = \sqrt{1-P_\mathrm{D}}$ is the reflection coefficient. Consequently, for a single transition through the avoided crossing at time $t = 0$ the total evolution matrix is:

$$U(\zeta_f)\,NU(\zeta_i) = \begin{pmatrix} Re^{-i(\phi_s+\zeta_i+\zeta_f)} & -Te^{-i(\zeta_i-\zeta_f)} \\ Te^{i(\zeta_i-\zeta_f)} & Re^{i(\phi_s+\zeta_i+\zeta_f)} \end{pmatrix} \tag{4.27}$$

where $\zeta_i := \zeta(0, t_\mathrm{i}) \neq \zeta(t_\mathrm{f}, 0) := \zeta_f$. By passing through the avoided crossing twice, as depicted in Fig. 4.3(b), the initial state evolves under the transfer matrix:

$$\Xi \equiv \sqrt{U_2}N^{-1}U_1N\sqrt{U_2} = \begin{pmatrix} \Xi_{11} & \Xi_{12} \\ \Xi_{12} & \Xi_{11}^* \end{pmatrix} \tag{4.28}$$

where:

$$\begin{aligned} &\Xi_{11} = -R^2e^{-i\zeta_+} - T^2e^{-i\zeta_-} \\ &\Xi_{12} = -2iRT\sin(\Phi_\mathrm{St}) = -\Xi_{12}^* \\ &\zeta_+ = \zeta_1 + \zeta_2 + 2\phi_S, \quad \zeta_- = \zeta_1 - \zeta_2 \\ &\zeta_1 = \frac{1}{2\hbar}\int_{t_1}^{t_2}\Delta E(t)dt, \quad \zeta_2 = \frac{1}{2\hbar}\int_{t_2}^{t_1+T_\mathrm{d}}\Delta E(t)dt \\ &\Phi_\mathrm{St} = \phi_\mathrm{S} + \zeta_1 \end{aligned} \tag{4.29}$$

By initializing the system in the lower energy state, it adiabatically evolves, passes through the avoided crossing, creates a superposition of the diabatic states, and evolves adiabatically again. In the whole process, it accumulates a relative phase between the two states called *Stückelberg* phase Φ_St, which becomes relevant at the second passage through the avoided crossing, where the two states interfere with each other and the probability of finding the system in the state $|E_+\rangle$ at the end is:

$$P_+^\mathrm{double} = |\Xi_{12}|^2 = 4P_\mathrm{D}(1-P_\mathrm{D})\sin^2\Phi_\mathrm{St} \tag{4.30}$$

The whole process acts analogously to an optical *Mach-Zehnder interferometer*, with the avoided crossings acting as beam splitters for the light, which subsequently acquires a relative phase between the two branches. Constructive interference of multiple passages through the avoided crossing can be probed in the form of Ramsey fringes with oscillation frequency given by Φ_St; more information can be found in [ISN23].

4.5.2 Control of normal mode coupling

LZSM transitions happen in the presence of coupled two-level systems. By considering two normal modes of an ion crystal, I describe their coupling arising from the rotation of the trapping potentials or in the presence of a radial field. I focus on the cases of a single trapped ion, two ions of the same species and two ions of different species. I then give an overview of how these methods apply to longer ion chains.

Single ion

We consider one ion of mass m and charge e to be trapped with a Taylor expanded potential up to the second order:

$$V(y,z,t) = \frac{1}{2}\left(V_{zz}z^2 + V_{yy}y^2 + V_{zy}zy\right) \tag{4.31}$$

where we restricted to the 2D case from Eq. 2.3, with $V_{zz} = V_{\mathrm{D}}\alpha_z$ and $V_{yy} = V_{\mathrm{D}}\alpha_y + \frac{e\beta_y^2 V_{\mathrm{RF}}^2}{2m\Omega_{\mathrm{RF}}^2}$, in which we applied the pseudopotential approximation. We are introducing the term $V_{zy}zy$ that couples the harmonic oscillators in the two directions as their equations of motion cannot be described independently anymore. This might be a result of a quadrupole potential generated by the DC electrodes or, as in [Fab+24], by the shims. For $V_{zy} = 0$, the bare normal modes are trivially $\omega_z^2 = \frac{e}{m}V_{zz}$ and $\omega_y^2 = \frac{e}{m}V_{yy}$. For $V_{zy} \neq 0$, the Hessian matrix of this potential is:

$$H'_{zy} = \frac{e}{m}\begin{pmatrix} V_{zz} & V_{zy}/2 \\ V_{zy}/2 & V_{yy} \end{pmatrix} \tag{4.32}$$

which can be diagonalized to retrieve the angular frequencies of the coupled vibrational modes $\omega_\pm^2 = \frac{e}{2m}\left(V_{zz} + V_{yy} \pm \sqrt{(V_{zz} - V_{yy})^2 + V_{zy}^2}\right)$. Diagonalizing the Hessian matrix is equivalent to rotating the coordinate system by an angle $\theta = \frac{1}{2}\arctan\left(\frac{V_{zy}}{V_{zz}-V_{yy}}\right)$ [Fab+24], such that in this basis the Hessian is diagonal. Consequently the quadrupole potential couples the bare normal modes, modifies their frequencies and rotates the potential wells by an angle θ.

Once the Hessian is diagonalized, we can rewrite the Hamiltonian of the system in the normal mode coordinates as described in Sec. 2.3, obtaining:

$$H_{\mathrm{D}} = \frac{1}{2}\sum_{\alpha=\pm} p_\alpha'^2 + \omega_\alpha^2 \xi_\alpha'^2. \tag{4.33}$$

where are p'_α and ξ'_α are defined according to Eq. 2.42. To describe the dynamics in the quantum regime, we can quantize the Hamiltonian and rewrite the normal mode position and momentum operators by the raising and lowering operators of Eq. 2.42 with respect to the coupled modes to get the convenient form:

$$\hat{H}_{\mathrm{D}} = \hbar\sum_{\alpha=\pm}\omega_\alpha \hat{a}_\alpha^\dagger \hat{a}_\alpha \tag{4.34}$$

from which we subtracted the zero-point energy which does not affects the dynamics. The Hilbert space for the two quantum harmonic oscillators has infinite size, but we can consider the subsystem in which there is one vibrational quantum in one of the two modes, obtaining the matrix representation of the Hamiltonian:

$$\hat{H}_{\mathrm{D}} = \hbar\begin{pmatrix} \omega_- & 0 \\ 0 & \omega_+ \end{pmatrix}. \tag{4.35}$$

If we didn't diagonalize the Hessian of Eq. 4.32 and represented the quantized Hamiltonian in the ladder operators with respect to the uncoupled vibrational frequencies $\omega_{z/y}$, we would get:

$$\hat{H} = \hbar\begin{pmatrix} \omega_z & V_{zy}/\sqrt{4\omega_z\omega_y} \\ V_{zy}/\sqrt{4\omega_z\omega_y} & \omega_y \end{pmatrix}. \tag{4.36}$$

If the uncoupled vibrational frequencies vary over time, we can subtract their average value from Eq. 4.36 to retrieve the Hamiltonian of the LZSM transitions of Eq. 4.9. This shows that we can describe the dynamics of the coupled motional states through the LZSM theory and that we can control the coupling strength through a quadrupole potential. As long as at most two modes are interacting, this description applies analogously to longer ion chains and for the other coupling methods described above.

Single-species crystal

We now consider two ions of the same species trapped together in a harmonic potential, in which each ion j experiences the potential:

$$V_j(y,z,t) = \frac{1}{2}\left(V_{zz}z_j^2 + V_{yy}y_j^2\right) \tag{4.37}$$

and the Coulomb potential $V_{\mathrm{C}} = ke/(|\vec{u}_2 - \vec{u}_1|)$, where $k = 1/(4\pi\varepsilon_0)$ and $\vec{u}_j = (z_j, y_j, x_j)$. From now on we focus only on the $z-y$ plane, omitting the x coordinate. The total potential experienced by the array is then:

$$V_{\mathrm{tot}} = V_1 + V_2 + V_{\mathrm{C}}. \tag{4.38}$$

Let's assume the ions are located along the trap axis, with $y_j = 0$. Their axial equilibrium distance d can be computed analytically through $\partial V_{\mathrm{tot}}/\partial z_j = 0$, which gives $d = 2[ke/(4V_{zz})]^{1/3}$. The Coulomb potential changes the total potential curvature experienced by each ion. We indicate the ions displacement vector as $\vec{u}_d = \vec{u}_2 - \vec{u}_1 = (z_d, y_d)$ and compute the curvature of the Coulomb potential at the equilibrium position as [Fab+24]:

$$\begin{aligned} \left.\frac{\partial^2 V_{\mathrm{C}}}{\partial z_d^2}\right|_{\{u_d^0\}} &= \frac{2ke}{d^3} = V_{zz}, \\ \left.\frac{\partial^2 V_{\mathrm{C}}}{\partial y_d^2}\right|_{\{u_d^0\}} &= -\frac{ke}{d^3} = -\frac{V_{zz}}{2}. \end{aligned} \tag{4.39}$$

Consequently we can approximate the Coulomb term to second order in the total potential with:

$$V_{C,0} \simeq \frac{1}{2}V_{zz}\left(z_d^2 - \frac{y_d^2}{2}\right) = \frac{1}{2}V_{zz}\left((z_2 - z_1)^2 - \frac{1}{2}(y_2 - y_1)^2\right). \tag{4.40}$$

The Coulomb interaction does not create any term proportional to xy in the potential, thus the normal modes remain uncoupled. Consequently in the Hessian matrix of the total potential, computed from the partial derivatives with respect to the position coordinates z_1, z_2, y_1 and y_2, the elements related to different directions are null:

$$H'_{ik} = \frac{e}{m}\begin{pmatrix} 2V_{zz} & -V_{zz} & 0 & 0 \\ -V_{zz} & 2V_{zz} & 0 & 0 \\ 0 & 0 & V_{yy} - V_{zz}/2 & V_{zz}/2 \\ 0 & 0 & V_{zz}/2 & V_{yy} - V_{zz}/2 \end{pmatrix} \tag{4.41}$$

which gives the normal mode frequencies $(\omega_{Z1}^2, \omega_{Z2}^2, \omega_{Y1}^2, \omega_{Y2}^2) = e/m(V_{zz}, 3V_{zz}, V_{yy}, V_{yy} - V_{zz})$.

The application of an additional quadrupole potential in the zy plane gives rise to a $V_{zy}\,(z_1y_1 + z_2y_2)$ term that rotates the ion crystal, modifies the normal modes and creates

mode cross-coupling in the original mode basis. However, only some vibrational modes can be coupled. This can be seen by writing the ion positions in the normal mode coordinates. Neglecting constant terms that do not affect the dynamics and linear terms that vanish near the equilibrium, we obtain:

$$\begin{aligned} z_1 y_1 + z_2 y_2 &\simeq \frac{1}{m} \sum_{\substack{\alpha\in\{Z1,Z2\}\\ \beta\in\{Y1,Y2\}}} \left(e'_{z1,\alpha} e'_{y1,\beta} + e'_{z2,\alpha} e'_{y2,\beta}\right) \xi'_\alpha \xi'_\beta \\ &= \frac{1}{m} \left[\left(e'_{z1,Z1} e'_{y1,Y1} + e'_{z2,Z1} e'_{y2,Y1}\right) \xi'_{Z1} \xi'_{Y1} \right. \\ &\quad + \left(e'_{z1,Z1} e'_{y1,Y2} + e'_{z2,Z1} e'_{y2,Y2}\right) \xi'_{Z1} \xi'_{Y2} \\ &\quad + \left(e'_{z1,Z2} e'_{y1,Y1} + e'_{z2,Z2} e'_{y2,Y1}\right) \xi'_{Z2} \xi'_{Y1} \\ &\quad \left. + \left(e'_{z1,Z2} e'_{y1,Y2} + e'_{z2,Z2} e'_{y2,Y2}\right) \xi'_{Z2} \xi'_{Y2}\right] \\ &= \frac{1}{\sqrt{2}m} \left[2\xi'_{Z1} \xi'_{Y1} + 2\xi'_{Z2} \xi'_{Y2}\right] \end{aligned} \tag{4.42}$$

where the terms proportional to $\xi'_{Z1}\xi'_{Y2}$ and $\xi'_{Z2}\xi'_{Y1}$ are null due to the opposite sign of the eigenvectors for the out-of-phase modes, while the amplitudes are all equal to $1/\sqrt{2}$ due to the ions having the same mass. This indicates that COM and STR modes do not couple to each other. Considering that $\omega_{Z1} < \omega_{Z2}$ while $\omega_{Y1} > \omega_{Y2}$, no more than two modes can be coupled at the same time in the zy plane in this way. In the radial plane spanned by y and x, in both cases the COM modes have the highest frequency, then a rotation of the potential in this plane can be exploited to couple Y1/X1 and Y2/X2 simultaneously. By changing the modes dynamically through the two simultaneous avoided crossings, each of them induces LZSM transitions of the motional states.

Mixed-species crystal

We now consider two ions of different species with masses m_j and same charge. In this case each ion experiences a different pseudopotential, due to the mass dependence of the latter. The resulting ion-dependent radial curvature is:

$$V_j(y,z,t) = \frac{1}{2}\left(V_{zz} z_j^2 + V_{yy,j} y_j^2\right). \tag{4.43}$$

This modifies the mode spectrum and ion participations, but does not induce mode coupling, even when including the Coulomb interaction. The total potential experienced by the array is then similar to Eq. 4.38 with Coulomb term approximated as in Eq. 4.40.

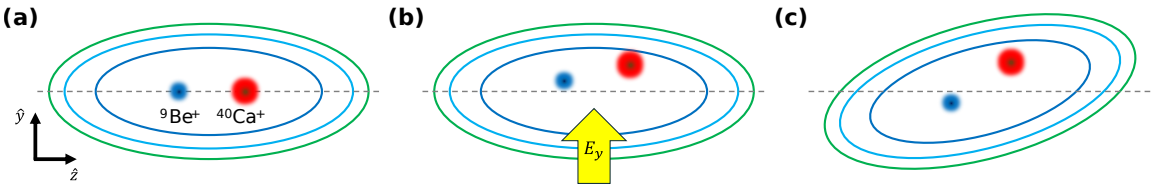

Figure 4.4: Methods for coupling the normal modes of a Be–Ca crystal. (a) Be–Ca crystal confined at the trap center with near-degenerate curvatures (not on scale), in the absence of coupling. Mode cross-coupling is induced by (b) applying a radial electric field E_y and/or (c) rotating the trapping potentials.

The application of a radial electric field E_y displaces the ions radially by an amount that is inversely dependent on the mass, as shown in Eq. 2.18 and in Fig. 4.4(b). This

shifts and tilts the ion crystal and creates a coupling between the axial and radial normal modes through the Coulomb potential. To compute the strength of the coupling we first find the equilibrium ion displacement with coordinates $\vec{u}_d^0 = (z_d^0, y_d^0)$. For a small E_y we approximate $z_d^0 \simeq d$ and $z_d^0 \gg y_d^0$ such that:

$$y_d^0 \simeq 2E_y \frac{V_{yy,1} - V_{yy,2}}{-2V_{yy,1}V_{yy,2} + V_{yy,1}V_{zz} + V_{yy,2}V_{zz}} \tag{4.44}$$

In this configuration we expand the Coulomb potential at the second order [Fab+24]:

$$\left.\frac{\partial^2 V_C}{\partial z_d \partial y_d}\right|_{\{u_d^0\}} \simeq \frac{3y_d^0}{2d} V_{zz} \tag{4.45}$$

which adds to the total potential the term:

$$V_{C,zy} \simeq \frac{3y_d^0}{2d} V_{zz} z_d y_d. \tag{4.46}$$

The product $z_d y_d$ constitutes a shifted rotation in the zy plane. The strength of the coupling of different modes is sensitive to the ions' participation and masses:

$$z_d y_d \simeq \sum_{\substack{\alpha\in\{Z1,Z2\}\\ \beta\in\{Y1,Y2\}}} \left(\frac{e'_{z2,\alpha}}{\sqrt{m_2}} - \frac{e'_{z1,\alpha}}{\sqrt{m_1}}\right)\left(\frac{e'_{y2,\beta}}{\sqrt{m_2}} - \frac{e'_{y1,\beta}}{\sqrt{m_1}}\right)\xi'_\alpha \xi'_\beta. \tag{4.47}$$

As opposed to the result obtained for the single-species case, for mixed-species arrays in- and out-of-phase modes can be coupled in every combination. For the axial and radial COM modes this is increasingly harder to achieve for higher mass ratios of the ions, as their energy gap widens considerably and the mode eigenvectors become biased towards one particular species. The eigenvectors scale non-trivially with the mass ratio of the ions, thus their analytical expression is not shown in Eq. 4.47. It is simpler and more insightful to show a simulation of the mode cross-coupling as a function of the radial field in the segmented 3D Paul trap, which we show in Fig. 4.5 (a)-(b).

In the presence of only a rotated potential as shown in Fig. 4.4(c), mixed-species arrays experience mode cross-coupling. Analogously to the application of a radial electric field, the rotated potential translates the center-of-mass and geometric center of the ion chain. The orientation of this displacement depends on the order of the ions and the rotation angle of the potential. The Coulomb interaction also adds a mixing term analogous to the one discussed above. A simulation of this type of mode cross-coupling is shown in Fig. 4.5 (c)-(d) and the coupling strengths are compared to the radial field-induced coupling.

The application of both radial electric field and rotated potential at the same time can be used to enhance the strength of the coupling, and this was performed in [Fab+24] with the aim of transferring heat between normal modes. For the experiments of mixed-species ion transport and separation described in Ch. 8 the heat transfer induced by mode-mode coupling was a detrimental effect, consequently we minimized it by compensating the stray electric fields and applied a compensating quadrupole to remove residual rotated potentials. The duality of the approaches highlights the versatility of these methods to manipulate motional states.

For longer single-species ion chains radial electric field and rotated potential will displace and rotate the entire array. In the mixed-species case they can induce local deformations to the crystal, which can be exploited for more complex manipulations of the motional states, analogous to [Hou+24], although performed with a different approach.

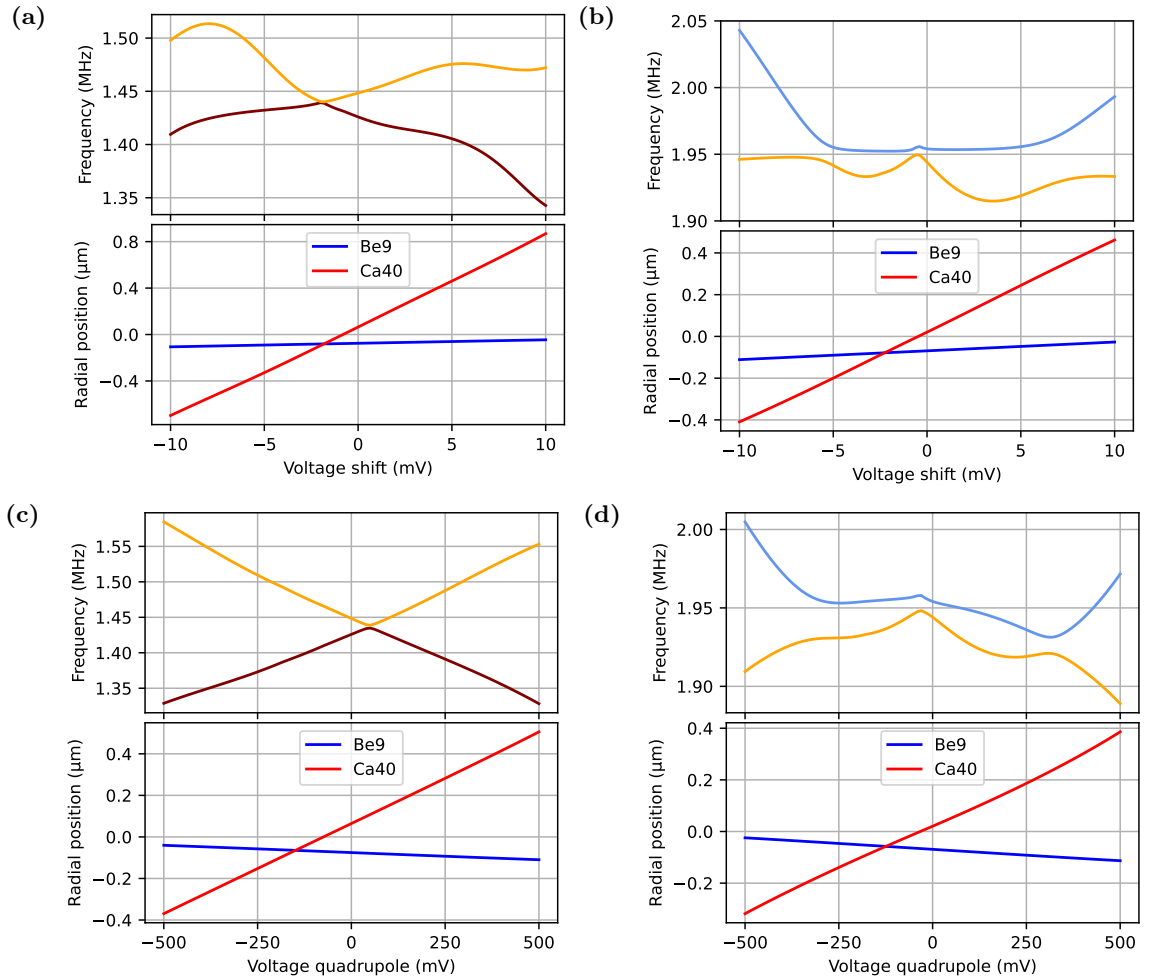

Figure 4.5: Simulation of normal modes coupling for a Be–Ca crystal in the splitting region of the trap. (a) and (b) show the lifting of frequency degeneracy of Z1/Y2 and Y2/Z2 modes, respectively, due to a mode cross-coupling induced by a radial field generated by applying a positive voltage shift to the DC electrodes in the range [19, 23] (see Fig. 2.3(e)) and an opposite shift to the DC electrodes in the range [4, 8]. (c) and (d) show the lifting of frequency degeneracy of Z1/Y2 and Y2/Z2, respectively, due to a quadrupole potential generated by applying a positive voltage shift to the DC electrodes 5 and 22 and an opposite shift to the DC electrodes 7 and 20. For (a) and (c) the single $^{40}Ca^{+}$ frequencies are $[\omega_z, \omega_y, \omega_x] = 2\pi\times$ [1.2, 1.6, 3.8] MHz, while for (b) and (d) they are $[\omega_z, \omega_y, \omega_x] = 2\pi\times$ [0.6, 2, 3.7] MHz. The voltage ranges are chosen to show significant splittings, with the same intervals between (a)-(b) and (c)-(d). The crossing Z1/Y2 shows stronger sensitivity to the perturbation around the minimum distance for both methods. For each plot the horizontal radial positions of the ions are shown, with a slight tilt with zero perturbation due to the low radial confinement.

5 Control system

In this chapter I describe the control system and laboratory instrumentation, with a focus on the major improvements that I introduced during the work of this thesis. The system upgrades mostly involve software and hardware of the control system, remote control and automation of different voltage and laser sources, and stabilization of the magnetic field.

5.1 Control system overview

The control system behind the trapped ion experiment is based on a complex architecture of devices. At the hardware level, the system has to control the trapping potentials, laser pulses and data acquisition while working with synchronous and asynchronous devices. This is based on RF, analog and digital voltages, satisfying stability and low-latency requirements. At the software level, the system is controlled by a C++ based code, a set of Python scripts and a C++ Graphical User Interface (GUI) called *Ionizer2* for the user.

The core of the hardware architecture is described in detail in the PhD thesis of Vlad Negnevitsky [Neg18], with extensions described in the future PhD thesis of Martin Stadler [Sta]. The C++ code and the GUI are described in the PhD thesis of Matteo Marinelli [Mar20], with upgrades described in the future PhD thesis of Tanja Behrle [Beh] and Brennan De Neeve [Nee]. Here I summarize the structure of the hardware architecture, as it is relevant for the next sections describing the work I performed.

In Fig. 5.1 the structure of the control system is depicted. This is called *M-ACTION*. The core is composed of an Avnet Zedboard, which is a commercial device hosting a Xilinx Zynq-7000 chip which has two ARM CPUs and one Field-Programmable Gate Array (FPGA). It has several input and output ports for communicating with the PC and synchronized devices. The Zedboard is connected to the Direct-Digital Synthesizer (DDS) boards with their own FPGAs, which produce RF signals to control the Acousto-Optic Modulators (AOMs) for controlling laser pulses. Other devices directly controlled by the Zedboard are the two PMTs for detection (one for each ion species) as well as several RF and Transistor-Transistor Logic (TTL) switches and triggers. M-ACTION is also composed of some custom-made Arbitrary Waveform Generators (AWGs) called Direct Ethernet-Adjustable Transport Hardware (DEATHs). These devices are used to synchronously control the voltages applied to the DC electrodes of the trap chip. More details can be found below in Sec. 5.2. A set of Raspberry Pi (RPi) boards [Fou12] control asynchronous devices, e.g. piezo controllers, Digital-to-Analog Converters (DAC) boards, RF sources and Proportional–Integral–Derivative (PID) controllers for the stabilization of the lasers. The RPis are managed in different ways depending on the purpose, but mostly through the control PC by means of software servers. For some of them we use the library *TIQI Plugin*, developed by Matt Grau, for creating a Remote Procedure Call (RPC) server with a web interface and Ionizer2 integration.

I describe now the parts of the control systems that were improved during the work of this thesis.

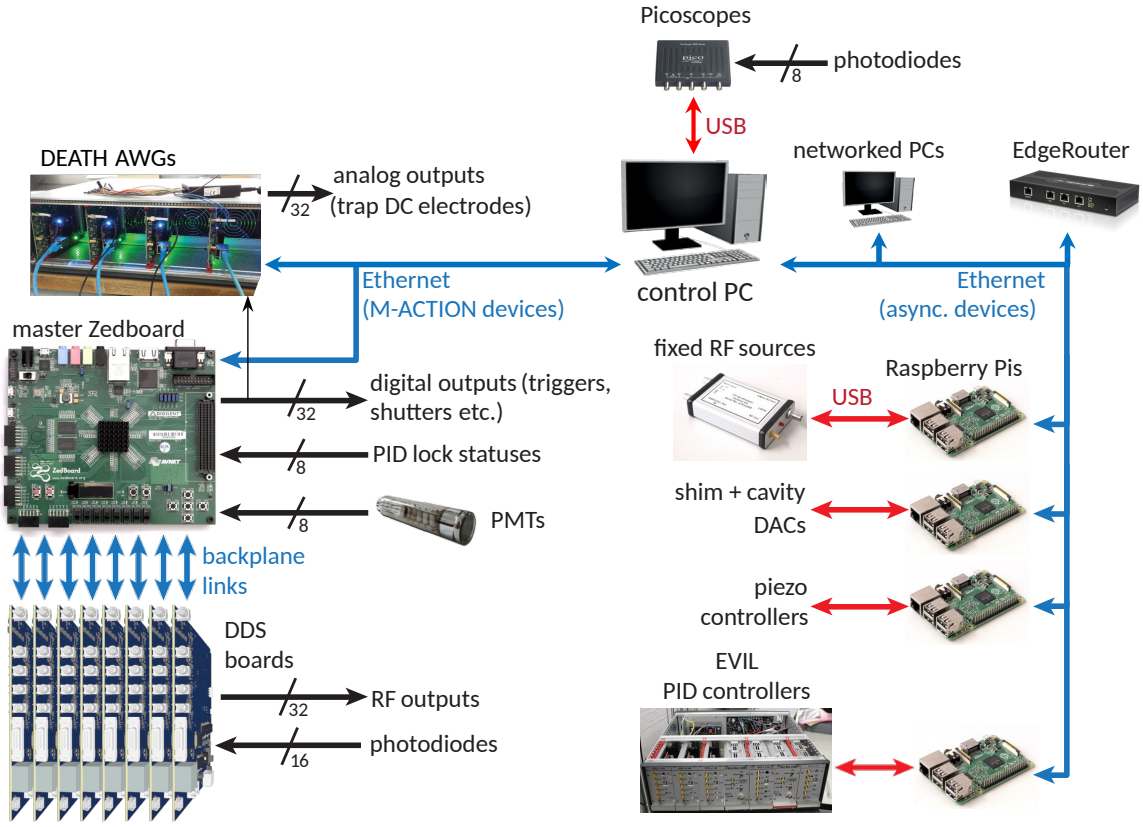

Figure 5.1: Control system overview. The network dedicated to the asynchronous devices and networked PCs is shown on the right-hand side. The network dedicated to the M-ACTION system is shown on the left-hand side. Here only 16 RF channels, 32 analog outputs of the DEATHs, 32 digital outputs and 2 PMTs are currently in use. The image is modified from [Neg18] and updated to the current configuration.

5.2 DEATHs

The control of the DC voltages is a fundamental part of the experiments described in this thesis. This is performed by the DEATH boards. They were developed by Ludwig de Clercq [Cle15], with improvements in the software by David Nadlinger [Nad16].

The DEATH is composed of an Avnet Microzed board, featuring the same Zynq chip as used on the Zedboard, which is mounted on a custom-made board. This board hosts two dual-channel 16-bit DACs running at 100 MSPS, whose clock is generated by the Microzed. Each output of the DACs gets amplified and low-pass filtered in an output stage, resulting in a voltage range of around [-9.5, 9.5] V with a 50 MHz cutoff frequency. The two outputs of a single DAC are used to drive corresponding DC electrodes on different wafers such that any drift (due to temperature, humidity or aging) do not induce differential voltages, which would generate radial fields that displace the ions radially. The custom board also features a TTL input for external triggering, currently controlled by the Zedboard, and an external clock input, which is unused at the moment. Both surfaces of the custom board are covered by thermal pads to minimize thermal fluctuations. This is required as the cooling is performed by means of fans and it was added during the course of this thesis. We have noticed that in each DEATH one of the DACs had lower nonlinearities over the whole output voltage range compared to the other despite being the same model. The ones with better

performances were connected to the DC electrode from the left loading zone to the central experimental zone, where it was mostly required.

The FPGA gateware is described in Verilog and is composed of Block Random Access Memories (BRAM) that store different data. Most importantly here four memories store the *voltage waveforms*, which define the time-varying voltages for the DEATH outputs. These are composed of arrays of digital voltage samples that are sent sequentially to the DACs. The samples can be passed in forward or reverse order, after a triggering signal and with an adjustable *slowdown*. The slowdown defines the number of clock cycles for which the same sample must be held, such that the total time required for a single waveform is $T = n(s+1)t_{clock}$, where n is the number of samples, s is the slowdown and t_{clock} is the clock period, which is 10 ns. A slowdown of 0 means that the waveform is run at the maximum sample rate of 100 MSPS, for a slowdown of 1 the rate is halved to 50 MSPS, and so on. The maximum slowdown is 65535 by design [Nad16]. A typical value for the experiments discussed in Ch. 8 is 80, which means a rate of ≈ 1.23 MSPS. The total number of samples that can be stored is 16384, divided into up to 256 waveforms. Each sample goes through a stage that performs an affine linear transformation, useful for correcting first-order imperfections in the DAC output voltages [Nad16]. The BRAMs also store *waveform sequences* which are used to define the sequence of waveforms employed in a single experimental shot.

The ARM CPU runs software programmed in C++ and implements a server that receives *waveform sets* from Ionizer2, consisting of the waveforms and additional metadata, for which more details are given in the Subsec. 5.2.2. The waveform sets are generated in the PC by numerical techniques described in Ch. 7 and are structured according to the JavaScript Object Notation (JSON) format, which is parsed by Ionizer2 and distributed to different DEATHs and the Zedboard. The waveforms in a waveform set have different purposes: loading, recrystallization, reordering, transporting and separation, which will be described more in detail in Ch. 7.

The setup employs 8 DEATH boards with 32 voltage outputs in total, controlling 30 electrodes and leaving 2 unconnected. In some of the experiments described in Ch. 8, one DEATH is used to control the shim electrodes, such that each output of a single board drives an entire shim row, and the stray fields are corrected through the excess micromotion compensation described in Sec. 6.2.

During this thesis, I worked in collaboration with Martin Stadler to update the software and gateware libraries to the latest versions. Moreover I extended the software's capabilities, enabling more flexible manipulation and scanning of the waveforms as described in Subsec. 5.2.2. The affine transformation parameters were periodically calibrated as described in Subsec. 5.2.1 to compensate for drift and aging of the components. A TIQI Plugin server was developed by Carmelo Mordini to simplify the integration of the waveform set generation, managing and running.

5.2.1 Voltage calibration

The affine linear transformation stage rescales the waveform samples and applies the floor function, according to [Nad16]:

$$y(x) = \left\lfloor \frac{k}{32768} x + d \right\rfloor \tag{5.1}$$

where k is the sample gain in the interval of [0, 2^{16}-1], corresponding to a voltage gain of [0, 2), and d is the sample offset within [0, 2^{16}-1], which shifts the voltages in the full output range. The calibration is generally performed by setting the default values $k = 32768$ (voltage gain 1) and $d = 0$ (voltage offset of 0 V) and then running waveform samples in the set $V_{\text{req}} = \{-8, -5, -2, 0, 2, 5, 8\}$ V, while measuring the output voltages for each channel with a digital multimeter (generally the *Keithley 2100*). We then perform a linear fit of the function $V_{\text{out}} = k_v V_{\text{in}} + d_v$, where k_v and d_v are the voltage gain and offset obtained from the linear fit. These values are then converted into 16-bit representation and used for the linear transformation stage. Generally the output voltages show drifts in the order of a few millivolts over several months.

5.2.2 Waveform interpolation

For the experiments related to shuttling and reconfiguration of ion crystals it was necessary to quickly modify waveform voltages in response to experimental requirements or calibrations, without regenerating them in the control PC and reloading into the system. In this way we could improve the flexibility of the control system and allowed for fine-tuning of the waveform parameters. For this reason in the work of this thesis we developed the *waveform interpolation* or waveform linear combination routine, which allows us to perform linear combinations of waveforms directly in the DEATHs' CPU. This routine can perform an interpolation of an arbitrary number N_w of waveforms. For each DEATH output, the kth sample of each waveform w_i is computed as:

$$w_{\text{int}}[k] = \sum_{i}^{N_w} a_i w_i[k] \tag{5.2}$$

where a_i are *interpolation weights* or linear combination weights. Both interpolation weights and samples are floating-point numbers. In the process, the code checks if the sum induces overflow, sending the user an error if this happens. To perform the computation, the processing system requires access to the waveform samples. This was not possible before the upgrade work, as the processing system had no access methods for the BRAMs where the samples are stored. Consequently a second memory was allocated in the RAM to store the waveforms and their metadata.

The interpolation is centrally managed by the Zedboard software. There are two routines that can perform the interpolation, with different purposes. The simplest and most used is the *manual* interpolation: the user defines the waveforms to use and the corresponding weights in Ionizer2, which communicates with the Zedboard that sends the same command to all the DEATHs. We can scan the weights while performing the experiments, such that they can be calibrated depending on the experimental results. This is a typical method we employ to improve the performance of the waveforms or compensate for experimental imperfections in the voltage control. In Ch. 8 we show how this method allowed us to manipulate the waveforms and achieve low excitation separation of mixed-species ion crystals.

The second routine is an extension of the first one and it is referred to as the *automatic* interpolation. This feature aims to be employed when several different transport waveforms are loaded into the memory, and used to generate a transport event automatically. This is based on defining the required initial and final position of the ions, which are then used by the system to find two appropriate waveforms that, interpolated, can produce the required transport event. It becomes particularly relevant when we want to scan the initial or final position of the ions due to a transport event without regenerating new waveforms in the

PC. More in detail, this method exploits a set of metadata peculiar to each waveform. Before this work, they were composed of a "slot" indicating the position in the DEATH's waveform memory, a unique ID (UID) to uniquely identify them, a description, and starting and ending voltages. These were mostly relevant for Ionizer2 visualization. For a more advanced manipulation of the waveforms, more fields were added to the individual metadata: the number of samples, a flag indicating if the waveform was generated in the PC or is a product of the DEATH manipulation (PcGen), and four additional arrays indicating the positions of the potential wells in the initial and final sample which are used to find the waveforms to use for the interpolation. These are the User Defined Initial Position (UDIP), Real Initial Position (RIP), User Defined Final Position (UDFP) and Real Final Position (RFP). The positions refer to the axial one, and the distinction between "user defined" (integer number) and "real" (floating-point number) is to give flexibility to the system. The automatic method for performing waveform interpolation takes from the user the number of potential wells of the desired waveform and the initial (UDIP) and final (RFP) desired positions of one of the wells. The initial one is based on the UDIP to be more generic. Then it finds two waveforms in the loaded waveform set that have the required number of wells, have the specified initial position and are the closest in terms of final position for one of the wells. The distances of the found waveforms' RFPs from the desired final position are used to compute the weights. The slot of the found waveforms and their weights are then sent to the DEATHs. This is more convoluted and, although fully functional, it is not commonly used yet.

For both interpolation methods, the waveform memories get updated with the newly generated waveforms. The use of the interpolation routines might fill the BRAMs used to store the waveforms, which currently do not give any error message. In a future version this can be checked, possibly through the processing unit memory. The waveform memories of the Zedboard and DEATHs are synchronized at each restart/reprogram of the boards.

5.3 Improvements on voltage control

5.3.1 Shim control

The shim electrodes are controlled by either the DEATHs or other low-cost low-bandwidth DACs, depending on the experiment. In the latter case, this is performed by means of the DAC AD5371 evaluation board from Analog Devices [65] which is commonly used in the group. This device can control up to 40 channels with 14-bit resolution at a sampling rate of 540 KSPS. The output range is [V_{SS}+1.4, V_{DD}-1.4], where V_{SS} is the negative supply voltage which is given within the range [-16.4, -4.5] V, and V_{DD} is the positive supply voltage within [9, 16.5] V. It is controlled over by an RPi through a Serial Peripheral Interface (SPI) line. It was set up by Tanja Behrle [Beh], who also wrote the RPi software. Successively, in the work of this thesis the code was rewritten to be compatible with the TIQI plugin system, which has a better web interface and integration with Ionizer2 GUI.

Due to the voltage supply, currently the output of the DAC reaches voltage limits around [-7.4, 9.9] V. To perform proper compensation of the excess micromotion, the output range needed to be amplified by a factor of 3 by an amplification stage. This was performed by a simple unboxed custom board which was controlling the shim electrodes in each radial quadrant of the trap commonly. A new design was implemented in the work of this thesis which used 28 voltage amplifiers, based on the operational amplifier OPA454 from Texas Instruments. This allows the control of each shim electrode individually for local compens-

ation of the electric stray fields in the different zones. If no local compensation is needed, a set of switches can be employed to connect 4 blocks of 7 different operational amplifiers to the same 4 DAC signals to commonly control the shim electrodes of each quadrant. For each amplifier there is also an LED that indicates an overcurrent or overtemperature condition. Detailed schematics can be found in Appendix A. The board is partially covered by thermal pads for thermal stability and enclosed by a grounded aluminum box for shielding from electric fields. The cable that connects the board to the feedthrough connector (which delivers the voltages to the trap chip) is shielded and grounded for the same reason. The case was also isolated from the optical table to avoid possible ground loops [Hor15].

5.3.2 RF circuit

The trap RF voltage is supplied through a helical resonator to the trap [Kie15; Col18]. This is composed of a transformer, an impedance-matching circuit, a resistive drain for the accumulated static charges and a pickoff. The entire structure was originally implemented using an aluminum shield and connected to the chamber via an aluminum base. In the work of this thesis, both of the parts were rebuilt with the same shape but using Teflon to prevent ground loops. For the same reason several parts of the amplification circuit for the RF were galvanically isolated by transformers. Despite these measures, we found that certain electrical connections to the trap chip had resistive contact with the trap chamber, creating ground loops. These loops could not be removed from the outside, leading to a 50 Hz noise experienced by the ion and affecting the motional coherence. In the future, these connections can be isolated to reduce this source of noise.

It was also found that the RF source SMC100A from Rohde&Schwarz we were using to drive the RF at 113.7 MHz was generating higher harmonics at 227.5 MHz and 341.2 MHz. Although the second and the third harmonics were ~ 52 dBm and ~ 46 dBm less than the carrier, they were amplified more than the latter from the nonlinearities of the RF amplification circuit which reduced the gap by more than 20 dBm. Despite these harmonics being filtered by the helical resonator along their path toward the trap, they can still reach the ions and other circuits requiring the RF, for example for intrinsic micromotion compensation 6.1. The higher harmonics were reduced by exchanging the RF source with a less noisy device of the same model and by setting it to the "normal operation mode", as it was found that the "low noise mode" and "low distortion mode" were performing worse. A few bandpass filters with cut-off frequencies of 87 MHz and 117 MHz were also added in the RF circuit, where relevant.

5.3.3 Mains filters

Many electrical devices in the setup are connected to two Uninterruptible Power Supplies (UPSes) to supply power and reduce voltage spikes in case of power cuts. The model of the UPSes is APC Smart-UPS SRT2200RMXLI. Thanks to the suggestion of Nick Schwegler, it was found that they inject discrete noise lines at different frequencies, e.g. 5.75 kHz, 30 kHz, 60 kHz, etc. To reduce this noise, two mains filters FN2080-16-06 from Schaffner were connected between the mains socket and the UPSs.

5.4 Remote control

During the work of this thesis, several devices were switched from a manual control to a remote one. This offers several advantages: finer and more reproducible tuning, easier

monitoring of the parameters in the short and long term, distributed control among different laboratories using shared resources and control of the devices from inside and outside the lab. The latter was one of the main reasons behind this effort, especially due to the Covid-19 pandemic and the consequent temporary halting of laboratory activities. Thanks to the upgrades to the experimental setup, we were able to reach the state where experiments could be performed fully remotely. Here I describe some of the improvement implemented in the control system.

Laser control: 729 nm

As described in Subsec. 3.2.2, the optical qubit of the calcium ion is manipulated through a 729 nm laser. This is generated by a diode laser of the model DL pro from Toptica [Top98]. The diode laser is based on an external cavity whose orientation is tuned by a piezo. Its voltage is controlled by an analog controller, which features an input to modulate the applied voltage. The remote control system acts on this input. This is performed by means of a DAC AD5370 evaluation board which works similarly to the DAC AD5371 but with 16-bit voltage resolution. The output is connected to a current buffer and voltage limitation stage, to supply enough current while protecting the piezo controller input with a [-0.3, 1] V range. Just a few tens of mV are generally enough for setting the desired laser wavelength. The DAC is controlled by an RPi, which has also a software voltage limitation for further protection and is connected to the lab network via wifi.

Laser control: 423 nm

The photo-ionization of calcium is performed by a 423 nm and a 375 nm lasers [Kie15]. The first wavelength needs to be precisely tuned to resonantly drive the transition $4s^2\ {}^1S_0 \leftrightarrow 4s4p{}^1P_1$ in neutral ^{40}Ca, while the second just needs to have a wavelength smaller than 390 nm to complete the ionization [Luc+04]. The 423 nm laser is generated by an 846 nm diode laser (similar to the one for 729 nm) which passes through a Second Harmonic Generation (SHG) stage. The current of the diode laser is regulated by its analog controller. It gets modulated by a voltage output of the same DAC used for the 729 nm laser piezo driver, and it is conditioned by a current buffer and voltage limitation stage. Just a few tens of mV are generally enough for setting the desired laser wavelength.

The temperature of the nonlinear chip of the SHG stage affects the conversion efficiency. Its temperature is stabilized by a temperature controller TED200C from Thorlabs [89], but we noticed that it generally drifts over the course of the day. For this reason we remotely manage the temperature controller analogously to the current for the 846 nm diode laser. To ensure power stability while loading ions, we also measure the actual temperature of the SHG chip through the temperature controller and the 423 nm laser amplitude through a photodiode. The output voltages are measured by two analog-to-digital converters (ADC) ADS1115 from Texas Instruments which communicate to the RPi. The maximum sampling rate is 0.86 KSPS and it is tunable depending on the need.

Laser control: 940 nm

The photo-ionization of beryllium is performed by a 235 nm laser. This is generated by a diode laser at 940 nm which pass through two SHG stages [Lo+14]. The diode laser is also managed by an analog controller, whose piezo driver is voltage modulated by a DAC AD5370 communicating with an RPi, similarly to that described above. In this case there

is no current buffer and voltage limitation stage at the output of the DAC, but there is a software voltage limitation of [-1, 1] V.

We also added one of the custom PID controllers developed in the group called Electronically Variable Interactive Lockbox (EVIL) to perform the locking of the first SHG through a Pound-Drever-Hall (PDH) technique, similarly to what is described in [Cle15]. Before this the locking was performed manually through a commercial device.

Other devices

For the other diode lasers used in out setup, there was a simultaneous contribution from different members of the group to make them remotely controllable. At the moment, all the diode lasers for both calcium and beryllium can be controlled remotely and most of the parameters are continuously logged on the Grafana platform.

Also the control of the EOMs for the compensation of the intrinsic micromotion were switched to a remote control. More details are given in Sec. 6.1.

5.5 Laboratory monitoring

The alignment and electronic controlling of the laser beam lines is checked on a daily basis to ensure their optimality. Given the complexity of the beam lines and the different types of pulses employed, this might be time-consuming and error-prone. To automate this process, I collaborated with Matteo Simoni to implement a lab monitoring system. It is based on a set of photodiodes installed after the ion trap which measure the intensities of some laser pulses, send the signal to dedicated inputs of two oscilloscopes Picoscope 2406B, which communicates with a script in the control PC that recognizes the pulses and verifies that their amplitudes are the expected ones. If this is not the case, the user can act on the setup accordingly. We started to use this system in the laboratory towards the end of my time in the laboratory, but further improvements are needed to improve the reliability and automation.

5.6 Magnetic field

The magnetic field of the setup is generated through the use of two coils in Helmholtz coils [Kie15]. They are controlled though an Agilent 6682A current supply that generates a current of around 115 A. The power supply requires a reference voltage for stabilizing the current, which is generated by averaging five voltage reference sources Ref102CU from Texas Instruments and regulated by a voltage divider network [Flü19]. The voltage divider can be manually tuned by means of a mechanical potentiometer. During the work of this thesis, I collaborated with Tenzan Araki [Ara21] and Giorgio Fabris [Fab21] to build a remotely controllable voltage reference source. It is based on the voltage reference LTC6655BHMS8-2.5#PBF from Analog Devices, and can be interfaced with different magnetic field sensors for stabilization and can communicate through Serial Peripheral Interface (SPI) for setting of the reference voltage. It is currently controlled by an RPi with software based on the TIQI-plugin. The voltage reference source is protected from external electric fields by an aluminium case with a temperature controller, which has not been tested yet. The functionalities were tested and it worked, but it was noticed that the output noise spectral density was compared to the system currently in use and showed a worse performance [Fab21]. Nonetheless, the functionalities of this device make it suitable for a wide range of applications

and it is in use in other experiments in the group, e.g. for a careful variation of the magnetic field.

The high current induces heating in the Helmholtz coils which needs to be dissipated through water cooling. The temperature of the water is stabilized through the building infrastructure, but it was noticed that in the laboratory it might vary by at most 0.5° over the day, especially in the summer. This changes the calcium optical transition frequency by up to 1 kHz. To reduce this effect we increased the gain of the proportional part of the PID loop for the magnetic field stabilization, which reduced the fluctuations down to roughly 0.5 kHz. We also planned to install a water chiller to stabilize the water temperature. Given that this was not needed for the work of this thesis, we did not proceed any further, but it might be needed for the implementation of further quantum algorithms.

5.7 Laboratory network

The laboratory network was previously managed by a central RPi before, which was controlling the interface between the internal and external network and was assigning IPs to the devices. This was substituted by Matt Grau with an Ubiquiti EdgeRouter Lite, due to better performance, higher reliability and easier configuration. The current network topology is shown in Fig. 5.1. During the course of this thesis, the network was maintained and more functionalities were added, such as an updated authentication scheme for the Virtual Private Network (VPN).

6 Micromotion compensation and trap model

Compensation of intrinsic and excess micromotion is fundamental for optimizing the control over the ions' internal and motional states. It is also particularly important when working with mixed-species ion chains, since the presence of stray electric fields distorts the ion array and changes the characteristics of the normal modes. In this chapter I explain how these unwanted effects are minimized in the experimental setup. I then describe how the compensation of excess micromotion led us to develop a method to improve the model of the trap potentials and how this deviates from the ideal one.

6.1 Intrinsic micromotion

In Subsec. 2.1.2 I introduced the motivations that cause intrinsic micromotion and what the consequences are. Here I describe how it is accounted for in the experimental setup.

Intrinsic micromotion affects the laser-ion interaction for laser beams with non-negligible axial components. In the ion rest frame, the main effect is to create sidebands in the laser spectrum at $\pm n\Omega_{\mathrm{RF}}$, with $n \in \mathbb{N}$. For the n-th sideband the Rabi frequency gets modulated as [Neg18]:

$$\Omega_{\mathrm{mm},n} = \Omega_0 \, |J_n(\beta)| \tag{6.1}$$

where Ω_0 is the carrier Rabi frequency in absence of micromotion, J_n are the Bessel functions of the first kind and $\beta = k_z e E_{\mathrm{RF,z}}/m(\omega_z^2 - \Omega_{\mathrm{RF}}^2)$ is the modulation amplitude. Fig. 6.1 (b) shows the dependence of the Rabi frequency on β. Due to its inverse proportionality to the ion mass, in the experimental setup the intrinsic micromotion mostly affects the beryllium lasers, in particular the detection and the Raman beams in the 90°configuration. For this reason we employ EOMs which we drive at the same frequency as the RF drive with a particular phase, which we use to modulate the laser light and maximize (minimize) the carrier (sideband) Rabi frequency. The beams are modulated at the frequency Ω_{RF}, with adjustable amplitudes and phases.

The beryllium detection beam is modulated with a single EOM whose amplitude is fixed and the phase is electronically controlled through a phase shifter. The calibration is performed by changing the phase and maximizing the carrier detection fluorescence. This optimization is rarely required and no further characterization was performed.

The Raman beams require a finer calibration of the modulation for minimizing the intrinsic micromotion and the EOM setup was improved through different steps during the work of this thesis. The modulation is applied to the Raman 90 of Fig. 3.4. At the start of this thesis, this modulation was performed by means of two cascaded resonant EOMs EO-T115D3-UV from Qubig [08], as shown in Fig. 6.1 (a). Two EOMs were necessary as individually they were not able to reach the required modulation amplitude before their resonances became unstable due to the high RF input power. However the use of two EOMs poses challenges in the calibration procedure. They modulate an incoming beam according to:

$$A e^{i\omega t} \rightarrow A e^{i\omega t + i\beta_1 \sin(\Omega_{\mathrm{RF}} t + \phi_1) + i\beta_2 \sin(\Omega_{\mathrm{RF}} t + \phi_2)} \tag{6.2}$$

where β_1/β_2 are the modulation amplitudes of the two EOMs and ϕ_1/ϕ_2 are the phases. This shows that their calibration needs to be performed by carefully choose their parameters, as for some values of the phases the two modulations may cancel each other, while only for some others they sum up. The calibration process is performed by initially disconnecting EOM2 and only driving EOM1 at low power. Its phase is adjusted to minimize the ratio of the Rabi frequencies $\Omega_{\mathrm{mm},1}/\Omega_{\mathrm{mm},0}$ and $\Omega_{\mathrm{mm},2}/\Omega_{\mathrm{mm},0}$ (shown in Fig. 6.1 (d)) measured on the ion. Then the EOM1 is connected and calibrated analogously. The RF amplitude of EOM1 is gradually increased up to $\sim$ 34 dBm, while calibrating the phase. Finally the RF amplitude of EOM2 is increased analogously. In this way we were able to reduce the measured β from 2.94 down to 0.64, mostly limited by the circuit controlling the RF amplitude and phase, as we describe below. During this process, the EOMs dissipate a lot of heat and their temperature is stabilized through a Peltier cooler, a heatsink and a fan. The RF amplitude needs to be slowly increased to ensure the thermalization of the EOMs, whose resonances need to be manually tweaked to ensure the transmission of most of the RF power to the nonlinear crystal. The calibration of the two EOMs is time-consuming but, once performed, it does not require further adjustments unless the RF power is turned off. In this case, only a small recalibration is needed if the RF source returns to the previous settings.

The RF amplitudes and phases are each manipulated by one Voltage Variable Attenuator (VVA) ZX73-2500+ and two voltage-controlled Phase Shifters (PS) JSPHS-150+, from Mini-Circuits [68]. Before this work, the control voltages were generated by a power supply and tuned through the use of three resistive potentiometers. We modified this by substituting the potentiometers with a DAC AD5370 evaluation board (described in Ch. 5) controlled by an RPI. This allowed us to remotely perform the compensation in a simpler, finer and more reproducible way. Thanks to these improvements, we reached a measured modulation index of $\beta \simeq 0.04$.

While applying the modifications to the RF circuit described in Subsec. 5.3.2, we decided to further improve the intrinsic micromotion compensation circuit by substituting the two EOMs with a newly developed EOM PM8-VIS 113.7 from Qubig. The advantage of this EOM is that we can reach a modulation index of 3 with an RF input power of just 16 dBm with a single unit. The disadvantage is that it suffers from higher optical attenuation, with a transmission efficiency of around 60% from the datasheet, while the previous ones had an efficiency of more than 98% from the datasheet. We decided that this difference was acceptable since we have plenty of power from the laser. With the use of only one EOM we modified the control circuit, removing one branch after the VVA and using both PS in the remaining branch, such that we can shift the RF by 360°. This circuit is shown in Fig. 6.1 (c). In the meanwhile we implemented a removable optical beam path to detect the beat-note of the Raman 90 with one of the co-propagating beams onto a photodiode, such that we can have a direct measurement of the modulation amplitude of the EOM as a first step. A fine-tuning of the amplitude and a scan of the phase shifters, while measuring the ratio of the Rabi frequencies with the ion, concludes the calibration procedure. With the new EOM and control circuit we were able to reduce the modulation index to 0.25, which was not as low as before for unknown reasons, but good enough for the experiments of the next chapters. The scan of the control voltages for the VVA and PS was integrated into the rest of the lab control system, which could be employed to perform the intrinsic micromotion compensation automatically in the future.

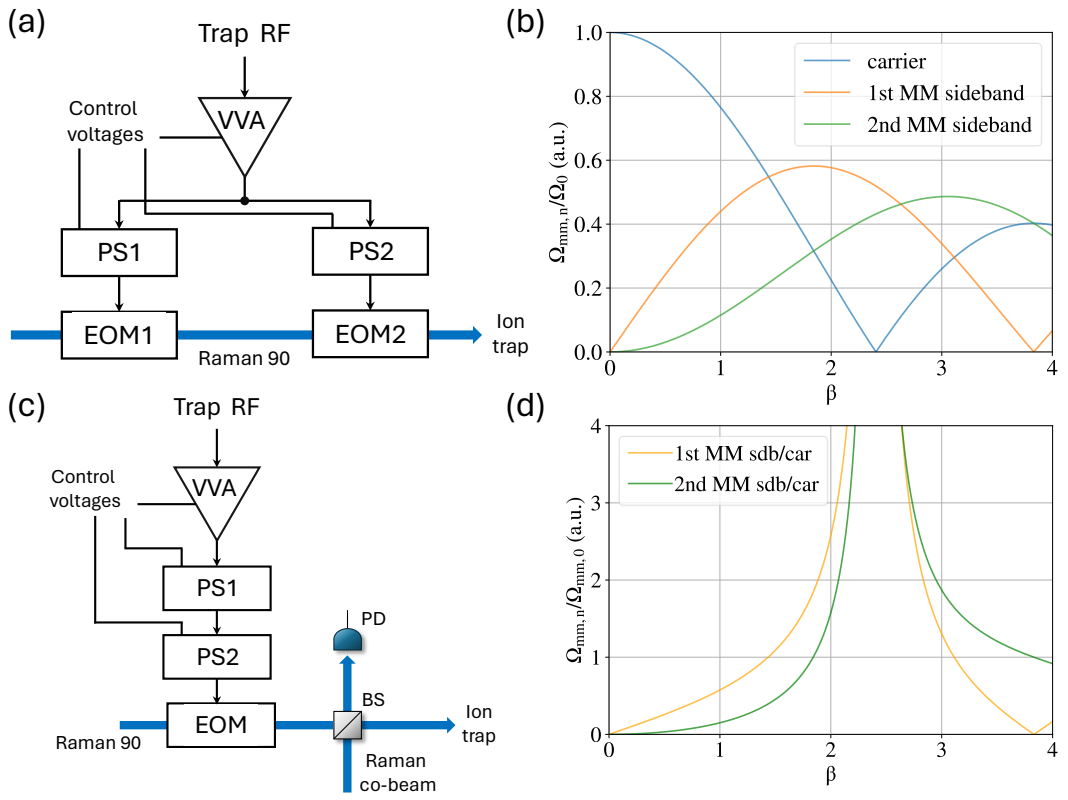

Figure 6.1: Compensation of the intrinsic micromotion. (a) Circuit for intrinsic micromotion compensation based on two Electro-Optic Modulators (EOM). The trap RF reaches the EOMs after passing through a Voltage Variable Attenuator (VVA) and two Phase Shifters (PS), which are tuned by control voltages, discussed in the main text. (c) Circuit for intrinsic micromotion compensation based on one EOM. An additional optical beam path can be used to measure the beat-note of the Raman 90 with one of the co-propagating beams at a Photodetector (PD) to simplify the calibration. The Beam Splitter (BS) is removable and used only for this calibration. (b) Modulation of the Rabi frequencies for the carrier, first and second micromotion sidebands due to the intrinsic micromotion. (d) Ratio of the Rabi frequencies of the two micromotion sidebands and the carrier, which are used to compute the modulation amplitude experienced by the ion.

6.2 Excess micromotion

In Subsec. 2.1.2 I explained the motivations that generate stray radial electric fields and how they induce excess micromotion. The main consequences are a displacement of the ions in the radial direction, modifying the normal modes, and modulation of the laser-ion interaction. It is important to minimize excess micromotion when performing cooling and manipulation of trapped ions. In the experiments involving transport and separation of mixed-species crystals it was crucial to compensate stray fields throughout the waveform in order to avoid re-ordering and mode cross-coupling.

There are several methods to detect excess micromotion [Ber+98; Kel+15]. We employ a parametric excitation method for different reasons: it requires a simple experimental configuration, can be performed along the entire trap and requires only a single laser beam with projection onto all the normal modes. Here I describe in detail how we perform the excess micromotion compensation and then discuss experimental results.

6.2.1 Parametric excitation

The parametric excitation of the ion's motional states is based on modulating the RF amplitude with an oscillating drive of frequency ω_d and amplitude (or modulation index) $h \ll 1$. This is informally called *RF tickle* in the group. It creates a parametric oscillator at the ion position $\bar{u}_i$ due to the radial electric field along direction $i = (x, y)$ [ITU11]:

$$E_{\mathrm{RF},i}(\bar{u}_i, t) = E_{\mathrm{RF},i}(\bar{u}_i)\left[(1 + h\cos\omega_\mathrm{d} t)\cos\Omega_\mathrm{RF} t\right]. \tag{6.3}$$

We can apply the pseudopotential approximation of Subsec. 2.1.1 and average over the RF period:

$$\begin{aligned}\left\langle E_{\mathrm{RF},i}(\bar{u}_i, t)^2\right\rangle_{\Omega_\mathrm{RF}} &= E_{\mathrm{RF},i}(\bar{u}_i)^2\left\langle\left(1 + 2h\cos\omega_\mathrm{d} t + h^2\cos^2\omega_\mathrm{d} t\right)\cos^2\Omega_\mathrm{RF} t\right\rangle_{\Omega_\mathrm{RF}} \\ &\approx E_{\mathrm{RF},i}(\bar{u}_i)^2\left\langle(1 + 2h\cos\omega_\mathrm{d} t)\cos^2\Omega_\mathrm{RF} t\right\rangle_{\Omega_\mathrm{RF}} \\ &= \frac{1}{2}E_{\mathrm{RF},i}(\bar{u}_i)^2(1 + 2h\cos\omega_\mathrm{d} t),\end{aligned} \tag{6.4}$$

where the term proportional to h^2 can be neglected and $\cos\omega_\mathrm{d} t$ is quasi-static in the RF period. As shown in Eq. 2.13 the force due to the pseudopotential acting on the ion is proportional to its spatial derivative:

$$\begin{aligned}\bar{F}_i(\bar{u}_i) &= -e\frac{\partial\left\langle E_{\mathrm{RF},i}(\bar{u}_i, t)^2\right\rangle_{\Omega_\mathrm{RF}}}{\partial\bar{u}_i} \\ &= -\frac{e^2}{4m\Omega_\mathrm{RF}^2}\left[E_{\mathrm{RF},i}(\bar{u}_i)\frac{\partial E_{\mathrm{RF},i}(\bar{u}_i)}{\partial\bar{u}_i}\right](1 + 2h\cos\omega_\mathrm{d} t)\end{aligned} \tag{6.5}$$

which means that the pseudopotential is modulated by the factor $(1 + 2h\cos\omega_\mathrm{d} t)$. Considering also the contribution of the DC potential and a stray radial electric field $\vec{E} = (E_i)_i$ which displaces the ion and that we want to detect, the ion is subjected to the following equations of motions [Nad+21]:

$$\frac{\mathrm{d}^2\bar{u}_i}{\mathrm{d}t^2} + \left(\frac{\Omega_\mathrm{RF}}{2}\right)^2\left[a_i + \frac{q_i^2}{2}\left(1 + h\cos\omega_\mathrm{d} t\right)^2\right]\bar{u}_i = \frac{eE_i}{m} \tag{6.6}$$

with the usual Mathieu parameters a_i and q_i such that $|a_i| \ll |q_i| \ll 1$, and resulting angular frequency:

$$\omega_i = \frac{\Omega_\mathrm{RF}}{2}\sqrt{a_i + \frac{q_i^2}{2}\left(1 + \frac{h^2}{2}\right)} \tag{6.7}$$

which shows that this frequency is also modulated. If we define the "effective" modulation index:

$$\tilde{h} \equiv \frac{h}{1 + h^2/2}\left(1 - \frac{a_i\Omega_\mathrm{RF}^2}{4\omega_i^2}\right) \tag{6.8}$$

and we neglect terms proportional to h^2, we can cast Eqs. 6.6 into the Mathieu's equations:

$$\frac{\mathrm{d}^2\bar{u}_i}{\mathrm{d}t^2} + \left(\frac{\omega_\mathrm{d}}{2}\right)^2\left(A + 2Q\cos(\omega_\mathrm{d} t)\right)\bar{u}_i = \frac{eE_i}{m} \tag{6.9}$$

with Mathieu parameters $A \equiv (2\omega_i/\omega_\mathrm{d})^2$ and $Q \equiv \tilde{h}A$. Here we are generally not working in the usual regime where the Mathieu parameters are much smaller than 1, but where they are close to instability due to parametric resonances. This happens for:

$$\omega_\mathrm{d} = \frac{2\omega_i}{n}, \quad \text{with } n \in \mathbb{N}. \tag{6.10}$$

At these resonances the ion trajectory is oscillatory with exponentially growing amplitude over time. The linewidth of the resonances gets broader for larger h, but narrower for higher n (scaling as h^n [LL76]). For $n = 1$ there is the strongest resonance, but we typically employ $n = 2$, such that $\omega_\mathrm{d} = \omega_i$ to simplify the frequency calibration process. In the pseudopotential approximation and neglecting the Heisenberg uncertainty, the parametric excitation does not happen for the conditions $\bar{u}_i = 0$ and $\dot{\bar{u}}_i = 0$, which makes it suitable to detect the presence of excess micromotion. It can also be used as a method to measure mode frequencies, including for axial modes due to the presence of axial RF fields away from the trap center.

6.2.2 Excess micromotion compensation

Excess micromotion is compensated by applying a set of DC voltages to the shim electrodes, such that the generated electric fields cancel the stray fields and move the ions back to the RF null. The four shim rows are composed of seven electrodes which are currently commonly driven. The voltages of each row are defined by two parameters α and β (not related to the modulation index) such that:

$$v_A = -v_D = \frac{1}{4}(\alpha + \beta), \quad v_C = -v_B = \frac{1}{4}(\alpha - \beta) \tag{6.11}$$

or conversely:

$$\alpha = (v_A + v_C) - (v_B + v_D), \quad \beta = (v_A + v_B) - (v_C + v_D), \quad v_A = -v_D, \quad v_C = -v_B \tag{6.12}$$

where the subscripts A, B, C and D indicate different shim rows according to Fig. 6.2 (a). A positive value of α and β makes the shim generate electric fields along the $-x$ and y directions, respectively. The intensity of the electric fields in the two directions is not the same: 1 V applied to the shim row B generates an electric field with components $E_x \simeq 2.4$ V/m and $E_y \simeq 30.9$ V/m at the central experimental zone.

Manual excess micromotion compensation

The calibration of the required (α, β) for compensating the stray fields using a single ion as a probe is based on the following steps:

1. set an initial α_c and arbitrary β;
2. scan of the parametric excitation drive ω_d to find the two radial mode frequencies. On resonance the ion fluorescence reduces and the frequencies are found;
3. 2D scan of β against ω_d for each vibrational mode X and Y to find two β_c for which each of the radial modes cannot be excited. At these two points the stray fields along the two spatial directions are independently compensated;
4. repeat steps 1-3 for a set of $\{\alpha_\mathrm{c}\}$, generally more than 2. The sets of $\{\beta_\mathrm{c}\}_\mathrm{X}$ and $\{\beta_\mathrm{c}\}_\mathrm{Y}$ found for the two modes lie on two lines in the (α, β) plane. The intersection of the two lines gives the optimal coordinates $(\alpha_\mathrm{opt}, \beta_\mathrm{opt})$ which compensates for the stray fields in the radial spatial plane.

A schematic of the step 4 is shown in Fig. 6.2 (b). During the compensation the set $\{\alpha_c\}$ should preferably be chosen close to the α_{opt} or should converge to it, given that far from this point the β_c do not lie on a straight line. In step 3 we employ a 2D scan given that the mode frequencies change for a large variation of β due to the shim potential curvature and anharmonic potential terms of the other electrodes. This generally does not happen near the compensation point and for a parametric modulation amplitude that is high enough to make the change in the shim potential curvature negligible.

One advantage of this method is that it can be employed to compensate stray fields in any part of the trap chip and for any voltage configuration. Starting with an ion trapped in the central experimental zone, we can gradually modify the voltages of the DC electrodes to reach the final configuration, trigger the RF tickle and then return to the initial configuration, where the ion's state can be detected. This feature was essential for the experiments of transport and separations of mixed-species ion crystals described in Ch. 8, where stray field compensation was required throughout the transport trajectories of the ions.

Calibration of the stray field compensation was found to be necessary on a timescale of a few weeks and requires a few tens of minutes. We performed it with a single calcium ion and found that the same compensation is valid also for small mixed-species ion arrays. Typically the optimum points are such that $0 \leq \alpha_{opt} \leq 20$ and $-2 \leq \beta_{opt} \leq 0$, but they vary depending on the position, charging of the trap and exact DC voltage configuration. The latter, for which we show some examples in Subsec. 6.2.3, might be caused by an imperfect calibration of the DACs and/or a deviation between the trap model and the actual situation in the ion trap, for example due to imperfect fabrication. The former is generally minimized by periodic calibration of the DACs, while for the latter we developed a routine based on shifting the voltages of the DC electrodes and measuring the variation of the required stray fields compensation. This method is described in Subsec. 6.2.3 and requires many iterations of the compensation procedure described above, which would make it highly time-consuming. To reduce this time and automatize the process we developed an automatic compensation procedure based on the one described above. In the next sections I describe this method and the steps we took to improve the model.

Automatic excess micromotion compensation

The automatic stray field compensation is based on finding $(\alpha_{opt}, \beta_{opt})$ by scanning the shim voltages and checking the parametric excitation of the ions, but it differs in how the scans are performed. It is implemented as a Python script used by the control system and it is based on the following steps:

1. set of an initial (α, β);
2. simulate the radial mode frequencies Y and X for the given set of voltages;
3. scan of ω_d to find the Y mode frequency near the simulated one;
4. scan of (α, β) along a given direction while RF tickling at ω_y, until the coordinates $(\alpha_c, \beta_c)_y$ that compensate stray fields along this direction (which results in lower loss of fluorescence from the tickle) are found;
5. repeat point 3 for the X mode frequency;
6. repeat point 4 while RF tickling at ω_x to find the compensation $(\alpha_c, \beta_c)_x$ for the stray fields in the other direction;

7. repeat steps 3-6 until consecutive points are closer than a threshold or enough points have been collected, such that a linear interpolation can be performed to find the intersection $(\alpha_{\text{opt}}, \beta_{\text{opt}})$.

In steps 3 and 5 the scans are automatically fitted with a Lorentzian function and the quality of the fit is analyzed. Depending on the outcome, the result might be accepted or the scan might be repeated with a different range. If the amplitude of the Lorentzian is smaller than a threshold, the coordinates $(\alpha_c, \beta_c)_{y/x}$ are accepted for this iteration. In step 4 (6) the direction of the scan of the shim electric field should be parallel to the direction of the radial mode X (Y). Initially these directions were simulated, but we then found experimentally from different sets of $\{(\alpha_c, \beta_c)\}_{y/x}$ that an angle of $\theta_y = 0.74°$ with respect to the horizontal axis for step 4 and an angle of $\theta_x = -3.95°$ for step 6 make the algorithm converge quickly for a large range of DC voltage configurations. The angles might be computed and updated while running the algorithm, but this was not needed. The number of datapoints for each scan was experimentally chosen to make the fit robust. The algorithm ideally requires only one iteration to converge, but it generally employs around 2-3 iterations, including a verification step that the optimal point is reached. A schematic of the convergence of the algorithm is shown in Fig. 6.2 (c). The compensation is generally performed in a few minutes, depending on the initial guess, and with an uncertainty that is less than 2 V/m.

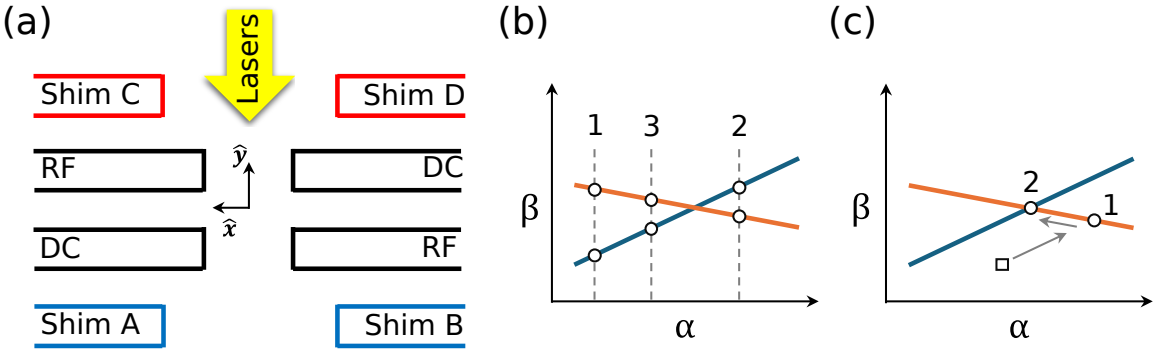

Figure 6.2: Excess micromotion compensation. (a) Schematic of the DC and shim electrodes. Parameters α and β generate compensating electric fields along the horizontal and vertical directions, respectively. (b) Manual compensation of the stray fields. For each α we find the two β that compensate the stray fields along the two mode directions. The resulting optimal point is found by linearly interpolating through the compensation points (circles). (c) Automatic compensation of the stray fields. From a generic position (square), we move along a given direction until we find a compensation point for one of the modes. From there we move in another direction and find another point for the other mode. These steps are repeated until the algorithm either converges to the optimal point or finds it from a linear interpolation when enough points are collected.

6.2.3 Potential model calibration

The generated potentials are simulated starting from a perfect trap model. Manufacturing imperfections might cause the actual electric fields to deviate from the ideal ones. For this reason, we worked on experimentally compensating for these deviations, focusing on those associated with the DC electrodes. We tested different approaches, but here I describe the most promising one.

The improvement of the potential model relied on measuring the magnitude of the electric fields generated by DC electrodes on different wafers. The ratio of magnitudes could be used to rescale the DC electrode voltages to compensate for deviations. This routine started with confining a single calcium ion at the center of two selected DC electrodes. The voltages of the electrodes that were not strictly necessary for confinement were set to zero to minimize external disturbances. The stray fields were compensated with the methods described in the previous sections to give a reference configuration for the shim voltages in the (α, β) plane. The voltages of the selected DC electrodes were then shifted by a small amount δV and the stray fields were compensated again, saving the new shim configurations. An example of this step is shown in Fig. 6.3 (a). We repeated these measurements for different values and signs of δV, generally taken to be around ± 0.1 V, from which we computed the mean values of the compensation changes. During this procedure we measured the exact voltage outputs of the DACs, to ensure we applied the correct shifts within half a millivolt. We then computed the magnitude of the shifts in the required compensation due to each electrode, and computed their ratios R_v. These were used to rescale the voltages applied to the DC electrodes symmetrically. This procedure was repeated for the pairs of DC electrodes 6/21, 7/22 and 8/23 of Fig. 2.3 (e) and the resulting ratios are shown in Tab. 6.1. We notice that the DC electrodes in the top wafer (6, 7 and 8) have a stronger influence at the ion position than the electrodes in the bottom wafer (21, 22 and 23), which suggests imperfect manufacturing of the trap such that the top wafer is closer to the ion.

To see how the ratios change for different confining wells, we also shifted the pairs of electrodes by a common amount ΔV_com, which is of the order of a few volts, and obtained changes in the required shim configuration similar to that shown in Fig. 6.3 (a) for the electrodes 6/21. We notice that the displacements in the (α, β) plane caused by δV for different electrodes are not parallel, inducing a displacement for a large ΔV_com. If the shifts caused by δV were parallel, common changes in the voltages of the pairs of electrodes would not change the required stray field compensation, making it independent of the exact DC voltage configuration. For the same reason a symmetric rescaling of the voltages of the pairs of electrodes is not enough to maintain the ion at the RF null. We also computed the ratios R_v depending on ΔV_com and the results for the electrodes 6/21 are shown in Fig. 6.3 (b). We can notice that the ratios are roughly similar, although a clear behavior is hard to obtain due to the large error bars.

Electrode pair	R_v
6/21	1.033(7)
7/22	1.040(7)
8/23	1.028(7)

Table 6.1: Ratios computed according to Fig. 6.3 for different pairs of electrodes, averaged over measurements performed with different ΔV_com. Ratios higher than 1 indicate that the first set of electrodes (6, 7 and 8) affect the ion at the RF null more than the second set of electrodes (21, 22 and 23).

We tested the use of rescaled voltages using the factors of Tab. 6.1 for transporting a Be–Ca crystal from the central experimental zone (in front of electrodes 8/23) to the left separation zone (electrodes 6/21), but residual stray fields were still intense enough to cause a reordering of the ions. This independently confirms that a constant rescaling of the electrode voltages is unable to keep the ions at the RF null. To solve this issue, we employed time-varying shim voltages that were able to compensate for stray fields while transporting

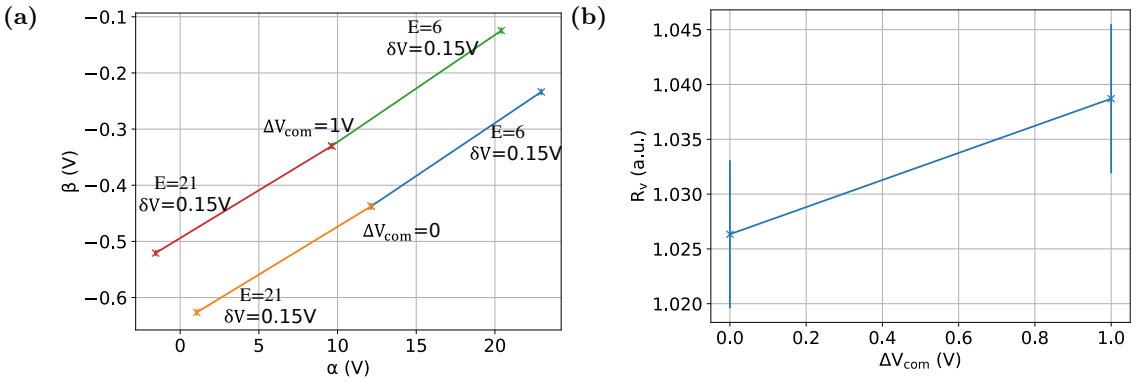

Figure 6.3: Potential model calibration for the electrodes 6 and 21. (a) Stray field compensation points for a given trapping configuration when no common voltage shift is applied ($\Delta V_{\text{com}} = 0$) and with a common shift ($\Delta V_{\text{com}} = 1$ V). For each of them, a small voltage shift $\delta V = 0.15$ V is applied to each electrode individually, generating radial fields that are compensated by the shim electrodes. Connected points have the same ΔV_{com}, while for the central ones $\delta V = 0$. (b) Ratios of the amplitudes of the displacements caused by δV applied on electrode 6 and the one applied on electrode 21 for different ΔV_{com}. Ratios higher than 1 indicate that electrode 6 affects the ion at the RF null more than electrode 21.

the ions.

In conclusion, with the method presented here we were able to detect and quantify a discrepancy between the model and the actual trap potentials, where the electrodes of the top wafer have a stronger influence at the ion position than their counterparts in the bottom wafer. This information can be included in the routines for designing the trapping voltages described in Ch. 7. Unfortunately we were not able to find a method to keep the stray field compensation constant while changing the DC voltages, which is required for experiments involving the shuttling of mixed-species ion crystals. Further characterization of the potential model for larger voltage ranges might find a solution to this problem, although a large amount of datapoints might be necessary for a proper characterization with low uncertainty.

7 Waveform generation

Waveform generation was first implemented in our group during the Ph.D. of Ludwig deClerq [Cle15] and master thesis of Robin Oswald [Rob15]. Consequently, Vlad Negnevitsky [Neg18] extended the previous work and developed a Python library compatible with M-ACTION called *Pytrans*. In the work of this thesis, I extended the functionalities of this library for waveform analysis, manipulation and simulation. Then Pytrans was rewritten and generalized in a modular approach by Carmelo Mordini, with contributions from me, Robin Oswald and Tobias Sägesser. A technical description of the package tools and features can be found in the documentation of [Mor+23] and will be the subject of a future publication.

In this chapter, I describe the trapping potential generation for controlling the positioning of the ions and its implementation in the first version of Pytrans, similarly to how it is illustrated in the Ph.D. thesis of Vlad Negnevitsky. Then I describe the more recent extensions to this library and the new features of the second version of Pytrans. This overview will be particularly relevant for the experiments described in the next chapters.

7.1 Trapping potential

As described in Sec. 2.2, the trapping of ions is performed by means of a segmented 3D trap composed of multiple RF, DC and shim electrodes. If a voltage v_j is applied to the electrode $j \in 1, 2, \ldots, J$, it creates an electric potential $V_j(x, y, z)$ which depends on the geometry of the electrode itself and the surrounding environment. The potential is expressed as:

$$V_j(x, y, z) = v_j \phi_j(x, y, z) \tag{7.1}$$

where $\phi_j(x, y, z)$ is a dimensionless parameter which we call the *potential moment*, defined as the potential generated at position (x, y, z) when 1V is applied to electrode j and the others are grounded. The potential generated by applying a set of voltages $\{v_j\}$ to the DC and shim electrodes is then given by the sum of the potentials generated by each electrode due to the superposition principle. If the pseudopotential is also taken into account (defined in Subsec. 2.1.1), the total potential is:

$$V(x, y, z) = \sum_{j=1}^{J} v_j \phi_j(x, y, z) + V_{ps}(x, y, z) \tag{7.2}$$

and the electric field along coordinate $u \in \{x, y, z\}$ is:

$$\vec{E}_u(x, y, z) = -\frac{\partial V(x, y, z)}{\partial u} = -\sum_{j=1}^{J} v_j \frac{\partial \phi_j(x, y, z)}{\partial u} - \frac{\partial V_{ps}(x, y, z)}{\partial u} \tag{7.3}$$

In the segmented 3D trap there are 30 DC electrodes and they are used for confinement and shuttling, while there are an additional 28 shim electrodes which are primarily and they are mostly used for compensating radial micromotion, as described in Sec. 6.2. The

2 RF electrodes are used to produce radial confinement. As shown in Fig. 2.3, in an ideal trap, opposing DC electrodes would be geometrically symmetric. If the voltages applied to opponent electrodes are equal, ideally no radial electric fields are present, and the ions sit along the trap axis (x=0, y=0). Consequently, the contribution of the shim electrodes can be neglected, and the ions are located at the RF null, which makes $V_{ps}(x, y, z) = 0$ and $\vec{\nabla} V_{ps}(x, y, z) = 0$ by definition. From now on the x and y dependencies can be suppressed, describing the confining potential only along the z axis. In this scenario, a positively charged ion will stay confined at the local minimum of the total potential $z = p$. Close to this minimum, the potential is well approximated by a harmonic well potential $V_h(z)$ over a few tens of µm [Win+98; Hom+11], which can be described as:

$$V_h(z) = \frac{m}{2e}\omega_{com}^2(z-p)^2 + d \tag{7.4}$$

where m is the ion mass, ω_{com} is the axial angular frequency experienced by a single ion or the common mode of motion for a short string of equal-mass singly-charged ions and d is a constant DC offset. The angular frequency can be found close to the local minimum as:

$$\omega_{com}^2 = \frac{e}{m}\frac{\partial^2}{\partial z^2}V(z)\bigg|_{z=p} \tag{7.5}$$

It is worth noting that ω_{com} depends on the charge-to-mass ratio of the ions, so the formula above is not valid for mixed-species chains. For the exact formula see Sec. 2.3. The DC offset d is controlled by the common voltage shift v_{C} applied to the DC electrodes described in Sec. 2.1, which changes the quadrupole in the radial plane as discussed at the end of Subsec. 2.1.1. It is used as a parameter to control the frequency and direction of the radial modes with respect to the trap axis. The potential moments of all the trap electrodes are obtained from an electrostatic boundary-element simulation performed in COMSOL, discretized on a 3D grid with arbitrary steps of 5 μm between each point around the trap axis. In Fig. 7.1 the potential moments for DC electrodes $1, \ldots, 10$ and for shim electrodes $2, \ldots, 5$ along the trap axis are shown. Due to the symmetry of the trap structure, the potential moments of opponent electrodes are equal along the trap axis, and the ones related to the DC electrodes $11, \ldots, 15$ and the shim electrodes 6, 7 and 8 are mirrored around $z = 0$ (this is of course a simplification, as illustrated in the work of the previous chapter).

7.2 Waveform generation libraries

7.2.1 Pytrans version 1

Static harmonic wells

As described in Sec. 7.1, the confining harmonic well can be parameterized by the axial position p, frequency ω and potential offset d. In the presence of N desired static wells, they can be described by $\{\{p_1, \omega_1, d_1\}, \ldots, \{p_N, \omega_N, d_N\}\}$. The routine for generating the waveforms, which are introduced in Sec. 5.2, aims to find a set of electrode voltages $\{v_1, \ldots, v_{30}\}$ such that the following cost function is minimized:

$$C_{\text{static}} = \int_{z_{\mathrm{L}}}^{z_{\mathrm{R}}} \sum_{n=1}^{N} G_n(z') D_n(z') dz' \tag{7.6}$$

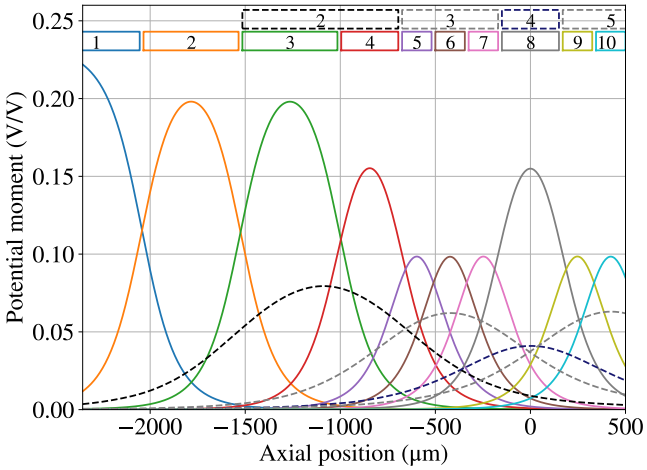

Figure 7.1: Electrode potential moments for the top DC and shim electrodes, with relative electrodes shown on top. Only the moments for the electrodes located from the left loading zone to the central experimental zone are shown, while the right side and the bottom ones are symmetric. The moments of the shim electrodes, due to the lower magnitudes, are magnified by a factor of 10 and electrode 1 is not shown as it is not relevant for the work of this thesis. The image is modified from one taken from [Neg18].

where z_L and z_R are the trap boundaries. For each potential well n with $\{\{p_n, \omega_n, d_n\}$, we have the Gaussian term $G_n(z)$ defining the relative region of interest:

$$G_n(z) = \exp\left[-\frac{(z-p_n)^2}{2R_n^2}\right] \tag{7.7}$$

where R_n parametrizes its width. It is chosen such that it coincides with a fixed minimum well depth V_R (usually few mV), such that $R_n^2 = 2V_R e/m\omega_n^2$. The difference term $D_n(z)$ is the quadratic distance between the desired harmonic potential well as described in Eq. 7.4 and the potential generated by the electrode voltages $\{v_1, \ldots, v_{30}\}$:

$$D_n(z) = [V(z) - V_{h,n}(z)]^2 = \left[\left(\sum_i^{30} v_i\phi_i(z)\right) - \left(\frac{m}{2e}\omega_n^2\,(z-p_n)^2 + d_n\right)\right]^2 \tag{7.8}$$

This method is well-suited for statically confining the ions. It can also be used for slow adiabatic transport by stacking the computed solutions for a varying set of harmonic wells. For faster transport, the cost function needs to be modified, as described in the next subsection.

Transport waveform

Transport waveforms are defined by a set of time-varying voltages $\{v_1(t), \ldots, v_{30}(t)\}$ applied to the electrodes. Consequently, each of the N desired wells is described by the time-dependent parameters $\{p_n(t), \omega_n(t), d_n(t)\}$. The Gaussian term, difference term and cost function can then be expressed as:

$$G_n(t,z) = \exp\left[-\frac{(z-p_n(t))^2}{2R_n^2(t)}\right] \tag{7.9}$$

$$D_n(t,z) = [V(t,z) - V_{h,n}(t,z)]^2 = \left[\left(\sum_i^{30} v_i(t)\phi_i(z)\right) - \left(\frac{m}{2e}\omega_n^2(t)\left(z - p_n(t)\right)^2 + d_n(t)\right)\right]^2 \tag{7.10}$$

$$\begin{aligned} C_{\text{transp}} = \int_{t_0}^{t_f} \Bigg[& \int_{z_\text{L}}^{z_\text{R}} \sum_{n=1}^{N} G_n(t',z') D_n(t',z') dz' \\ & + \sum_{j=1}^{30} \left\{ r_0 \left[v_j(t') - v_\text{def}\right]^2 + r_1 \left[\frac{dv_j(t')}{dt'}\right]^2 + r_2 \left[\frac{d^2 v_j(t')}{dt'^2}\right]^2 \right\} \Bigg] dt' \end{aligned} \tag{7.11}$$

where t_0 and t_f are initial and final transport times. The cost function contains several terms in the Taylor expansion with respect to time, which are relevant for transport. The first one, weighted by the constant r_0, disfavors voltage deviations from the default one v_def, constraining the voltages for electrodes outside the region of interest of $G_n(t,z)$. The value of v_def is typically set to 5 V, making a trade-off between deep potential wells and agreement of p, ω and d values with the required ones. The second and third terms, weighted by r_1 and r_2, disfavor the first and second derivatives of the waveform, reducing high frequency components and limiting the voltage slew rate, which are technically limited by the DEATH output stage (with a maximum slew rate of $4\,\text{V}\,\mu\text{s}^{-1}$ [Rob15]) and out-of-vacuum filters. The weights r_0, r_1 and r_2 are experimentally optimized by measuring the single ion excitation caused by the transport waveform; a summary of their typical values is shown in Tab. 7.1 and more details of this optimization can be found in [Neg18]. During the generation of the waveform, there are additional hard constraints that are imposed. The first one is that the $\{v_j(t_0)\}$ and $\{v_j(t_f)\}$ are fixed to the results obtained by solving for C_static, such that different transport waveforms can be connected without provoking discontinuous voltages. Note that this condition is not always fully satisfied, for instance due to experimental adjustment of the C_static parameters. Although we worried that these might induce motional excitation in related experiments, in practice we didn't see any. To avoid the repeated concern about these effects however, we more recently compensated by linearly interpolating the voltages through a few tens of samples. We also constrain $|v_j(t)| \leq 8.9V$, such that the voltages have some margin from the DEATH output limits, leaving space for summing with other waveforms (discussed in Subsec. 5.2.2) or filtering and ensuring that voltage saturation of the DEATH output stage does not provoke nonlinearities. Voltage saturation has not been noticed in the limits described above, and other nonlinearities in this voltage range figure as deviations of around a few tenths of mV from the desired voltages. These are accounted for by calibrating the offset and gain of the DEATH output stage as described in Subsec. 5.2.1.

Numerical optimization

The minimization of the cost functions is performed through *quadratic programming*. It uses the CVXPY library [Agr+18; DB16], with the MOSEK solver backend [MOS19].

For the numerical optimization of Eq. 7.11, the spatial and temporal dimensions need to be discretized. The trap axis is divided into $K = 943$ points, at 5 µm interval, from -2355 µm to 2355 µm. The COMSOL trap simulation provides a $K \times J$ matrix $\mathbf{\Phi}$, in which the potential of the $j \in 1, 2, \ldots, J$ electrode is evaluated at $k \in 1, 2, \ldots, K$ points along the trap axis. The transport time is discretized in M timesteps, where typically $1 \leq M \leq 2000$. Once the optimization is performed, the library returns the waveform in the form of a $J \times M$

matrix $\mathbf{W}$, which is the output for use in the experiment. The trapping potentials at the trap axis can be computed as the $k \times M$ matrix $\mathbf{V} = \mathbf{\Phi W}$.

Separation process

Next we move to consider how the separation waveform works. During this operation, the ions of a multi-ion chain gradually transition from being co-trapped in a single well to being distributed into two distinct wells. This process is intrinsically non-harmonic, and the required trapping potential can be approximated by a 4-th order polynomial described as:

$$V_{sep}(z_s) = \alpha(t)(z - z_s)^2 + \beta(t)(z - z_s)^4 + \gamma(t)(z - z_s) + \delta(t) + g(t)(z - z_s)^3 \tag{7.12}$$

where z_s is the separation point, which is $-422.5\,\mu\text{m}$ ($422.5\,\mu\text{m}$) for the left (right) separation zone, as shown in Fig. 2.3. We impose the potential to be locally symmetric around z_s by setting the cubic term $g(t)(z-z_s)^3 \simeq 0$, which can be well satisfied thanks to the symmetric electrode geometry of this zone. Moreover, the size of the electrodes is particularly small to allow the generation of stronger quadratic and quartic potential terms [HS05]. The Taylor expansion is still a valid approximation of the potential along the trap axis as the positions of the ions vary by a small range around z_s compared to the width of $155\,\mu\text{m}$ of the central electrode of the separation zone [Kau+14]. For larger distances, higher-order terms in the potential need to be taken into account. The parameter δ is the DC offset at z_s, while γ is the axial electric field, which ideally is null but in practice will be present in the experiment, due to stray fields and potential moment imperfections, we find that it needs to be experimentally calibrated. The parameters α and β are related to the ion separation distance $s(t)$, the axial in-phase angular frequency $\omega_{\text{Z1}}(t)$ and the axial out-of-phase angular frequency $\omega_{\text{Z2}}(t)$ of a two single-species ion chain. The equilibrium positions of the ions are $z = z_s \pm s/2$, in which s is a solution of [HS05]:

$$\beta s^5 + 2\alpha s^3 = \frac{e}{2\pi\epsilon_0} \tag{7.13}$$

which is generally solved numerically given α and β, while the axial angular frequencies are computed as:

$$\omega_{Z1}^2 = \left(2\alpha + 3\beta s^2\right)\frac{e}{m} \tag{7.14}$$

$$\omega_{Z2}^2 = \omega_{Z1}^2\left(1 + \frac{e^2}{\pi\epsilon_0 m\omega_{Z1}^2 s^3}\right) \tag{7.15}$$

where ϵ_0 is the free-space permittivity, m is the ion mass and e is the ion charge. In the case of two-ion mixed-species chains, the equilibrium positions are unchanged. The axial angular frequencies can be computed by taking into account the quartic term as a perturbation of the usual harmonic well, as described in [Hom+11]. If we consider the characteristic ion distance as $l = (q/8\pi\epsilon_0\alpha)^{1/3}$, in the regime in which $l^2\,|\beta/\alpha| \ll 1$, the axial angular frequencies can be approximated as:

$$\omega_\pm \simeq \sqrt{\frac{2e\alpha}{m_1}}\left(1 + \mu \pm \sqrt{\mu^2 - \mu + 1}\right)^{1/2}\left[1 + \frac{1}{3\times 2^{4/3}}\frac{\mp(1+\mu) + 7\sqrt{\mu^2-\mu+1}}{\sqrt{\mu^2-\mu+1}}\left|\frac{\beta}{\alpha}\right| l^2\right] \tag{7.16}$$

where $\omega_- \equiv \omega_{\text{Z1}}$, $\omega_+ \equiv \omega_{\text{Z2}}$, m_1 is the mass of the heaviest ion ($^{40}\text{Ca}^+$ in our case), m_2 the mass of the lightest ion and $\mu = m_1/m_2$ is their mass ratio.

The separation process is composed of different stages. Initially, the typical scenario is that the ions are confined in the same potential well, with α positive and β small. Since the lowest frequency of the separation process is close to the *critical point* where $\alpha = 0$ and the trap frequencies are given by β, we then raise β to the maximum possible value. This allows the waveform to be run as fast as possible without violating adiabaticity constraints. Once this is done, we decrease α from its initial value through the critical point, until it reaches a negative value and the ions are separated by a distance of around 120 µm. The process described above is generally preceded and followed by transport waveforms, which bring the multi-ion crystal to the separation location, and transport the ions from their separated well positions to the final destinations.

Separation waveform

In the segmented 3d Paul trap, there are two separation regions. The relevant one for the experiments of this thesis is the left one shown in Fig. 2.3. Here the electrodes involved on one of the trap wafers are labelled from 4 to 8, and their counterparts on the other trap wafer from 19 to 23. During the waveform generation, the potential moments of these electrodes are fitted with 4-th order polynomials in a region of interest (ROI) with a range of 200 µm around $z_s = -422.5$ µm. The fit for each electrode $i \in \{4, \ldots, 8, 19, \ldots, 24\}$ gives the fitted parameters $\tilde{\alpha}_i$, $\tilde{\beta}_i$, $\tilde{\gamma}_i$ and $\tilde{\delta}_i$ for the approximating quartic polynomial potential in the ROI:

$$\tilde{\phi}_i(z) = \tilde{\alpha}_i(z - z_s)^2 + \tilde{\beta}_i(z - z_s)^4 + \tilde{\gamma}_i(z - z_s) + \tilde{\delta}_i + \tilde{g}_i(z - z_s)^3 \tag{7.17}$$

which gives the fitted total potential $\tilde{V}_{sep}(z) = \sum_i v_i \tilde{\phi}_i(z - z_s)$ in the ROI. The $\{\alpha, \beta, \gamma, \delta\}$ parameters of Eq. 7.12 can be computed by using the following set of linear equations:

$$\begin{bmatrix} \alpha \\ \beta \\ \gamma \\ \delta \end{bmatrix} = \begin{bmatrix} \tilde{\alpha}_4 & \ldots & \tilde{\alpha}_8 & \tilde{\alpha}_{19} & \ldots & \tilde{\alpha}_{23} \\ \tilde{\beta}_4 & \ldots & \tilde{\beta}_8 & \tilde{\beta}_{19} & \ldots & \tilde{\beta}_{23} \\ \tilde{\gamma}_4 & \ldots & \tilde{\gamma}_8 & \tilde{\gamma}_{19} & \ldots & \tilde{\gamma}_{23} \\ \tilde{\delta}_4 & \ldots & \tilde{\delta}_8 & \tilde{\delta}_{19} & \ldots & \tilde{\delta}_{23} \end{bmatrix} \begin{bmatrix} v_4 \\ \vdots \\ v_8 \\ v_{19} \\ \vdots \\ v_{23} \end{bmatrix}. \tag{7.18}$$

To achieve a maximal β, and take into account voltage limits, we perform a minimization of the cost function:

$$C_{\text{sep}} = \sum_i \left[q_1 \left(\alpha(t) - \tilde{\alpha}_i v_i(t)\right)^2 + q_2 \left(\gamma(t) - \tilde{\gamma}_i v_i(t)\right)^2 + q_3 \left(\delta(t) - \tilde{\delta}_i v_i(t)\right)^2 \right] - \sum_i \tilde{\beta}_i v_i(t) \tag{7.19}$$

where the constants q_1, q_1 and q_3 are weights for each term. Their typical values used for the experiments of this thesis are shown in Tab. 7.1. This cost function can be numerically minimized similarly to the transport cost function of Eq. 7.11, taking into account the DEATH voltage limit constraint $|v_i| \leq 8.9$ V.

More details on how the trajectories of the parameters $\{\alpha, \beta, \gamma, \delta\}$ vary over time have been chosen are given in Subsec. 8.3.1.

Auxiliary waveforms

Pytrans is also used to generate other waveforms that are used for additional tasks. The *loading conveyor waveform* is used to load the ions in the left loading zone while keeping the

Cost function weight	Typical value
r_0	5×10^{-10}
r_1	5×10^{-4}
r_2	2×10^{-6}
q_1	100
q_2	10
q_3	0

Table 7.1: Typical values for the Weights used in the cost functions for the generation of transport (Eq. 7.11) and separation (Eq. 7.19) waveforms.

ones that are already in the trap in an additional well at the central experimental zone. The two wells are then merged and transported to the central experimental zone for subsequent experimental operations.

The *reordering waveform* is used to deterministically set the order of the ions of a mixed-species chain. In the work of this thesis, this was performed in the central experimental zone by applying a radial displacement of the ions by increasing the voltages applied to the DC electrodes 7, 8 and 9, which pushes calcium further than beryllium according to Eq. 2.18. Afterward, a twisting quadrupole potential is generated by increasing the voltages of the DC electrodes 7 and 24, while decreasing the ones of the electrodes 9 and 22. This pushes both ions axially, but the calcium one experiences a stronger force due to the reduced distance to the DC electrodes. The radial displacement and, subsequently, the quadrupole potential are removed, realigning the ions along the trap axis but in a specific order. The voltage shifts used for the radial displacement and the quadrupole potential depend on the exact ion chain configuration and desired final order. They are experimentally tuned until the order of the ions is set deterministically, and we notice that they need to be recalibrated after a few months.

The *recrystallization waveform* is used for improving the cooling of multi-ion chains after being subjected to collision with the background gas atoms. This interaction causes considerable motional excitation, which induces a chaotic dynamic of the ions and strongly detunes the detection and Doppler cooling beams from the ions' internal transitions. This event happens approximately every 30 s per beryllium ion. Decreased detection fluorescence is automatically recognized by the control system, which triggers the recrystallization waveform. This causes the axial frequency to reduce down to around a few hundreds of kHz for a single calcium, reducing the heating induced by the RF drive while the ions are not crystallized and subjected to chaotic motion [Van+22] and allowing for an efficient cooling. As soon as the detection fluorescence returns to a high level, the axial frequency is set to the original value. The low frequency of the recrystallization waveform needs to be recalibrated depending on the exact crystal configuration. Generally it is set to ~ 400 kHz, but in the case of four-ion mixed-species experiments described at the end of this thesis a value of 200 kHz (calculated on a single calcium ion) was used.

Extension of the library

The Pytrans 1 library includes a set of functions for analyzing waveforms, visualizing the generated potentials and some additional utilities. During the work of this thesis, I extended the Pytrans 1 library by adding some functionalities. These involve 1D classical simulation of axial ion transport and separation, a set of functions for waveform management, manipu-

lation and visualization (e.g. linear combination, interpolation, voltage modifications), trap characterization and filter compensation. The latter were implemented but not used in the work of this thesis.

1D dynamic simulation

The 1D dynamic simulator of Pytrans 1 is used for simulating ion trajectories controlled by any arbitrary waveform along the trap axis. The ions are treated as classical particles subjected to classical dynamics. This approximation is valid as long as the ions are not subjected to squeezing of their states or wavepacket dispersions, which translates into the condition that the trapping frequencies or, in the presence of anharmonicities, electrode voltages changes slowly with respect to the harmonic oscillator dynamics [Für+14]. In the work of this thesis, we mostly consider adiabatic shuttling which satisfies these requirements. In the simulator, an arbitrary number of ions are initialized at any desired position, and they are controlled by an arbitrary transport or separation waveform, which is polynomially interpolated in space and time. The library then computes the forces acting on the particles, including the Coulomb repulsion, and integrates their equations of motion along the trap axis at arbitrary timesteps. In the end, the axial normal modes are computed from the Hessian matrix and they are used to fit the ion oscillations, whose amplitudes are employed in calculating the motional excitation. The library can also be used to run multiple simulations with different initial conditions to compute the mean phonon number, the waveforms can be run at different velocities, and different external perturbations (such as the effect of waveform filtering or the excitation induced by anomalous heating) can be considered.

7.2.2 Pytrans version 2

The newest version of the library has been designed with a more general and modular approach than the previous one. In this subsection, I describe the Pytrans 2 library and its functionalities, highlighting the improvements over the previous verion. A schematic of the structure of Pytrans 2 is shown in Fig. 7.2.

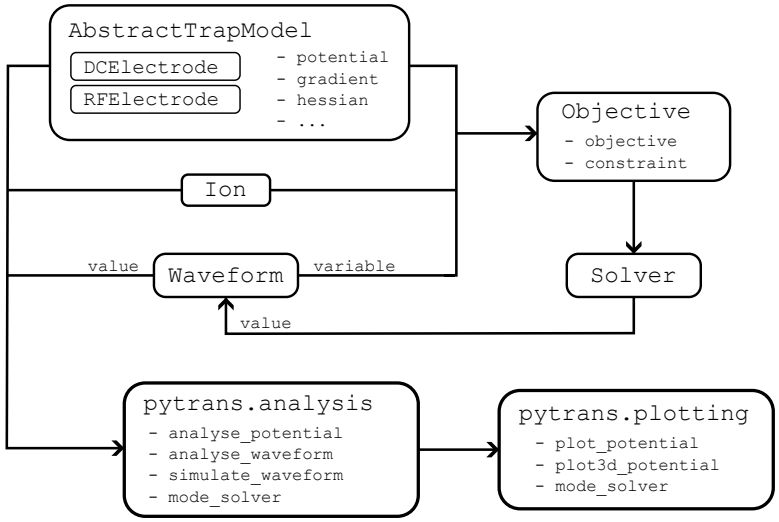

Figure 7.2: Class diagram of Pytrans version 2. The ovals show the classes, while the arrows indicate that a class is used by another one to compute the output.

Trap model

Pytrans 1 was specifically developed for the segmented 3D Paul trap used for the experiments described in this thesis (as explained in Sec. 2.2). Consequently, using this library for different traps required some modifications. Pytrans 2 was developed to manage any generic ion trap architecture: it introduces the use of an *abstract trap model*, which is an interface between the specific data describing one particular ion trap and the generic algorithms implemented for generating waveforms. In this way, the user can describe their trap electrodes, potential moments, electric field moments, etc. in different forms, e.g. through analytical expressions or numerical simulations, and encapsulate it into a compatible Python class. Pytrans 2 has been used with the segmented 3D Paul trap of this thesis, but also for transporting in a surface trap [Mor+24] and in a Penning trap [Jai+23].

Arbitrary ion crystal

Pytrans 1 can only work with defined potential wells. On the contrary Pytrans 2 takes into account an arbitrary trapped ion chain. The crystal can be composed as a list of *ion* objects, which is used for waveform analysis (for waveform generation this feature is under development). Each ion object specifies the particle's mass and charge, and this information is accounted for by a mode solver. These are taken into account by employing a *mode solver*, which was initially developed by Matt Grau in the group and then integrated into the project by Carmelo Mordini. The mode solver can compute the 3N normal modes of an N ion crystal as explained in Sec. 2.3, incorporating in a single framework elements that were previously scattered among different libraries.

Arbitrary cost function

Pytrans 1 manipulates the cost functions defined in Subsec. 7.2.1 inside specialized functions. Whenever a new type of waveform needs to be generated, a new function needs to be rewritten. Pytrans 2 takes into account a modular approach: the cost function is "assembled" as a linear combination of terms from a set of objective primitives. These can be used to enforce specific terms in the potential (linear, quadratic, cubic and quartic), Hessian, electrode potentials or in their time-derivatives.

3D Dynamic simulation

In Pytrans 1 I developed a 1D classical simulator for the trajectories of ions subjected to transport and separation waveforms. Pytrans 2 features a comparable simulator, but thanks to the 3D simulation of the trap potential, it can analyze ion trajectories in 3D. This is particularly relevant for the simulation of the transport and separation experiments described in the next chapters.

Extension of the library

During the work of this thesis, I worked on testing, debugging and extending the functionalities of the package. These include the computation of ions energies during the 3D dynamic simulation, improved analysis and visualization of the waveforms.

8 Transport and separation results

In this chapter, I describe the work performed to improve the trapping, positioning, transport, separation and recombination of the ion crystals, which are all fundamental building blocks of the QCCD architecture. Starting from the description of how to choose the parameters for each routine, I then describe the experimental results for single-species crystals, obtained in collaboration with Matteo Marinelli and Vlad Negnevitsky. This formed the basis for later experiments I performed, in which the performance of the ion shuttling and separation was improved and extended to more complex mixed-species ion crystals. In this process, a deeper understanding of the underlying mechanisms has been developed. Some of the results showed in this chapter are published in [Lan+24].

8.1 Static Confinement

In Sec. 7.1 I described the general shape of an axial harmonic well for confining a short string of equal ions. Experimentally this potential needs to take into account additional requirements enforced by the specific ion string structure and the experimental setup. Ions confined in a static potential are typically subjected to cooling, state preparation and qubit manipulation. For this purpose, the normal modes involved (generally all) need to have a projection on the laser beams' wave vector $\vec{k}$. In the segmented 3D trap this requirement is easily satisfied for the axial modes, but since we have the ability to rotate the radial modes, it is possible to choose nonoptimal configurations where one radial mode is perpendicular to the laser beams. For this reason we check the cooling of all modes of a single ion for any new trap potential we use. Another requirement for cooling the ions is to avoid the degeneracy of vibrational modes [Ami+11]. Degenerate modes do not have well-defined directions and only the motion along the cooling laser wave vector will be cooled, while the motion along other directions will be heated by photon recoil. In the segmented 3D trap the axial mode frequency can be controlled by the DC electrodes, easily avoiding degeneracy with the radial ones. For the radial modes, by acting on the potential offset and on the axial curvature (which has an impact on the radial directions due to Laplace's equation 2.2) the degeneracy can be lifted. Regarding the motional frequencies, we attempt to realize confining potentials that should maximize them. As will be described in Subsec. 8.2.3, the heating rate of normal modes in Paul traps scale as $1/\omega^{\alpha}$, where ω is mode angular frequency and α is a positive experimental constant, favouring higher trapping frequencies for keeping the ions as cool as possible. The limit to this is placed when working with ion strings, for which excessively high axial frequency can induce a zig-zag structure. We also observe that this leads to inefficient recrystallization after collision with background gases, as described in Subsec. 7.2.1. For all these reasons, the choice of the static well properties depends on the ion string and specific experiment. Some of the most relevant ones used in this thesis are shown in Fig. 8.1.

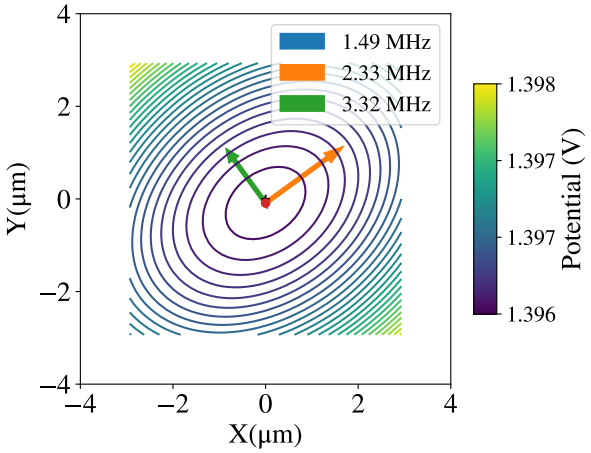

Figure 8.1: Simulation of the vibrational modes for a single $^{40}Ca^{+}$ confined at the start of the transport waveform T0. Laser beams are aligned along the y axis.

Waveform	Z	Y	X	Angle
T0	1.49	2.33	3.32	126°
T1	1.49	1.78	3.66	55°
T2	1.49	2.52	3.19	67°

Table 8.1: Vibrational modes (in MHz) for a single $^{40}Ca^{+}$ confined at the start of some relevant transport waveforms (see Subsec. 8.2.3 for definitions) and angle of the mode X with respect to the horizontal axis.

8.2 Transport

The first demonstration of a single ion *adiabatic* transport in a segmented 3D Paul trap for quantum computing was reported in [Row+02]. *Diabatic* transport of up to two identical ions crystal was shown in [Wal+12; Bow+12]. Transport of mixed-species strings was reported in different publications, among which is interesting to note [Bar+04; Hom+09]. Over this period several methods were proposed for minimizing transport excitation, based on optimal control [Sch+06] and invariant-based inverse engineering [Tor+11; Lu+14; Für+14]. An automatic routine for transport waveform optimization was implemented in [Ste+22]. In this section I give an overview of how the well trajectories for the transport experiments of this thesis were chosen and optimized, and I describe the obtained results.

8.2.1 Transport trajectory

Adiabatic transport involves a very slow change of the confining well, in such a way that an ion starting in the ground state will end up in the same state after transport due to the adiabatic theorem. Consequently the exact trajectory of $\{p_n(t), \omega_n(t), d_n(t)\}$ should not affect the final state. This requires a timescale of hundreds of microseconds for the transport of ions through hundreds of micrometers, which is comparable to the recooling time. No real transport is adiabatic, thus it is worth considering the effects of diabaticity to see the limits on how well transport could be performed. As described in [LJ11; Bow+12], constant frequency $\omega_n(t) = \omega_n$ diabatic transport produces a coherent motional state $\alpha(t)$:

$$\alpha(t_f) = \sqrt{\frac{m\omega_n}{2\hbar}} \left[-e^{-i\omega_n t} \int_{t_0}^{t_f} \frac{dp_n(t')}{dt'} e^{i\omega_n t'} dt' \right] \tag{8.1}$$

For a constant velocity transport profile $v = dp_n(t)/dt$, with initial and final impulsive acceleration/deceleration, the coherent state becomes:

$$\alpha(t_f) = \sqrt{\frac{m\omega_n}{2\hbar}} \left[\frac{i}{\omega} \frac{dp_n(t)}{dt} \left(1 - e^{-i\omega_n (t_f - t_0)} \right) \right]. \tag{8.2}$$

This state can be nullified by choosing $\omega_n(t_f - t_0) = 2\pi k$, with $k \in \mathbb{N}$ or by applying a sharp voltage pulse at the end of the transport to counteract the displaced state [Wal+12]. This has allowed to transport ions over hundreds of micrometers in just a few microseconds. For most of the transport routines of this thesis, longer timescales were used, since these are more robust to parameter changes. For this reason, the position trajectories $p_n(t)$ were chosen according to smooth functions, in order to minimize the initial and final impulse of the ions, and they can be easily used for transport velocities of a few meters per second. These trajectories follow:

$$p_n(t) - p_n(t_0) = [p_n(t_f) - p_n(t_0)]\, P\left(\frac{t - t_0}{t_f - t_0} \right) \tag{8.3}$$

where:

$$P(x) = \frac{\rho(x) - \rho(0)}{\rho(1) - \rho(0)}, \quad \rho(x) = \ln \left| \frac{\zeta(x) - ie^{-a}}{\zeta(x) - ie^{a}} \right|, \quad \zeta(x) = e^{[ab(2x-1)]} \tag{8.4}$$

where the parameter a determines the sharpness at the start and end of the transport trajectory and b determines the slope in the middle. Typically $a = 3$ and $b = 1.5$ were used. Analogously, the trajectories of $\omega_n(t)$ and $d_n(t)$ were chosen according to Eq. 8.4. Fast variations of $\omega_n(t)$ can lead to motional squeezing, which can be avoided by ensuring that the following *adiabaticity condition* [Che+10; Bow+12; Rus+14] is fulfilled:

$$\delta = \left| \frac{1}{\omega^2} \frac{d\omega}{dt} \right| \ll 1. \tag{8.5}$$

For most of the transport waveforms used in this thesis, $\omega_n(t)$ was kept constant or slowly changed. An example of transport trajectory can be seen in Fig. 8.5. In order to control multiple wells simultaneously, adjustments to the transport cost function parameters were needed, as discussed in [Neg18].

8.2.2 Transport requirements

Designing of transport waveforms needs to take into account additional requirements given by the specific ion string and the experimental setup, including the ones described for static well in Sec. 8.1. While transporting, the trapping modes frequencies and directions need to be carefully designed in order to reduce excitations due to the specific trap noise model. Generally, the frequencies should be high in order to minimize heating rates. One of the key findings of the mixed-species experiments was that while ramping the motional frequencies, any intersection of two modes in the presence of coupling terms can lead to a transfer of phonon populations, as described in Sec. 4.5. If a vibrational mode is required to be cold for a specific reason, e.g. for quantum gates, it might get excited by interaction with a hotter one, which is not relevant to the computation. Not only the intersection of modes can lead to phonons transfer. In the presence of potential anharmonicities, due to the waveform or the Coulomb interaction between the ions [Hom+11], one vibrational mode can couple to another one or more, especially when the frequencies are in some resonant conditions [Win+98; MSJ03].

8.2.3 Transport results

In this subsection I describe the performance of different transport waveforms applied on different ion chains and how the transport requirements were managed. Assessment of the transport waveforms is carried out in different ways: here I focus on the after-shuttling phonon distribution, while in Sec. 9.1 I consider the degradation of motional coherence, which is essential for interferometric measurements of motional states. Motional excitation is generally measured by cooling down the ion chain close to the ground state in the experimental zone, initializing the internal state, triggering a transport event, keeping the system static for an idle waiting time and subsequently triggering the previous transport event in reversed order, returning to the original configuration. Finally, the phonon distribution is probed, which is performed by driving a blue or red sideband transition, which correlates the vibrational state to the spin as described in Sec. 3.1, followed by a detection of ions internal state. An example of this protocol for a mixed-species ion crystal is shown in Fig. 8.2.

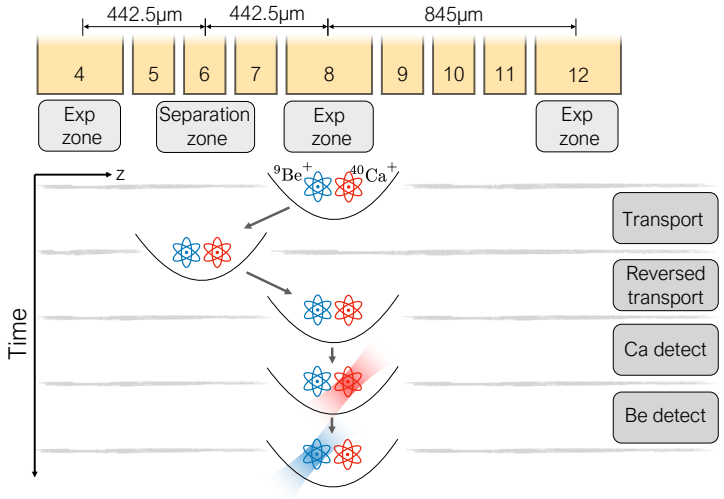

Figure 8.2: Spatial and temporal schematic of the transport experiments. One row of the segmented DC trap electrodes is shown. Single $^{9}Be^{+}$ and $^{40}Ca^{+}$ ions are shown as blue and red icons, respectively. The positions of the ions at different steps of the experimental protocol are indicated.

Heating rate

Ions confined in a Paul trap are continuously subjected to heating due to technical noise, anomalous heating and other sources depending on the system [Bro+15]. The resulting heating rate scales as [Hom13]:

$$\Gamma_h(\omega) = \frac{e^2}{4\hbar\omega_\alpha} S_{E,\alpha} \tag{8.6}$$

where:

$$S_{E,\alpha} = 4\int_0^\infty \xi_\alpha(t)\xi_\alpha(t+\tau)\, e^{i\omega_\alpha \tau} d\tau \tag{8.7}$$

$$\xi_\alpha(t) = \vec{E}(t) \cdot \left(\sum_{j=1}^{3N} \frac{\vec{e}'_{j,\alpha}}{\sqrt{m_j}} \right) \tag{8.8}$$

where $E(\vec{t})$ is the electric field and $\vec{e}'_{j,\alpha}$ is the α normal mode eigenvector component along direction j. $S_{E,\alpha}$ reduces to $S_E(\omega_\alpha)/m$ for a single ion of mass m affected by an electric field noise spectral density of $S_E(\omega_\alpha)$. This was characterized in the segmented 3D Paul trap. As described in [Mar20], in the experimental zone the frequency of the axial vibrational mode of a single calcium ion was adiabatically changed from $f_z = 1.1\,\text{MHz}$ to a desired f'_Z, where the ion was left for a variable waiting time, for then returning to the original configuration and measuring the final thermal state mean phonon number using the blue sideband method. By repeating the measurement for different waiting times, one can compute the derivative of the mean phonon number for specific values of f'_Z. The result of this measurement is shown in Fig. 8.3, where the data fit gives a scaling of:

$$\Gamma_h(f_z) = 1/f_z^\alpha + c, \quad \alpha = 5.84(5), \quad c = 48(5)\,1/\text{s} \tag{8.9}$$

where f_z is in units of MHz. Given that $\alpha > 2$ this indicates that the electric field noise spectral density is affected by strong low-frequency components. For motional frequencies higher than 1 MHz, we extrapolate the heating rate from Eq. 8.9, as we expect to not have strong electric field noise components in this regime. The measured electric field noise

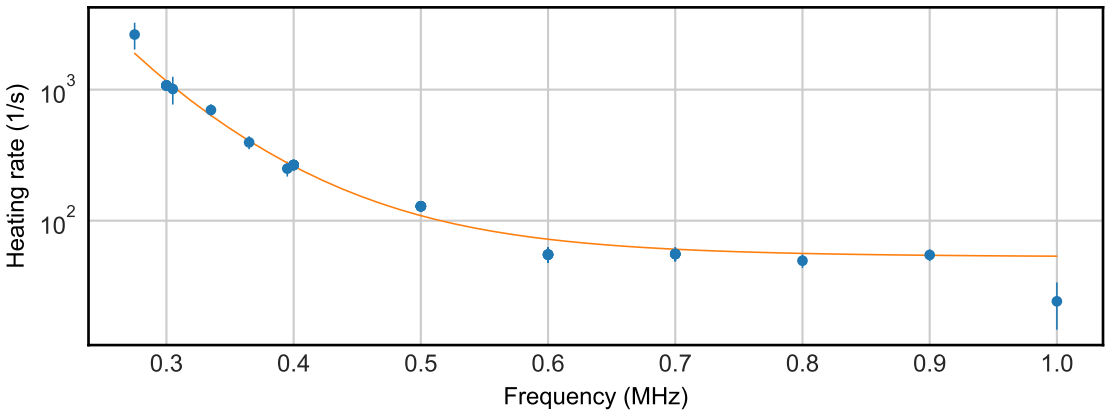

Figure 8.3: Heating rate measurement as a function of the axial vibrational mode frequency for a single calcium ion trapped in the experimental zone. The solid line is a fit of the datapoints, resulting in a scaling of $\Gamma_h(f_z) = 1/f_z^\alpha + c$, where $\alpha = 5.84(5)$ and $c = 48(5)\,1/\text{s}$. Data was acquired with Matteo Marinelli and the plot is taken from [Mar20].

spectral density for a single ion can be rescaled to account for an ion string according to Eq. 8.8. While performing the experiments of transport and separation of a Be–Ca crystal discussed in the next sections, it was noticed that one radial out-of-phase mode was subjected to a heating rate that was considerably stronger than the one predicted by Eq. 8.9, even considering the rescaling for this ion chain. In Fig. 8.4a a typical static well used for ion state preparation in the experimental zone is analyzed. The three lowest vibrational modes for the three directions of a Be–Ca crystal are highlighted. The mode at the frequency of 1.42 MHz is oriented between the DC electrodes. The value of the heating rate for this mode was estimated to be around ~ 3000 quanta/s, which is much higher than values found for the axial mode. To understand the reason behind this, in another experiment a Be–Ca crystal was confined in the static potential configuration shown in Fig. 8.4b, which has a similar radial frequency of 1.41 MHz, but oriented along the RF electrodes. The heating rate of this mode was measured, obtaining a value of 79(17) quanta/s, revealing that a strong source of electric field noise in the segmented 3D Paul trap is oriented between the

DC electrodes. The high radial mode high heating rate along the axis between the DC electrodes was not a limiting factor for the experiments of this thesis, so no further steps have been performed to reduce it, but it needs to be taken into account in all the situations in which there might be transfer of energy between the vibrational modes, as discussed later in this chapter.

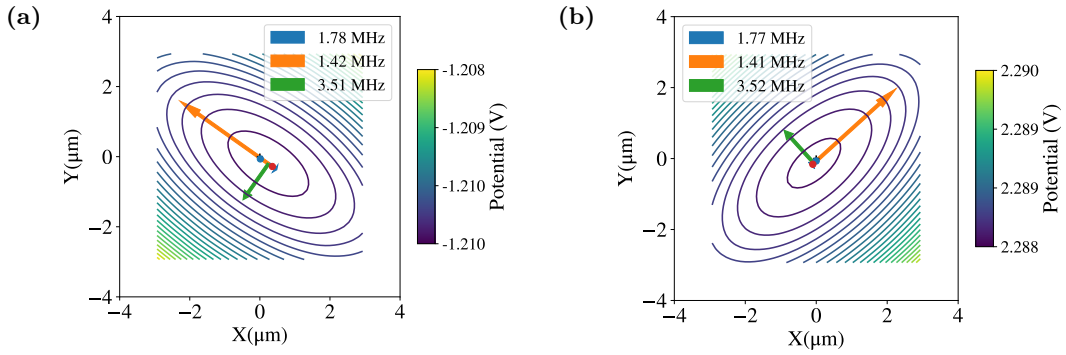

Figure 8.4: Simulation of radial trapping potentials for two different static wells. The ion crystal is composed of one $^{9}Be^{+}$ (in blue) and one $^{40}Ca^{+}$ (in red). The lowest frequency vibrational modes for each direction are shown, where the blue is related to Z1, the orange to Y2 and the green to X2. The arrows indicate the direction of the modes and the length is proportional to $^{40}Ca^{+}$ participation. The ions are slightly tilted radially due to the low radial confinement compared to the axial one.

Single-species transport excitation

Once the parameters of the transport waveform cost function (Eq. 7.11) are experimentally optimized, the single $^{40}Ca^{+}$ transport excitation can be measured. In the PhD thesis of Vlad Negnevitsky [Neg18] it is reported that adiabatic transport waveforms with axial frequency higher than 1 MHz induce an axial excitation that is less than 0.2 quanta. For frequencies lower than 500 kHz, the mode gets excited by several quanta, which can be attenuated by transporting faster than 4 m/s. For $^{9}Be^{+}$, the same transport waveforms induce lower excitation due to higher frequencies. This data was taken with trap electrode filters with a cutoff of 260 kHz. Since then, the cutoff frequency has been lowered down to 68 kHz, but no appreciable difference in behaviour was observed. Instead, additional characterization has been carried out. Adiabatic transport of single $^{40}Ca^{+}$ ions with axial vibrational modes lower than 1 MHz induces an axial excitation of several quanta. Strong heating might be caused by the lack of a proper electrical connection to parts of the DC electrode number 11, as noted in Sec. 2.2. In one experiment a single $^{40}Ca^{+}$ was confined with an axial frequency of 1.4 MHz, shuttled from the central experimental zone to the right one and back, covering 1690 μm in 1732 μs (see Fig. 8.2), and the entire process excited the axial mode by ~ 4 quanta. Transport of longer single-species chains of up to 7 ions performs reliably without losses and additional adjustments, but no detailed characterization of transport of these longer strings has been performed.

Mixed-species transport excitation

The transport of mixed-species ion chains has been extensively studied and improved during the work of this thesis. Achieving low excitation adiabatic transport from the central experimental zone to the left splitting zone was important, covering a distance of 442.5 μm, as shown in Fig. 8.2. As reported in [Mar20], this was first tested by shuttling a Be–Ca

crystal, with $^{9}Be^{+}$ on the left and $^{40}Ca^{+}$ on the right, with a waveform in which the DC offset d was gradually ramped from d=1.4 V down to d=−1.5 V, while the simulated axial frequencies are $f_{Z1} = 1.77$ MHz and $f_{Z2} = 4.59$ MHz, as shown in Fig. 8.5(a). The change of DC offset was needed as in the central experimental zone the cooling laser had better projection onto the radial modes for an offset of 1.4 V, while in the left splitting zone the lower DC offset was used to achieve higher confining frequencies during separation. Due to the importance of this waveform in later separation experiments, it will be referred to as T0 waveform. After a round trip transport of 1 ms, the axial in-phase mode Z1, axial and radial out-of-phase modes Z2 and Y2 got excited by roughly $\Delta\bar{n}_{Z1} = 0.71(6)$, $\Delta\bar{n}_{Z2} = 0.49(3)$ and $\Delta\bar{n}_{Y2} = 4.82(72)$ quanta. The intense excitation of the mode Y2 is due to the strong heating rate affecting low-frequency radial modes aligned along the DC electrodes, described in the previous section.

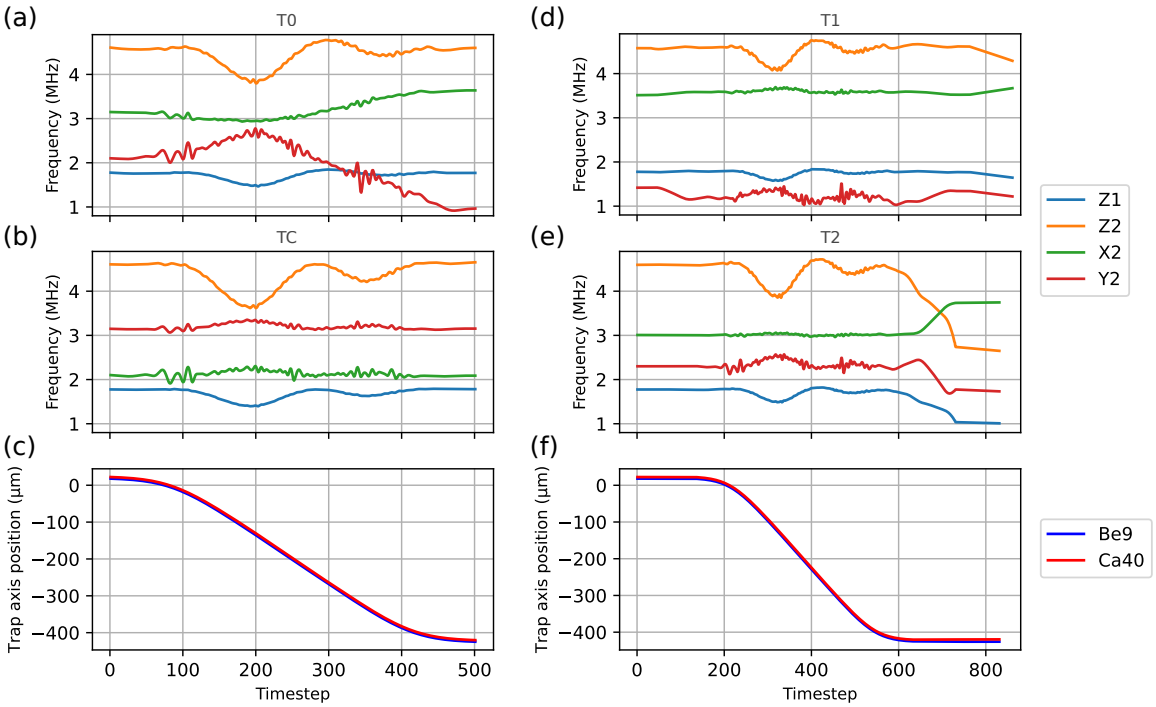

Figure 8.5: Analysis of the most relevant transport waveforms discussed in the text, performed with Pytrans 2. On the top, the simulation of the lowest four energetic vibrational modes' frequencies for a Be–Ca chain for (a) T0, (b) TC, (d) T1 and (e) T2 transport waveforms are shown. On the bottom, the simulated position of the ions along the trap axis as a function of the waveform timesteps for (c) T0 and TC, for (f) T1 and T2 are shown. Waveform T1 has 30 more timesteps than T2, but the position of the ions remains invariant in the final samples and is thus not indicated. The timestep duration depends on the slowdown (see Sec. 5.2), but we typically set it to 0.81 µs, unless stated otherwise, such that T0 and TC take around 405 µs, while T1 requires 697 µs and T2 requires 672 µs. The other mode frequencies are not shown as they are higher than 10 MHz and are not considered in the analysis of the text. The frequencies show small ripples that are an artifact of Pytrans 2 simulation and not physical.

In a second transport waveform, denoted as TC and analyzed in Fig. 8.5(b), the DC offset was kept constant to a value of d=1.4 V, with axial frequencies similar to above, and the final mode temperature showed better results as $\Delta\bar{n}_{Z1} = 0.21(3)$, $\Delta\bar{n}_{Z2} = 0.01(2)$ and $\Delta\bar{n}_{Y2} = 0.04(5)$ quanta. The low excitation of mode Y2 is due to its orientation along the RF electrodes. Although TC offered an improvement, the DC offset at the splitting zone

was too high for separation. Moreover, it was noticed that, after a round trip, the order of the ions was systematically set to Be–Ca, independent of the initial configuration. This was attributed to the presence of radial stray fields, which displace the ions radially by an amount which is proportional to the mass, as shown in Eq. 2.18, and was inducing a systematic reordering. We also noted that the stray fields change with the DC electrode voltages, as described in Sec. 6.2.3, most likely due to discrepancies between the trap model and the real trap. In all the experiments described so far the compensation of the stray electric fields was only calibrated at the start of the sequence and left unchanged for the remaining part, being unable to prevent reordering of the ions.

In a third transport waveform, referred to as T1, the DC offset was set to a constant value of d$=-1.2$ V for most of the time and was ramped down to d$=-1.5$ V in the last steps. In this way, the radial modes could be properly cooled at the start, while keeping the Be–Ca axial modes unchanged and Y2 mode higher than 1 MHz. We also aimed to implement time-varying compensation for the stray electric fields synchronously to the transport events. This was not possible initially, as the shim voltages were controlled by the AD5371 DAC, which has a sampling rate of 540 KSPS, slower than the 100 MSPS of the DEATHs. For this reason, 4 DEATH outputs were disconnected from the DC electrodes 14-15-29-30, and were then grounded, since they are not involved in the experiments of this section. These DEATH controllers were connected to the 4 shim rows, commonly controlling all the electrodes of each row. Afterwards, the stray fields were compensated at the start, middle and final step of the transport waveform and the compensation voltages were linearly interpolated between these values. This was enough to maintain the initial order of the ions (Be–Ca or Ca–Be) along the entire sequence, which was verified by separating the ions at the end, excluding a possible double reordering that could have happened during a round trip. At this point, it was important to characterize the heating caused by the transport waveform T1. It was found that the axial mode Z1 was excited by coupling to the radial mode Y2, which is subjected to a strong heating rate as already mentioned. This was happening because the two vibrational modes were getting closer to each other by less than 100 kHz and were also coupling. This was found to happen when the ions were positioned close to the gap between electrodes 7 and 8, in which the confining well cannot keep the frequencies constant with the voltage limits of our system. A first attempt to mitigate the coupling was to change the shim voltages during the crossing, similar to the approach shown in [Bla+11] where the authors employ shim electrodes to maintain a constant orientation of the modes and, consequently, minimize their coupling. This showed an effect, but no clear improvement was obtained. A more successful approach was to modify the transport waveform to increase the frequency gap between the modes Z1 and Y2, by lowering the potential offset, leading to the modes not coming close to each other. The initial and final conditions were not changed and they were connected to the intermediate potential offset configuration by a smooth transition. This offset was experimentally tweaked and the best results were obtained with a value of d$=-1.4$ V. This waveform made it possible to perform a Be–Ca round-trip transport in 1.08 ms with a thermal excitation of $\Delta\bar{n}_{Z1} = 0.60(5)$ quanta. It is important to take into account that fluctuations in the AWG voltage calibrations make the measured excitation slightly change thus the transport performances need to be checked periodically. In the experiments of this thesis, it was necessary to set the voltage offset to -1.55 V at a different point of the waveform T1 in which the modes Z1 and Y2 get close a few months after the initial calibration to counteract these drifts, obtaining a round-trip thermal excitation of $\Delta\bar{n}_{Z1} = 0.82(8)$, $\Delta\bar{n}_{Z2} = 0.36(7)$ in 1.39 ms. While doing so, it was noted that the minimum frequency gap between the modes Z1 and Y2 necessary to nullify any phonon transfer for

a Be–Ca crystal is around 230 kHz. This value was then kept as a reference and taken into account for other waveforms too. The calibration of the frequency trajectories not only depends on the number of ions for each species but might depend also on their order due to the presence of pseudopotential gradients and anharmonicities that shift the modes [Mar20]. The T1 waveform was tested for a Ca–Be crystal (so with $^{40}Ca^{+}$ on the left and $^{9}Be^{+}$ on the right) and the required offset for enlarging minimum frequency gap was −1.45 V, instead of −1.55 V. The final configuration of the waveform T1, including the changes in the offset to increase frequency gaps, is the one shown in Fig. 8.5(d). Due to the variations introduced to the parameter trajectories of T1 described so far, the stray fields were compensated at an increasing number of points of up to 11, to prevent any reconfiguration of the crystals.

Once waveform T1 was characterized, we generated a new transport waveform T2 as shown in Fig. 8.5(e), in which the frequency of mode Y2 was maintained throughout to be higher than Z1, motivated by the separation experiment described in Subsec. 8.3.6. Several requirements had to be satisfied at the same time for this waveform, reducing the available parameter space size. Firstly the lowest axial frequency mode Z1 for Be–Ca had to be higher than 1 MHz, as described before. During transport, mode Y2 should be at least 230 kHz higher than Z1, while minimizing the number of intersections with Z2, the latter being 2.6 times larger than Z1 for a harmonic well (see Eq. 2.32). Similarly to the previous waveforms, the radial modes of the initial sample should have the same projection onto the cooling laser, while connecting to the low DC offset required for the separation waveform at the end. The waveform T2 was able to satisfy most of these requirements, and the position of the ions follows the smooth trajectory described by Eq. 8.4, while the frequencies and offset of d=0 V are not changed until the ions reach the splitting zone and then are linearly ramped to a specific configuration. The performance of T2 was tested in different ways. Initially, we measured a Be–Ca round-trip thermal excitation of $\Delta\bar{n}_{Z1} = 0.46(3)$, $\Delta\bar{n}_{Z2} = 0.59(7)$ and $\Delta\bar{n}_{Y2} = 1.07(27)$ for a slowdown of 80 (which is the sample holding time, see Sec. 5.2), as for the previous transport waveforms, requiring a transport duration of 1.34 ms. The transport duration does not include an additional wait time of 150 µs applied after each transport event to ensure the stabilization of the voltages, which was used for this and the next measurements. These results show a low transport excitation. For the Y2 mode, the heating rate contribution is 1.07(27) quanta in 1.34 ms, which we interpret as being due to a reduction of Y2 heating rate down to ∼ 800 quanta/s due to the higher frequency of 2.28 MHz.

In another experiment, the timescale of the whole Be–Ca round-trip T2-T2^{-1} was scanned by changing the waveform slowdown, and the final excitation of the axial modes was measured, obtaining the results shown in Fig. 8.6. Here the data shows a low thermal excitation of $\Delta\bar{n}_{Z1} = 0.16(2)$ and $\Delta\bar{n}_{Z2} = 0.14(2)$ quanta for a single-way transport duration down to 46 µs (slowdown of 5), where the ions are shuttled at an average speed of 9.7 m s^{-1}. For faster operations (slowdown of 4), the motional population suddenly shows a combination of coherent and thermal fractions for mode Z1, indicating non-adiabatic excitation. The phonons relative to the data point of shortest duration have a thermal contribution of $\bar{n}^{th}_{Z1} = 0.04(6)$ and a coherent contribution of $\bar{n}^{coh}_{Z1} = |\alpha|^2 = 3.36(10)$ phonons. For even shorter transport durations, the coherent displacement increases and the sideband analysis becomes challenging, for this reason they are not shown in the plot. Diabatic changes to the curvature and ion position during transport might induce squeezing as well as coherent displacement, and the rise of these effects can generally be simulated by analyzing T2. In an attempt to quantify whether to expect squeezing during transport, we calculated the adiabatic parameter of Eq. 8.5 is satisfied throughout the whole process. For the fastest

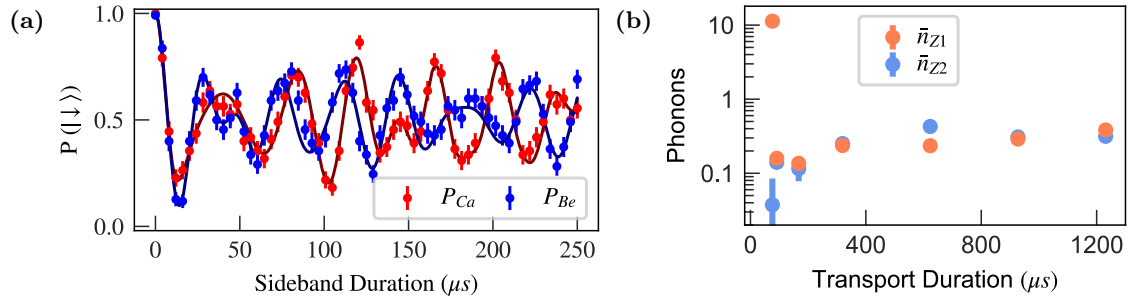

Figure 8.6: (a) Example of extrapolation of phonon population in the axial motional mode of $^{40}Ca^{+}$ (red) and $^{9}Be^{+}$ (blue) after a transport sequence. Datapoints are fit with the thermal phonon distribution of Eqs. 4.7 and 2.46 (solid lines) and mean phonon numbers of $\bar{n} = 1.40(8)$ for the calcium ion and $\bar{n} = 1.44(9)$ for the beryllium ion are extracted. (b) Excitation of the axial modes after the transport protocol T2-T2^{-1}. Mean phonon numbers are plotted as a function of the total protocol time and they are composed by the sum of the thermal and coherent contributions. The plots are also shown in [Lan+24].

data point of Fig. 8.6 we simulated a value of $\delta \leq 0.04$. Moreover, no sudden change in δ as a function of the transport duration is visible. Regarding the coherent displacement, we simulated the classical ion dynamics using Pytrans and projected their displacements and velocities at each timestep onto the normal modes as described in Sec. 2.3, from which we computed the energy of each mode and converted it into phonons. In the diabatic transport regime, the simulation showed a strong variation of the final phonon number depending on the slowdown, even including the effect of the out-of-vacuum low-pass filters, which slow and distort the resulting transport potentials. This suggests that the transport waveform needs to be modified to be robust in the diabatic regime [Bow+12; Wal+12], without excluding a possible contribution coming from an imperfect control of the trapping potentials.

Waveform T2 was used to transport a reversed order Ca–Be crystal for a round-trip transport time of 1.2 ms, obtaining a thermal excitation of $\Delta\bar{n}_{Z1} = 0.57(5)$ and $\Delta\bar{n}_{Z2} = 0.20(3)$ quanta, showing similar results to the Be–Ca transport.

Larger ion crystal transport

After an extensive study of transport and separation with two-ion chains, we extended this work by transporting three- and four-ion mixed-species crystals. For the former, we trapped both Be–Ca–Be and Ca–Be–Ca and we could readily use waveform T2 to transport them, for which the vibrational modes for the first sample are shown in Tab. 2.5. Thanks to the separation waveform, we could also verify that the order of the ions is maintained after a single transport event, proving that the same stray field compensation used for two-ion chains works for these crystals too. In these configurations, no additional characterization of the transport process was performed. We also performed a similar test with a Ca–Be–Ca–Be ion crystal. In this configuration, it was found that the first sample of T2 did not allow for efficient cooling of the ions, requiring frequent uses of the recrystallization sequence described in Subsec. 7.2.1 for initializing the state of the ions. For this reason, T2 was substituted with a transport waveform of lower axial trap curvature and DC offset, corresponding to an axial in-phase mode frequency for Ca–Be–Ca–Be ion crystal of $f_{Z1} = 1.274$ MHz, as shown in Fig. 2.6, and a DC offset of $d = 0$ V. This allowed a more efficient cooling but required a different transport waveform. The new one kept the ions confined in a similar potential well during the whole transport from the central experimental zone to

the left splitting zone, where the potential was linearly ramped to connect to the separation waveform. During the whole process, the stray field compensation was performed by using the same shim potential configuration of the T2 waveform and, despite the different DC electrode voltages, it was possible to maintain the order of the ions, which was verified by separating them.

8.3 Separation

The first demonstration of a two ion crystal adiabatic separation in a segmented 3D Paul trap for quantum computing was reported in [Row+02], which was also employed in more complex experiments in [Bar+04]. Diabatic separation of ion chains was discussed in [Bow+12; Rus+14]. Interesting analyses about this process can be found in [HS05; Kau+14]. In this section I give an overview of how the parameters for the separation waveforms were chosen and optimized in the experiments reported in this thesis, and I describe the obtained results.

8.3.1 Separation trajectory

As discussed in Subsec. 7.2.1, the separation waveform is characterized by four time-varying parameters $\{\alpha, \beta, \gamma, \delta\}$. Here I describe how the trajectories of these parameters have been chosen according to previous work described in more depth in the thesis of [Neg18].

Firstly the trajectory of $\alpha(t)$ is chosen. At the initial time t_0, $\beta_0 \simeq 0$ and $\alpha_0 = 5 \times 10^6$ V/m^2, such that the single calcium axial frequency, computed from Eqs. 7.12 and 7.4, is $\omega_0 = \sqrt{\alpha_0 2e/m_{CA}} = 2\pi \times 780\,\text{kHz}$. This value is chosen arbitrarily halfway between the minimum axial frequency experienced during the separation process and the usual one of the transport waveforms, which will be connected by a linear interpolation. At the final time t_f, β_f is kept as high as possible while $\alpha_f = -\alpha_0 = -5 \times 10^6$ V/m^2. In between, the parameter trajectories are chosen to minimize motional excitation. As discussed before, β is kept as high as possible. In the meantime, in order to minimize impulsive acceleration around the critical point, the waveform is re-parameterized in terms of the ion separation distance $s(t)$, which gives $\alpha(t)$ by solving Eq. 7.13. This is done in different steps:

- A trajectory of α is defined between α_0 and α_f. This trajectory is composed of three linear segments of different slopes and 100 points each, where the second part is centered around $\alpha = 0$ and is less steep.
- For each point k of the trajectory of α, the cost function of Eq. 7.19 is minimized by the solver and returns a set of voltages $\vec{v}[k]$ and the simulated attainable values of $\alpha[k]$ and $\beta[k]$. The latter two values are used to determine an estimate of the attained ion separation $s[k]$.
- Since $s[k]$ is monotonic with respect to $\alpha[k]$, a 4-th order spline is used to interpolate the coordinate sets $(x, y) = (s[k], \vec{v}[k])$, obtaining a re-parametrization of the voltages $\vec{v}(s)$ as a function of separation distance s, instead of time.
- The separation distance trajectory between the initial (s_0) and final (s_f) values is chosen according to a power-law function [Kau+14]:

$$s(t) = s_0 + \tau(t)^\epsilon \, (s_f - s_0) \tag{8.10}$$

with the normalized time $\tau = (t - t_0)/(t_f - t_0)$ and $2 \leq \epsilon \leq 3.5$. For the mixed-species experiments described in this thesis, the separation distance changes from $s_0 \simeq 7\,\mu\text{m}$

to $s_f = 120\,\mu\text{m}$, employing an exponent of $\epsilon = 3$, which is chosen due to the trade-off between minimizing the time in the shallow well and ion acceleration. The computed parameter trajectories are shown in Fig. 8.7.

Finally, τ is chosen at 300 evenly-spaced points, at which $s(t)$ and, in turn, the voltages $\vec{v}(t)$ are directly calculated from the spline function, obtaining a voltage matrix that is the waveform.

Experimentally it was found that the presence of stray axial potential curvature induced an additional second-order term in the quartic potential, which shifts the time at which the critical point happens. Since this is uncontrolled, there is a possibility that this modifies the separation distance trajectory and might induce impulsive acceleration, increasing axial motional excitation. In order to mitigate this phenomenon, the separation waveform can be linearly combined (using the routine described in Subsec. 5.2.2) with a second waveform that offsets the axial curvature around the separation region-of-interest. This waveform, referred to as *axial potential curvature waveform*, smoothly adds 1 V to the electrodes at the center of the separation zone (electrodes 6 and 21). The weight of this waveform, corresponding to a multiplication of it by a dimensionless factor, is experimentally adjusted such that the critical point happens at the correct time.

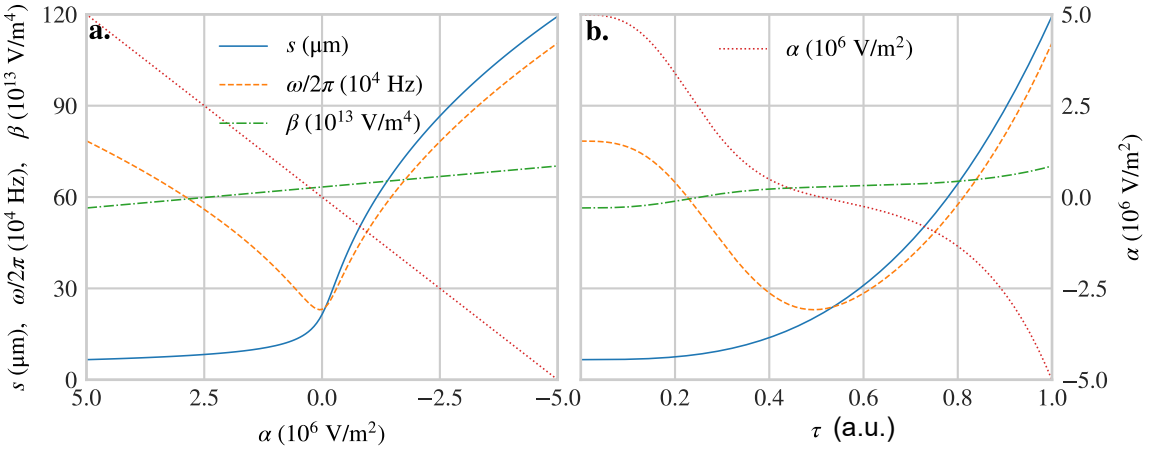

Figure 8.7: Parameter trajectories of the separation process. Ion separation distance s, axial in-phase motional frequency ω for a Ca–Ca crystal and polynomial coefficients α and β are plotted as function of **a.** α and **b.** normalized time τ. The critical point is located at $\tau = 0.5$, where $\alpha = 0$ and $\omega = 230\,\text{kHz}$. The plot is taken from [Neg18].

The axial potential gradient (or axial electric field) parameter γ is required to be set to $\gamma = 0$ for a symmetric separation. Due to imperfect potential moments and stray electric fields, it experimentally assumes a different value than that expected from simulations. Initially, several waveforms were generated with different axial electric fields in the range $-300 \leq \gamma \leq 300$ V/m and then tested experimentally. Afterward, this parameter has been set to $\gamma = 0$ in the separation waveform, and the waveform was linearly combined with a second waveform that aims to add a finely tuned axial potential gradient around the separation region of interest. This waveform, which will be referred to as *axial electric field waveform*, smoothly increases by 1 V the voltages of the electrodes on the left of the separation zone (electrodes 5 and 20) and decreases by 1 V the voltages of the electrodes on the right (electrodes 7 and 22) as shown in Fig. 8.10 (right). This adds an axial field of magnitude 1372.8 V/m. By experimentally choosing the summing weight of this waveform,

the axial field is finely tuned. As shown in the next sections, generally the required axial field magnitude is in the range of [-50, 50] V/m.

The DC potential offset parameter δ is generally not constrained, thus its cost weight q_3 of Eq. 7.19 is set to 0. Consequently, the solver let this parameter change throughout the separation waveform, reaching the lowest negative value of $-1.5\,\mathrm{V}$ at the critical point in order to maximize the axial frequencies.

In order to complete the separation waveform, the two potential wells have to be individually transported from a separation of 120 µm to 865 µm, leaving the left well in the left experimental zone and the right well in the central experimental zone. This is achieved by a two-well linear transport, whose velocity is computed as $ds(t)/dt|_{t=t_f}$ from the previous part of the waveform and is kept constant almost until the end of the process, where it gets smoothly reduced to minimize final excitations. The number of timesteps of this part of the waveform depends on the velocity and the distance to cover. The final separation waveform is shown in Fig. 8.8. Recombination of the ions is performed by reversing the separation waveform, with the possibility to adjust the tunable axial electric field if necessary.

8.3.2 Auxiliary waveforms for separation

Separation experiments of ion chains not only require the separation waveform described above but also some auxiliary ones. Firstly, the ions should be shuttled from the central experimental region to the left separation zone using a transport waveform, for which an in-depth analysis and optimization have been carried out; the results we discussed in Subsec. 8.2.3. An example of such a waveform is shown in Fig. 8.8. Second, once the separation is completed and the two potential wells are located in the central and left experimental zone, we need to detect the state the ions trapped in both potential wells. For the well located at the central experimental zone, this can be performed directly after the crystal separation. In the left experimental zone, for which no laser beam line is present, this cannot be done. Consequently, an additional waveform called *parallel transport waveform* and referred to as PT waveform is required, which transports the left potential well to the central experimental zone, while shuttling the right well to the right experimental zone, located at +845 µm. The generation of this waveform can be performed with the usual transport waveform generation routine. Thanks to this procedure, we can also operate on the ions trapped in the left potential well. A sketch of the ion positions during the sequence is shown in Fig. 8.9.

8.3.3 Assessment of the separation process

Assessment of the separation waveform performances is based on the induced motional excitation of the ions or their detection fluorescence for a specific separation time duration. The presence of high thermal excitation, non-adiabatic effects (creation of displaced coherent or squeezed states) and/or low detection fluorescence are all unwanted behaviors of badly performing waveforms.

Separation experiments are based on cooling down the ions and initializing their states in the experimental zone, then transporting the chain to the separation region, where it gets separated employing the separation waveform. The phonon distribution of the vibrational modes of the ions in the right potential well can be probed by driving a blue or red sideband transition and detecting the internal state. The ions are then subjected to the parallel transport waveform and the motional state of the ions in the left potential well is probed

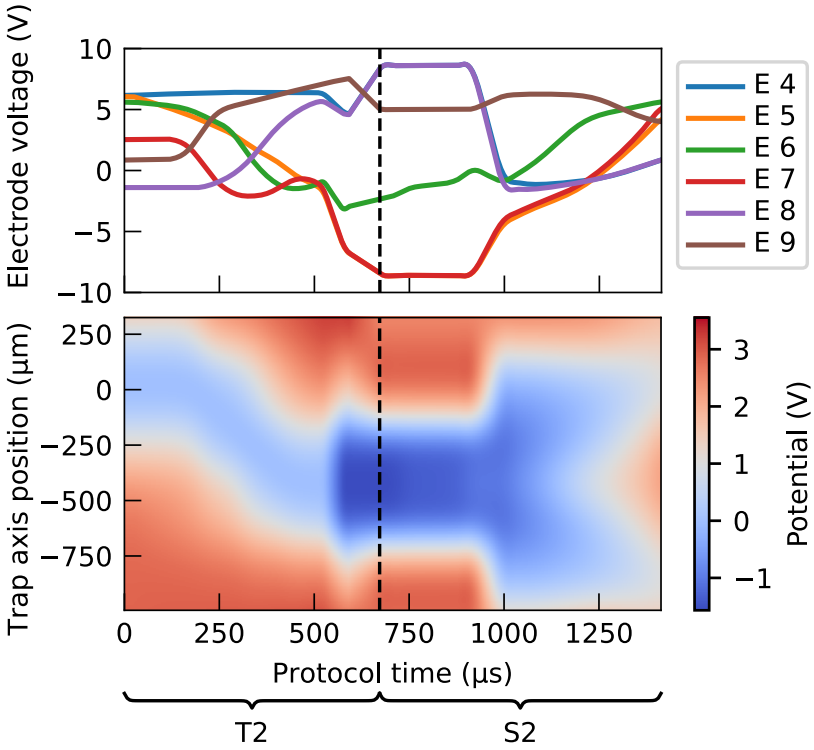

Figure 8.8: (top) Voltages applied to the relevant trap electrodes shown in Fig. 8.9 and (bottom) generated potentials at the trap axis while running the transport and separation waveforms, respectively T2 and S2 in text. The origin of the trap position axis corresponds to the central experimental zone, shown in the trap schematic in Fig. 8.9. The plots are also shown in [Lan+24].

in an analogous manner. Finally, the waveform sequence is run in reversed order, returning to the initial configuration. Here the motional state of the ions might be further probed. Generally, the phonon distributions are interrogated either after the ions get separated or after they return to the original configuration. In the first case, the experiment focuses on characterizing the performances of the separation process or calibrating some of the involved parameters, and the sequence of waveforms is also referred to as $T-S-PT$, where T stands for a generic transport waveform, S for separation and PT for the parallel transport. A sketch of this sequence is shown in Fig. 8.9. In the second case, the sequence of waveforms is also indicated as $T-S-S^{-1}-T^{-1}$, where the superscript denotes the time order direction of the waveform. This form allows transport and separation waveforms to be run until a specific sample and then reversed, in order to probe some particular feature. More details will be given in Subsec. 8.3.6.

8.3.4 Single-species separation results

In this subsection, I describe the results obtained after separating ion chains composed of only one ion species, either calcium or beryllium. Most of the experiments involved two-ion crystals, but the separation process was also tested on longer ion chains of up to seven ions.

For the Ca–Ca and Be–Be crystals, the waveform sequence T0–S1–PT was applied, where T0 is the transport waveform described in Subsec. 8.2.3, S1 is the separation waveform computed as described in Subsec. 8.3.1 and PT is the parallel transport waveform described in Subsec. 8.3.2. This sequence is experimentally optimized by running several iterations

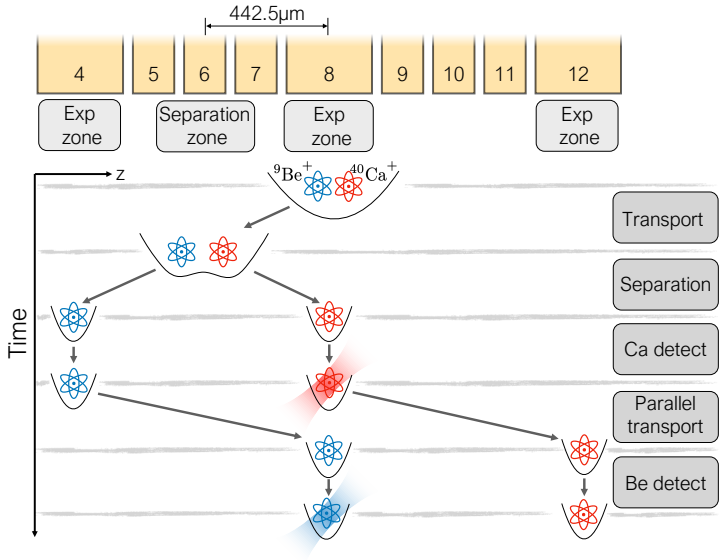

Figure 8.9: Spatial and temporal schematic of the separation experiment. One row of the segmented DC trap electrodes is shown. Single $^{9}Be^{+}$ and $^{40}Ca^{+}$ ions are shown as blue and red icons, respectively. The positions of the ions at different steps of the experimental protocol are indicated. The image is also shown in [Lan+24].

while scanning the axial electric field γ over a range of tens of $\mathrm{V\,m^{-1}}$. This term changes the number of ions distributed to each well during separation. We then detect the fluorescence of the ions in each well as a function of γ, obtaining a characteristic n-step function, where n is the number of ions involved. Any deviation from uniform steps indicates a suboptimality of the sequence, which might be relevant if it affects the region around the chosen γ. An example of this type of scan is shown in Fig. 8.10 (left): the chosen γ for the low-excitation separation sequences is the value in the middle of the step where the ions end up trapped in individual well, $-17.5\,\mathrm{V\,m^{-1}}$ in the plot. This parameter is calibrated on a daily basis in order to ensure the optimality of the process, but deviations of at most $1\,\mathrm{V\,m^{-1}}$ were observed over several weeks. Once γ has been chosen, the separation experiment can be executed again and characterization of the motional states of the ions can be performed. For the Ca–Ca chain, the vibrational states are initially cooled down close to the ground state, achieving axial motional states with mean thermal occupation of $\bar{n}_{Z1} = 0.18(2)$ and $\bar{n}_{Z2} = 0.11(1)$ phonons. After transporting the crystal for 355 µs (slowdown 70) and performing separation in 721 µs (slowdown 70), the thermal occupation of the axial mode of each ion is $\bar{n}_{W1,Z} = 1.56(6)$ and $\bar{n}_{W2,Z} = 1.63(7)$ quanta, respectively for the ion in the right (well 1) and left well (well 2). For the Be–Be chain the initial thermal occupation of the axial modes is $\bar{n}_{Z1} = 0.13(2)$ and $\bar{n}_{Z2} = 0.19(2)$ phonons, they are transported for 255 µs (slowdown 50) and separated in 518 µs (slowdown 50), resulting in thermal occupations of $\bar{n}_{W1,Z} = 0.37(1)$ and $\bar{n}_{W2,Z} = 0.51(2)$ quanta. Thanks to the results of the mixed-species separation presented later in the chapter, we can now understand the reason behind the difference in final temperatures Ca–Ca and Be–Be. By analyzing the vibrational modes of the Be–Be and Ca–Ca chains while being transported by T0, as shown in Fig. 8.11(a) and (b) respectively, we can notice that the vibrational modes Y1 and Y2 intersect with both axial vibrational modes Z1 and Z2. As mentioned before in this chapter, Y2 is affected by a strong heating rate (which might also be true for Y1 due to its low frequency, but it was

not verified). The intersection of Y1 and Y2 with Z1 and Z2, respectively, might induce energy transfer between these modes, while this is prevented in the other cases as single-species crystals in-phase and out-of-phase modes cannot couple to each other (see Subsec. 4.5.2). This phenomenon happens again when the separation waveform S1 reduces the axial mode frequencies. During separation, the energy of Z1 and Z2 are distributed among the axial modes Z of the individually confined ions. These could be the reasons behind the stronger Ca–Ca separation excitation, while Be–Be ion chains are not affected by these effects, demonstrating a lower final temperature.

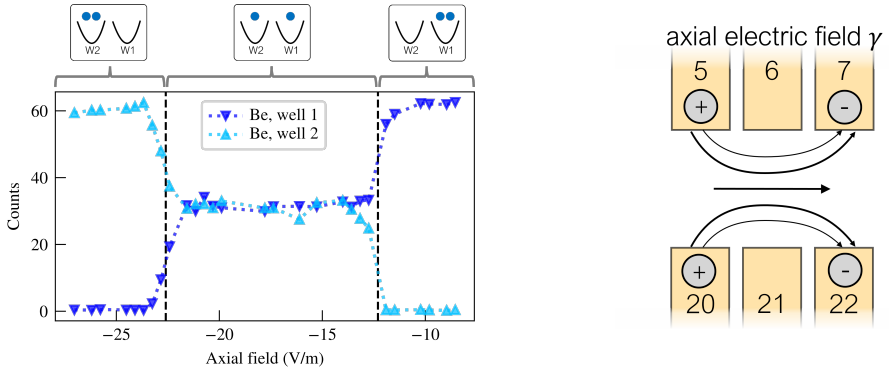

Figure 8.10: Application of the axial field γ for separating the ions. (left) Fluorescence detention of the two wells after separation of Be-Be crystal as a function of γ. On top of the plot, the schemes show the final arrangement in the different regions, delimited by dashed lines. (right) Schematic showing the signs of the shifts to the electrode voltages used to generate the axial electric field γ.

We further characterize the separation process by changing the transport and separation duration, through the slowdown, and measuring the final axial motional excitation of the ions employing a red sideband pulse. The results are illustrated in Fig. 8.12, where separation time duration is varied from 518 µs (slowdown 50) to 925 µs (slowdown 90). All the data points are obtained from a fit of a thermal population, which we found to perform reasonably well, indicating that non-adiabatic effects are not generated in this range of parameters. The general behavior has only a very small dependency on the time variation and an almost equal performance for ions stored in different wells. There is a small increase of phonons at 650 µs and 863 µs for the ion in well 1 in the Ca–Ca case, which could be attributed to experimental imperfections, e.g. imperfect calibration of γ. The nearly constant behavior of the data suggests that a more detailed characterization of the separation process can be achieved by repeating the measurement over a broader range of times, which might be considered in a future experiment.

The use of the separation experiment for single-species crystals has been also applied to ion chains of up to four $^{9}Be^{+}$ and seven $^{40}Ca^{+}$, as shown in Fig. 8.13. This works robustly and the steps are uniform in the four $^{9}Be^{+}$ chain. In the case of seven $^{40}Ca^{+}$, the steps are uneven for well 1, indicating a suboptimality, but no additional study was performed as this crystal was not used in experiments.

8.3.5 Introduction to mixed-species separation

Once the operation of single-species separation experiment was confirmed to work, we used the same waveform sequence T0-S1-PT for Be–Ca crystals. In initial experiments we were able to calibrate the axial electric field γ and separate the ions into the two final wells.

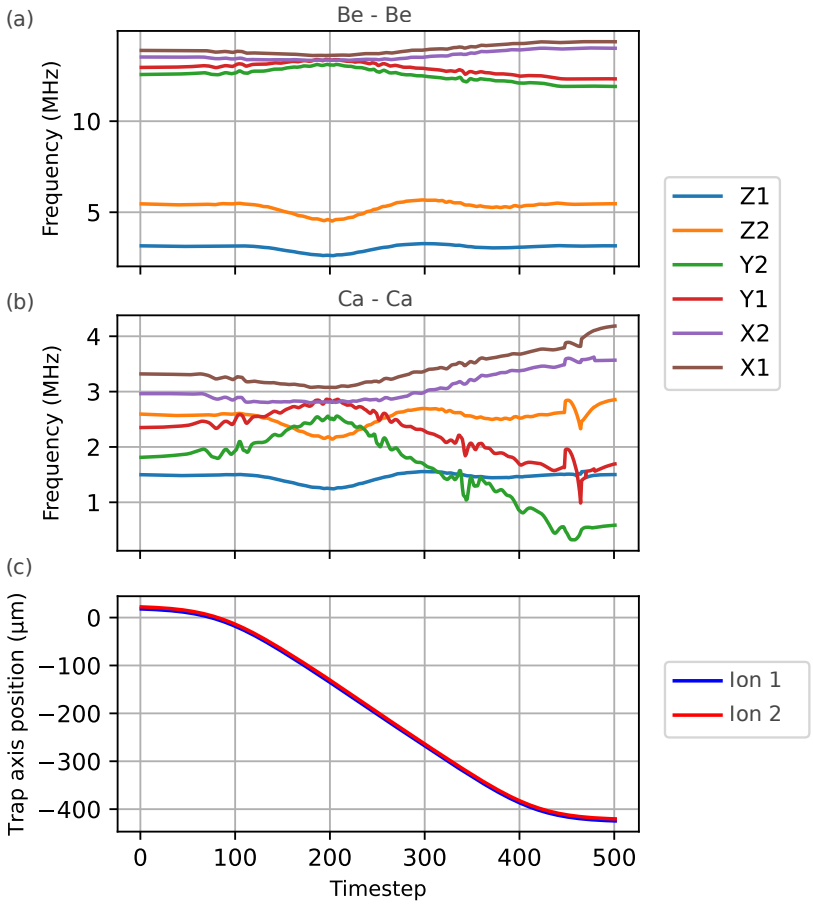

Figure 8.11: Analysis of the transport waveform T0 for single species ion chains, performed with Pytrans 2. On the top, the simulation of the vibrational mode frequencies for (a) Be–Be and (b) Ca–Ca ion crystals are shown. In (c) the position of the ions along the trap axis as a function of the waveform timesteps are simulated. The frequencies show small ripples that are an artifact of Pytrans 2 simulation and not physical.

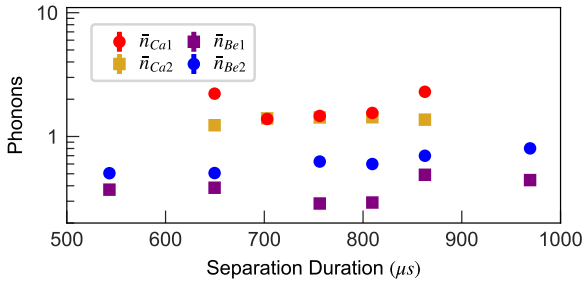

Figure 8.12: Excitation of the axial modes of Ca-Ca and Be-Be crystals after the separation sequence T0-S1-PT, scanning the total time of S1. The index 1 indicates the ion trapped in the first well that reaches the detection zone after separation, while the index 2 indicates the ion that arrives after parallel transport.

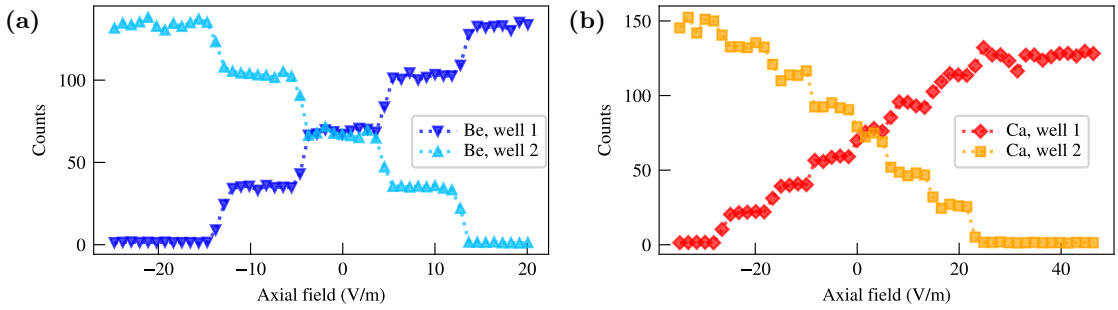

Figure 8.13: Fluorescence detection after separating multi-ion single-species chains. In particular, it is shown the separation of (a) four-ion $^{9}Be^{+}$ and (b) seven-ion $^{40}Ca^{+}$ crystal. The axial field offset has been subtracted for comparison.

However, the ions were lost after a few hundred shots and the characterization of the final phonon populations was a challenging task. To investigate the reasons behind these unwanted phenomena, the Pytrans 1 one-dimensional dynamic simulation was used to identify any suboptimality of the transport and separation waveforms. The results indicated an axial motional excitation of around $\bar{n}_{Ca} = 0.2(1)$ and $\bar{n}_{Be} = 0.05(2)$ for the typical experimental timescale. Together with the contribution of the anomalous heating, computed from the measurement of a single calcium, the code was not able to reproduce the experimental data. We also experimentally characterized the motional excitation after a round trip transport T0-T0^{-1}, obtaining the results shown in Subsec. 8.2.3. This process caused an intense excitation of the radial out-of-phase mode Y2, which was initially thought to be caused by the strong varying radial stray fields generated by the changing DC electrode voltages, which tilt the crystal by pushing the ions radially proportionally to their masses (Eq. 2.18). This led us to characterize the DC electrodes' potential moments as described in Sec. 6.2.3 to create a better model and mitigate the radial stray fields. Although showing promising results, the characterization was tested during the transport of a Be–Ca crystal, but residual stray fields were still intense enough to cause a reordering of the ions. We think that this happened because the adapted model was valid only in a small range of DC voltages, and an extension to a larger domain was experimentally demanding. For this reason, we adopted the strategy of using time-varying compensation of the stray fields through the shim electrodes, correcting for an imperfect model of the trap. It was later found that the intense excitation of Y2 was caused by the strong radial heating rate, and an improvement to the transport waveform was performed through several steps described in detail in Subsec. 8.2.3. In the next subsections, I describe the key steps that led us to solve several issues affecting the separation process when applied to a mixed-species crystal and the obtained results.

8.3.6 Mixed-species separation results

Separation improvements

The first important step involved the use of time-varying compensation of the radial stray fields while running the transport and separation waveforms. As discussed in Subsec. 8.2.3, this was an important aspect of the mixed-species transport waveform that allowed the shuttling of the crystal while avoiding unwanted and uncontrolled re-ordering of the ions, which could cause motional excitation. This calibration was performed for 12 points throughout the waveform, with lower density after the critical point, where it has reduced importance

due to the trapping of the ions in individual wells. This compensation was checked daily and it was required to be re-calibrated on a timescale of a few weeks. Subsequently, we observed that the order of the ions was maintained. Nevertheless, the re-ordering waveform was still run at the start of each shot to compensate for changes in the crystal configuration due to collisions with background gas. The excess micromotion compensation, together with the use of the improved transport waveform T1, brought the final phonon population to the limit of the regime where it could be characterized by sideband spectroscopy (around $\bar{n} \simeq 10$), which was then used for the next steps of optimization at the expense of acquiring more data.

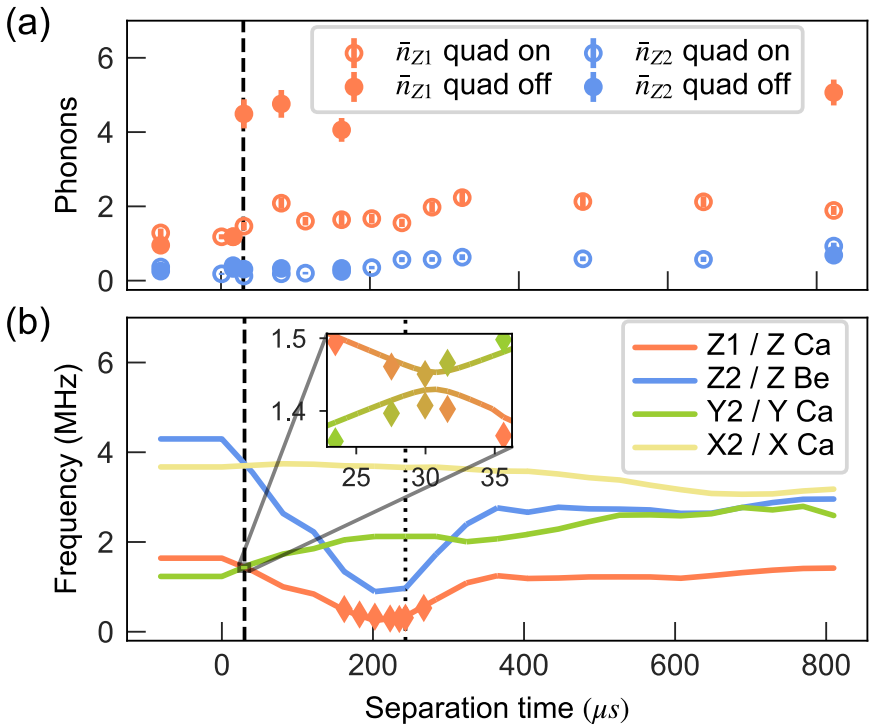

Figure 8.14: (a) Time-resolved measurement of the axial phonon populations after running the separation sequence forward up to a certain separation time, wait for an idle time of 150 µs and then execute the sequence backward. The separation waveform S1 starts at $t = 0$, with negative times belonging to the transport waveform T1. (b) Simulated (solid lines) and measured (diamond points) mode frequencies of the lowest four modes throughout the separation sequence. Uncertainties on the measured data points are smaller than the marker size. The position of Z1/Y2 mode crossing at 30 µs is indicated by the vertical black dashed line. The critical point is denoted by the vertical dotted line at 243 µs, after which the ion separation is greater than 29 µm and the normal modes smoothly become uncoupled. During this transition, their color is kept constant due to the strong uneven mode participation. The inset shows measurements and simulations close to the avoided crossing between Z1 and Y2. The plots are also shown in [Lan+24].

The second improvement involved the use of a time-resolved measurement of the phonon population in the axial modes during the separation of the Be–Ca crystal. This was performed by running the separation sequence T1-S1 up to a certain timestep, keeping the ions static for an idle time of 150 µs, which ensured the reach of the desired voltage configuration, and reversing the waveform sequence, returning to the central experimental zone. Finally, the phonon population was characterized by sideband spectroscopy on calcium and beryllium for the modes Z1 and Z2, respectively, according to their highest axial mode participation. The results for some samples of the S1 waveform are shown in Fig. 8.14

(a). In part (b), the simulated frequencies for the modes Z1, Z2, Y2 and X2 (the latter being the second radial out-of-phase mode) of S1 are shown, while the frequencies of the modes Z1 and Z2 were also measured by parametric excitation for some significant separation times. All the waveforms are executed with a slowdown of 80, high enough to avoid any non-adiabatic effect caused by the sudden truncation of the sequence. At this slowdown, the entire T1 waveform requires 697 µs and S1 is run for 823 µs. The populations measured at negative times are related to the transport waveform T1, which induces $\bar{n}_{Z1} \simeq 1.17(11)$ and $\bar{n}_{Z2} \simeq 0.18(9)$ quanta. This measurement revealed that a sharp increase in the phonon population of Z1 was occurring around 30 µs from the start of S1 (corresponding to sample 38, highlighted by the black dashed line). This is close to the expected crossing of the modes Z1 and Y2. We therefore conjectured that this induces a transfer of phonons from the radial mode (which is affected by a strong heating rate) to the colder axial mode according to the Landau-Zener-Stückelberg-Majorana theory explained in Subsec. 4.5.1. In order to control this coupling mechanism, we need to act on the coupling term Δ of Eq. 4.22. The goal was to maximize the diabatic transition probability P_D, which in turn minimizes the probability of exchanging phonons between the modes. The parameter Δ results from an off-diagonal term in the Hessian of the trapping potential. As discussed in Subsec. 4.5.2, for single-species crystals this term corresponds to a rotation of the confining potential axis with respect to the trap axis. For the mixed-species case, the presence of radial electric fields displaces the ions proportionally to their masses, resulting in a tilted configuration that changes the normal modes' orientations, producing an additional channel for introducing the coupling terms. This behavior is minimized by the radial stray field compensation mentioned before. To further reduce the coupling term, we generated a heuristic quadrupole potential by adding 1 V to electrodes 5 and 22, and −1 V to electrodes 7 and 20, as shown in Fig. 8.15 (a). This voltage is turned on before the start of S1 and turned off a few samples after the crossing point to not affect the remaining part of S1, obtaining the *quadrupole potential waveform*. A schematic of the timing at which the potentials are turned on is shown in Fig. 8.14 (d). This waveform is then linearly combined with S1 and its weight a_q is scanned to minimize the phonon population transferred to the Z mode of calcium at the end of S1, given that this ion has the highest participation in Z1. This is estimated by driving the blue sideband with a pulse significantly shorter than a pi time and then measuring the spin population, giving a proxy that indicates, for higher values, a lower mean phonon number for the final thermal state. An example of this scan is shown in Fig. 8.15 (b). This plot correlates with 8.15 (c), in which a lower coupling between the modes results in a reduced distance between the vibrational modes Z1 and Y2 at the crossing point. In the shown example, their difference is reduced down to $\simeq 11$ kHz. This became a typical regime of working, giving a probability of diabatic transition of $P_D = 0.99$ and experimentally allowing to obtain a $\Delta\bar{n}_{Z1} = 0.27(18)$ quanta after a round trip. Although the frequency difference between the modes close to the crossing can be reduced even further by individually calibrating the potentials applied to each electrode, this was not needed for the work of this experiment. For a higher minimum separation of the modes the probability P_D gets reduced. As an example, in the inset of Fig. 8.14 (b) the minimum difference without using the quadrupole waveform is $\simeq 23$ kHz, which results in $P_D = 0.7$ and induces an excitation of Z1 of $\Delta\bar{n}_{Z1} = 3.13(38)$ quanta. These results demonstrate the efficacy of the quadrupole term in decoupling the modes. Regarding mode Z2, the crossing with modes Y2 and X2 does not induce an appreciable increase in phonons, and no dependency on the quadrupole waveform weight factor is noted. This phenomenon can be associated with the high mode participation of calcium in Y2 and X2, while this quantity is low for Z2, effectively decoupling the modes by the high mass ratio of the two ion species.

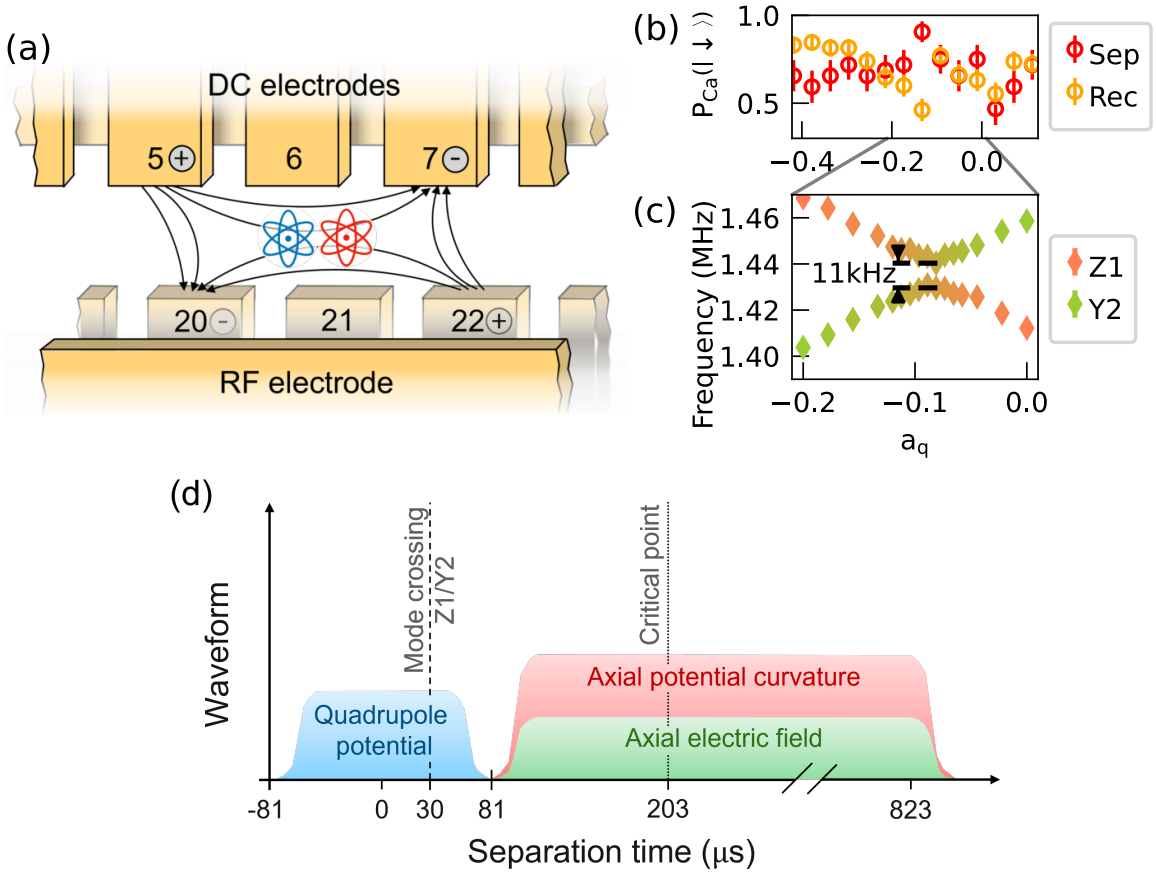

Figure 8.15: Application of a quadrupole potential for decoupling the vibrational modes. (a) Schematic showing the signs of the shifts to the electrode voltages used to generate the quadrupole potential. (b) Calibration of the quadrupole scaling factor a_q for the separation sequence (T1-S1) and recombination one (T1-S1-S1^{-1}-T1^{-1}). At the end of the two sequences, a short blue sideband pulse tuned at the axial mode Z or Z1, respectively, is driven and the calcium spin population is measured as a proxy for mode excitation. A high value indicates low excitation. (c) Measurement of the Z1/Y2 mode frequencies as a function of a_q close to the avoided mode crossing. (d) Timing of the waveforms that are linearly combined with S1. The separation waveform starts at $t = 0$ and ends at $t = 823\,\mu s$, while for negative times the ions are transported by T1.

For the other datapoints, the truncation of the separation waveform shows a small increase in the axial mode excitation right after the critical point and in the linear transport parts, which is reduced by running the waveform until the end.

Some additional aspects relate to the use of the quadrupole potential. We noticed that the calibration of the required quadrupole term needed to be performed on a daily basis, as the mode coupling is sensitive to the voltage drifts of the trap. This was a key element of this calibration that was underestimated in the first sets of data acquisition. Secondly, the weight factors for the quadrupole term were different for the separation and recombination parts of the sequence, as shown in Fig. 8.14 (b), where the recombination weight is calibrated by running a blue sideband transition on Z1 on calcium after a full round trip. We observe that not only are the required weights different, but the one used for separation is the worst choice for recombination. The reason behind this phenomenon is unclear. Another interesting aspect of the separation-recombination sequence is that the double passage through the avoided crossing creates a Landau-Zener-Stückelberg-Majorana

interferometer as described in Sec. 4.5.1. This means that, in the case of no use of the quadrupole potential, the phonon populations of the modes Z1 and Y2 are split into the two modes during separation, acquire a phase for the rest of the sequence and then interfere during the recombination. This phenomenon leads to a fluctuation of the phonon population in the two modes depending on the exact mode trajectories. A large energy gap induces a considerable dynamical phase, which relates to the population probability through Eq. 4.30. As an example, in Fig. 8.14 (a) we can estimate the dynamical phase ζ_1 of Eq. 4.29 acquired by the modes Z1 and Y2 after the crossing point at 30 µs, where we stop the waveform at 81 µs, wait for an idle time $t_{\text{idle}} = 150\,\mu\text{s}$ and then return to the mode crossing again. The dynamical phase is computed by the frequency difference of the diabatic vibrational states around the crossing point that scales as $f_{Y2}(t) - f_{Z1}(t) \simeq mt$, where $m = 14 \times 10^9\,\text{Hz}\,\text{s}^{-1}$, and the minimum energy gap of the coupled modes $\Delta/h = 23\,\text{kHz}$, where h is the Planck's constant. The total dynamical phase is then $\zeta_1 \simeq 459\,\text{rad}$, which highlights how quickly the probability of the mode occupancy changes between the data points. For this reason, the hopping of phonons between the modes is not noticeable in the acquired undersampled data. Additional analysis of this type of experiment can be found in Ch. 9.

Once the contribution of the mode crossing was characterized and controlled by exploiting the quadrupole waveform, we could focus on the performance of the entire separation and recombination processes. This was achieved by running different waveforms at a slowdown of 80, and the final excitation for different sequences involving T1, S1 (linearly combined with the axial electric field waveform, quadrupole potential waveform and axial potential curvature waveform) and PT waveforms are summarized in Tab. 8.2. The time duration of each sequence is also shown. It is important to highlight that the PT waveform required around 1.1 ms, which constituted a significant amount of sequence time, but we did not try to optimize this further as it induces an excitation of less than 0.2 quanta (for the left well, for the right one it is considerably higher due to the disconnected electrode number 11, as described in 8.2.3, but it does not affect the separation sequence). Moreover, the excitations caused by the recombination sequence T1-S1-S1^{-1}-T1^{-1} are higher than the ones for separation T1-S1-PT. While for Z mode of beryllium and Z2 of Be–Ca the mean phonon numbers are in a ratio of roughly 2 (considering the contribution of PT), this is not the case for the Z mode of calcium and Z1 of Be–Ca for unknown reasons.

The relevance of the study of mode coupling increases with the number of ions involved in the transport and separation operations. For more complex crystals, due to the higher number of vibrational modes, more mode crossings are possible which can couple phonon populations of several modes. While in the particular case of dealing with shorter ion chains, as described in this chapter, the crossing of vibrational modes can be avoided altogether by carefully designing the initial and final potential wells, this gets harder for more complex ion chains. For the Be–Ca crystal, in order to remove the crossing of the modes Z1 and Y2 (the other intersections are not subjected to coupling, as mentioned before), we had to generate a new transport waveform called T2 and a new separation waveform S2. For the former, a detailed description can be found in Subsec. 8.2.3, while for the latter it was sufficient to remove the first 100 samples of S1 (corresponding to the first 81 µs in Fig. 8.14). This ensures that Z1 and Y2 are separated by at least 380 kHz for both T2 and S2. Afterward, the performance of the transport sequence T2-T2^{-1}, separation sequence T2-S2-PT and recombination sequence T2-S2-S2^{-1}-T2^{-1} (the latter two involving the linear combination of S2 with the axial electric field waveform and axial potential curvature waveform) was

Sequence	Duration	$\bar{n}_{Z1}$	$\bar{n}_{Z2}$
T1 - $T1^{-1}$	1.4 ms	0.82(8)	0.36(7)
T2 - $T2^{-1}$	1.34 ms	0.46(3)	0.59(7)
T1 - S1 - $S1^{-1}$ - $T1^{-1}$	3.2 ms	2.26(23)	0.98(11)
T2 - S2 - $S2^{-1}$ - $T2^{-1}$	2.8 ms	3.01(20)	1.12(13)
Sequence	Duration	$\bar{n}_{Ca}$	$\bar{n}_{Be}$
T1 - S1 - PT	2.7 ms	1.85(15)	0.79(9)
T2 - S2 - PT	2.5 ms	1.40(8)	1.44(9)

Table 8.2: Mean phonon number in the axial modes of motion for different transport/separation sequences. The upper four are for forward and back operations, probing mode Z1 using $^{40}Ca^{+}$ sidebands and mode Z2 using $^{9}Be^{+}$. The lower two are mean axial excitations of the calcium and beryllium ions, with the latter measured after the PT segment. The sequence duration is the time for running the full waveform sequence.

characterized and the results are shown in Tab. 8.2. The performance for T1-S1 and T2-S2 are comparable, demonstrating the efficacy of the quadrupole potential in decoupling the modes. The sequence T2-S2-$S2^{-1}$-$T2^{-1}$ shows an excitation that is higher than the one-directional T2-S2-PT for $^{40}Ca^{+}$, with the Z1 mode being heated the most, as would be expected given that this low-frequency mode would be most affected by heating. For $^{9}Be^{+}$ the sequence T2-S2-$S2^{-1}$-$T2^{-1}$ shows lower excitation than the separation sequence only. Although the reason is unknown, we suspect that this might be caused by the fluctuations in the control voltages affecting the performance of PT. Despite this phenomenon, the results lie in an acceptable range.

Dynamic simulation

I performed a 3D dynamic simulation of the separation and recombination sequence S1-$S1^{-1}$ for a Be–Ca crystal using Pytrans 2 and computed the thermal mean phonon population of each normal mode during the entire process. Although this simulation only gives approximated results due to a high sensitivity to the actual experimental potential, we can use it to get a deeper understanding of the process. The results are shown in Fig. 8.16. The waveforms include the contributions of an axial electric field to separate the ions, an axial potential curvature and a quadrupole potential to match the experimentally measured frequencies.

In Fig. 8.16 (c) and (d) the motional states have an initial energy to simulate the induced heating due to the transport T1-T^{-1} and the heating rate of the trap. In (c) the quadrupole is such that at the avoided crossing of Y2/Z1 the strength of the coupling is higher, while in (d) the strength is reduced. The exchange of energy between Y2 and Z1 shows different magnitudes for the two cases. After recombination the interaction between the modes induces constructive interference of phonon populations in one mode and destructive in the other. By changing the time in between the two avoided crossing of Y2/Z1 or the coupling strength the distributions in the two branches can be tuned. The intersection of Y2/Z2 shows only a small exchange of phonons due to the low coupling strength. A small transfer of phonons between different modes is also visible when the frequencies are in integer ratios due to the anharmonicity of the Coulomb potential [Hom+11].

In Fig. 8.16 (e) the motional states of all modes are initially in the ground state and the increase in the energies is due to the separation and recombination processes only, which

show excitations of at most one quanta in the axial vibrational modes.

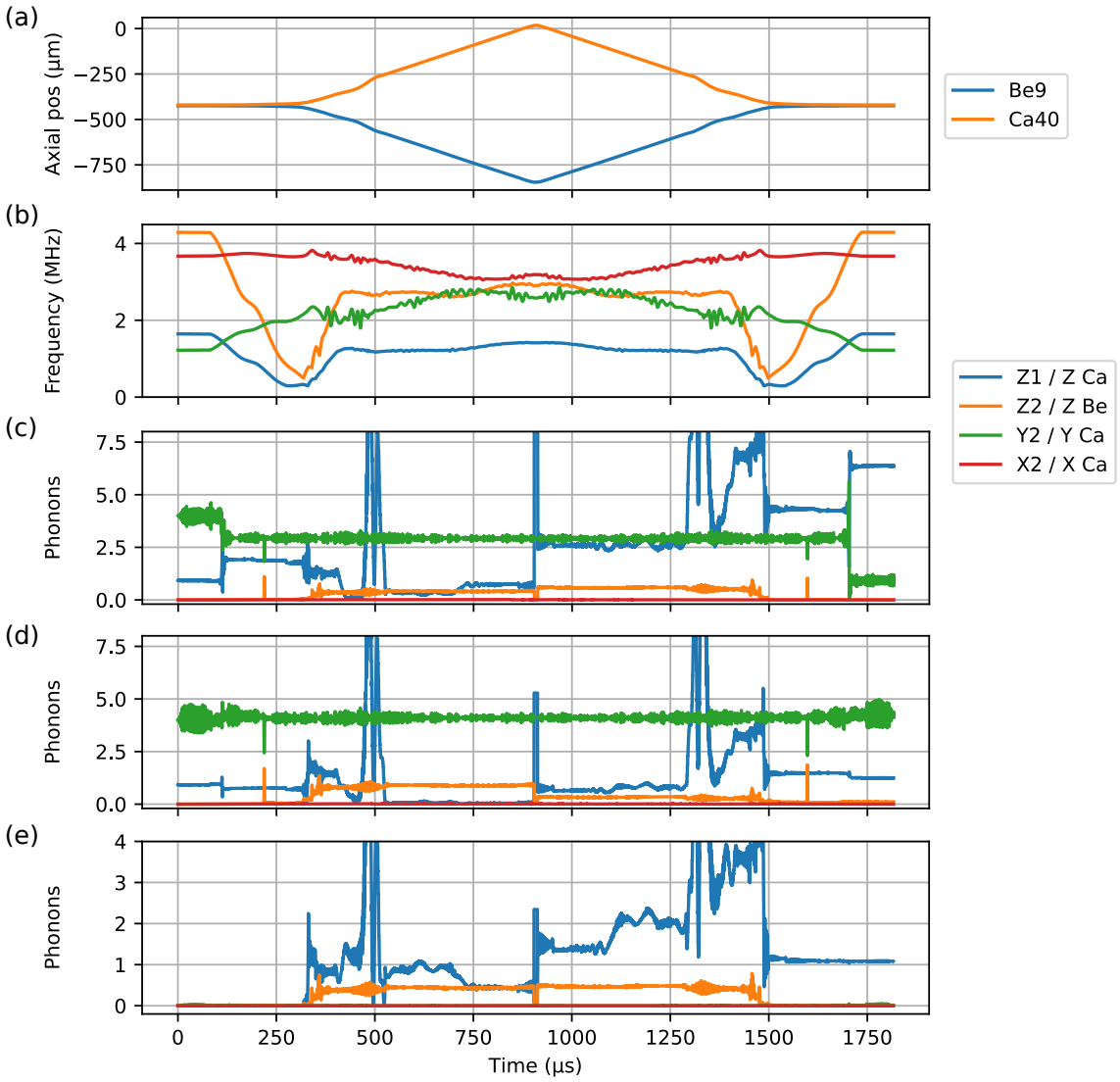

Figure 8.16: Simulation of the separation and recombination sequence S1-S1^{-1} for a Be–Ca crystal. In between the two waveforms, the ions are statically confined for 4 µs and the waveforms are run with a slowdown of 80. (a) Axial positions of the ions. (b) Mode frequencies of the lowest four vibrational modes. The small ripples are an artifact of Pytrans 2 simulation. (c) Simulation of the mean phonon numbers for the relevant modes. The initial energies are similar to the experimental ones and the quadrupole is chosen such that the minimum frequency difference between Y2 and Z1 is $\sim$ 46 kHz, so in a high-coupling regime. (d) Simulation of the mean phonon numbers for a quadrupole that induces a minimum frequency difference between Y2 and Z1 of $\sim$ 9 kHz, so in a low-coupling regime. (e) Same as (d) but for motional states initially in the ground state. For (c), (d) and (e) the excitation in between the waveforms is due to the sudden stop of S1 and was not noticed in the experiments due to the trap filters. The increase in thermal energy shown around 500 µs and 1300 µs can be attributed to the waveform solver transitioning from the separation phase to the two-well linear transport that brings the ions to their final positions (see Subsec. 8.3.1), and was not observed in the experiments.

Separation process duration

In another experiment, the duration of S2 in the separation sequence T2-S2-PT was scanned by changing the waveform slowdown, and the final excitation of the axial modes of Be–Ca was measured, obtaining the results shown in Fig. 8.17. Here the data show a low thermal excitation of $\Delta\bar{n}_Z = 1.53(9)$ quanta for calcium and $\Delta\bar{n}_Z = 1.06(8)$ quanta for beryllium for a S2 duration down to 559 µs (slowdown of 60). For a duration of 375 µs (slowdown of 40), the motional populations start to show a combination of thermal and coherent contributions, which for calcium they are $\bar{n}_Z^{\text{th}} = 0.42(15)$ and $\bar{n}_Z^{\text{coh}} = |\alpha|^2 = 0.93(4)$ phonons, respectively. Instead, for beryllium they are $\bar{n}_Z^{\text{th}} = 0.18(10)$ and $\bar{n}_Z^{\text{coh}} = 0.80(4)$ quanta. For an even shorter separation of 192 µs (slowdown 20), non-adiabatic effects become very pronounced, with $\bar{n}_Z^{\text{th}} = 0.44(14)$ and $\bar{n}_Z^{\text{coh}} = 2.64(6)$ phonons for calcium, $\bar{n}_Z^{\text{th}} = 0.31(14)$ and $\bar{n}_Z^{\text{coh}} = 0.85(5)$ quanta for beryllium. For this timescale, we calculated an adiabatic condition of $\delta \leq 0.03$ from Eq. 8.5, indicating that the resulting states should not be squeezed. These outcomes show a positive scenario: the thermal contribution is pretty low and decreases with the separation duration. Moreover, even if the coherent contribution becomes relevant at shorter timescales, it was shown in [Bow+12; Wal+12] that this term can be removed by RF de-excitation or employing sharp "kick" potentials, which could be applied in a further extension.

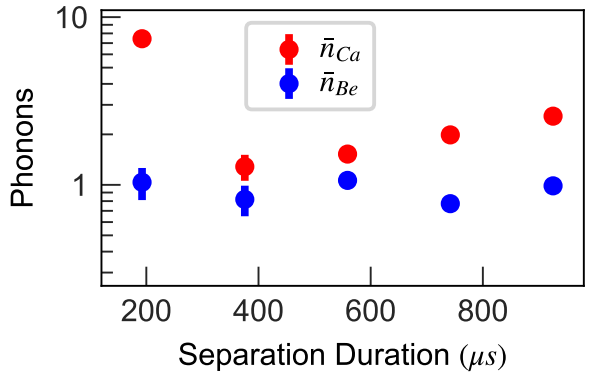

Figure 8.17: Excitation of axial modes after the separation sequence T2-S2-PT, scanning the total time of S2. Excitation is composed of the sum of the thermal and coherent contributions. The plot is also shown in [Lan+24].

Separation of Be–Ca vs. Ca–Be

Another interesting aspect of the separation process involved the comparison of the performance for different orders of the two-ion chain, namely Be–Ca and Ca–Be. By executing the separation sequence T2-S2-PT with the usual time duration of 2.5 ms on both configurations, we originally noticed very strong excitation in the case of Ca–Be, such that proper thermometry by sideband spectroscopy was challenging. The first step to investigate the reasons behind this phenomenon involved the re-calibration of the axial electric field, which changes by a few V/m depending on the exact ion crystal configuration, as shown in Fig. 8.18. This suggests the presence of a pseudopotential gradient along the trap axis [Hom13]. The separation of Ca–Be strongly improved by reducing the slowdown of the S1 waveform from the usual value of 80 down to 23, requiring a separation duration of 220 µs. In this way the resulting axial thermal excitation is $\bar{n}_{\text{Ca}} = 3.8(6)$ and $\bar{n}_{\text{Be}} = 0.24(3)$. This was achieved by using an axial field of $-31.6\,\text{V}\,\text{m}^{-1}$. We also set the axial field to a value of

$-32.3\,\mathrm{V\,m^{-1}}$, obtaining $\bar{n}_{\mathrm{Ca}} = 3.2(5)$ and $\bar{n}_{\mathrm{Be}} = 1.9(2)$, which shows an improvement on the calcium performance, but a degradation for the beryllium one.

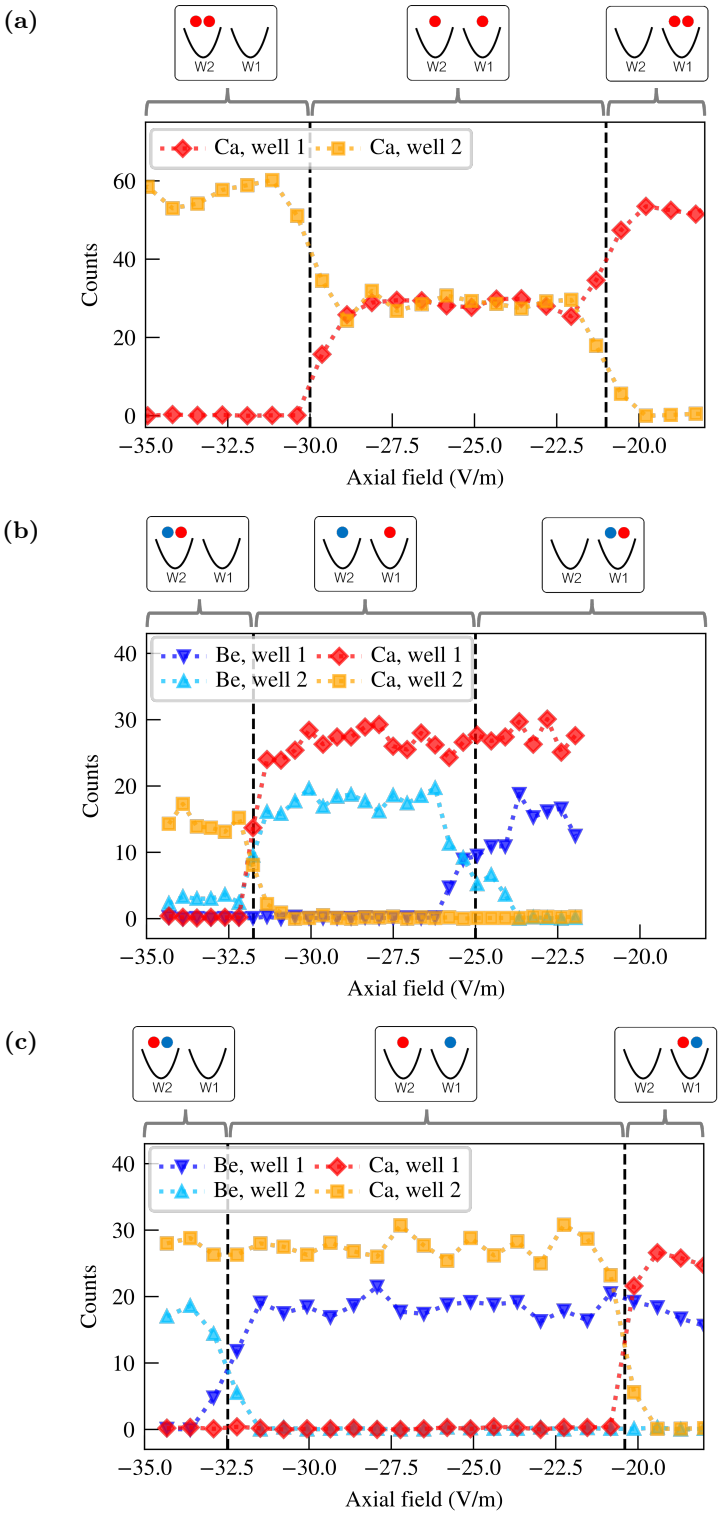

Figure 8.18: Fluorescence detention of the two wells after separation of two-ion chains as a function of the axial electric field. In particular, the crystals are: (a) Ca–Ca, (b) Be–Ca and (c) Ca–Be. Data was measured on the same day and the axial field ranges are the same for comparison.

A further study was performed by measuring the frequency and heating rate of Z1 in the two ion configurations close to the critical point, and the results are shown in Fig. 8.19. Here the minimum of Z1 frequency and the timestep at which this is reached vary depending on the ions' order. The exact reason behind this phenomenon has not been investigated, but this might be caused by anharmonic terms in the potentials (as described in [Hom+11]) or by different positioning of the ions in the two configurations. Regarding the heating rates, a large discrepancy can be noticed in the two cases, and in particular the highest value is reached for Ca–Be, despite the motional frequency being higher. Before the critical point, at similar frequencies, the heating rate is considerably lower in the Ca–Be case, while for Be–Ca it is comparable. No further studies were performed on this phenomenon, but it might be caused by an asymmetric radial orientation of the crystal induced by residual stray fields, which makes the two modes prone to different electric field noise sources. These results also highlight a discrepancy noticed when performing heating rate measurement on a single calcium ion (Subsec. 8.2.3), even after rescaling for the two-ion case (as shown in Eq. 8.8). Considering that in between the two measurements the experimental setup was modified, the electric field noise spectrum might have changed accordingly.

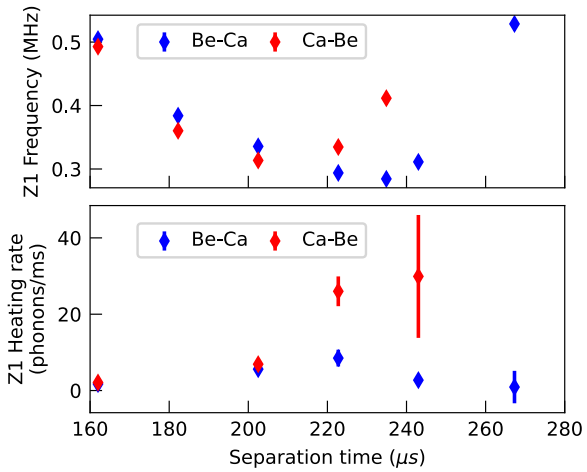

Figure 8.19: Z1 frequency (top) and heating rate (bottom) measurements for the Be–Ca and Ca–Be chains as a function of time during separation waveform S1. The critical point is at ∼235 µs for Be–Ca and at ∼203 µs for Ca–Be. The heating rate measurements are shown only at relevant separation times and where the measurement uncertainty is sufficiently low. The plots are also shown in [Lan+24].

Separation of longer mixed-species ion crystals

Once the separation of two-ion crystals was optimized, the next step involved separation of longer ion arrays. The extension to three-ion chains was performed by using the same waveforms for reordering, transport, separation (linearly combined with the axial electric field waveform and axial potential curvature waveform) and parallel transport. Consequently, we could easily load Ca–Be–Ca and Be–Ca–Be crystals and deterministically set their orders, which was maintained while running the sequence T2-S2-PT. We could then calibrate the axial electric field during separation and detect the ions in each well. The results are shown in Fig. 8.20 (a) and (b). In the Ca–Be–Ca case, the ions generally show no loss of fluorescence and the steps are clear. Only for a very negative axial field the detection counts decrease, indicating a possible nonoptimal beam alignment or excitation of the vibrational modes, but in this regime all the ions end up in the left well (*W2* in the figure) and they

are not separated. For the Be–Ca–Be chain, the steps are clear, but the fluorescence of the ions collected in the left well is low, possibly indicating beam misalignment or motional excitation. In this situation, even the fluorescence detected during the usual Doppler cooling, which happens after recombination, decreases by 1/3 and 3/4 for calcium and beryllium, respectively, suggesting that the waveforms are not optimized and a longer cooling process is required.

In another experiment, we employed a Ca–Be–Ca–Be crystal. In this case, as described in Subsec. 8.2.3, in the initial potential well the vibrational modes were not efficiently cooled. For this reason, the transport waveform T2 was substituted by one that had a lower axial trap frequency and lower DC offset. This also required a recalibration of the reordering waveform, while S2 and PT were left unchanged. Afterward, the separation experiment was performed analogously to the three-ion cases and the result is shown in Fig. 8.20 (c). Also in this case the steps are clear, and we notice a loss of fluorescence only when three or more ions are trapped in W2.

For the experiments described in this subsection, no additional measurement of the after-separation temperature of the vibrational modes was performed.

8.3.7 Next steps

Currently the adiabatic transport and separation processes applied to single and mixed-species crystals work reliably and in the low excitation regime. Faster timescales and longer ion arrays have been initially exploited and characterized.

One current limitation is that in the mixed-species separation the calcium ion is occasionally lost. This is thought to be caused by an imperfect cooling of the vibrational modes in which calcium has high participation. In the future, a better cooling scheme might be found. Moreover, diabatic transport and separation should be further studied and optimized, even by automatically designing the waveform parameter trajectories, as described for a single ion in [Ste+22]. Longer ion chains and multiple wells might also be investigated, allowing the implementation of complex algorithms involving the use of multiple qubits, without the use of extensive sympathetic recooling.

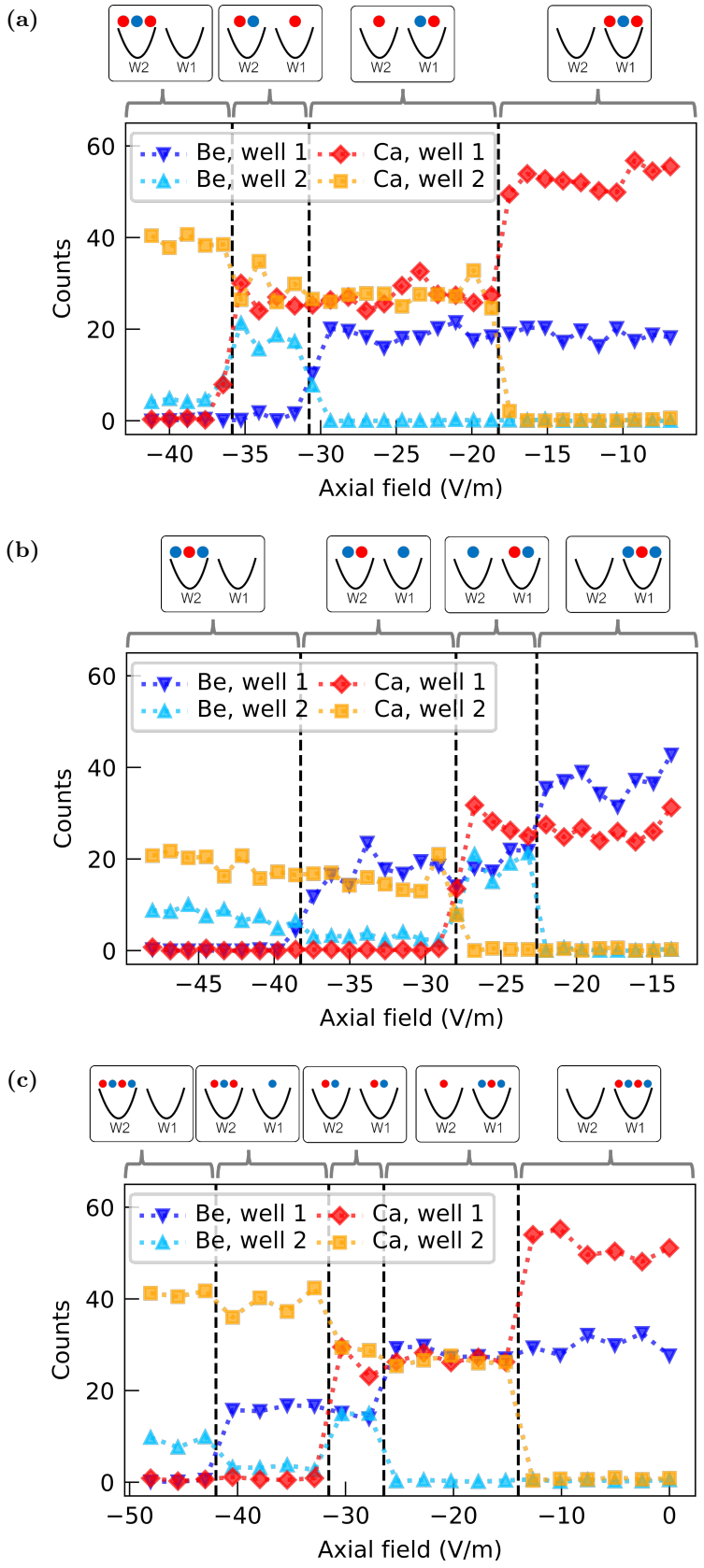

Figure 8.20: Fluorescence detention of the two wells after separation of three- and four-ion chains as a function of the axial electric field, similarly to Fig. 8.18. In particular, the crystals are: (a) Ca–Be–Ca, (b) Be–Ca–Be and (c) Ca–Be–Ca–Be. Axial field ranges depend on the ion array.

9 Motional state interferometry

In Ch. 4 I described the theory behind the Landau-Zener-Stückelberg-Majorana transitions, and discussed that consecutive interactions of two normal modes can give rise to interference of their phonon populations. In other trapped-ion systems this phenomenon was analyzed involving the internal states of an ion in [Zha+14; ISN23], but not by exploiting the motional states.

In this chapter I describe a preliminary experiment in which two vibrational modes of a single calcium ion were made to interact to obtain an interferometric measurement of their phonon occupancies. To analyze the interference we employed a modified motional coherence measurement scheme. I first describe this technique and then analyze the experimental results. This experiment serves as a test bench for a broad class of experiments involving manipulation of interacting motional states.

9.1 Motional coherence

The motional coherence of a superposition of Fock states of a vibrational mode can be measured by employing a modified Ramsey sequence. We first initialize the state of the ion in $|\downarrow, 0\rangle$ and then we apply a $\pi/2$ carrier pulse followed by a π red-sideband pulse, obtaining the state:

$$|\Psi_{\text{init}}\rangle = \frac{1}{\sqrt{2}} \left[|\downarrow, 0\rangle + |\downarrow, 1\rangle \right]. \tag{9.1}$$

The confining potential is modified to a desired one (which could involve a transport process), wait for a time t_{wait}, for then returning to the initial configuration. The whole process requires a time τ. This process induces a relative phase shift between the two Fock states:

$$|\Psi_{\text{probe}}\rangle = \frac{1}{\sqrt{2}} \left[|\downarrow, 0\rangle + e^{i\varphi(\tau)} |\downarrow, 1\rangle \right]. \tag{9.2}$$

A final sequence of π red-sideband pulse and $\pi/2$ carrier pulse induces the state:

$$|\Psi_{\text{final}}\rangle = \frac{1}{2} \left[(1 + e^{i\varphi(\tau)}) |\downarrow, 0\rangle + (1 - e^{i\varphi(\tau)}) |\uparrow, 0\rangle \right]. \tag{9.3}$$

If we scan the phase ϕ of the last carrier pulse, we can measure the probability of the spin population in $|\downarrow\rangle$ state to be:

$$P_{|\downarrow\rangle}(\tau, \phi) = \frac{1}{2} \left[1 - C(\tau) \cos(\varphi(\tau) - \phi) \right] \tag{9.4}$$

where the contrast $C(\tau)$ is 1 in the ideal case. Heating rate and fluctuations in the trap voltages make the ion experience a different $\varphi(\tau)$ at each measurement shot, reducing the contrast. By scanning ϕ, we can retrieve the contrast as a function of τ, which is then fit with an exponential decay to obtain the coherence time. In the experimental setup, the motional coherence for the axial mode of a statically confined calcium ion was measured

to be around 10 ms, while for the radial ones it reduces down to $\simeq 1$ ms due to the non-stabilized RF circuit [Flü19]. If the axial frequency changes but stays above 0.5 Mhz during the transport part, we noticed no appreciable reduction in its motional coherence. Below this threshold we noticed a drop in the contrast, due to electrical noise. Transporting the ion from the central experimental zone to any other zone reduces the coherence time by one order of magnitude, but further characterization is required to understand this better, also for the radial modes.

9.1.1 LZSM interferometry

Motional coherence was also measured for a transport process affected by mode cross-coupling. The waveform keeps the calcium ion in the central experimental zone but modifies the radial mode frequencies such that one mode intersects and interacts with the axial one, as shown in Fig. 9.1. This experiment measures the motional coherence of the axial mode by creating a superposition of Fock states, running the transport waveform, waiting for a final idle time $t_{\text{wait}} = 2.8\,\mu\text{s}$, before returning to the original configuration by an inverse transport process and measure the spin probability contrast. Both the transport and its inverse are run with decreasing speed (increasing slowdown), and the probability contrast as a function of the total transport duration is shown in Fig. 9.2.

There are several aspects to take into account. The mode cross-coupling induces a superposition between the states $|\downarrow, 0_{\text{ax}}, 0_{\text{Y}}\rangle$, $|\downarrow, 1_{\text{ax}}, 0_{\text{Y}}\rangle$ and $|\downarrow, 0_{\text{ax}}, 1_{\text{Y}}\rangle$, where the subscript indicates the mode of the state. The probability for the ion to be in the second or third state after the first mode interaction depends on the diabatic transition probability $P_{\text{D}} = \exp\left(-\pi\Delta^2/2\hbar v\right)$, introduced in Subsec. 4.5.1, which changes with the velocity of the transition v. In the process, the phase of the two states is shifted by a Stokes phase ϕ_{S} given by Eq. 4.23, which also depends on v. Afterwards, the two states acquire a relative dynamic phase ζ_1 as shown in Eq. 4.29, until they interact again when the transport process is reverted. Given that the dynamic phase depends on the difference between the two mode frequencies, which changes from $\simeq 7\,\text{kHz}$ to $\simeq 201\,\text{kHz}$ after the avoided crossing in the simulation, it reaches values that are much larger than the Stokes phase, which is in the range of $[0, \pi/4]$. The two phases are summed together to get the Stückelberg phase $\Phi_{\text{St}} = \phi_{\text{S}} + \zeta_1$. The probability for the phonon to be measured in the axial mode after returning to the original trapping configuration is given by $1 - P_{+}^{\text{double}} = 1 - 4P_{\text{D}}(1 - P_{\text{D}})\sin^2\Phi_{\text{St}}$, obtained from Eq. 4.30. Its amplitude changes depending on the transport speed, as shown in the simulation of Fig. 9.2. The final state of the ion after the π red-sideband pulse and $\pi/2$ carrier pulse is:

$$
\begin{aligned}
|\Psi_{\text{final}}\rangle = \frac{1}{2}\Big[&\left(1 + e^{i\varphi(\tau)}\left(-2i\sqrt{P_{\text{D}}(1-P_{\text{D}})}\sin(\Phi_{\text{St}})\right)\right)|\downarrow, 0_{\text{ax}}, 0_{\text{Y}}\rangle \\
&+ \left(1 - e^{i\varphi(\tau)}\left(-2i\sqrt{P_{\text{D}}(1-P_{\text{D}})}\sin(\Phi_{\text{St}})\right)\right)|\uparrow, 0_{\text{ax}}, 0_{\text{Y}}\rangle \\
&+ e^{i\theta(\tau)}\left(-P_{\text{D}}e^{-i\zeta_+} - (1-P_{\text{D}})e^{-i\zeta_-}\right)\left(|\downarrow, 0_{\text{ax}}, 1_{\text{Y}}\rangle - |\uparrow, 0_{\text{ax}}, 1_{\text{Y}}\rangle\right)\Big].
\end{aligned}
\tag{9.5}
$$

where ζ_+ and ζ_- are given in Eq. 4.29 and $\theta(\tau)$ is the dephasing between the axial and radial mode. The experimental data suggests that this dephasing reduces the maximum contrast, but a proper experimental characterization is required. Moreover, we expect that this effect is enhanced due to the coupling of an axial mode with a radial one, as the DC and RF voltages are generated by different sources.

From a comparison of the experimental data and the oscillations of $1-P_{+}^{\text{double}}$, it becomes evident that the Ramsey fringes are undersampled. A finer sampling would enable a better characterization. Furthermore, the data suggests a reduction in their oscillation range with increasing transport duration.

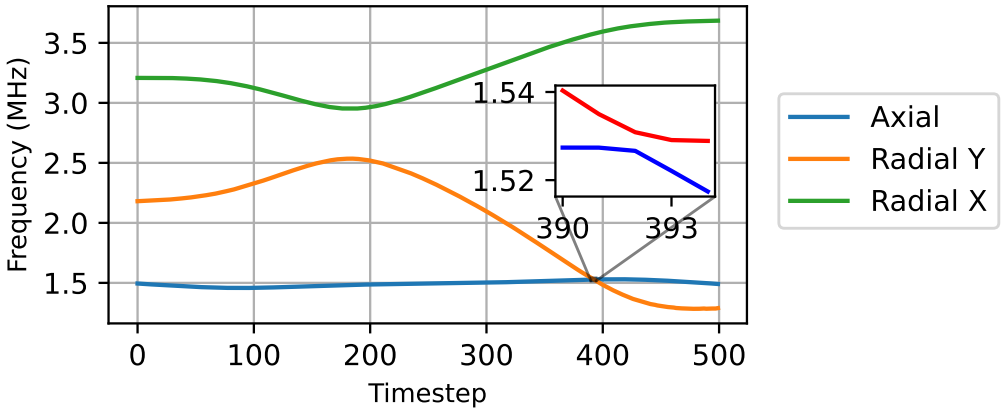

Figure 9.1: Simulation of the normal mode frequencies for the waveform employed in the LZSM interferometry experiment. The radial mode Y and the axial mode are coupled and subjected to an avoided crossing, as shown in the inset.

9.1.2 Outlook

In future experiments, the mode frequencies have to be measured precisely to better characterize the interferometer, as small deviations from the simulation would strongly affect the overall behavior. In particular, the probability of the diabatic transition is exponentially sensitive to the frequency separation at the crossing. For a simpler characterization, the experiment could be modified to perform the transport process at a constant speed, changing only the wait time t_{wait} and measuring the probability contrast. The probability of being in the $|\downarrow, 1_{\text{ax}}, 0_{\text{Y}}\rangle$ state could be measured in a simpler way by means of a red-sideband transition on the axial mode, which is possible only if the phonon populates this state. This measurement can also be performed on the radial mode to correlate the two results.

This experiment shows an application of the interaction of motional states, which can be employed in a broader range of experiments with applications in cooling of vibrational modes [Fab+24], in quantum computing and simulation with motional states [LB99; Toy+15; Che+21] and quantum sensing [DRC17]. If an ion array is employed, the mode cross-coupling between multiple vibrational modes can be exploited for creating high-dimensional entangled states, which are generally challenging to prepare [EKZ20].

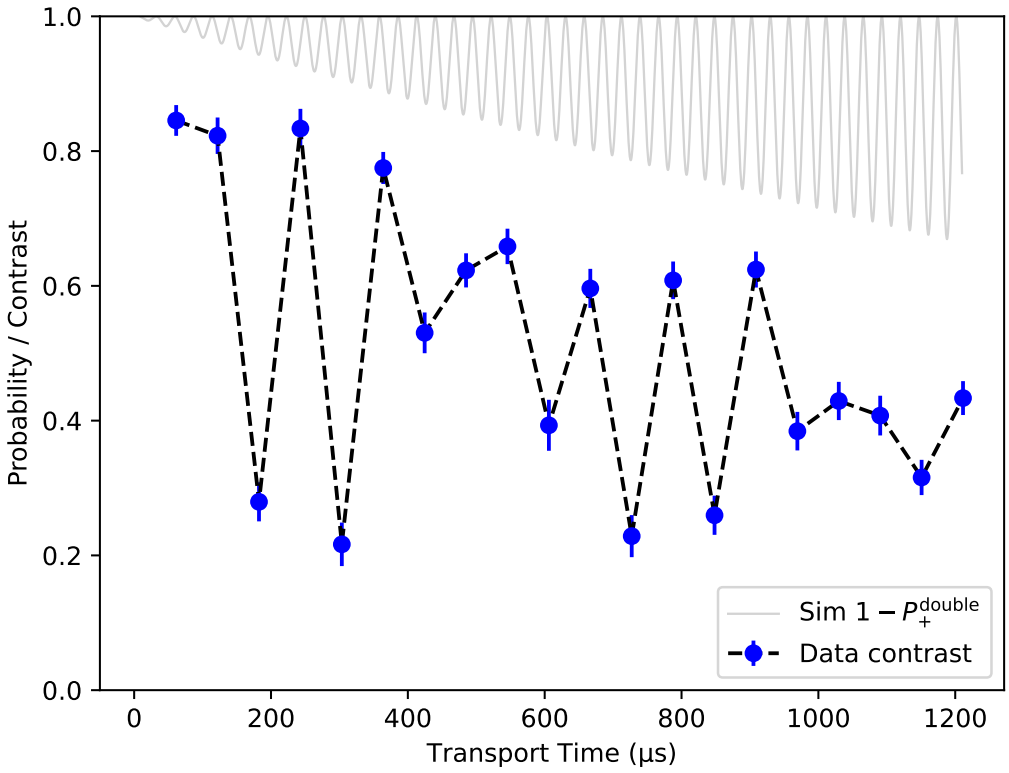

Figure 9.2: Preliminary results of the LZSM interferometer. The experimental data show the spin probability contrast, indicating that the motional coherence of the axial mode oscillates due to the coupling with the radial mode Y. The connecting lines are used solely for readability and do not indicate the actual underlying behaviour. The simulation shows the probability of finding the phonon in the axial vibrational mode after interacting two times with the radial one.

10 Summary and outlook

This thesis covers the implementation of mixed-species shuttling and reconfiguration tasks for QCCD architectures for building a scalable trapped-ion quantum computer. We investigated the working principles of ion traps involving mixed-species crystals and the main components of the experimental setup used for the experiments of this thesis. We described the set of tools necessary to manipulate and diagnose the state of the ions. We analyzed the control of cross-coupling of normal modes of motion employing different methods. We presented the control system of the setup along with its recent upgrades. We analyzed the methods we employ to compensate and account for intrinsic and excess micromotion, alongside with an analysis of the validity of the trap model. We showed the working principles and implementation of the library Pytrans used for designing waveforms to shuttle and reconfigure ion crystals, highlighting how different requirements of different waveforms are accounted for. These waveforms were then employed with single- and mixed-species ion crystals, characterizing the induced motional excitation. In this process, several sources of heating were studied and quantified, and diverse solutions for minimizing their impacts were identified. In particular the tunable interaction of different vibrational modes was employed to manipulate the motional states of the ions.

In chapter 6 we analyzed the influence of intrinsic and excess micromotion. We described the improvements in the control system to account for intrinsic micromotion, almost nullifying its impact. We also developed an automatic routine for excess micromotion compensation, which yields the required shim voltages to cancel the radial stray fields in a few minutes. By performing this compensation for a set of different trapping conditions, we noticed that manufacturing imperfections of the trap were a major source of stray fields, where the electrodes of one chip wafer have a stronger influence at the ion position than the other electrodes. We subsequently rescaled the DC voltages to account for this deviation, but this measure did not eliminate stray fields while changing trap potentials and more sophisticated methods are necessary.

In chapter 8 we described relevant experimentally-driven designing criteria related to waveforms used for static confinement, transport and separation of single and mixed-species ion crystals. We characterized heating rates caused by technical noise for the axial vibrational modes of a single calcium ion, and compared to the mixed-species case, for axial and radial vibrational modes and for different orders of the ions. We analyzed the performance of the transport process for a two-ions mixed-species array in different conditions, showing that multi-point compensation of stray fields was necessary to maintain the order of the ions. Different transport velocities were analyzed, obtaining excitations as low as $\bar{n}_{Z1} = 0.16(2)$ and $\bar{n}_{Z2} = 0.14(2)$ quanta for the axial in-phase and out-of-phase modes, respectively, after a round trip through a distance of 442 µm in 46 µs. For higher velocities, we showed the transition from the adiabatic to the diabatic regime. We also transported larger single-species crystals of up to 7 ions and mixed-species ion arrays of up to 4 ions. A full characterization was not performed, but the methods we developed allowed us to easily design ready-to-use transporting waveforms for these crystals too. We characterized the separation of single-species arrays of two $^{9}Be^{+}$ or two $^{40}Ca^{+}$ ions and measured excitations

of $\bar{n}_{Be} < 0.8$ and $\bar{n}_{Ca} < 2.3$ phonons for the axial vibrational modes respectively. These waveforms were not readily applicable to the mixed-species scenario, due to reordering induced by stray fields and coupling of vibrational modes that led to heat transfer from a hot radial mode into the axial modes, typically used for quantum gates. Multi-position compensation of stray fields prevented ion reordering, while the application of a quadrupole potential enabled decoupling of normal modes, thereby reducing the motional excitation below $\bar{n}_{\mathrm{Be}} = 1.44(9)$ and $\bar{n}_{\mathrm{Ca}} = 1.40(8)$ quanta. We also varied the separation time and demonstrated the transition into the diabatic regime. We compared the separation of ion crystals of different orders, revealing strong deviations in performance. We employed the same separation routines for longer arrays and demonstrated arbitrary separation into two parts, but no further characterization was performed. We expect that the methods we developed in this thesis can be readily applied to these larger crystals to retrieve low-excitation operations.

In chapter 9 we demonstrated the employment of cross-coupling of two vibrational modes of a calcium ion for measuring Landau-Zener-Stückelberg-Majorana interferometry. The preliminary results showed Ramsey fringes in the phonon occupancy of one of the modes as a function of the transport duration, indicating a periodic swapping between the modes. A simulation of the occupation probability was performed and suggestions for improvements of the experiment were made. Future applications for these methods involve the cooling of vibrational modes [Fab+24] and the generation of high-dimensional entangled states among several motional states [EKZ20].

The methods developed in this study pave the way for numerous potential future experiments. The in-depth characterization of the heating processes associated to transport and separation of mixed-species ion crystals could facilitate the development of an automatic optimization routine for generating and testing optimal waveforms, based on the work of [Ste+22] but applied to longer crystals. An obvious extension is to investigate further how fast such operations can be performed, aiming to control non-adiabatic operations, allowing the shuttling and reconfiguration of the crystals faster and with lower excitation [Bow+12; Rus+14; Che+10].

The capability to transport, separate and recombine arbitrary mixed-species ion crystals, along with an improved laser and control system, allows us to perform more complex algorithms in the experimental setup. These involve quantum error correction schemes [LR14; Rya+24], quantum simulation [Fos+24] or Measurement-Based Quantum Computing (MBQC), for which first studies were carried out in parallel work to this thesis [Mar20; Beh]. In the future, larger multi-zone traps, where multiple chains of ions are continuously reconfigured, will become essential to demonstrate quantum computing with many qubits [Mos+23]. This technological advantage will require a large number of optimally controlled electrical connections, automatic characterization and compensation of trapping electric fields, stable laser beams (even using integrated optics [Mor+24]) and high-fidelity quantum gates and detection.

The Pytrans library has now reached a release stage and it is available at [Mor+23]. While its documentation and certain features are still in the development phase, it is already usable by other teams. The objective is to establish a unified software framework that can be applied across various experimental setups, accelerating research and standardizing solutions for common problems in the field. It is already in use in many experiments across our research group, and I hope to see its adoption more widely in the community. Once this library is adopted by other institutes and companies, collective efforts can be made to

enhance it.

A Shim amplification board

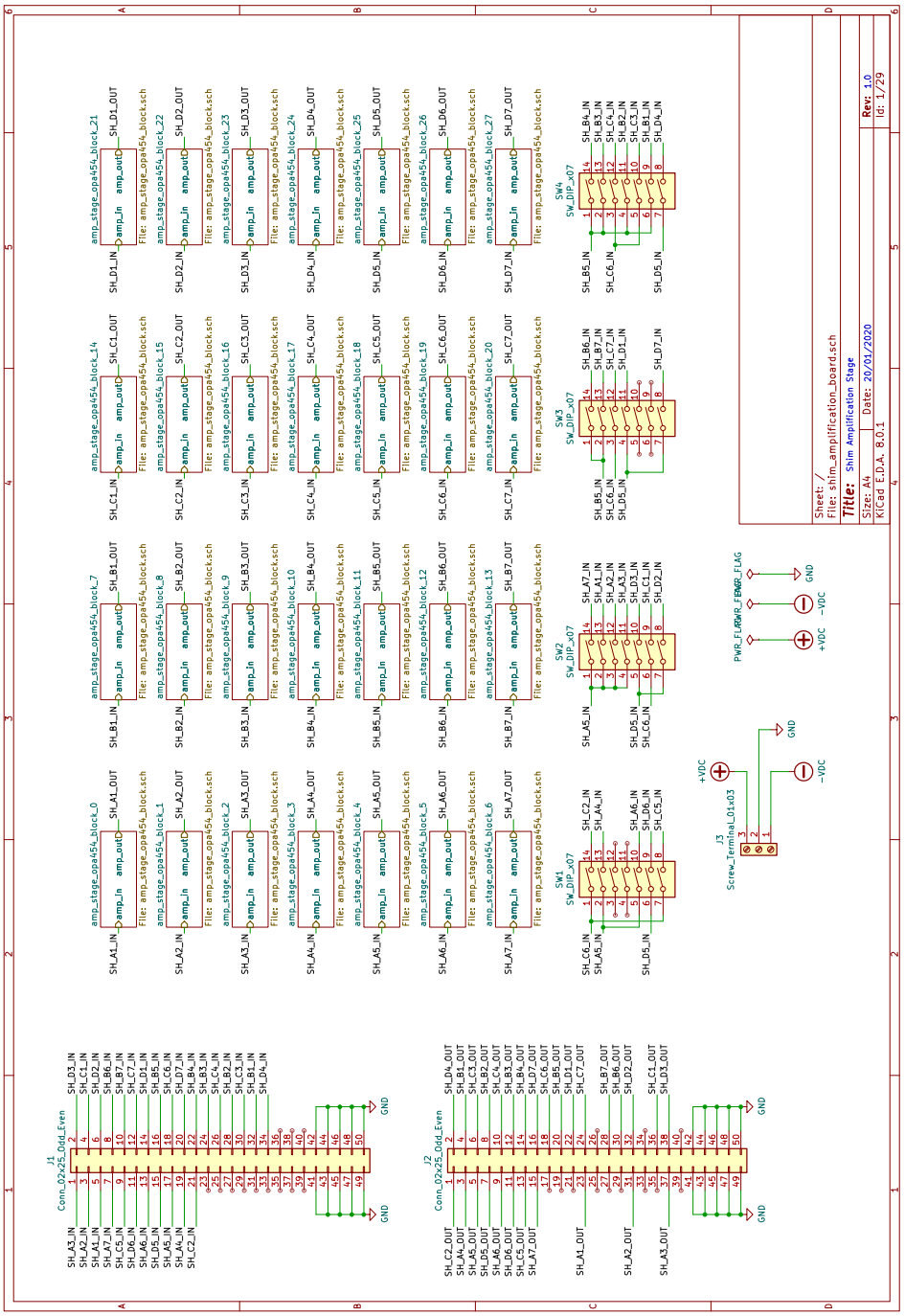

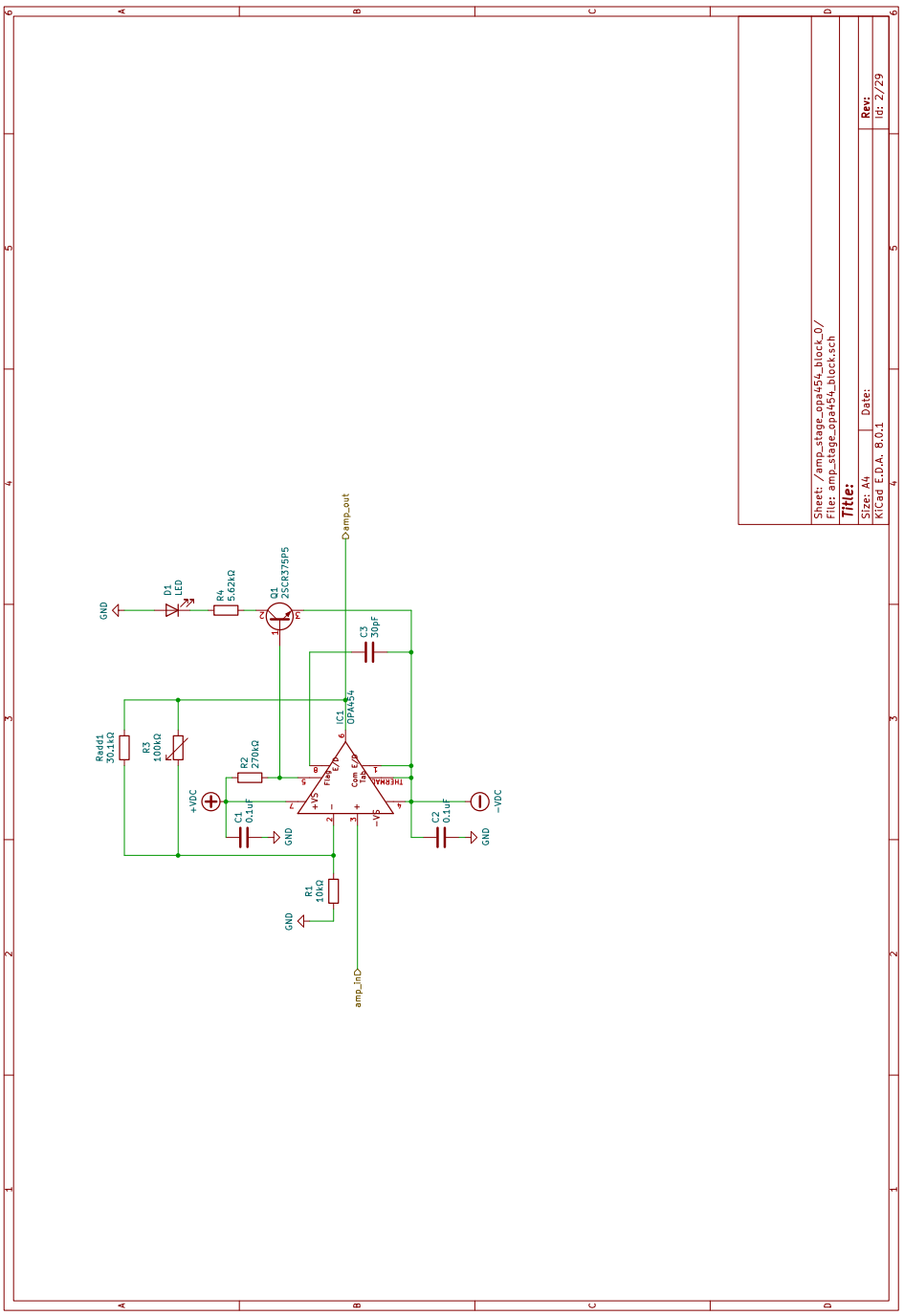
Sheet: /amp_stage_opa454_block_0/
File: amp_stage_opa454_block.sch
Title:
Size: A4
Date:
Rev:
KiCad E.D.A. 8.0.1
Id: 2/29
amp_out
GND
D1
LED
R4
5.62kΩ
Q1
2SCR375P5
C3
30pF
IC1
OPA454
Radd1
30.1kΩ
R3
100kΩ
R2
270kΩ
+VDC
C1
0.1uF
GND
−VDC
C2
0.1uF
GND
R1
10kΩ
GND
amp_inD

Bibliography

[Tur37] A. M. Turing. "On Computable Numbers, with an Application to the Entscheidungsproblem". In: *Proceedings of the London Mathematical Society* s2-42.1 (1937), pp. 230–265. DOI: 10.1112/plms/s2-42.1.230 (cit. on p. 1).

[Pre18] J. Preskill. "Quantum Computing in the NISQ era and beyond". In: *Quantum* 2 (Aug. 2018). arXiv:1801.00862 [cond-mat, physics:quant-ph], p. 79. DOI: 10.22331/q-2018-08-06-79 (cit. on p. 1).

[Aru+19] F. Arute et al. "Quantum supremacy using a programmable superconducting processor". In: *Nature* 574.7779 (Oct. 2019), pp. 505–510. DOI: 10.1038/s41586-019-1666-5 (cit. on p. 1).

[Ben82] P. Benioff. "Quantum mechanical hamiltonian models of turing machines". In: *Journal of Statistical Physics* 29.3 (Nov. 1982), pp. 515–546. DOI: 10.1007/BF01342185 (cit. on p. 1).

[Fey82] R. P. Feynman. "Simulating physics with computers". In: (1982) (cit. on p. 1).

[BB84] C. H. Bennett and G. Brassard. "Quantum cryptography: Public key distribution and coin tossing". In: *Theoretical Computer Science* 560 (1984), pp. 7–11. DOI: 10.1016/j.tcs.2014.05.025 (cit. on p. 1).

[Deu85] D. Deutsch. "Quantum theory, the Church–Turing principle and the universal quantum computer." In: 400 (1985), pp. 97–117. DOI: https://doi.org/10.1098/rspa.1985.0070 (cit. on p. 1).

[DJ92] D. Deutsch and R. Josza. "Rapid solution of problems by quantum computation". In: 439 (1992), pp. 553–558. DOI: https://doi.org/10.1098/rspa.1992.0167 (cit. on p. 1).

[BV97] E. Bernstein and U. Vazirani. "Quantum Complexity Theory". In: *SIAM Journal on Computing* 26.5 (1997). _eprint: https://doi.org/10.1137/S0097539796300921, pp. 1411–1473. DOI: 10.1137/S0097539796300921 (cit. on p. 1).

[Sim97] D. R. Simon. "On the Power of Quantum Computation". In: *SIAM Journal on Computing* 26.5 (1997). _eprint: https://doi.org/10.1137/S0097539796298637, pp. 1474–1483. DOI: 10.1137/S0097539796298637 (cit. on p. 1).

[Gro96] L. K. Grover. "A fast quantum mechanical algorithm for database search". In: *Proceedings of the Twenty-Eighth Annual ACM Symposium on Theory of Computing*. STOC '96. event-place: Philadelphia, Pennsylvania, USA. New York, NY, USA: Association for Computing Machinery, 1996, pp. 212–219. DOI: 10.1145/237814.237866 (cit. on p. 1).

[Sho94] P. Shor. "Algorithms for quantum computation: discrete logarithms and factoring". In: *Proceedings 35th Annual Symposium on Foundations of Computer Science*. 1994, pp. 124–134. DOI: 10.1109/SFCS.1994.365700 (cit. on p. 1).

[GAN14] I. M. Georgescu, S. Ashhab and F. Nori. "Quantum simulation". In: *Reviews of Modern Physics* 86.1 (Mar. 2014), pp. 153–185. DOI: 10.1103/RevModPhys.86.153 (cit. on p. 1).

[DiV00] D. P. DiVincenzo. "The Physical Implementation of Quantum Computation". In: *Fortschritte der Physik* 48.9-11 (Sept. 2000), pp. 771–783. DOI: 10.1002/1521-3978(200009)48:9/11<771::AID-PROP771>3.0.CO;2-E (cit. on p. 1).

[Deh68] H. Dehmelt. "Radiofrequency Spectroscopy of Stored Ions I: Storage". In: *Advances in Atomic and Molecular Physics*. Vol. 3. Elsevier, 1968, pp. 53–72. DOI: 10.1016/S0065-2199(08)60170-0 (cit. on pp. 1, 7).

[Pau90] W. Paul. "Electromagnetic traps for charged and neutral particles". In: *Reviews of Modern Physics* 62.3 (July 1990), pp. 531–540. DOI: 10.1103/RevModPhys.62.531 (cit. on pp. 1, 5, 6).

[Win+98] D. Wineland et al. "Experimental issues in coherent quantum-state manipulation of trapped atomic ions". In: *Journal of Research of the National Institute of Standards and Technology* 103.3 (May 1998), p. 259. DOI: 10.6028/jres.103.019 (cit. on pp. 2, 6, 8, 9, 11, 15–17, 25, 36, 37, 39, 67, 77).

[GKP01] D. Gottesman, A. Kitaev and J. Preskill. "Encoding a qubit in an oscillator". In: *Physical Review A* 64.1 (June 2001), p. 012310. DOI: 10.1103/PhysRevA.64.012310 (cit. on p. 2).

[CZ95] J. I. Cirac and P. Zoller. "Quantum Computations with Cold Trapped Ions". In: *Physical Review Letters* 74.20 (May 1995), pp. 4091–4094. DOI: 10.1103/PhysRevLett.74.4091 (cit. on p. 2).

[Lei+03] D. Leibfried et al. "Quantum dynamics of single trapped ions". In: *Reviews of Modern Physics* 75.1 (Mar. 2003), pp. 281–324. DOI: 10.1103/RevModPhys.75.281 (cit. on pp. 2, 6, 17, 20, 21, 30, 32, 37, 39).

[Wan+17] Y. Wang et al. "Single-qubit quantum memory exceeding ten-minute coherence time". In: *Nature Photonics* 11.10 (Oct. 2017), pp. 646–650. DOI: 10.1038/s41566-017-0007-1 (cit. on p. 2).

[Ste97] A. Steane. "The ion trap quantum information processor". In: *Applied Physics B: Lasers and Optics* 64.6 (June 1997), pp. 623–643. DOI: 10.1007/s003400050225 (cit. on p. 2).

[HLH22] J. Ha, J. Lee and J. Heo. "Resource analysis of quantum computing with noisy qubits for Shor's factoring algorithms". In: *Quantum Information Processing* 21.2 (Feb. 2022), p. 60. DOI: 10.1007/s11128-021-03398-1 (cit. on p. 2).

[MK13] C. Monroe and J. Kim. "Scaling the Ion Trap Quantum Processor". In: *Science* 339.6124 (Mar. 2013), pp. 1164–1169. DOI: 10.1126/science.1231298 (cit. on p. 2).

[KMW02] D. Kielpinski, C. Monroe and D. J. Wineland. "Architecture for a large-scale ion-trap quantum computer". In: *Nature* 417.6890 (June 2002), pp. 709–711. DOI: 10.1038/nature00784 (cit. on p. 2).

[Kau+20] V. Kaushal et al. "Shuttling-based trapped-ion quantum information processing". In: *AVS Quantum Science* 2.1 (Feb. 2020), p. 014101. DOI: 10.1116/1.5126186 (cit. on p. 2).

[Mos+23] S. A. Moses et al. "A Race-Track Trapped-Ion Quantum Processor". In: *Physical Review X* 13.4 (Dec. 2023), p. 041052. DOI: 10.1103/PhysRevX.13.041052 (cit. on pp. 2, 109).

[Meh+20] K. K. Mehta et al. "Integrated optical multi-ion quantum logic". In: *Nature* 586.7830 (Oct. 2020), pp. 533–537. DOI: 10.1038/s41586-020-2823-6 (cit. on p. 2).

[MAB23] M. Malinowski, D. Allcock and C. Ballance. "How to Wire a 1000 - Qubit Trapped-Ion Quantum Computer". In: *PRX Quantum* 4.4 (Oct. 2023), p. 040313. DOI: 10.1103/PRXQuantum.4.040313 (cit. on p. 2).

[Kie+00] D. Kielpinski et al. "Sympathetic cooling of trapped ions for quantum logic". In: *Physical Review A* 61.3 (Feb. 2000), p. 032310. DOI: 10.1103/PhysRevA.61.032310 (cit. on pp. 2, 13, 15–17).

[HRB08] H. Haffner, C. Roos and R. Blatt. "Quantum computing with trapped ions". In: *Physics Reports* 469.4 (Dec. 2008), pp. 155–203. DOI: 10.1016/j.physrep.2008.09.003 (cit. on p. 2).

[Bar+03] M. D. Barrett et al. "Sympathetic cooling of 9 Be + and 24 Mg + for quantum logic". In: *Physical Review A* 68.4 (Oct. 2003), p. 042302. DOI: 10.1103/PhysRevA.68.042302 (cit. on p. 2).

[Hom+09] J. P. Home et al. "Complete Methods Set for Scalable Ion Trap Quantum Information Processing". In: *Science* 325.5945 (Sept. 2009). Publisher: American Association for the Advancement of Science, pp. 1227–1230. DOI: 10.1126/science.1177077 (cit. on pp. 2, 76).

[Wan+19] Y. Wan et al. "Quantum gate teleportation between separated qubits in a trapped-ion processor". In: *Science* 364.6443 (May 2019), pp. 875–878. DOI: 10.1126/science.aaw9415 (cit. on p. 2).

[Pin+21] J. M. Pino et al. "Demonstration of the trapped-ion quantum CCD computer architecture". In: *Nature* 592.7853 (Apr. 2021), pp. 209–213. DOI: 10.1038/s41586-021-03318-4 (cit. on p. 2).

[Rya+21] C. Ryan-Anderson et al. "Realization of Real-Time Fault-Tolerant Quantum Error Correction". In: *Physical Review X* 11.4 (Dec. 2021), p. 041058. DOI: 10.1103/PhysRevX.11.041058 (cit. on p. 2).

[Row+02] M. A. Rowe et al. *Transport of Quantum States and Separation of Ions in a Dual RF Ion Trap*. arXiv:quant-ph/0205094. May 2002 (cit. on pp. 2, 76, 85).

[Lei+07] D. Leibfried et al. "Transport quantum logic gates for trapped ions". In: *Physical Review A* 76.3 (Sept. 2007), p. 032324. DOI: 10.1103/PhysRevA.76.032324 (cit. on p. 2).

[Bow+12] R. Bowler et al. "Coherent Diabatic Ion Transport and Separation in a Multizone Trap Array". In: *Physical Review Letters* 109.8 (Aug. 2012), p. 080502. DOI: 10.1103/PhysRevLett.109.080502 (cit. on pp. 2, 76, 77, 84, 85, 99, 109).

[Wal+12] A. Walther et al. "Controlling Fast Transport of Cold Trapped Ions". In: *Physical Review Letters* 109.8 (Aug. 2012), p. 080501. DOI: 10.1103/PhysRevLett.109.080501 (cit. on pp. 2, 76, 77, 84, 99).

[Rus+14] T. Ruster et al. "Experimental realization of fast ion separation in segmented Paul traps". In: *Physical Review A* 90.3 (Sept. 2014), p. 033410. DOI: 10.1103/PhysRevA.90.033410 (cit. on pp. 2, 37, 38, 77, 85, 109).

[Kau+14] H. Kaufmann et al. "Dynamics and control of fast ion crystal splitting in segmented Paul traps". In: *New Journal of Physics* 16.7 (July 2014), p. 073012. DOI: 10.1088/1367-2630/16/7/073012 (cit. on pp. 2, 70, 85).

[CE15] D. Clercq and L. E. "Transport Quantum Logic Gates for Trapped Ions". Accepted: 2017-09-28T12:21:23Z. Doctoral Thesis. ETH Zurich, 2015. DOI: 10.3929/ethz-a-010584586 (cit. on p. 2).

[Ste+22] J. D. Sterk et al. "Closed-loop optimization of fast trapped-ion shuttling with sub-quanta excitation". In: *npj Quantum Information* 8.1 (June 2022). Number: 1 Publisher: Nature Publishing Group, pp. 1–6. DOI: 10.1038/s41534-022-00579-3 (cit. on pp. 2, 76, 102, 109).

[Cla+23] C. R. Clark et al. "Characterization of fast ion transport via position-dependent optical deshelving". In: *Physical Review A* 107.4 (Apr. 2023), p. 043119. DOI: 10.1103/PhysRevA.107.043119 (cit. on p. 2).

[Bar+04] M. D. Barrett et al. "Deterministic quantum teleportation of atomic qubits". In: *Nature* 429.6993 (June 2004), pp. 737–739. DOI: 10.1038/nature02608 (cit. on pp. 2, 76, 85).

[Lo15] H.-Y. Lo. "Creation of Squeezed Schrödinger's Cat States in a Mixed-Species Ion Trap". Accepted: 2017-09-28T08:11:10Z. Doctoral Thesis. ETH Zurich, 2015. DOI: 10.3929/ethz-a-010592649 (cit. on pp. 3, 25–27).

[Mor+23] C. Mordini et al. *pytrans*. Nov. 2023. DOI: 10.5281/zenodo.10204606 (cit. on pp. 3, 66, 109).

[Neg18] V. Negnevitsky. "Feedback-stabilised quantum states in a mixed-species ion system". PhD thesis. ETH Zürich, 2018 (cit. on pp. 3, 12, 15, 48, 49, 57, 66, 68, 69, 77, 80, 85, 86).

[Sch+05] P. O. Schmidt et al. "Spectroscopy Using Quantum Logic". In: *Science* 309.5735 (July 2005), pp. 749–752. DOI: 10.1126/science.1114375 (cit. on p. 3).

[Kin+22] S. A. King et al. "An optical atomic clock based on a highly charged ion". In: *Nature* 611.7934 (Nov. 2022), pp. 43–47. DOI: 10.1038/s41586-022-05245-4 (cit. on p. 3).

[Sch+23] N. Schwegler et al. "Trapping and Ground-State Cooling of a Single H 2 +". In: *Physical Review Letters* 131.13 (Sept. 2023), p. 133003. DOI: 10.1103/PhysRevLett.131.133003 (cit. on p. 3).

[Cor+21] J. M. Cornejo et al. "Quantum logic inspired techniques for spacetime-symmetry tests with (anti-)protons". In: *New Journal of Physics* 23.7 (July 2021), p. 073045. DOI: 10.1088/1367-2630/ac136e (cit. on p. 3).

[ISN23] O. V. Ivakhnenko, S. N. Shevchenko and F. Nori. "Nonadiabatic Landau-Zener-Stückelberg-Majorana transitions, dynamics, and interference". In: *Physics Reports* 995 (Jan. 2023). arXiv:2203.16348 [cond-mat, physics:quant-ph], pp. 1–89. DOI: 10.1016/j.physrep.2022.10.002 (cit. on pp. 3, 39–42, 104).

[LB99] S. Lloyd and S. L. Braunstein. "Quantum Computation over Continuous Variables". In: *PHYSICAL REVIEW LETTERS* 82.8 (1999) (cit. on pp. 3, 106).

[McL47] N. McLachlan. *Theory and Application of Mathieu Functions*. Clarendon Press, 1947 (cit. on p. 6).

[Mal21] M. Malinowski. "Unitary and Dissipative Trapped-Ion Entanglement Using Integrated Optics". Accepted: 2021-11-24T07:09:27Z. Doctoral Thesis. ETH Zurich, 2021. DOI: 10.3929/ethz-b-000516613 (cit. on p. 8).

[Kie15] D. Kienzler. "Quantum Harmonic Oscillator State Synthesis by Reservoir Engineering". Accepted: 2017-08-21T10:05:10Z. Doctoral Thesis. ETH Zurich, 2015. DOI: 10.3929/ethz-a-010479887 (cit. on pp. 8, 10, 11, 13, 25, 27, 28, 53–55).

[Ami+11] J. Amini et al. "Microfabricated Chip Traps for Ions". In: Atom Chips, WILEY-VCH Verlag, Weinheim, -1, Apr. 2011 (cit. on pp. 8, 10, 30, 75).

[Zha21] C. Zhang. "Scalable technologies for surface-electrode ion traps". Accepted: 2022-03-10T09:28:40Z. Doctoral Thesis. ETH Zurich, 2021. DOI: 10.3929/ethz-b-000536415 (cit. on pp. 8, 34).

[Ber+98] D. J. Berkeland et al. "Minimization of ion micromotion in a Paul trap". In: *Journal of Applied Physics* 83.10 (May 1998), pp. 5025–5033. DOI: 10.1063/1.367318 (cit. on pp. 8, 9, 59).

[Kel+15] J. Keller et al. "Precise determination of micromotion for trapped-ion optical clocks". In: *Journal of Applied Physics* 118.10 (Sept. 2015), p. 104501. DOI: 10.1063/1.4930037 (cit. on pp. 8, 59).

[Ber+17] A. Bermudez et al. "Micromotion-enabled improvement of quantum logic gates with trapped ions". In: *New Journal of Physics* 19.11 (Nov. 2017), p. 113038. DOI: 10.1088/1367-2630/aa86eb (cit. on p. 8).

[Hom13] J. P. Home. "Quantum Science and Metrology with Mixed-Species Ion Chains". In: *Advances In Atomic, Molecular, and Optical Physics*. Vol. 62. Elsevier, 2013, pp. 231–277. DOI: 10.1016/B978-0-12-408090-4.00004-9 (cit. on pp. 9, 13, 14, 19, 22, 30, 35, 36, 78, 99).

[Bla+09] R. B. Blakestad et al. "High-Fidelity Transport of Trapped-Ion Qubits through an X -Junction Trap Array". In: *Physical Review Letters* 102.15 (Apr. 2009), p. 153002. DOI: 10.1103/PhysRevLett.102.153002 (cit. on p. 11).

[Cle15] L. D. Clerq. "Transport Quantum Logic Gates for Trapped Ions". PhD thesis. ETH Zürich, 2015 (cit. on pp. 12, 49, 55, 66).

[Col18] P. Colciaghi. "Towards the Realisation of Transport Entangling Gates with Trapped Ions". MA thesis. ETH Zurich, 2018 (cit. on pp. 13, 53).

[Mar20] M. Marinelli. "Quantum information processing with mixed-species ion crystals". Accepted: 2020-06-15T08:39:34Z. Doctoral Thesis. ETH Zurich, 2020. DOI: 10.3929/ethz-b-000420229 (cit. on pp. 13, 15, 21, 25, 27, 30, 32, 48, 79, 80, 83, 109).

[SCM21] K. Sosnova, A. Carter and C. Monroe. "Character of motional modes for entanglement and sympathetic cooling of mixed-species trapped-ion chains". In: *Physical Review A* 103.1 (Jan. 2021), p. 012610. DOI: 10.1103/PhysRevA.103.012610 (cit. on p. 14).

[Wüb+12] J. B. Wübbena et al. "Sympathetic cooling of mixed-species two-ion crystals for precision spectroscopy". In: *Physical Review A* 85.4 (Apr. 2012), p. 043412. DOI: 10.1103/PhysRevA.85.043412 (cit. on pp. 15, 17).

[Lin+09] G.-D. Lin et al. “Large-scale quantum computation in an anharmonic linear ion trap”. In: *EPL (Europhysics Letters)* 86.6 (June 2009), p. 60004. DOI: 10.1209/0295-5075/86/60004 (cit. on p. 17).

[Lo+14] H.-Y. Lo et al. “All-solid-state continuous-wave laser systems for ionization, cooling and quantum state manipulation of beryllium ions”. In: *Applied Physics B* 114.1-2 (Jan. 2014), pp. 17–25. DOI: 10.1007/s00340-013-5605-0 (cit. on pp. 25, 54).

[Saw+15] B. C. Sawyer et al. “Reversing hydride-ion formation in quantum-information experiments with Be +”. In: *Physical Review A* 91.1 (Jan. 2015), p. 011401. DOI: 10.1103/PhysRevA.91.011401 (cit. on p. 26).

[Hom+06] J. P. Home et al. “Deterministic entanglement and tomography of ion–spin qubits”. In: *New Journal of Physics* 8.9 (Sept. 2006), pp. 188–188. DOI: 10.1088/1367-2630/8/9/188 (cit. on p. 28).

[Pos+09] U. G. Poschinger et al. “Coherent manipulation of a ^{40} Ca $^{+}$ spin qubit in a micro ion trap”. In: *Journal of Physics B: Atomic, Molecular and Optical Physics* 42.15 (Aug. 2009), p. 154013. DOI: 10.1088/0953-4075/42/15/154013 (cit. on p. 28).

[Rus+16] T. Ruster et al. “A long-lived Zeeman trapped-ion qubit”. In: *Applied Physics B* 122.10 (Oct. 2016), p. 254. DOI: 10.1007/s00340-016-6527-4 (cit. on p. 28).

[MEK00] G. Morigi, J. Eschner and C. H. Keitel. “Ground State Laser Cooling Using Electromagnetically Induced Transparency”. In: *Physical Review Letters* 85.21 (Nov. 2000), pp. 4458–4461. DOI: 10.1103/PhysRevLett.85.4458 (cit. on p. 32).

[Lee+05] P. J. Lee et al. “Phase control of trapped ion quantum gates”. In: *Journal of Optics B: Quantum and Semiclassical Optics* 7.10 (Oct. 2005), S371–S383. DOI: 10.1088/1464-4266/7/10/025 (cit. on p. 34).

[Flü19] C. Flühmann. “Encoding a qubit in the motion of a trapped ion using superpositions of displaced squeezed states”. Accepted: 2020-07-31T07:02:11Z. Doctoral Thesis. ETH Zurich, 2019. DOI: 10.3929/ethz-b-000355836 (cit. on pp. 36, 55, 105).

[Hom+11] J. P. Home et al. “Normal modes of trapped ions in the presence of anharmonic trap potentials”. In: *New Journal of Physics* 13.7 (July 2011), p. 073026. DOI: 10.1088/1367-2630/13/7/073026 (cit. on pp. 38, 39, 67, 70, 77, 97, 101).

[Hom06] J. Home. “Entanglement of two trapped-ion spin qubits”. PhD Thesis. Oxford University, 2006 (cit. on p. 38).

[Kin+21] S. A. King et al. “Algorithmic Ground-State Cooling of Weakly Coupled Oscillators Using Quantum Logic”. In: *Physical Review X* 11.4 (Dec. 2021), p. 041049. DOI: 10.1103/PhysRevX.11.041049 (cit. on p. 39).

[SS21] R. T. Sutherland and R. Srinivas. “Universal hybrid quantum computing in trapped ions”. In: *Physical Review A* 104.3 (Sept. 2021), p. 032609. DOI: 10.1103/PhysRevA.104.032609 (cit. on p. 39).

[MSJ03] C. Marquet, F. Schmidt-Kaler and D. James. “Phonon-phonon interactions due to non-linear effects in a linear ion trap”. In: *Applied Physics B: Lasers and Optics* 76.3 (Mar. 2003), pp. 199–208. DOI: 10.1007/s00340-003-1097-7 (cit. on pp. 39, 77).

[NRJ09] X. R. Nie, C. F. Roos and D. F. James. "Theory of cross phase modulation for the vibrational modes of trapped ions". In: *Physics Letters A* 373.4 (Jan. 2009), pp. 422–425. DOI: 10.1016/j.physleta.2008.11.045 (cit. on p. 39).

[Din+17] S. Ding et al. "Cross-Kerr Nonlinearity for Phonon Counting". In: *Physical Review Letters* 119.19 (Nov. 2017), p. 193602. DOI: 10.1103/PhysRevLett.119.193602 (cit. on p. 39).

[Gor+14] D. J. Gorman et al. "Two-mode coupling in a single-ion oscillator via parametric resonance". In: *Physical Review A* 89.6 (June 2014), p. 062332. DOI: 10.1103/PhysRevA.89.062332 (cit. on p. 39).

[Lan32] L. Landau. "Zur theorie der energieubertragung. II". In: *Physikalische Zeitschrift der Sowjetunion* 2 (1932), p. 46 (cit. on p. 39).

[Zen32] C. Zener. "Non-adiabatic crossing of energy levels". In: *Proceedings of the Royal Society of London. Series A, Containing Papers of a Mathematical and Physical Character* 137.833 (1932). Publisher: The Royal Society London, pp. 696–702 (cit. on p. 39).

[Stu32] E. Stueckelberg. "Theorie der unelastischen Stösse zwischen Atomen". In: *Helv. Phys. Acta* 5 (1932), p. 369 (cit. on p. 39).

[Maj32] E. Majorana. "Atomi orientati in campo magnetico variabile". In: *Il Nuovo Cimento (1924-1942)* 9.2 (1932). Publisher: Springer, pp. 43–50 (cit. on p. 39).

[Nov10] L. Novotny. "Strong coupling, energy splitting, and level crossings: A classical perspective". In: *American Journal of Physics* 78.11 (Nov. 2010), pp. 1199–1202. DOI: 10.1119/1.3471177 (cit. on p. 39).

[ISN18] O. V. Ivakhnenko, S. N. Shevchenko and F. Nori. "Simulating quantum dynamical phenomena using classical oscillators: Landau-Zener-Stückelberg-Majorana interferometry, latching modulation, and motional averaging". In: *Scientific Reports* 8.1 (Aug. 2018). Number: 1 Publisher: Nature Publishing Group, p. 12218. DOI: 10.1038/s41598-018-28993-8 (cit. on p. 39).

[BF28] M. Born and V. Fock. "Beweis des Adiabatensatzes". In: *Zeitschrift für Physik* 51.3-4 (Mar. 1928), pp. 165–180. DOI: 10.1007/BF01343193 (cit. on p. 40).

[GS23] E. P. Glasbrenner and W. P. Schleich. "The Landau–Zener formula made simple". In: *Journal of Physics B: Atomic, Molecular and Optical Physics* 56.10 (May 2023), p. 104001. DOI: 10.1088/1361-6455/acc774 (cit. on p. 40).

[SZ97] M. O. Scully and M. S. Zubairy. *Quantum Optics*. Cambridge University Press, 1997 (cit. on p. 41).

[Fab+24] M. I. Fabrikant et al. *Cooling trapped ions with phonon rapid adiabatic passage*. arXiv:2403.02315 [physics, physics:quant-ph]. Mar. 2024 (cit. on pp. 43, 44, 46, 106, 109).

[Hou+24] P.-Y. Hou et al. "Indirect Cooling of Weakly Coupled Trapped-Ion Mechanical Oscillators". In: *Physical Review X* 14.2 (Apr. 2024). arXiv:2308.05158 [physics, physics:quant-ph], p. 021003. DOI: 10.1103/PhysRevX.14.021003 (cit. on p. 46).

[Sta] M. Stadler. "To be published". Doctoral Thesis. ETH Zurich (cit. on p. 48).

[Beh] T. Behrle. "To be published". Doctoral Thesis. ETH Zurich (cit. on pp. 48, 52, 109).

[Nee] B. de Neeve. "To be published". Doctoral Thesis. ETH Zurich (cit. on p. 48).

[Fou12] R. P. Foundation. *Raspberry Pi, https://www.raspberrypi.org/*. 2012 (cit. on p. 48).

[Nad16] D. P. Nadlinger. "Experimental control and benchmarking for single-qubit trapped-ion transport gates". In: (2016) (cit. on pp. 49, 50).

[65] *Analog Devices, https://www.analog.com/en/index.html*. 1965 (cit. on p. 52).

[Hor15] P. Horowitz. *The art of electronics*. Third edition. New York, NY: Cambridge University Press, 2015 (cit. on p. 53).

[Top98] Toptica. *Toptica, https://www.toptica.com/products/tunable-diode-lasers/ecdl-dfb-lasers/dl-pro*. 1998 (cit. on p. 54).

[Luc+04] D. Lucas et al. "Isotope-selective photoionization for calcium ion trapping". In: *Physical Review A* 69.1 (Jan. 2004), p. 012711. DOI: 10.1103/PhysRevA.69.012711 (cit. on p. 54).

[89] *Thorlabs, Inc., https://www.thorlabs.com*. 1989 (cit. on p. 54).

[Ara21] T. Araki. *Error Signal Generation for Ultrastable Voltage Source*. 2021 (cit. on p. 55).

[Fab21] G. Fabris. "Error Signal Generator for Ultrastable Voltage Source". In: (2021) (cit. on p. 55).

[08] *QUBIG GmbH, https://www.qubig.com/*. 2008 (cit. on p. 57).

[68] *Mini Circuits, https://www.minicircuits.com/*. 1968 (cit. on p. 58).

[ITU11] Y. Ibaraki, U. Tanaka and S. Urabe. "Detection of parametric resonance of trapped ions for micromotion compensation". In: *Applied Physics B* 105.2 (Nov. 2011), pp. 219–223. DOI: 10.1007/s00340-011-4463-x (cit. on p. 60).

[Nad+21] D. P. Nadlinger et al. *Micromotion minimisation by synchronous detection of parametrically excited motion*. arXiv:2107.00056 [physics, physics:quant-ph]. June 2021 (cit. on p. 60).

[LL76] L. D. Landau and E. M. Lifshitz. *Mechanics*. 3d ed. Course of theoretical physics v. 1. Oxford New York: Pergamon Press, 1976 (cit. on p. 61).

[Rob15] Robin Oswald. *Velocity Control of Trapped Ions for Transport Quantum Logic Gates*. 2015 (cit. on pp. 66, 69).

[Agr+18] A. Agrawal et al. "A rewriting system for convex optimization problems". In: *Journal of Control and Decision* 5.1 (Jan. 2018), pp. 42–60. DOI: 10.1080/23307706.2017.1397554 (cit. on p. 69).

[DB16] S. Diamond and S. Boyd. "CVXPY: A Python-Embedded Modeling Language for Convex Optimization". In: 17.83 (2016), pp. 1–5 (cit. on p. 69).

[MOS19] MOSEK ApS. *MOSEK Optimizer API for Python 10.1.17*. 2019 (cit. on p. 69).

[HS05] J. P. Home and A. M. Steane. *Electrode Configurations for Fast Separation of Trapped Ions*. arXiv:quant-ph/0411102. Sept. 2005 (cit. on pp. 70, 85).

[Van+22] M. W. Van Mourik et al. "rf-induced heating dynamics of noncrystallized trapped ions". In: *Physical Review A* 105.3 (Mar. 2022), p. 033101. DOI: 10.1103/PhysRevA.105.033101 (cit. on p. 72).

[Für+14] H. A. Fürst et al. "Controlling the transport of an ion: classical and quantum mechanical solutions". In: *New Journal of Physics* 16.7 (July 2014), p. 075007. DOI: 10.1088/1367-2630/16/7/075007 (cit. on pp. 73, 76).

[Mor+24] C. Mordini et al. *Multi-zone trapped-ion qubit control in an integrated photonics QCCD device*. arXiv:2401.18056 [physics, physics:quant-ph]. Feb. 2024 (cit. on pp. 74, 109).

[Jai+23] S. Jain et al. *Unit cell of a Penning micro-trap quantum processor*. arXiv:2308.07672 [quant-ph]. Aug. 2023 (cit. on p. 74).

[Lan+24] F. Lancellotti et al. "Low-excitation transport and separation of high-mass-ratio mixed-species ion chains". In: *Physical Review Research* 6.3 (Sept. 2024), p. L032059. DOI: 10.1103/PhysRevResearch.6.L032059 (cit. on pp. 75, 84, 88, 89, 93, 99, 101).

[Sch+06] S. Schulz et al. "Optimization of segmented linear Paul traps and transport of stored particles". In: *Fortschritte der Physik* 54.8-10 (2006). _eprint: https://onlinelibrary.wiley.com/doi/pdf/10.1002/prop.200610324, pp. 648–665. DOI: 10.1002/prop.200610324 (cit. on p. 76).

[Tor+11] E. Torrontegui et al. "Fast atomic transport without vibrational heating". In: *Physical Review A* 83.1 (Jan. 2011), p. 013415. DOI: 10.1103/PhysRevA.83.013415 (cit. on p. 76).

[Lu+14] X.-J. Lu et al. "Fast shuttling of a trapped ion in the presence of noise". In: *Physical Review A* 89.6 (June 2014), p. 063414. DOI: 10.1103/PhysRevA.89.063414 (cit. on p. 76).

[LJ11] H.-K. Lau and D. F. V. James. "Decoherence and dephasing errors caused by the dc Stark effect in rapid ion transport". In: *Physical Review A* 83.6 (June 2011), p. 062330. DOI: 10.1103/PhysRevA.83.062330 (cit. on p. 76).

[Che+10] X. Chen et al. "Fast Optimal Frictionless Atom Cooling in Harmonic Traps: Shortcut to Adiabaticity". In: *Physical Review Letters* 104.6 (Feb. 2010), p. 063002. DOI: 10.1103/PhysRevLett.104.063002 (cit. on pp. 77, 109).

[Bro+15] M. Brownnutt et al. "Ion-trap measurements of electric-field noise near surfaces". In: *Reviews of Modern Physics* 87.4 (Dec. 2015). arXiv:1409.6572 [quant-ph], pp. 1419–1482. DOI: 10.1103/RevModPhys.87.1419 (cit. on p. 78).

[Bla+11] R. B. Blakestad et al. "Near-ground-state transport of trapped-ion qubits through a multidimensional array". In: *Physical Review A* 84.3 (Sept. 2011), p. 032314. DOI: 10.1103/PhysRevA.84.032314 (cit. on p. 82).

[Zha+14] J. Zhang et al. "Realization of geometric Landau-Zener-Stückelberg interferometry". In: *Physical Review A* 89.1 (Jan. 2014), p. 013608. DOI: 10.1103/PhysRevA.89.013608 (cit. on p. 104).

[Toy+15] K. Toyoda et al. "Hong–Ou–Mandel interference of two phonons in trapped ions". In: *Nature* 527.7576 (Nov. 2015), pp. 74–77. DOI: 10.1038/nature15735 (cit. on p. 106).

[Che+21] W. Chen et al. "Quantum computation and simulation with vibrational modes of trapped ions". In: *Chinese Physics B* 30.6 (June 2021), p. 060311. DOI: 10.1088/1674-1056/ac01e3 (cit. on p. 106).

[DRC17] C. L. Degen, F. Reinhard and P. Cappellaro. "Quantum sensing". In: *Reviews of Modern Physics* 89.3 (July 2017), p. 035002. DOI: 10.1103/RevModPhys.89.035002 (cit. on p. 106).

[EKZ20] M. Erhard, M. Krenn and A. Zeilinger. "Advances in high-dimensional quantum entanglement". In: *Nature Reviews Physics* 2.7 (June 2020), pp. 365–381. DOI: 10.1038/s42254-020-0193-5 (cit. on pp. 106, 109).

[LR14] A. J. Landahl and C. Ryan-Anderson. *Quantum computing by color-code lattice surgery*. arXiv:1407.5103 [quant-ph]. July 2014 (cit. on p. 109).

[Rya+24] C. Ryan-Anderson et al. "High-fidelity teleportation of a logical qubit using transversal gates and lattice surgery". In: *Science* 385.6715 (Sept. 2024), pp. 1327–1331. DOI: 10.1126/science.adp6016 (cit. on p. 109).

[Fos+24] M. Foss-Feig et al. *Progress in Trapped-Ion Quantum Simulation*. arXiv:2409.02990 [cond-mat, physics:quant-ph]. Sept. 2024 (cit. on p. 109).